Effects of Secondary Electron Emission on the Plasma Sheath and Local Electron Energy Distribution with Application to Hall Thrusters

by

Kapil Umesh Sawlani

A dissertation submitted in partial fulfillment
of the requirements for the degree of
Doctor of Philosophy
(Nuclear Engineering and Radiological Sciences)
in The University of Michigan
2015

Doctoral Committee:

Associate Professor John E. Foster, Chair
Professor Alec D. Gallimore
Professor Ronald M. Gilgenbach
Professor Mark J. Kushner
Yevgeny Raitses, Princeton Plasma Physics Laboratory

"*If you want to inform yourself only roughly about something, present a paper about the subject; but, if you want to gain an in-depth knowledge about it - you have to write a book.*"

- Richard Kieffer

To my parents and uncle Jay Datwani.

Thank you for the constant support and believing in me.

ACKNOWLEDGEMENTS

The journey to achieve this degree has been a very interesting one. From the kid who didn't really want to study to the high school student who was very interested in everything mechanical and wanted to be a rocket scientist some day. Having been through various peaks and valleys of academic environment and expectations, I would like to say the overall journey was worth it. This achievement would not have been even remotely possible had it not been through the support, guidance and encouragement from various people. This section lists only a few of them but there are so many many more that I will always remember and thank for what they did in order to shape my success at different points.

Firstly, I would like to thank Prof. John E. Foster, my dissertation advisor as well as mentor, who has been encouraging me to succeed through out the journey as well as has been patient with me. Before being my thesis advisor, he was the first professor whose class (NERS 471 - Introduction to Plasma Physics and Controlled Fusion) I enrolled in at the University of Michigan. My desire to learn more about space propulsion existed since my undergraduate days and being presented an opportunity to discuss and work on this project was rewarding. With Prof. Foster I had the opportunity to work on many other projects over the years which will definitely help me through my career. All I can say is, thank you for all the opportunities provided to me. The number of skills learned in the duration would not have been possible at any other place or time.

Secondly, my committee members who have been supportive through out the

Ph.D. process - Prof Gallimore, Prof. Gilgenbach, Prof. Kushner and Dr. Raitses. There was a lot I learned from you in classes that you offered and our personal interactions, as well as part of my PhD experience. The guidance helped me think better about tough problems.

In addition to the academic faculty, having good colleagues and friends made the journey a lot easier. The members from Plasma Science and Technology Laboratory - Aimee, Ben, Brad, Brandon, Eric, Sarah, Alex - It was enjoyable working with you and learning from your experiences. The new group - Janis, Yao, Adrian, Neil, Selman, Kenneth and Karl, it was a pleasure meeting you all and working with you for a short duration. I hope I was able to part some of the knowledge I received from the previous PSTL members. I would also like to thank the undergraduate students (some of who are now graduate students) who worked with me making it truly a good teaching and learning experience - Athena, Yen Ying, Alison, Patrick, Joowon, Zachary, Joshua, Abraham, and Alexader and Nate. Thank you all !!

In addition, I would like to thank a lot of other group members from PEPL, NGPD, CPSEG, and many others from NERS and EECS.

From building electronic circuits and understanding automation systems from Aaron Borgman and David McLean to trying my hands at the art of glass blowing with Harold Eberhart, and learning how to machine and how to machine efficiently from Kent Pruss and Marv Cressey was one of the best experiences of graduate school. I cannot thank you all enough for all the support and guidance you have been. The friendship that developed as part of working with you all would be something I would definitely miss in the months and years to follow.

I also must thank many staff members in NERS who have helped me to get required hardware or software in short term notice, or for ordering lab equipment as well as providing administrative support throughout for academic and non-academic issues. Ed Birdsall, James White, Caroline, Cherilyn, Peggy, Rose, Sheena and others,

I will always remember your support and friendship.

A special shout out to Rachel for all her support throughout graduate school and making me realize the size of UM libraries. I would also like to thank many friends I made at the UM libraries over the years.

To my relatives and friends, thank you for being there and keeping me in the loop even though there were times I got too caught up with graduate school related tasks. I would also like to thank you for the good wishes.

Finally, I would like to say special thanks to my parents and uncle Jay Datwani. The guidance and wisdom they offered helped me remain calm and focus on the task. It would not have been possible without the love and support provided.

There are so many others that deserve acknowledgement for their support at different times in my life that allowed me to reach this stage. I apologize for not having you listed here.

Kapil Umesh Sawlani

2015

TABLE OF CONTENTS

DEDICATION ii

ACKNOWLEDGEMENTS iii

LIST OF FIGURES x

LIST OF TABLES xv

LIST OF ABBREVIATIONS xvi

LIST OF SYMBOLS xviii

ABSTRACT xxi

CHAPTER

I. Introduction 1

1.1 Problem Statement 1
1.2 Crossed Field Plasma Devices 2
1.3 Research Objectives and Goals 2
1.4 Dissertation Hypothesis 3
1.5 Dissertation Organization 4

II. Theoretical Considerations 7

2.1 Introduction 7
2.2 Plasma Material Interaction 9
2.2.1 Basic Plasma Physics 10
2.2.2 Need for Plasmas 11
2.2.3 Reaction Rate 12
2.2.4 Influence of Magnetic Fields 16
2.2.5 Plasma Sheath Theory 18
2.2.6 Electron Energy Distribution Function 25
2.3 Secondary Electron Emission 33

2.3.1 Energy Loss of Primary Electrons 34
2.3.2 Secondary Electron Emission Yield 35
2.3.3 SEE in Vacuum 36
2.3.4 Influence of SEE on Plasma Sheath 38
2.3.5 Influence of SEE on Plasma EEDF 39
2.4 Space Propulsion 40
2.4.1 Different Propulsion Technologies 44
2.4.2 Why Electric Propulsion? 44
2.4.3 Hall Thruster Design 46
2.4.4 Hall Thruster Operation 47
2.4.5 Complex Interactions 50
2.4.6 Magnetic Shielding 52
2.5 SEE and Hall Thrusters 52

III. Bench-top Experimental Apparatus and Setup 54

3.1 Introduction 54
3.2 Vacuum Facilities 56
3.2.1 Tall Cylindrical Chamber 57
3.2.2 'Rocket' Chamber 57
3.3 Variable Magnetic Field Bench-top Apparatus 58
3.3.1 Helmholtz Coil 58
3.4 Impact Angle 64
3.5 Plasma Sources 66
3.6 Electron Beam Source 66
3.7 Materials: Preparation and Surface Characterization 69
3.7.1 Copper 69
3.7.2 Graphite 73
3.7.3 Boron Nitride (HP Grade) 73
3.8 Manufacturing and Assembly 77
3.9 Computer Programs for Data Acquisition and Control 79

IV. Plasma and Electron Beam Diagnostics 83

4.1 Langmuir Probes Diagnostics 83
4.1.1 Orbital Motion Limited Theory 87
4.1.2 Electron Energy Distribution Function 87
4.1.3 Sheath Size in Langmuir Probe Operations 88
4.1.4 Plasma Parameters 90
4.1.5 Second Derivative of a Langmuir Probe 91
4.1.6 Numerical Smoothing and Differncing Schemes . . . 92
4.1.7 Multi-Component Plasma Environment 105
4.1.8 Experimental Approach 107
4.1.9 Langmuir Probe Construction and Circuit 109
4.1.10 Sample Langmuir Probe Data Analysis 110

4.1.11 Problems with Langmuir Probes . . . 115
4.2 Emissive Probe Diagnostics . . . 121
4.2.1 Theory of Emissive Probes . . . 122
4.2.2 Probe Construction Techniques . . . 123
4.2.3 Emissive Probe Methods for Plasma Potential Determination . . . 123
4.2.4 Emissive Probe Construction . . . 126
4.2.5 Experimental Procedure and Electrical Circuit . . . 127
4.2.6 Sample Analysis of Emissive Probe Data . . . 128
4.2.7 Influence of Magnetic Field on Emissive Probes . . . 128
4.3 Retarding Potential Analyzer . . . 130
4.3.1 Probe Design . . . 133

V. Low-Cost, Low-Energy, High-Current Electron Gun . . . 136

5.1 Introduction . . . 136
5.2 Thermionic Emission . . . 138
5.2.1 Richardson-Dushman Equation . . . 140
5.2.2 Cathode Coatings . . . 142
5.3 Experimental Setup . . . 144
5.3.1 Electrical Circuit for the Electron Gun . . . 146
5.4 Electron Beam Characterization in Vacuum . . . 147
5.4.1 Beam Perveance . . . 147
5.4.2 Spatial Profile of Beam . . . 148
5.4.3 Beam Energy Characteristics using RPA . . . 151
5.5 Electron Beam Operation in Plasma . . . 153
5.5.1 Beam Energy Characterization using RPA . . . 153
5.6 Electron Beam Characterization in a Uniform Magnetic Field in Vacuum . . . 156

VI. Results and Discussion . . . 160

6.1 Discharge Characterization . . . 160
6.2 Presence of SEE . . . 166
6.3 Sheath Behavior in Presence of SEE . . . 168
6.4 EEDF Behavior in Presence of SEE . . . 187
6.5 Post Operation Material Analysis . . . 198

VII. Conclusion and Future Work . . . 204

7.1 Summary of Research Intent . . . 204
7.2 Conclusions . . . 205
7.3 Implication for Hall Thrusters . . . 208
7.4 Future Work . . . 209
7.4.1 Electron Gun Experiments . . . 211

7.4.2 Vacuum SEE Experiments 212
7.4.3 Plasma SEE Experiments 213
7.4.4 Suggestion to Improve Plasma Source 213
7.4.5 Suggestion to Improve Plasma Diagnostics 214
7.4.6 Experimental and Numerical Validation 217
7.4.7 EEDF Measurement 217
7.4.8 Sheath Saturation 217

BIBLIOGRAPHY 219

LIST OF FIGURES

Figure

2.1	States of matter and their corresponding energy range	8
2.2	Examples of several important plasma applications	9
2.3	Interaction of plasma with materials	10
2.4	Schematic diagram of potential variation through sheath and pre-sheath	22
2.5	Schematic showing variation of plasma density and electric potential in sheath and pre-sheath	22
2.6	Comparison of Maxwellian and Druyvesteyn Distribution	27
2.7	Electron energy distributions in various cases	29
2.8	Production of secondary electrons on impact of primary electron beam	36
2.9	Energy distribution of secondary electrons	36
2.10	SEE yield curve	37
2.11	SEE yield data for common HET wall materials	37
2.12	Plasma sheath distribution theories	38
2.13	Plasma sheath distribution in presence and absence of SEE	39
2.14	Velocity distribution function in presence of secondary electrons	39
2.15	Small missions for advanced research in technology-1 (concept image)	41
2.16	Asteroid redirect mission (concept image)	41
2.17	Satellite industry revenue	42
2.18	List of commercial satellites employing electric propulsion	43
2.19	Comparison of electric propulsion with chemical propulsion	44
2.20	Hall thruster operation	49
2.21	Different phenomena that take place in a HET	51
3.1	Experimental concept	55
3.2	Hall Parameter vs Ratio of Larmor radius to Debye length for HETs and Bench-top apparatus	56
3.3	Vacuum Facility - Tall Cylindrical Chamber	58
3.4	Experimental facility for Bessie	59
3.5	Vacuum Facility - Rocket Chamber	60
3.6	Experimental facility for rocket chamber	61
3.7	3D drawing of the electromagnet coils oriented in Helmholtz coil arrangement	61
3.8	Circuit diagram for the Helmholtz coil	62

3.9 Simulation of a Helmholtz coil geometry 63
3.10 Experimental characterization of the Helmholtz coil geometry . . . 64
3.11 Electromagnet as a structural member to hold the target 65
3.12 Impact angle fixture with target holding assembly 65
3.13 Circuit diagram for the thermionic plasma source 66
3.14 The bench-top apparatus in vacuum facility. 67
3.15 Bench-top apparatus in operation using Xenon plasma 68
3.16 Polishing materials before tests on a grinding wheel 69
3.17 Image of the stylus profilometer - Dektak 70
3.18 Closeup of BN sample being analyzed for surface roughness 71
3.19 Oxide growth on Copper at room temperature 72
3.20 Sputter yield of Cu in Xe and Ar 73
3.21 Pretest material image of copper (Magnfication: 8x) 74
3.22 Pretest material image of copper (Magnfication: 35x) 74
3.23 Pretest material image of graphite (Magnfication: 8x) 75
3.24 Pretest material image of graphite (Magnfication: 35x) 75
3.25 Pretest material image of BN (Magnfication: 8x) 76
3.26 Pretest material image of BN (Magnfication: 35x) 76
3.27 Surface roughness measurements before exposure to plasma 77
3.28 Main control program for data acquisition and system control . . . 80
3.29 Electron beam profile analyzer program 81
3.30 [Electron beam energy analyzer program 82
4.1 Probe opreation regimes 84
4.2 General cosine window of length 65. 100
4.3 Demonstration of polynomial fitting. 102
4.4 Langmuir probe I-V characteristics in presence of Maxwellian, two-temperature non-Maxwellian, and energetic beams in plasma. 106
4.5 Suite of diagnostic probes built for the experiment 107
4.6 Schematic effect of a magnetic field on the probe characteristics. . . 109
4.7 Example of first derivative in magnetized plasma with parallel and perpendicular probes. 110
4.8 Example of EEPF with parallel and perpendicular probes in a mangetized plasma. 111
4.9 Langmuir probe circuit. 112
4.10 Raw I-V characteristics from a Langmuir probe. 113
4.11 Ion saturation correction applied to a raw I-V characteristics obtained from a Langmuir probe 113
4.12 Analysis of I-V characteristics to obtain plasma properties 114
4.13 I-squared analysis for obtaining ion density 114
4.14 Equivalent electrical circuit with contamination layer on Langmuir probes. 115
4.15 Comparison of I-V characterstics of contaminated Probes. 117
4.16 Hysteresis test for Langmuir probes. 118
4.17 Comparison of contaminated Langmuir probe with Pristine Langmuir probe. 119

4.18 Hysteresis test for Langmuir probes. 120
4.19 Effects of low and high energy beam on plasma. 121
4.20 Separation point technique I-V characteristic. 124
4.21 Floating point technique measurement of plasma potential. 124
4.22 Determination of inflection point using I-V trace of an emissive probe 125
4.23 Determination of floating potential using inflection points from an emissive probe 125
4.24 Schematic of an emissive probe. 126
4.25 Emissive probe cicuit employed in inflection point test. 127
4.26 Emissive probe cicuit employed in floating point test. 128
4.27 Sample analysis using floating point technique. 129
4.28 Sample analysis using separation point technique. 129
4.29 Sample analysis using inflection point technique. 130
4.30 Schematic of RPA grid bias and electron response 132
4.31 Images of RPA 134
4.32 Images of RPA grids 135
4.33 RPA Circuit 135
5.1 Determination of temperature of a filament and comparison of emission current from different materials 142
5.2 Electron gun used in this experiment 145
5.3 Electron gun exploded view 145
5.4 Electron gun circuit 146
5.5 Emission current of electron gun in vacuum 147
5.6 Ratio of emission current to grid current in vacuum operation . . . 148
5.7 Theoretical and experimental beam perveance for the electron gun . 149
5.8 Electron beam profile on target plane 150
5.9 Electron gun energy map obtained using a RPA in vacuum 151
5.10 Normalized first derivative of RPA data in vacuum 152
5.11 Emission current of electron gun in plasma 153
5.12 Normalized first derivative of RPA data in plasma 154
5.13 Comparison of the energy distribution of electron beam in plasma at different background plasma discharge currents 155
5.14 Effect of magnetic field on electron beam 157
5.15 Ratio of emission current to grid current in presence of magnetic fields158
6.1 A simplified schematic of the experimental test-bed and diagnostics for measuring sheath profile and EEDF 161
6.2 Plasma discharge characterization of different materials 163
6.3 Plasma discharge characterization of copper at 150 mA 164
6.4 Plasma discharge characterization of BN at different discharge currents165
6.5 Detection of the presence of SEE in the system 167
6.6 Current collected at the target in presence and absence of plasma and an electron beam 168
6.7 Emissive probe measurement positions 169
6.8 Sheath potential measured for copper at various axial locations . . . 171
6.9 Comparison of sheath potential for different materials 173

6.10 Equipotential profile for copper operated under 150 mA discharge current with 10 V beam voltage 174
6.11 Equipotential profile for copper operated under 150 mA discharge current with 30 V beam voltage 174
6.12 Equipotential profile for copper operated under 150 mA discharge current with 60 V beam voltage 175
6.13 Equipotential profile for copper operated under 150 mA discharge current with 80 V beam voltage 175
6.14 Charge distribution profile for copper operated under 150 mA discharge current with 10 V beam voltage 176
6.15 Charge distribution profile for copper operated under 150 mA discharge current with 30 V beam voltage 176
6.16 Charge distribution profile for copper operated under 150 mA discharge current with 60 V beam voltage 177
6.17 Charge distribution profile for copper operated under 150 mA discharge current with 80 V beam voltage 177
6.18 Sheath potential measured in a 6kW Hall thruster 178
6.19 Wall sheath potential for different materials at y = 0 mm 179
6.20 Wall sheath potential for different materials at y = 16 mm 179
6.21 Various SEE coefficient for BN in literature 180
6.22 SEE coefficient for copper at normal incidence under different conditions 181
6.23 SEE coefficient for graphite at normal incidence 182
6.24 Wall sheath potential for BN at y = 16 mm under different tests . . 182
6.25 Wall sheath potential for copper at different locations in a 150 mA plasma environment. 183
6.26 Wall sheath potential for copper at different pressures. 184
6.27 General behavior of sheath potential in presence of SEE 184
6.28 Comparison of experimental solution to that of Hobbs and Wesson . 187
6.29 Temperature distribution for a copper target based on beam energy. 188
6.30 Plasma properties for copper in a plasma of current 150 mA as a function of beam voltage. 190
6.31 Normalized EEDF of copper operated at a plasma discharge of 150 mA as a function of beam voltage. 191
6.32 Normalized Log (EEDF) of copper operated at a plasma discharge of 150 mA as a function of beam voltage. 192
6.33 Plasma properties for copper in a plasma of current 50mA as a function of beam voltage. 193
6.34 Normalized EEDF of copper operated at a plasma discharge of 50 mA as a function of beam voltage. 194
6.35 Plasma properties for copper in a plasma of current 50mA as a function of beam voltage. 195
6.36 Plasma properties for graphite in a plasma of current 50mA as a function of beam voltage. 196

6.37 Normalized EEDF of graphite operated at a plasma discharge of 50 mA as a function of beam voltage. 197
6.38 Post test copper image (8x zoom) 198
6.39 Post test copper image (35x zoom) 199
6.40 Post test graphite image (8x zoom) 199
6.41 Post test graphite image (35x zoom) 200
6.42 Post test BN image (8x zoom) 200
6.43 Post test BN image (35x zoom) 201
6.44 Comparison of plasma treated area vs untreated area of BN (35x zoom) 201
6.45 Energy dispersive spectroscopy of copper 202
6.46 Elemental contribution on surface of copper 203
6.47 SEM images of BN (HP grade) and copper 203
7.1 Potential future experiments 210

LIST OF TABLES

Table

2.1	Elementary electron reactions in plasma systems.	11
2.2	Hall thruster parameters	48
3.1	Experimental bench-top apparatus parameters	55
4.1	Characteristic length scales of importance in Langmuir probes	85
4.2	Correction factors (Child Langmuir current) for various probes.	89
4.3	Values of coefficients and coherent gain for general cosine windows	99
4.4	Parameters and their possible value for the four free parameter fitting method	105
5.1	Work function for various metals.	140

LIST OF ABBREVIATIONS

CF crossed field

CL Child Langmuir

CC Creative Commons

DAQ data acquisition

EED electron energy distribution

EEDF electron energy distribution function

EM electromagnetic

ES electrostatic

HET Hall effect thruster

IEDF ion energy distribution function

PEPL plasmadynamics and electric propulsion laboratory

PIC particle in cell

PSTL plasma science and technology laboratory

rf radio frequency

RPA retarding potential analyzer

RFEA retarding field energy analyzer

SC space charge

SCL space charge limit

SEE secondary electron emission

SPT stationary plasma thruster

STP standard conditions for temperature and pressure

TAL thruster with anode layer

OML orbital motion limited

LIST OF SYMBOLS

Roman Symbols

$a,\ r_p$	electrostatic (Langmuir) probe radius
b	ion collection sheath radius
I_p	plasma current collected by a probe
V_{pr}	probe bias
$V_p\ ,\ V_\phi$	plasma potential
$q,\ e$	elemental electric charge
Z	species charge number
n	species number density
m	species mass
k_B	Boltzmann'a constant
T	(species) temperature
I	current
j	current density
d_s	sheath thickness
K	rate coefficient
R	resistance
L	length
A	area
E	electric field
I_{sp}	specific impulse

T	thrust force
g_0	acceleration due to gravity
u_e	rocket exhaust velocity
M	mass of the spacecraft/satellite
g	degeneracy (density of states)
h	Planck's constant
E_F	Fermi energy
r	surface reflection coefficient
r_L	Larmor radius
A_R	Richardson's constant
P	power
Q	heat transfer
R	penetration depth (range) of electron in material

Greek Symbols

ω	angular frequency
ω_p	plasma frequency
ω_c	cyclotron frequency
τ_c	mean time between collisions
λ_D	Debye Length
λ_{mfp} , l	mean free path
δ_s	sheath thickness
σ	(electron) conductivity
ν_m	collision frequency
μ	mobility
Φ_{WF}	work function
ξ	effective integral coefficient of radiation (emissivity)
η	efficiency

δ	secondary electron emission (SEE) coefficient or SEE yield
α	absorption factor of the secondary electrons

Subscripts

s	species
e	electron
i	ion
g	neutral gas
$+$, 0	saturation state
d	discharge
p	plasma
B	ballast

ABSTRACT

Effects of Secondary Electron Emission on the Plasma Sheath and Local Electron Energy Distribution with Application to Hall Thrusters

by

Kapil Umesh Sawlani

Chair: John E. Foster

The nature of plasma transport across the magnetic field in crossed-field (CF) devices such as Hall effect thrusters (HETs) remains largely an unsolved problem. This can be further complicated by the presence of secondary electrons derived from the thrusters channel wall due to the impact of photons and electrons. The role of these secondary electrons in the operation of HETs has been a subject of investigation in recent years. Under normal operating conditions of a HET, several physical phenomena occur simultaneously and the interaction of the plasma with the channel walls of the thruster play an important role in its effective operation. These plasma wall interactions produce secondary electrons that have a non-linear coupling effect with the bulk plasma and affect the performance of crossed field devices by changing the sheath potential as well as the electron energy distribution. This influence is not yet fully understood in the community and thus the computational models are based on assumptions that are not highly accurate. Experimentally, there is little available data on the SEE yield in plasma and its effects to environments similar to that of a

Hall thruster, which could be used to validate existing numerical models. A test-bed apparatus is needed to understand these effects that could serve as a tool to validate and improve existing numerical models by providing the appropriate boundary conditions, secondary yield coefficients and variation of plasma parameters to aid the future design of HETs.

In this work, a bench-top apparatus is developed to elucidate the role that secondary electrons play in regards to crossed field transport and energy flow to the walls. An electron beam which simulates energetic electrons in Hall channel is used to generate a secondary electron plume at the surface of various targets (Cu, C, BN) which simulates channel wall. The response of the plasma to these secondary electrons is assessed by measuring changes to the potential distribution in the sheath of the irradiated target and the measured electron energy distribution. An attempt is made to relate phenomena and trends observed in this work with those in Hall thrusters.

CHAPTER I

Introduction

"*The very nature of science is discoveries, and the best of those discoveries are the ones you don't expect.*"

- Neil deGrasse Tyson

1.1 Problem Statement

Better understanding of the fundamental physics in crossed field (CF) plasma devices can lead to improved understanding and control of plasmas in various applications such as fusion, plasma processing of materials, and efficient space propulsion devices. Such applications have both societal impact as well as a commercial advantage over existing technologies. This dissertation focuses on the application of space propulsion, in particular, the Hall effect thruster (HET). The experimental apparatus and procedures developed, however, can be used to explore other crossed field plasma applications.

As humankind envisions daring missions such as retrieving asteroids from space [1, 2] and exploring the solar system[3], the need to understand ways to improve efficiency and life-time of the propulsion devices becomes very important. This dis-

sertation attempts to answer a question that has long been considered a challenge in the field of HET physics - how does secondary electron emission (SEE) from the HETs channel wall affect the behavior of the background plasma? Existing research, both experimental and numerical, suggests that SEE processes are important. While these research efforts acknowledge the influence of SEE on the background plasma, there is a lack of understanding regarding its actual effect on HET processes owing to the myriad of other physical processes at play. An experiment that can isolate the SEE physics and quantify its effects is thus desirable.

1.2 Crossed Field Plasma Devices

Crossed-Field (CF) plasma devices are configured such that $\vec{E}$ and $\vec{B}$ fields are perpendicular to each other. These devices are used in several areas of scientific research and also have commercial applications. Examples of these devices include HETs, magnetron systems, and fusion devices. They exhibit a range of physical phenomena dependent on operational regimes and the transport of plasma species in these devices is an unsolved problem as crossed field diffusion is still poorly understood in magnetized plasmas. Despite the challenges, these sources are used in practice and in particular provide an efficient means for ionization [4].

1.3 Research Objectives and Goals

The primary objective of this research effort is to study and quantify the effects of secondary electrons produced by electron bombardment of the acceleration channel wall of a HET. In order to better understand how SEE, produced by electron bombardment of a surface immersed in a plasma, changes the behavior of the plasma, a controlled electron beam source is utilized to study the response of plasma electron energy distribution function (EEDF) and sheath potential profile at an irradiated

surface. The following tasks define the scope of this dissertation:

- Design and construction of a variable magnetic field source, in this case, a Helmholtz coil arrangement to generate uniform magnetic fields in order to simulate the magnetic fields in a Hall thruster channel.
- Design and construction of a crossed field plasma source.
- Design, construction and characterization of a low energy high current electron beam source capable of operation in plasma.
- Preparation of a suite of diagnostics using electrostatic probes to study the sheath profile and the EEDF.
- Initial characterization of SEE effects on sheath and EEDF as a function of primary beam energy of the electrons.

The goal of the dissertation research is to better understand how SEE produced by electron bombardment of a surface changes the behavior of the plasma. This is achieved by studying the response of the local plasma EEDF and sheath potential profile on bombardment of primary electrons from a controlled beam source.

1.4 Dissertation Hypothesis

As mentioned in section 1.3, the improvement of Hall thruster efficiency and lifetime has been a focus of intense research for several decades. Many phenomena in these thrusters have been identified and mechanisms proposed to improve our physical understanding of the device performance. The SEE produced from the bombardment of primary electrons is identified by several authors to be a contributing factor that influences the thruster performance [5, 6, 7, 8, 9, 10, 11, 12]. It will be shown in chapter II that SEE from a wall material affects the plasma properties. A summary of the main effects of SEE are listed here:

- The sheath potential is reduced in the presence of secondary electron emission.
  - This leads to the modification of the tail of the EEDF and can result in 'cooling' the electron temperature in a HET.
- Thermalization of the high energy secondary electron population also modifies the EEDF.

As a consequence of these effects, it is hypothesized here that the ionization efficiency of a HET can be controlled by SEE processes. Knowledge of the effects of SEE on plasma properties can provide the design engineer an additional 'control knob' for thruster operation and can provide the following benefits in HETs:

- Increase scientific payload by reducing the propellant mass for a given mission (or alternately using a less massive gas compared to xenon).
- Decrease in power consumption by the thruster allowing more solar power budget on telemetry and other resources.
- Increase in thruster life-time by engineering the wall material to reduce sheath potential and sputter yield.
- Potential for a higher efficiency small scale thruster design that can be used in several applications such as cubesat [13].

1.5 Dissertation Organization

The thesis consists of seven chapters describing the effort to answer the question on influence of SEE on bulk plasma properties as well as to validate the hypothesis. Description of the chapters is as follows.

Chapter II provides a review of basic plasma physics and secondary electron emission. It also surveys the current understanding of all potential effects of SEE on

plasmas, including modification of sheath potential and change in the bulk and tail of the EED. It also presents a description of motivation for space travel and the working of Hall thrusters and enlists our current understanding of the effects of SEE on HETs.

Chapter III describes the construction of the experiment highlighting the constraints required to experimentally simulate a HET. This chapter outlines the details of the electromagnet design, plasma source information and considerations, the vacuum facilities used to test different components of the system prior to the overall assembly of individual components. Theoretical considerations for the design of these components along with diagnostics are discussed in this chapter. The design of the experiment was done keeping in mind future exploration of the topic and various features of the test-bed, not characterized in this dissertation are also discussed. Finally, a number of computer programs were developed to control various power supplies and acquire data, as well as carry out diagnostics with semi-automated data analysis. These programs are discussed in brief as well.

A suite of diagnostics were used to characterize the plasma as well as the electron beam. These included Langmuir probes, emissive probe and a retarding potential analyzer (RPA). Details on the design of diagnostics and special considerations required are discussed in chapter IV

In order to control electron irradiation of the target, an electron gun was developed. The design of this electron beam source and its operation are discussed in chapter V. Vacuum operation and plasma operation of the beam source are characterized and stability criteria of the beam is evaluated using the Penrose criterion. It is shown that most of the beam power goes into heating the plasma.

The results of the experiment are described in chapter VI. In this chapter, the presence of SEE is demonstrated using the collected current at the target. This is followed by the sheath potential profile analysis conducted using the emissive probe. Sheath potential with respect to beam voltage reveals a universal shape related to

the secondary electron emission of the material following a Hobbs and Wesson like profile with an effective SEE yield and an effective temperature. The chapter also discusses the findings from Langmuir probe and analysis of a multi electron temperature plasma. The EEDF tends to suggest that as the beam voltage increases, the effective SEE rate increases and electrons are lost to the wall. The measurements however are not very conclusive due to poor signal to noise. The chapter ends with a discussion of materials post plasma testing.

Finally, the lessons learned from this dissertation are summarized in chapter VII. Recommendations to move forward from the present results is discussed in future works.

CHAPTER II

Theoretical Considerations

"*The most creative people are motivated by the grandest of problems that are presented before them.*"

- Neil deGrasse Tyson

2.1 Introduction

It is often said that 99% of the visible universe (excluding dark matter[‡]) invariably consists of plasma. The existence of all living species on Earth is part of the 1% that is not plasma. Common states of matter that are observable in day to day life include solids, liquids, and gases. The forth state of matter classification is plasma, which is observed in natural phenomena such as lightning and auroras [14].

The change of states of matter can be achieved by providing energy to the system. For instance, water is known to exist as a solid (ice), liquid (water) and gas (steam) at different temperatures and pressures. If more energy is provided to the steam, the gaseous state of matter undergoes transformation from wet steam to dry steam, followed by molecular dissociation. Further addition of energy can result into atomic level excitations and eventually cause the electrons from individual atoms to

[‡]It is still not conclusive as to what comprises dark matter or dark energy. These terms are an outcome of the mathematical balance of cosmic theories.

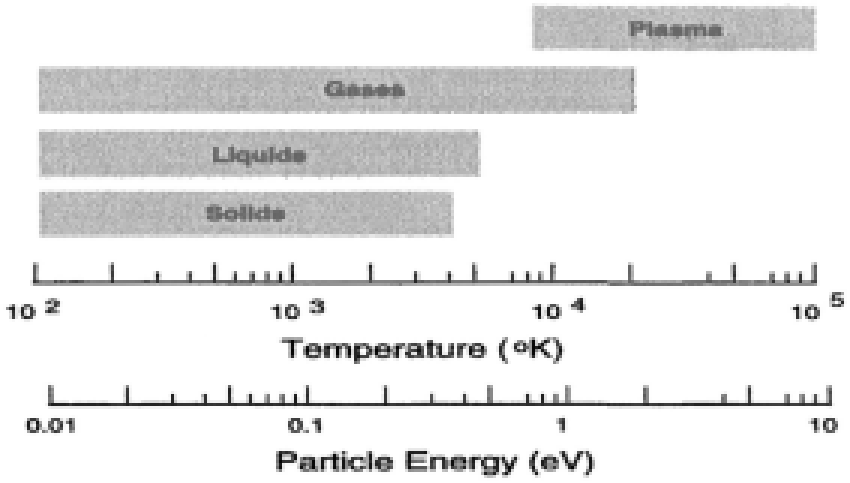

Figure 2.1: States of matter and corresponding energy range.

leave their orbits (in equilibrium state). The state of electrons and ions along with neutral gas molecules is called a plasma state. There are additional constraints on the definition of plasma and these will be discussed in section 2.2.1. Figure 2.1 shows the different states of matter and their corresponding energy range for low temperature plasmas.

From a technological view-point, the plasma methods offer opportunities that out perform other existing technologies, such as chemical methods and thermal methods. In many applications, plasmas can have temperature and energy density far higher than those produced by conventional methods. Another advantage of plasmas is that they able produce energetic species at low gas temperatures that would be either very difficult or impossible using ordinary chemical mechanisms [15]. The species produced as a result of the plasma activation mechanism includes electrons, ions, reactive radicals, and UV photons [16, 17].

The range of plasma applications have grown considerably in the last half century. It includes electronic fabrication, lighting, television, various thin film coatings on different materials, enhanced textile, improved space propulsion, as well as potential to achieve fusion energy. Figure 2.2 shows various applications and potential industry

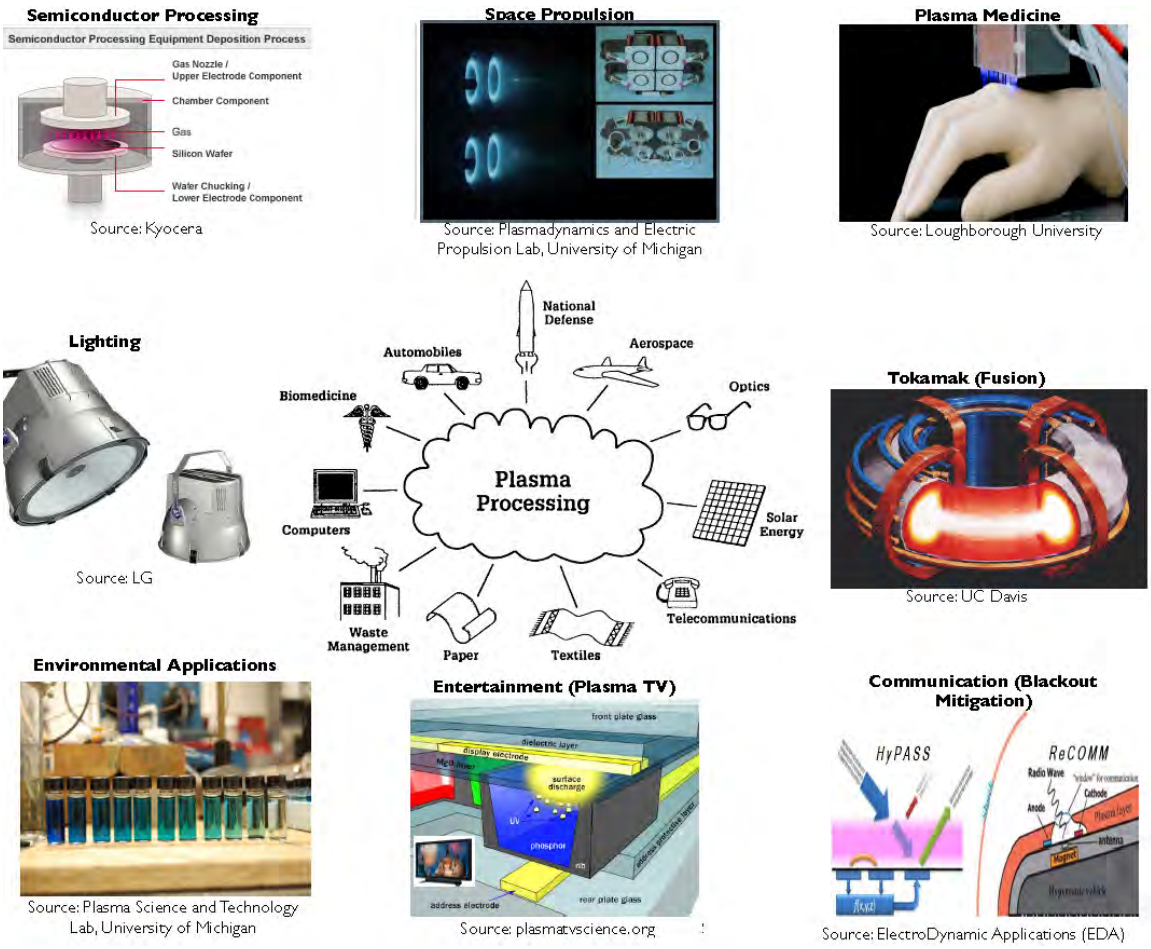

Figure 2.2: Examples of important plasma applications (Figures from various sources).

where plasmas play a role.

2.2 Plasma Material Interaction

In the various examples of plasma applications, the plasma generation approaches vary widely. These energy source may include methods such as DC breakdown, RF breakdown, microwave, and lasers

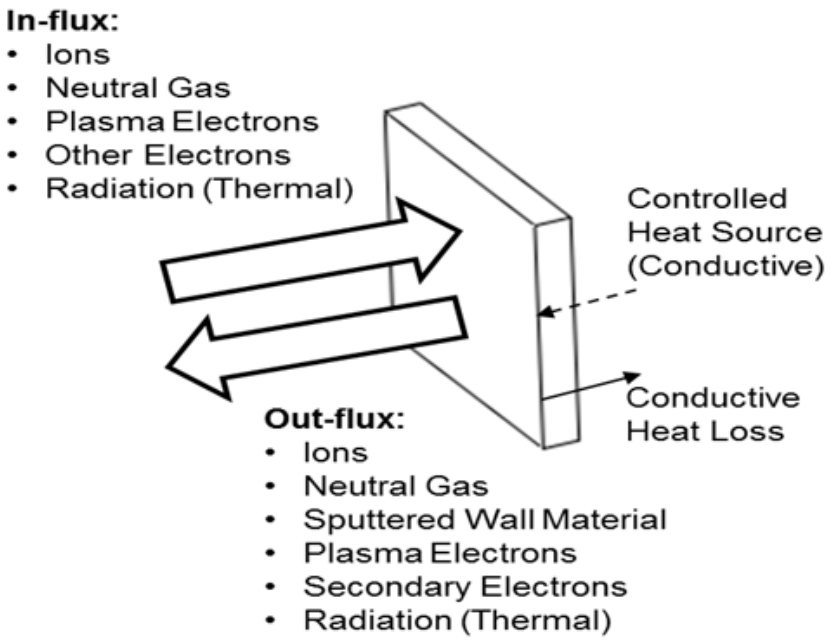

Figure 2.3: Interaction of plasma with materials.

2.2.1 Basic Plasma Physics

A plasma is a state in which the ionized particles are electrically (quasi-)neutral. This is expressed mathematically as shown in equation 2.1

$$\sum_i -q_i\, n_i = \sum_k q_k\, n_k \tag{2.1}$$

These charged particles orient themselves in a state that effectively shields them from electrostatic forces within a certain characteristic length scale. This shielding distance was first calculated by Peter Debye and is called the Debye length (Eq. 2.2)

$$\lambda_D = \left(\frac{\epsilon_0 k_B T_e}{e^2 n_e}\right)^{1/2} \tag{2.2}$$

This characteristic length scale is very important in defining a plasma sheath that is formed when an object is bounded by plasma, and is discussed in section 2.2.5. Another requirement for a state to be considered a plasma state is the requirement

that shielding requires many particles. This is typically expressed by equation 2.3, where the sphere of radius λ_D contains many plasma particles.

$$\frac{4}{3}\pi\lambda_D^3 n \gg 1 \tag{2.3}$$

For low temperature low pressure plasmas the plasma oscillation frequency (eq. 2.4) should also be much greater than the collision frequency (eq. 2.10) in order for the plasma state to exist. The characteristic time scale associated with plasma is related to the plasma frequency and is important in many applications relating to the wave propagation in plasma.

$$\omega_{pe} = \sqrt{\frac{\epsilon_0 n_e}{m_e e^2}} \tag{2.4}$$

The above condition does not strictly hold at higher pressure operations. At atmospheric pressure, the collision frequency can be higher than the plasma frequency. This dissertation focuses on a low pressure collisionless plasma application and the plasma oscillation frequency is higher than the collision frequency.

2.2.2 Need for Plasmas

Plasmas are an efficient media to transfer energy. In low temperature, low pressure plasma, electrons are more likely to collide with neutral gas atoms or molecules than other species. Electron collision with atoms/molecules can produce or consume electrons. Table 2.1 lists the reactions that are commonly seen in plasma systems.

Reaction Type	Reaction	e^- Gain/Loss
Electron Impact Ionization	$e + M \longrightarrow M^+ + e + e$	e^- Gain
Dissociative Attachment	$e + M_2 \longrightarrow M^- + M$	e^- Loss
Recombination	$e + M_2^+ \longrightarrow M + M$	e^- Loss
Photoionization	$h\nu + M \longrightarrow M^+ + e$	e^- Gain
Penning Ionization	$X^* + M \longrightarrow M^+ + e + X$	e^- Gain

Table 2.1: Elementary electron reactions with atoms and molecules in a plasma.

2.2.3 Reaction Rate

The balance of electron sources and sinks results in the rate equation for the various species and is given by equation 2.5.

$$\frac{dn_e}{dt} = \sum_i n_e K_i N_i - \sum_j n_e K_j N_j + S + \vec{\nabla} \cdot \vec{\Phi} \tag{2.5}$$

In the above equation, the first term on the RHS corresponds to the source within the plasma (e^- collisions with atoms and molecules) and the second term corresponds to the consumption of species. The quantity S is for any external sources such as photoionization, Penning ionization, and secondary electron emission [17]. The last term on the RHS is a flux transport term.

The rate coefficient, K, is a measure of the probability of a single electron undergoing a particular collision with a single atom/molecule. It is often expressed in units of cm^3/s. Collisions impart energy to the atom or molecule and can change the energy state. The various elementary processes that can occur include elastic collision, rotational excitations, vibrational excitations, and electronic excitations and finally ionization, recombination and attachment.

For a given distribution, f, and species cross-section σ_i, the rate constant can be expressed by equation 2.6

$$K_i = \int_0^\infty f(\epsilon)\sigma_i(\epsilon) \left(\frac{2\epsilon}{m_e}\right)^{1/2} d\epsilon \tag{2.6}$$

The average energy and average speed of the electron swarm is given by equation 2.7 and 2.8

$$< \epsilon >= \int_0^\infty f(\epsilon)\epsilon d\epsilon \tag{2.7}$$

$$< v >= \int_0^\infty f(\epsilon) \left(\frac{2\epsilon}{m_e}\right)^{1/2} d\epsilon \tag{2.8}$$

Electron conductivity (σ) in a plasma is dependent on the rate constant. This can be seen from equation 2.9 where the electron conductivity in absence of magnetic fields is inversely proportional to the collision frequency.

$$\sigma = \frac{q^2 n_e}{m_e \nu_m} \tag{2.9}$$

The collision frequency (ν_m) is directly proportional to the rate constant and is given by equation 2.10

$$\nu_m = \sum_i K_i N_i \tag{2.10}$$

On a circuit level (macroscopic level) we see the plasma current (I) and supply voltage (V_s) behavior based on Ohm's law given by equation 2.11. The discharge resistance (R_d) is related to the collision frequency (equation 2.12).

$$I = \frac{V_s}{R_B + R_d} \tag{2.11}$$

$$R_d = \frac{L}{A\sigma} \tag{2.12}$$

Equation 2.13 gives the discharge voltage as a function of plasma resistance, where R_B is the ballast resistance.

$$V_d = V_s \left(\frac{R_d}{R_B + R_d} \right) \tag{2.13}$$

The interface between these microscopic levels of detail (fundamental characteristics) and macroscopic level of detail (Ohm's law) is the kinetic formulation of the system. This corresponds to the distribution function $f(\epsilon)$ given by the Boltzmann transport equation. In the absence of magnetic fields, this is given by equation 2.14.

$$\frac{df(\epsilon)}{dt} = -\vec{v} \cdot \nabla_x f(\epsilon) - \frac{q\vec{E}}{m_e} \cdot \nabla_v f(\epsilon) + \left(\frac{df(\epsilon)}{dt} \right)_{collisions} \tag{2.14}$$

A generic form of the Boltzmann transport equation is given by equation 2.15.

$$\frac{df(\epsilon)}{dt} + \vec{v} \cdot \nabla_x f(\epsilon) + \vec{a} \cdot \nabla_v f(\epsilon) = \left(\frac{df(\epsilon)}{dt}\right)_{collisions} \tag{2.15}$$

2.2.3.1 Maxwell-Boltzmann Distribution

The Maxwell-Boltzmann velocity distribution function is given by equation 2.16 [14, 17]. This distribution can be defined by one parameter - the electron temperature (T_e).

$$f(\vec{v})d^3v = \left(\frac{m_e}{2\pi k_B T_e}\right)^{3/2} \exp\left(\frac{\frac{1}{2}m_e v^2}{k_B T_e}\right) d^3v \tag{2.16}$$

Based on this distribution it is possible to calculate the average speed (eq. 2.8) and average energy (eq. 2.7). These are given by equations 2.17 and 2.18 respectively.

$$< v >= \int_0^\infty f_{MB}(v) v 4\pi v^2 dv = \left(\frac{8k_B T_e}{\pi m_e}\right)^{1/2} \tag{2.17}$$

$$\frac{1}{2}m_e < v^2 >=< \epsilon >= \int_0^\infty f_{MB}(v) v^2 4\pi v^2 dv = \frac{3}{2}k_B T_e \tag{2.18}$$

The Maxwell-Boltzmann velocity distribution implies an energy distribution. This energy distribution (in units of eV^{-1} is given by equation 2.19.

$$f(\epsilon)d\epsilon = \left(\frac{2}{\pi^{1/2}(k_B T_e)^{3/2}}\right)^{1/2} \epsilon^{1/2} \exp\left(\frac{-\epsilon}{k_B T_e}\right) d\epsilon \tag{2.19}$$

2.2.3.2 Joule Heating

The power dissipated in a plasma is given by equation 2.20.

$$P = \vec{j} \cdot \vec{E} = \sigma E^2 \tag{2.20}$$

2.2.3.3 Electron Mobility

The electron mobility is given by equation 2.21

$$\mu_e = \frac{q}{m_e \nu_m} \tag{2.21}$$

Knowledge of the electron mobility provides information on the drift veloicty which is a function of the reduced electric field (eq. 2.22).

$$\vec{v}_{drift} = \mu_e \vec{E} = f\left(\frac{E}{N}\right) \tag{2.22}$$

2.2.3.4 Spitzer Conductivity

Plasmas maybe collisional or collisionless depending on the ionization fraction of the plasma. In general, electron-ion collisions are not considered important when $n_e/N_g << 1$. In these situations, it is the electron-neutral collisions that dominate the fundamental interactions within the plasma system. However due to large electron-ion cross sections, when the ratio is around 10^{-6} to 10^{-3}, the electron - ion collisions become influential and the description of collisions is given by Coulombic interactions. The electron-ion cross section is given by equation 2.23

$$\sigma_{e-ion}(\varepsilon) = 4\pi b_0^2 \ln 1 + \left(\frac{\lambda_D}{b_0}\right)^2 \tag{2.23}$$

The parameter b_0 is known as the impact parameter for a 90 degree deflection and is given by 2.24

$$b_0 = \frac{Zq^2}{8\pi\epsilon_0}\frac{1}{\varepsilon} \tag{2.24}$$

It can be easily seen that the electron ion cross-section is dependent on the inverse square of the energy. The rate constant for electron ion collision for a Maxweillian distribution is given by equation 2.25

$$K_{e-ion} = \frac{4\sqrt{2\pi}}{3}\left(\frac{m_e}{k_B\,T_e}\right)^{3/2}\left(\frac{q^2}{4\pi\,m_e\,\epsilon_0}\right)^{3/2}\ln\Lambda \propto \frac{1}{T_e^{3/2}} \tag{2.25}$$

Here the term $\ln\Lambda$ is known as the Coulomb logarithm and is typically between 5 and 10 for low temperature plasma applications.

Using equation 2.9, the conductivity of a plasma under these circumstances can be written as

$$\sigma = \frac{q^2 n_e}{m_e \nu_m} = \frac{q^2 n_e}{m_e(k_{e-neutral}N_g + k_{e-ion}n_i)} \tag{2.26}$$

$$\sigma = \frac{q^2}{m_e(k_{e-neutral}N_g/n_e + k_{e-ion}n_i/n_e)} = \frac{q^2}{m_e(k_{e-neutral}N_g/n_e + k_{e-ion})} \tag{2.27}$$

When $k_{e-ion} \gg k_{e-neutrals}$ (for higher degree of ionization systems, such as a Hall thruster), we get Spitzer conductivity of the system,

$$\sigma_{Spitzer} = \frac{q^2}{m_e k_{e-ion}} \neq f(n_e) \propto T_e^{3/2} \tag{2.28}$$

2.2.4 Influence of Magnetic Fields

Magnetic fields cause charged particles to gyrate with a characteristic gyroradius, also known as Larmor radius, given by equation 2.29.

$$r_L = \frac{v_\perp}{\omega_{ce}} \tag{2.29}$$

This is a characteristic length scale in magnetized plasmas and is important in Hall thrusters. The gyration or cyclotron frequency (ω_{ce}) is given by equation 2.30

$$\omega_{ce} = \frac{Bq}{m_e} \tag{2.30}$$

The generalized form of the Ohm's law in a magnetized plasma can be written as equation 2.31

$$J = \bar{\bar{\sigma}} E \tag{2.31}$$

The conductivity tensor ($\bar{\bar{\sigma}}$) is required to model a system with magnetic field ($\vec{\mathrm{B}} = \mathrm{B}_0\hat{\mathrm{z}}$) and is given by equation 2.32 [18].

$$\bar{\bar{\sigma}} = \begin{pmatrix} \sigma_P & \sigma_H & 0 \\ \sigma_H & -\sigma_P & 0 \\ 0 & 0 & \sigma_{||} \end{pmatrix} \tag{2.32}$$

The different elements of the conductivity tensor have their associated currents based on the generalized Ohm's law. These conductivities are described as

$$\sigma_P = \frac{\nu_c^2}{\nu_c^2 + \omega_c^2}\,\sigma_0 \quad \ldots \quad \text{Penderson Conductivity } (\perp \text{ B } \& \text{ } || \text{ E}) \tag{2.33a}$$

$$\sigma_H = \frac{\omega_c\,\nu_c}{\nu_c^2 + \omega_c^2}\,\sigma_0 \quad \ldots \quad \text{Hall Conductivity } (\perp \text{ B } \& \perp \text{ E}) \tag{2.33b}$$

$$\sigma_{||} = \sigma_0 = \frac{q^2 n_e}{m_e \nu_m} \quad \ldots \quad \text{Parallel Conductivity } (|| \text{ B}) \tag{2.33c}$$

The relationship between the cyclotron frequency and collision frequency essentially describes the behavior of the system. If the gyrofrequency is much less than the collision frequency ($\omega_{ce} \ll \nu_c$), then collisions are frequent and prevents gyromotion. Particles move parallel to the electric field vector and the contribution on the Penderson current is higher compared to the Hall current. This is different in the case where the collision frequency is less compared to the gyrofrequency ($\omega_{ce} \gg \nu_c$). In this situation, particles gyrate several times before any collision event occurs and the contribution of Hall current and ExB drift is observed. Hall thrusters typically work

in this region where the electron gyro frequency is much greater than the collision frequency.

2.2.5 Plasma Sheath Theory

When a plasma interacts with a floating surface or a grounded surface, an electrostatic sheath is formed in order to balance the flux of ion and electron currents directed at the surface. A sheath maybe thought of as a space-charge boundary layer that connects plasma state to another physical state of matter such as a solid or liquid. The boundary layer separating the wall and the quasi-neutral plasma is typically a few Debye lengths.

The sheath is responsible for the following:

1. Transfer of energy to and from walls
2. Loss of plasma particles

Because of these properties sheath physics find importance in all practical plasma applications such as diagnostics like Langmuir probes and emissive probes, material processing like deposition, etching and ion implantation, and acceleration of charged particles.

2.2.5.1 Sheath Derivation

Maxwell's electricity and magnetism equations in free space are given by :

$$\nabla \cdot \mathbf{E} = \frac{\rho}{\epsilon_0} \qquad \text{Gauss's Law} \tag{2.34a}$$

$$\nabla \times \mathbf{E} = -\frac{\partial \mathbf{B}}{\partial t} \qquad \text{Faraday's law of induction} \tag{2.34b}$$

$$\nabla \cdot \mathbf{B} = 0 \qquad \text{Gauss's law for magnetism} \tag{2.34c}$$

$$\nabla \times \mathbf{B} = \mu_0 \mathbf{J} + \mu_0 \epsilon_0 \frac{\partial \mathbf{E}}{\partial t} \qquad \text{Ampère's law} \tag{2.34d}$$

Electric field can be defined as the gradient of the potential, given by equation 2.35

$$E = -\vec{\nabla}\phi \tag{2.35}$$

In most low temperature plasmas, including Hall thrusters[†], electron temperatures are much greater than ion temperatures and due to higher mobility of electrons (see section 2.2.3.3) the electrons tend to travel to the walls faster, thereby causing any floating body to attain a negative potential with respect to the background plasma. A sheath is quickly formed at the bounding surfaces.

A sheath solution must satisfy Poisson's equation

$$\nabla^2\phi = \frac{d^2\phi}{dx^2} = -\frac{\rho}{\epsilon_0} = -\frac{e(n_i - n_e)}{\epsilon_0}$$

Since the ion density at every point within the sheath is greater than the electron density owing to the mobility differences between the species, the Poisson's equation will be negative and the curvature would be concave downwards, i.e., $\mathrm{d}^2\phi/\mathrm{dx}^2 < 0$.

It is clear from the above discussion that the random ion flux is lower than electron flux in the bulk plasma. However, because in the sheath $\mathrm{n}_i > \mathrm{n}_e$, the ion flux at the sheath edge must have a certain value. To assure that $\mathrm{n}_i > \mathrm{n}_e$ through out the sheath, ions must enter the sheath at or above a minimum speed. This constraint is called the Bohm speed.

Under the assumption that $\mathrm{T}_e \gg \mathrm{T}_i$, the ion flux at the sheath can be set as equation 2.36

$$\Gamma_i\,]_s = n_0 v_0 \tag{2.36}$$

[†]Hall thruster temperatures are not considered low temperature plasma applications as electron temperatures are typically in the range of 20 - 60 eV, and ion temperatures are about 1eV.

Within the sheath, the flux of particles must be conserved, thus the number of particles at a given location can be calculated,

$$\Gamma = n_0\, v_0 = n_i(x)\, v_i(x) = n_i\, v_i$$

$$n_i = \frac{n_0\, v_0}{v_i} \tag{2.37}$$

The ion velocity at any given location within the sheath can be determined using the energy conservation equation, given by equation 2.38

$$\frac{1}{2}M_i v_0^2 + e\phi(0) = \frac{1}{2}M_i v_i^2 + e\phi(x) \tag{2.38}$$

At the sheath edge, the potential is zero and the ion velocity is given by equation 2.39

$$v_i = \sqrt{\frac{2(\frac{1}{2}M_i v_0^2 - e\phi)}{M_i}} \tag{2.39}$$

Plugging this into equation 2.37 we get the number density of ions given by equation 2.40

$$n_i = \frac{n_0}{\sqrt{1 - \frac{2e\phi}{M_i\, v_0^2}}} \tag{2.40}$$

On substituting to the Poisson's equation and considering the Boltzmann relationship, the condition required to satisfy the existance of sheath is given by equation 2.41

$$v_0 > \sqrt{\frac{kT_e}{M_i}} \tag{2.41}$$

This condition is called the Bohm sheath condition, and the minimum speed of ions at the sheath edge is called ion acoustic speed or Bohm speed. The Bohm speed implies the existence of an additional ion acceleration zone. A presheath region,

typically a few ion-neutral mean free path lengths must exist to accelerate the ions to v_B. The voltage drop across the presheath is given by eq. 2.42

$$\Delta V = \frac{kT_e}{2}\frac{1}{e} \tag{2.42}$$

It is interesting to note that the ions diffuse from the bulk plasma towards the sheath by ambipolar diffusion. The ambipolar diffusion for a low temperature plasma is given by equation 2.43. This is applicable in the absence of magnetic fields and when the electron mobility is much greater than ion mobility.

$$D_{amb} = D_i \left(1 + \frac{T_e}{T_i}\right) \tag{2.43}$$

where $D_i = \frac{\mu_i k_B T_i}{q}$ and the mobility of the ions is given by $\mu_i = \frac{q}{M_i \nu_i}$. But D_{amb} is also given by equation 2.44

$$D_{amb} = \frac{v_D^2}{\nu_i} \tag{2.44}$$

where v_D^2 is the diffusion speed. On solving the above two equations to determine the diffusion speed, it is seen that it is equal to the Bohm speed given by equation 2.41. Thus the ambipolar diffusion begins to dominate within the pre-sheath. This is applicable in the absence of magnetic fields.

Due to its large interaction cross section with neutrals, ion-neutral collisions are unavoidable in the presheath and the potential difference is typically higher than $\frac{kT_e}{2e}$. Figure 2.4 shows the relative size comparison of sheath and presheath.

The density of electrons and ions are approximately similar in the presheath but varies greatly within the sheath. This is shown in figure 2.5. Substituting the potential within the presheath to the value described by equation 2.42, the plasma density at the sheath edge is seen to be 0.61 n_0.

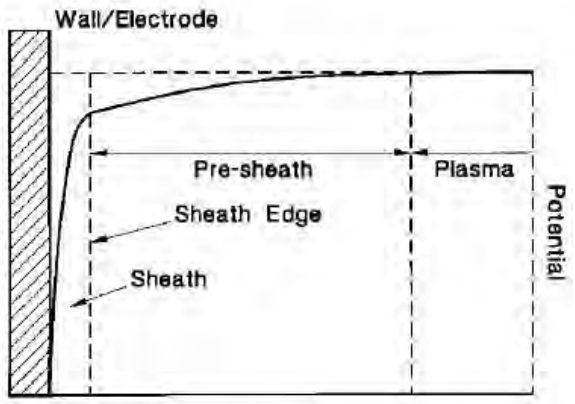

Figure 2.4: Schematic diagram of potential variation through sheath and pre-sheath. Image courtesy: Spenvis [19]

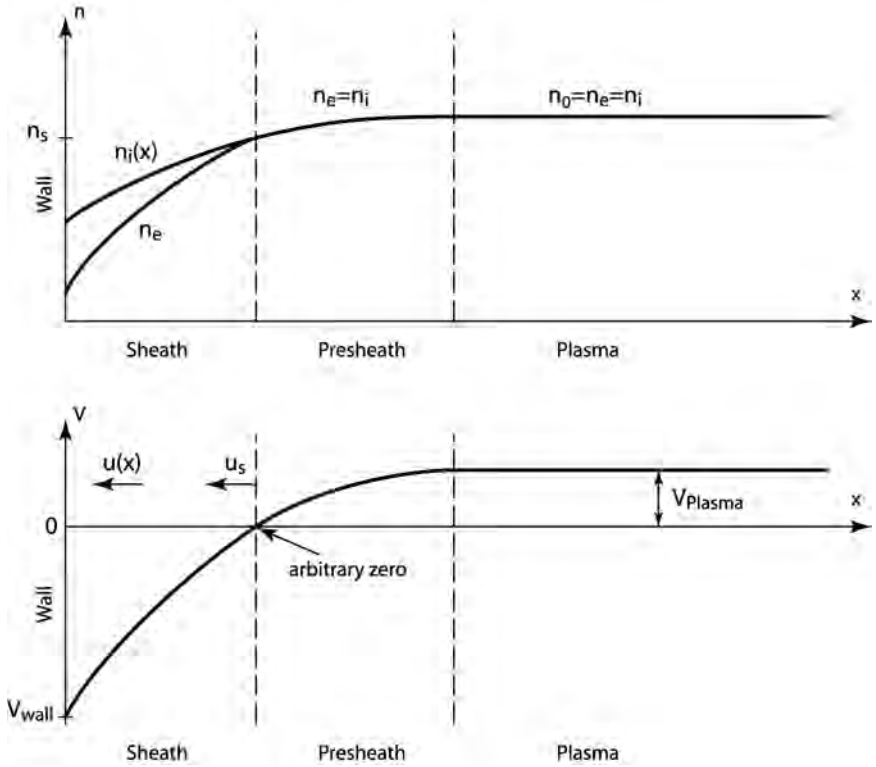

Figure 2.5: Schematic diagram showing the variation of plasma density and potential through sheath and pre-sheath regions. Image courtesy: Lukas Derendinger (CC-BY-SA-2.5)

The current density of ions at the sheath edge is thus given by equation 2.45

$$j_i = n_i \, v_i \, e = 0.61 \, n_0 \, e \sqrt{\frac{kT_e}{M_i}} \tag{2.45}$$

The error associated with the above relationship can be as high as 50% as collisionality within the pre-sheath is not considered.

2.2.5.2 Difference Between Floating, Conducting and Insulating Walls

It is clear now that a sheath forms when a body is immersed in plasma. However, the behavior of the sheath when the object is conductive or insulating, as well as when the body is floating or has a bias can vary widely. Each situation has interesting applications from diagnostics to material processing. Here only situations relevant to this thesis are discussed.

1. Insulating Walls : In the case of an insulator, due to lack of any conduction pathway, the electrons charge the surface instantly and the ions slowly flow towards the surface. In equilibrium, there is a net charge storage and the insulator acts as a capacitor. The charging produces a large negative potential which repels additional electrons. This capacitance can be given by equation 2.46

$$C = \varepsilon_R \varepsilon_0 \frac{A}{d_s} \tag{2.46}$$

   where A is the area of the insulator and d_s is the sheath thickness. For BN at room temperature, the relative dielectric constant is in the range of 4.0 - 4.6.

2. Conducting Walls : If a conducting wall is placed in the plasma which is electrically connected to the an external circuit, such as a ground point or an external bias, then net current will be drawn from the system. In this case, there is

no additional capacitance associated with the system provided the bias is not varying with time. Although this applies to perfect conductors, both graphite and copper used in this dissertation are treated as perfect conductors and they are analyzed without additional capacitance considerations in the system.

3. Floating Walls : If a body, whether it is a metal or an insulator, is floating in the plasma, i.e., not electrically connected to ground or an external bias, then the situation of this floating wall is similar to that in the case of an insulating wall discussed above. There is a finite capacitance of the charged surface that needs to be considered under analysis.

   The ions and electrons flux at the surface are equal. It can be shown that the flux of ions is given by equation 2.47a and that of electron given by equation 2.47b

$$\Gamma_i = \frac{n_i \, v_{th,i}}{4} \quad \text{Ion Flux} \tag{2.47a}$$

$$\Gamma_e = \frac{n_e \, v_{th,e}}{4} \exp\left(\frac{q \, \phi_s}{k_B \, T_e}\right) \quad \text{Electron Flux} \tag{2.47b}$$

   Solving this for sheath potential gives us the potential a floating body faces in plasma (eq. 2.48)

$$\phi_s = -T_e \ln\left(\frac{M_i}{m_e \, 2\pi}\right)^{1/2} \tag{2.48}$$

2.2.5.3 Types of Sheath

Typically the sheath thickness is in the order of several Debye lengths. The accurate estimate depends on the theory used to analyze the system. Different

kinds of sheaths have been proposed in literature for varying applications. The following list gives description of a few.

(a) Matrix Sheath:

Ion Matrix sheaths occur in situations where the change in potential is fast enough for the electrons to immediately leave the region but the ions remain fixed for the observation time [17]. In such cases, if the charge density is constant, there is a uniform electric field due to uniform distribution of ions within the sheath. The thickness of the sheath is given by equation 2.49.

$$\delta_{s,Matrix} = \lambda_D \left(\frac{2v_B}{k_B T_e/e} \right)^{1/2} \tag{2.49}$$

(b) Child Langmuir Sheath:

The Child Langmuir relationship is given by equation 2.50

$$J_0 = \frac{4}{9} \varepsilon_0 \left(\frac{2e}{m_e} \right)^{1/2} \frac{V^{3/2}}{d^2} \tag{2.50}$$

where V is the applied voltage between the anode-cathode gap (in case of sheath, it is the wall and the sheath edge) and d is the gap distance (in case of sheath, d = $\delta_{s,CL}$). The thickness of the CL sheath is given by equation 2.51

$$\delta_{s,CL} = \frac{\sqrt{2}}{3} \lambda_D \left(\frac{2v_B}{k_B T_e/e} \right)^{3/4} \tag{2.51}$$

2.2.6 Electron Energy Distribution Function

Discharge efficiency of a plasma source is intimately tied to the electron energy distribution function (EEDF). Its steady state value is a consequence of balance between

loss mechanisms and the peculiarities of how energy is injected into the plasma. Optimization of discharge efficiency whether inadvertent or not often requires alteration of the EEDF. The EEDF is a key not only for understanding the electron-wall interactions required in modeling of space propulsion thrusters, but also to give in depth understanding of the important processes that occur in a plasma (e.g. ionization, atomic and molecular excitation, and overall plasma-chemistry.)

The exact description of the plasma can often be challenging and is dependent on the operating regime of the system. It is often crucial to understand the system before selection a model of the EEDF as it impacts the results, both experimentally and computationally. Many theories for plasma diagnostics are based on the assumption of Maxwellian distribution, which as will be seen seldom applies for low pressure plasma systems.

2.2.6.1 Types of EEDFs

Low pressure plasmas can be approximated by either a Maxwellian distribution or Druyvesteyn distribution. Maxwellian distributions is realized when collision frequency is velocity independent, while Druyvesteyn distribution is realized when mean free path is velocity independent. Physically, Druyvesteyn distribution are characterized by depletion of high energy tail and a shift of the maximum towards a higher energy. [20]

1. Maxwell-Boltzmann Distribution

   For a mean electron energy ($< \varepsilon >$), the Maxwellian EEDF is given by the equation 2.52,

$$f(\varepsilon) =< \varepsilon >^{-3/2} \beta_1 \exp\left(-\frac{\varepsilon\,\beta_2}{< \varepsilon >}\right) \tag{2.52}$$

   where $\beta_1 = \Gamma(5/2)^{3/2}\,\Gamma(3/2)^{-5/2}$ and $\beta_2 = \Gamma(5/2)\,\Gamma(3/2)^{-1}$ and Γ is the upper

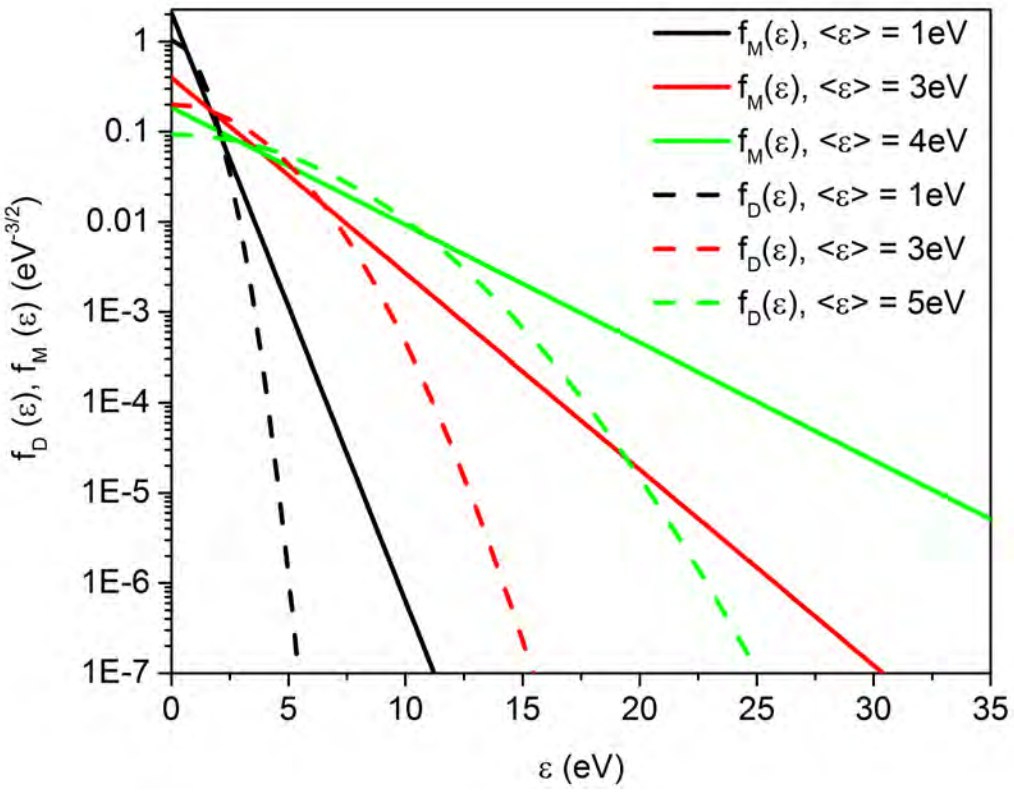

Figure 2.6: Comparison of Maxwellian and Druyvesteyn distribution for different mean energies.

incomplete gamma function.

2. Druyvesteyn Distribution

   Druyvesteyn EEDF is given by the equation 2.53,

$$f(\varepsilon) = 2 < \varepsilon >^{-3/2} \beta_1 \exp\left[-\left(\frac{\varepsilon\,\beta_2}{< \varepsilon >}\right)^2\right] \tag{2.53}$$

   where $\beta_1 = \Gamma(5/4)^{3/2}\,\Gamma(3/4)^{-5/2}$ and $\beta_2 = \Gamma(5/4)\,\Gamma(3/4)^{-1}$.

   Figure 2.6 shows the comparison of the EEDF for a Maxwellian distribution and a Druyvesteyn distribution.

3. Generalized Distribution

Most real plasma systems tend to have an EEDF in between the two limits provided above. As such, in order to describe such a system, two parameters are required. These parameters include the electron temperature and the power law parameter g, where $1 \leq g \leq 2$. This distribution is given by equation 2.54

$$f(\varepsilon) = g < \varepsilon >^{-3/2} \beta_1 \exp\left[-\left(\frac{\varepsilon\,\beta_2}{<\varepsilon>}\right)^g\right] \tag{2.54}$$

where $\beta_1 = \Gamma(5/2g)^{3/2}\,\Gamma(3/2g)^{-5/2}$ and $\beta_2 = \Gamma(5/2g)\,\Gamma(3/2g)^{-1}$.

This generalized distribution is not applicable for molecular gases and has very limited utility. The units for all distributions defined are given by $\mathrm{eV}^{-3/2}$.

2.2.6.2 Control of EEDFs for Process Optimization

Godyak demonstrates how varying operation frequency, gas pressure, discharge current among other parameters can be used to control the EEDF for process optimization [21]. Boris et al [22] demonstrated EEDF modification by varying the concentration of the molecular gas in an argon plasma. Figure 2.7 shows a few examples as to how EEDF can be controlled and optimized for the desired applications.

2.2.6.3 Measurement of EEDFs

EEDFs can be measured both invasively and non-invasively:

1. Electrostatic Probes: The simplest method of obtaineing an EEDF is via Langmuir probe. It can be shown that the EEDF is proportional to the second derivative of the electron current. This technique has been employed in this thesis and is discussed at length in section 4.1

2. Lasers: Laser based techniques such as laser induced fluorescence (LIF) can be used to determine the velocity distribution function of ions far more accurately compared to probes and have been applied to Hall thrusters [26, 27].

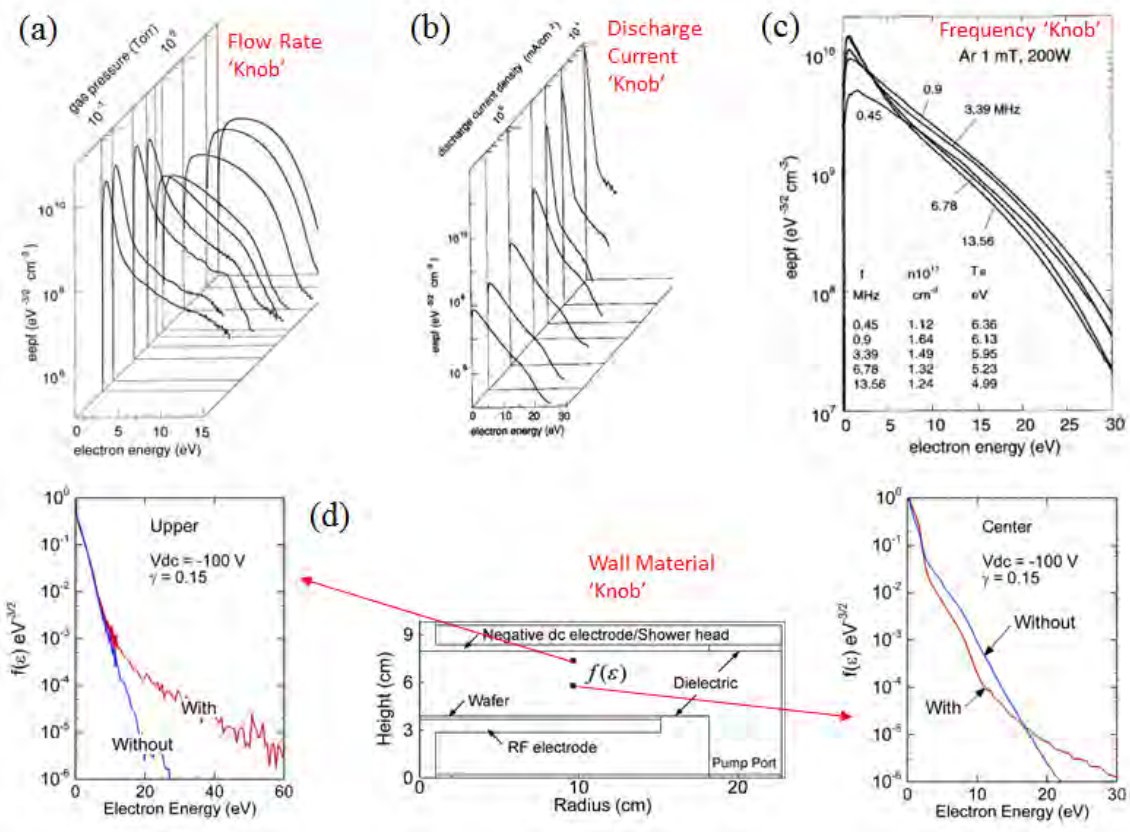

Figure 2.7: Electron energy distribution function. (a) function of pressure [23] (b) function of discharge current [24] (c) function of frequency [24] (d) function of wall material (and secondary emission coefficient) [25].

3. Spectroscopy: Electrostatic probes often tend to disturb the plasma and have high errors associated with them, however, they provide localized measurements. Lasers are a very effective non-intrusive measurement technique but require expensive instrumentation, and detailed interpretive models. Optical emission spectroscopy can provide a compromise in terms of equipment cost and often studies a localized region in the view of the spectrometer. These techniques have been utilized by Carbone et al [28] and Boffard et al [29] determine the EEDF information from a plasma.

2.2.6.4 Obtaining EEDFs using Electrostatic Probes

Section 4.1 discusses in detail the relationship of the I-V characteristics obtained using an electrostatic probe and the electron energy distribution function. It can be shown that the second derivative of the probe characteristic is proportional to the EEDF. This can be expressed as 2.55

$$f(\varepsilon) \propto \frac{d^2 I_{pr}}{dV_{pr}^2} \tag{2.55}$$

where the collected probe current (I_{pr}) due to a potential bias on a probe (V_{pr}) produces a distinct I-V characteristic described in chapter IV.

It is known that derivatives amplify noise as the differentiation operation describes the slope at a point. As a result it is sensitive to even a slight change in the shape of the function. A small change in the shape of a function can create large changes in its slope. This is a major problem to measure the EEDF accurately. Thus we need to smooth the data or fit it in a way to make the derivative process less sensitive to such sharp changes. The most popular ways this is accomplished in laboratories is by using operational amplifiers, lock in amplifiers, or numerical smoothing techniques. Sometimes combination of these techniques is also employed [30]. Novel methods are also proposed using sound cards found in modern computers [31]. Avoiding a

comprehensive review here, a summary of the methods along with their advantages and disadvantages are listed.

1. Differentiating Circuits: This method utilizes the fact that capacitors differentiate their voltage input, while inductors differentiate their current input [32]. Linear voltage signal which is a function of time to carry out the differentiation using R-C networks or operational amplifiers (Op-Amp). The current collected by the probe in the voltage domain and its derivatives are thus proportional to that in the time domain. Chakravarti and Sen Gupta [33] demonstrate the use of operational amplifiers to determine the electron energy distribution in a positive column of plasma.

   The advantage of this method is the ease of use of an Op-Amp and that the second derivative can be found very quickly, thus reducing the possibility of contaminating the probe. However, due to inherent non linearities in the Op-Amp, and limitations in sensor circuitry, the method is not accurate. To overcome this error one must perform an ensemble average over many trials in the same experimental conditions. This increases the time spent in collection of data at every point. The signal to noise ratio is usually low for this method due to the limitation of sensor resistance[34].

2. AC Modulation Methods: One of the popular methods used to determine the derivative of the I-V characteristic is by way of superimposing a small AC modulated signal on top of the probe signal. This method was first implemented by Sloane and MacGregor [35]. Crowley and Dietrich [36] use the same method for an inductively coupled plasma source using modern electronics to determine the EEDF with inexpensive data acquisition (DAQ) systems. The second derivative is proportional to the second harmonic term in probe current associated with the voltage perturbation. The second harmonic is determined using a lock-in

amplifier and is based on the Taylor series expansion (eq. 2.56)

$$I_{pr}(V_{pr}+\Delta V_{AC}) = I_{pr}(V_{pr}) + \Delta V_{AC}\left(\frac{d\,I_{pr}}{dV_{pr}}\right) + \frac{(\Delta V_{AC})^2}{2!}\left(\frac{d^2\,I_{pr}}{dV_{pr}^2}\right) + \frac{(\Delta V_{AC})^3}{3!}\left(\frac{d^3\,I_{pr}}{dV_{pr}^3}\right) + \ldots \quad (2.56)$$

For a harmonic signal, $\Delta \mathrm{V}_{AC} = \mathrm{V}_0 \sin(\omega\, t)$, on simplification equation 2.57 is found:

$$\begin{aligned} I_{pr}(V_{pr}+\Delta V_{AC}) = {} & \left[I_{pr}(V_{pr}) + \frac{(\Delta V_{AC})^2}{4}\left(\frac{d^2\,I_{pr}}{dV_{pr}^2}\right) + \frac{(\Delta V_{AC})^4}{64}\left(\frac{d^4\,I_{pr}}{dV_{pr}^4}\right) + \ldots\right] \\ & + \left[\Delta V_{AC}\left(\frac{d\,I_{pr}}{dV_{pr}}\right) + \frac{(\Delta V_{AC})^3}{8}\left(\frac{d^3\,I_{pr}}{dV_{pr}^3}\right) + \ldots\right]\sin(\omega\, t) \\ & - \left[\frac{(\Delta V_{AC})^2}{4}\left(\frac{d^2\,I_{pr}}{dV_{pr}^2}\right) + \frac{(\Delta V_{AC})^4}{48}\left(\frac{d^4\,I_{pr}}{dV_{pr}^4}\right) + \ldots\right]\cos(2\omega\, t) \\ & - \left[V_{AC}^3\left(\frac{d^3\,I_{pr}}{dV_{pr}^3}\right) + \ldots\right]\sin(3\omega\, t) + \left[\frac{(\Delta V_{AC})^4}{192}\left(\frac{d^4\,I_{pr}}{dV_{pr}^4}\right) + \ldots\right]\cos(4\omega\, t) \\ & + \ldots \quad (2.57) \end{aligned}$$

When the modulated signal is not too large, the higher order terms become negligible and the second harmonic term, $\cos(2\omega \mathrm{t})$ is proportional to the second derivative. A lock in amplifier can be used to isolate the second harmonic. This method has the advantage that it can determine the second derivative accurately if correctly implemented. The estimated error by this method is approximately 8%[37, 38].

3. Numerical Methods: Numerical techniques can also be applied to digitally smooth the noisy characteristic followed by numerical differentiation and is the

method used in this thesis. This is explained in greater detail in section 4.1.6.

2.3 Secondary Electron Emission

Secondary electron emission (SEE) are generated when a solid surface is bombarded with charged particles (ions and electrons) and photons. The phenomenon was first discovered in 1902 by German physicists L. Austin and H. Starke.

The SEE coefficient is primarily a function of the energy of the primary particles impacting the surface. The SEE coefficient (δ), sometimes referred to as SEE yield is given by equation 2.58

$$\delta = \int n(x, E_p) g(x) dx \tag{2.58}$$

The equation separates the SEE yield into two factors - production of secondary electrons and the probability that they will escape from the solid surface.

The average number of secondary electrons produced per incident primary electron in a layer of thickness dx at the depth x on a solid surface is given by $n(x, E_p)$ and is related to the average energy loss per unit path length, -dE/dx. The energy loss divided by average energy required to eject a secondary electron from the valance band of the material (ε) is equal to the number of secondary electrons produced by the primary electron per unit path length.

The probability that an electron will escape from the surface (secondary electron) is given by $g(x)$. This is generally approximated as $B \exp(-\alpha x)$ where B is a constant and α is the absorption factor of the secondary electrons.

$$\delta = \frac{-B}{\varepsilon} \int \left(\frac{dE_p}{dx} \right) \exp(-\alpha x) dx \tag{2.59}$$

Although the formulation of equation 2.59 appears intuitive, there are a few assumptions that need to be addressed.

- The production mechanism (probability) of secondary electrons is independent of the escape mechanism (probability).

  The energy band gap for insulators is much larger than compared to metals, thus it is easier to define the production and escape mechanism for insulators than metals.

- The SEE yield gives an indication of the total number of secondary electrons produced per primary incident electron at a given energy, but does not account for the energy distribution of the secondary electrons. This is obtained using some form of retarding field analyzers. The energy distribution of secondary electron population is shown in figure 2.9

- The function that defines the probability of secondary electron escape from a surface is assumed to be follow an exponential absorption law.

2.3.1 Energy Loss of Primary Electrons

From equation 2.59, it is clear that the energy loss per unit length of the primary electron requires modeling. Lye and Dekker [39] used a power law to describe the energy loss. This energy loss is given by a power law (eq 2.60).

$$\frac{dE_p}{dx} = -\frac{A}{E_p^{n-1}} \tag{2.60}$$

The primary electron absorption coefficient of the material is given by A. Salow [40], Bruining [41], and Baroody [42] also utilized the power-law with n = 2.

The penetration depth (also known as range) of the primary electrons can be obtained by integrating eq. 2.60 within the limits (0, E_p) to obtain eq. 2.61

$$R = \frac{E_p^n}{An} \tag{2.61}$$

Implication of equation 2.61 is that for a beam of given energy, there will be

only one distance where all the energy of the electron will be lost. This is not truly physical due to scattering events within the solid. Young [43] argued based on experimental observation of Al_2O_3 that energy loss was practically constant throughout the material. The number of transmitted electrons was decreasing roughly in a linear relationship with the distance. This theory came to be known as the 'constant loss theory' and is given by equation 2.62

$$\frac{dE_p}{dx} \propto \frac{E_p}{R} \tag{2.62}$$

2.3.2 Secondary Electron Emission Yield

Equation 2.60 and equation 2.59 yields equation 2.63

$$\delta = \frac{B}{\varepsilon}\left(\frac{An}{\alpha}\right)^{1/n} \exp\left(-\alpha R\right) \int_0^{y_m} \exp(y^n) dy \tag{2.63}$$

$$\delta = \frac{B}{\varepsilon}\left(\frac{An}{\alpha}\right)^{1/n} G_n(r) \tag{2.64}$$

$$\frac{\delta}{\delta_m} = \frac{G_n(r_m E_p/E_{pm})}{G_n(r_m)} \tag{2.65}$$

Equation 2.65 is independent of material dependent constants such as A, B and ε. This allows a universal representation of the yield curves. The yield normalized to the maximum yield as a function of the primary electron energy to the energy for which the SEE yield is maximum enables to easily represent the yield regardless of the materials.

Lye and Dekker [39] showed mathematically that for very low energies ($E_p \ll E_{pm}$) eq 2.64 can be represented as (eq. 2.66)

$$\delta \approx \frac{BE_p}{\varepsilon} \tag{2.66}$$

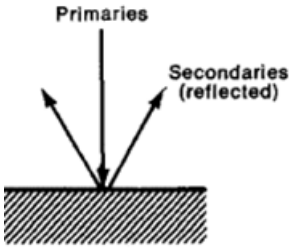

Figure 2.8: Production of secondary electrons on impact of primary electron beam. [41]

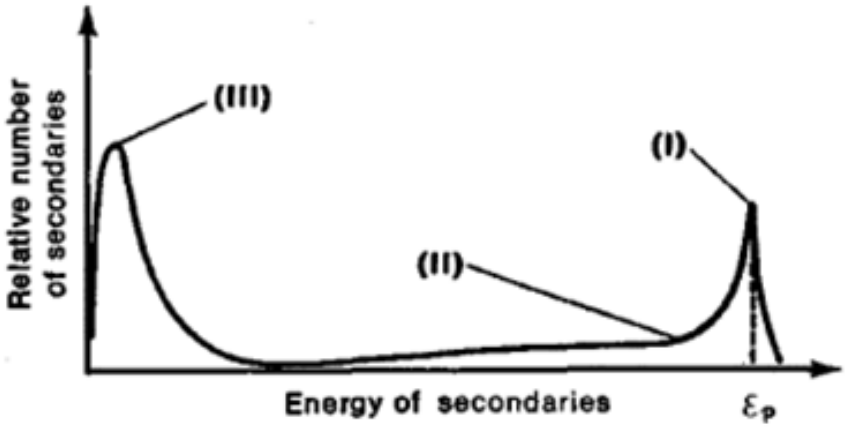

Figure 2.9: Energy distribution of secondary electrons. Region I are elastically scattered primary electrons, Region II are the in-elastically scattered primary electrons, and Region III are the true secondary electrons. [41]

2.3.3 SEE in Vacuum

The term secondary electrons is used when the electrons from the conduction or valance band are ejected on primary electron impact. For the purpose of this work, the incident energy of the primary beam is typically less than 100 eV. The actual emission process of the secondary electrons from the conduction or valance band can be complex [44]. Figure 2.10 shows a typical SEE yield curve for a material. It has two distinctive cross-over points where its yield is greater than one with one maximum at a given energy.

Figure 2.11 shows a the SEE yield taken in vacuum for materials commonly used in HETs.

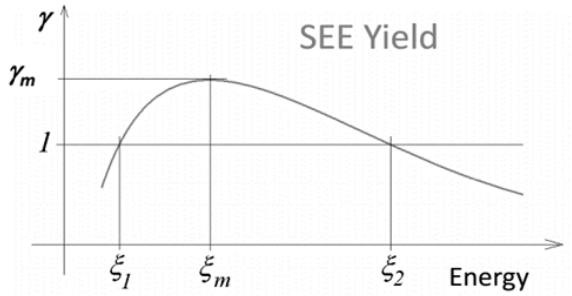

Figure 2.10: SEE yield curve indicating the two crossover points and a maximum yield point.

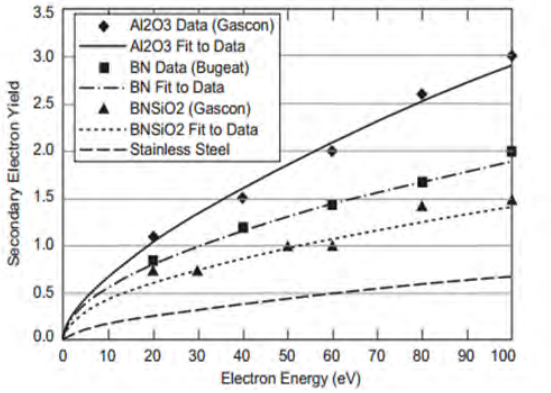

Figure 2.11: SEE yield data for common HET wall materials [45].

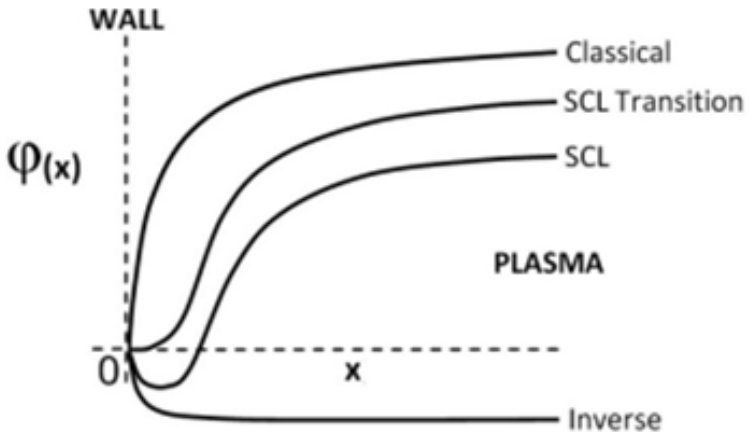

Figure 2.12: Plasma sheath profile theories in literature [47].

2.3.4 Influence of SEE on Plasma Sheath

Presence of secondary electrons tends to lower the sheath potential making it more positive with respect to the bulk plasma. This is seen from figure 2.13. Under strong emissions, the electron population are reflected back to the bulk plasma and lead to formation of virtual cathodes.

The reduction of sheath potential due to SEE processes find important applications in sputtering of channel walls in Hall thrusters and divertors in fusion devices, as well as in deposition processes of thin films. Yao [46] studied the effects of secondary electron emission on sheath potential in an ECR plasma source using RPA and found that the effects of SEE are important.

Pandey and Roy [48] derived the sheath potential in the presence of secondary electron emission and sputtering yield following the works of Hobbs and Wesson [49]. They showed that the combined impact of secondary electrons and sputtering yield can be given by equation 2.67

$$\phi_w \approx -T_e \ln \left[\left(\frac{1-\gamma}{1-Y} \right) \frac{\sqrt{M_i/2\pi m_e}}{1 - \frac{Y}{1-Y} \left(\frac{-E_0}{\phi_w} \right)^{1/2}} \right] \tag{2.67}$$

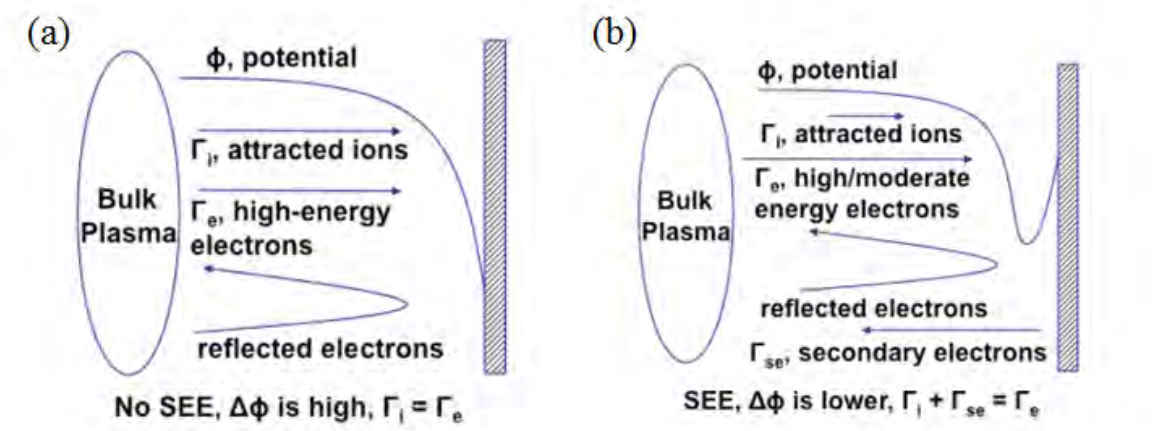

Figure 2.13: Plasma sheath profile. (a) in the absence of secondary electrons (b) in presence of secondary electrons [11].

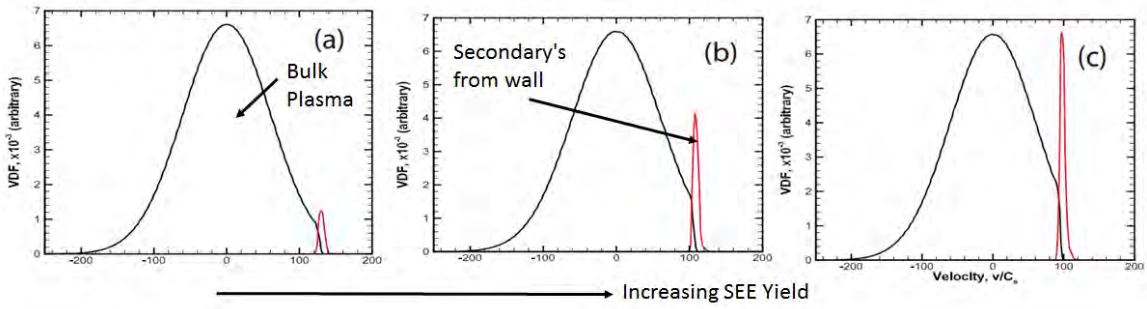

Figure 2.14: Velocity distribution function in presence of secondary electrons showing wall losses. [50]

In the limit where sputter yield is zero, the wall potential is identical to the one by Hobbs and Wesson [49] and is given by equation 2.68

$$\phi_w \approx -T_e \ln \left[(1-\gamma) \sqrt{\frac{M_i}{2\pi m_e}} \right] \tag{2.68}$$

2.3.5 Influence of SEE on Plasma EEDF

It is numerically shown that with increasing secondary emission from a wall, the velocity distribution of the primary electrons is depleted and the tail shifts [51]. This depletion is due to the reduction in sheath potential allowing energetic electrons to be lost to the wall. So the influence of SEE on plasma EEDF can be seen by a depletion of the tail.

Another region where the SEE may play a role would be modification of the bulk of the plasma. This is due to the cooling or heating of the plasma as a result of thermalization with the bulk population which would be reflected in the bulk population of the EEDF.

2.4 Space Propulsion

Space propulsion is important for deep space missions to understand the origins of the Universe and life as well as for missions which would someday in the future mine asteroids for rare earth metals. But besides answering the burning questions of are we special in the Universe, space propulsion serves the multi-million dollar satellite industry which uses advanced propulsion systems to correct orbits of satellites. It is in the interest of these two broad goals, the study of propulsion systems for space is important.

Over the last century, several missions have been deployed in both directions towards and away from the sun. Some of the modern missions employing Hall thrusters, which is a focus of this dissertation include the SMART mission (see Figure 2.15) and the ARM mission (see Figure 2.16) and several satellite missions. The development of these thrusters are funded by several countries such as United States of America, Russia, France, Europe, Japan, and India.

Besides deep space travel, satellite industry employs propulsion systems. This industry has been growing and is currently a 200 million dollar industry. Figure 2.17 shows the yearly revenue of the satellite business as reported by the satellite industry association. The number of electric propulsion devices on satellites have also significantly increases as the technology has matured. Aerojet compiles a list of all satellites that enter space and is shown in figure 2.18.

Figure 2.15: Concept image of small missions for advanced research in technology-1 (SMART-1) [52].

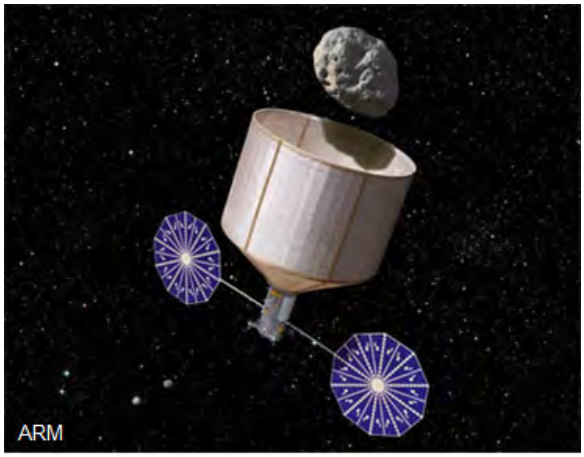

Figure 2.16: Concept image of asteroid redirect mission (ARM). [53]

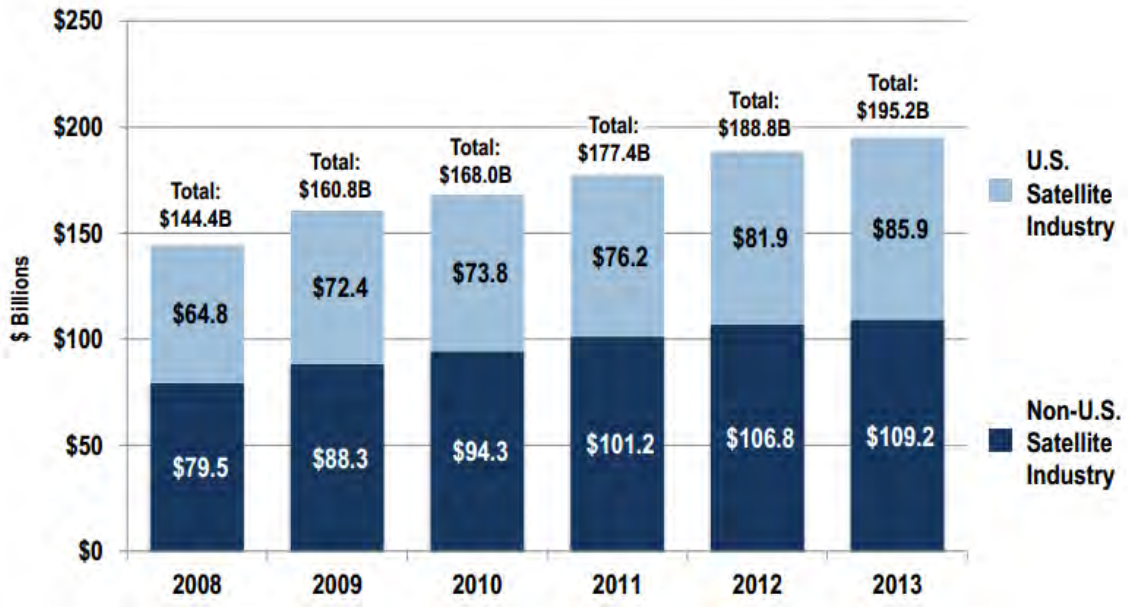

Figure 2.17: Satellite industry revenue showing consistent growth. Source: SIA

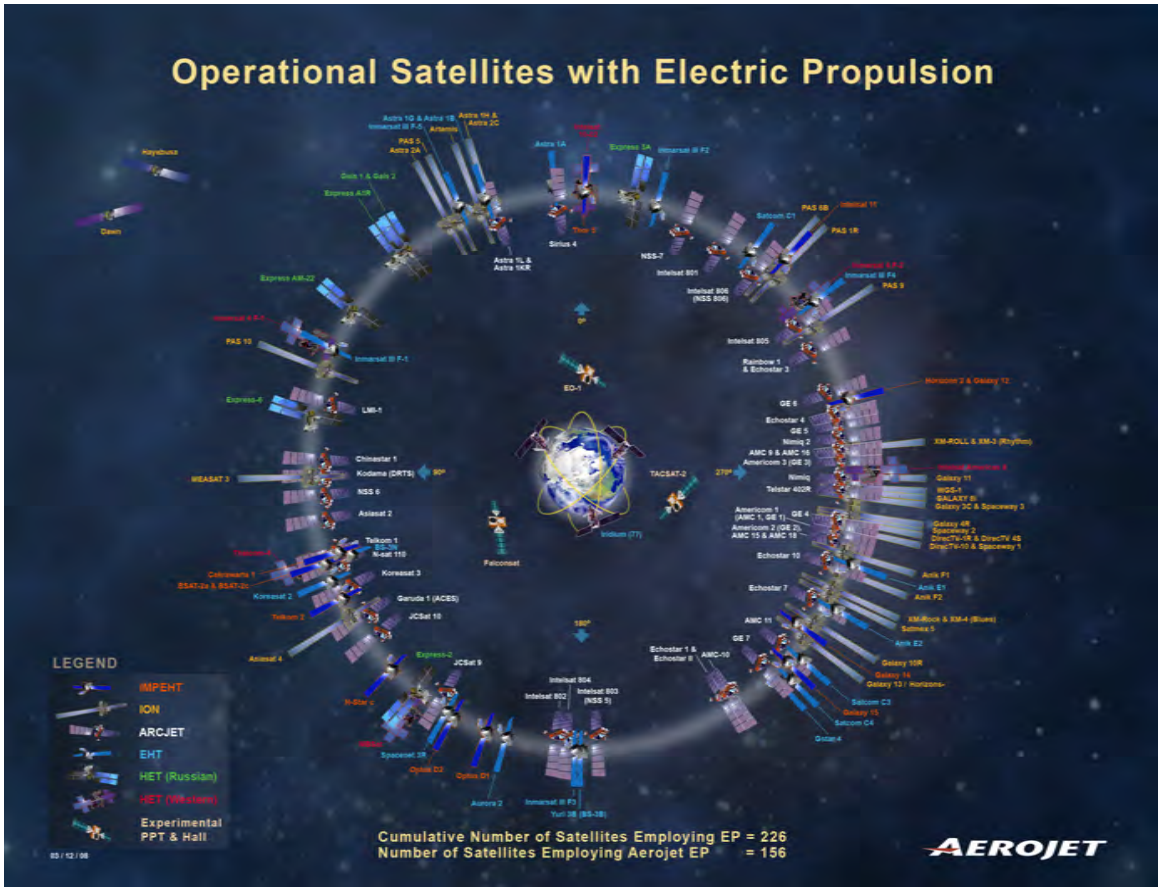

Figure 2.18: List of commercial satellites employing electric propulsion

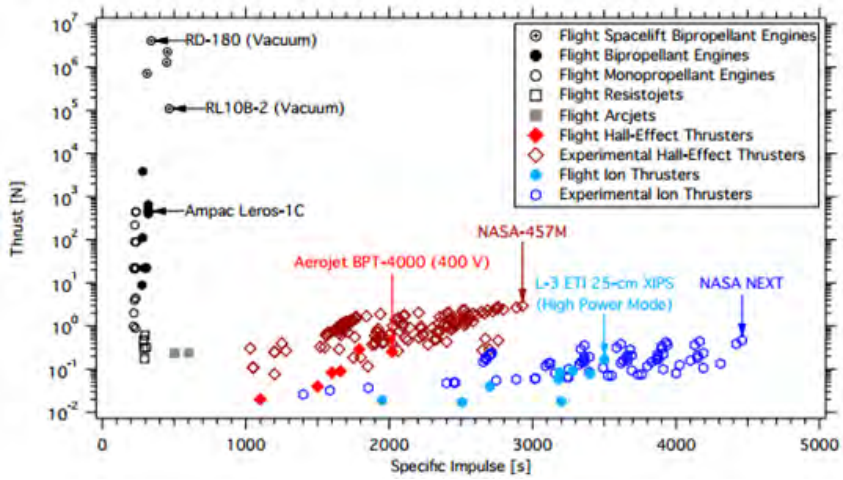

Figure 2.19: Comparison of electric propulsion with chemical propulsion thrusters (Source: Aerojet)

2.4.1 Different Propulsion Technologies

There are several kinds of propulsion technologies proposed, many of which have the potential to take humankind far in space. However, several of these cannot be attained with our present understanding of science. Among the mature technologies, chemical rockets and electric propulsion systems are well established. Other technologies such as nuclear have changing public opinion, tether based propulsion techniques have limitation with the location and finally futuristic technologies that are proven mathematically but difficult to construct at this time.

2.4.2 Why Electric Propulsion?

Of the established and mature technologies, electric propulsion fares well in most metrics when compared to chemical propulsion method. Figure 2.19 compares different classes of chemical and electric propulsion systems and while the thrust for most chemical systems is much higher than that of EP systems, the specific impulse of EP systems is better. The specific impulse is a measure of efficiency of thrusters.

Choueiri provides an excellent introduction to the early history of EP [54] which lays the foundation of modern day EP devices.

Effort is often taken by the EP community to provide a feedback on the activities among various research grounps such as academia, national labs, defense organizations as well as industry. An overview of the EP activities in the US industry have been provided by Curran[55], Hurby[56] and Lichtin [57]. Activities promoted by the US air force research groups have been provided by Spores et al. [58, 59]. Academic contributions in the US have been made from several Universities and research labs. These contributions are highlighted by Gallimore[60], Wilbur[61], and King [62]. Activities from France [63], Russia [64] and Europe [65] are also reported in litareture.

EP consists of three broad classes of thruster technologies – The electrothermal thrusters, the electrostatic thrusters, and the electromagnetic thrusters. These are described briefly below.

2.4.2.1 Electrothermal Propulsion

In Electrothermal propulsion thrusters the propellant is heated electrically using a heated surface or arcs discharges, and the heated gas is then expanded through a nozzle of a suitable shape to get the required acceleration. Examples in this class of thrusters include resistojets and arcjets.

2.4.2.2 Electrostatic Propulsion

Electrostatic propulsion thrusters accelerate the ions by application of electric fields, i.e., potential difference between a series of grids thereby accelerating the ions and neutralizing them in the free stream at a later point. This class of thrusters is the richest and examples include gridded ion thrusters, Hall thruster, colloid thruster, and the field emission electric propulsion thruster.

2.4.2.3 Electromagnetic Propulsion

The third class of the EP thrusters makes use of the combination of external and internal electromagnetic fields to propel the ionized stream of gas and is called the electromagnetic propulsion thrusters. Robert Jahn [66] states that "In comparison with pure electro-thermal and electro-static mechanisms, electro-magnetic interactions are phenomenologically more complex, analytically less tractable, and technologically more difficult to implement, and hence lagged in their engineering application". Examples in this class includes the pulsed plasma thruster (PPT), the Lorentz-Force accelerator or MPD thruster, plasma inductive thruster and the one which has most attention today, the VASIMR (Variable Specific Impulse Magneto-plasma Rocket) thruster.

Electrostatic thrusters have the ability to accelerate ions (typically Xenon) and high thrust efficiencies and specific impulses in the range of 2000 - 3600 seconds. From an operational standpoint, these thrusters are versatile and highly controllable as their thrust and specific impulse can be adjusted just by varying the acceleration voltage and the flow rate of the propellant gas. The following advantages of Hall thrusters make it potential candidates for space missions such as station keeping, orbit corrections or situations which require greater flexibility in maneuverability. This dissertation effort focuses on EP devices in general, but Hall thrusters in particular.

2.4.3 Hall Thruster Design

The magnetic field circuit can be argued to be the most critical design requirement for HET [67]. The conventional design philosophy for HET can be summarized by equations 2.69 and 2.70

$$r_{Le} \ll d < L \ll r_{Li} \tag{2.69}$$

$$\nabla_z B_r > 0 \tag{2.70}$$

where d is the discharge chamber diameter and L is the length of the acceleration channel. Equation 2.69 states that in HET electrons are always magnetized whereas the ions are not magnetized whereas equation 2.70 states that the the magnetic field must increase from the anode to the exit of the channel.

The radial magnetic field causes the electrons that enter the thruster channel to gyrate about

2.4.4 Hall Thruster Operation

Hall thrusters are designed in various sizes and shapes such as miniature Hall thruster[68], cylindrical Hall thruster[69]. However the conventional categorization depends on the wall material of the acceleration channel. These are categorized as stationary plasma thruster (SPT) or thruster with anode layer (TAL).

For the conventional thrusters, the geometry consists of an axis-symmetric annual chamber with a metal anode on one end of the annulus that serves as the gas feed and an acceleration zone defined by the class of SPT or TAL thrusters. For this thesis, all further thrusters are going to assume SPT kind thrusters with dielectric walls in the acceleration zone. An electron source is mounted outside the thruster geometry, either at the axis center or at one of the outer periphery of the cylinder. The electron source is typically a hollow cathode, though use of ECR based electron sources for Hall thrusters have been recommended[70]. Approximately 20% of these electrons produced by the external electron source gets attracted by the positive anode and the remaining electrons are used to neutralize the ion beam used for propulsion[71]. The anode also acts as the gas supply line injecting typically Xenon gas into the chamber volume. Due to the large radial magnetic fields closer to the exit channel, the electrons that enter the channel are trapped and tend to ionize the gas. The trapped electrons

move azimuthally due to an ExB force, while gyrating at the electron gyro radius (or Larmor radius). This causes a very high potential resulting in efficient ionization and the ionized gas are accelerated through this potential and following Newton's laws tend to leave the thruster propelling the spacecraft in the opposite direction. The remaining 80% of the electrons from the electron source recombine with the ions downstream to keep the spacecraft neutral. Figure 2.20 shows the electrical schematic of a HET as well as a 3D view indicating the azimuthal drift and gyro-orbits of the electrons.

Table 2.2 lists the typical parameters that describe most conventional Hall thrusters.

Property	Typical Range
Diameter	1 - 100 [cm]
Neutral Density	10^{12} - 10^{13} [cm^{-3}]
Pressure	$\approx 10^{-4}$ [Torr]
Plasma Density	10^{11} - 10^{12} [cm^{-3}]
Electron Temperature	20 - 60 [eV]
Magnetic Fields	150 - 300 [G]
Ion Temperature	≈ 1 [eV]
Acceleration Electric Fields	500 - 1000 [V/cm]
Wall Electric Fields	5 - 10 [V/cm]

Table 2.2: Hall effect thruster parameters.

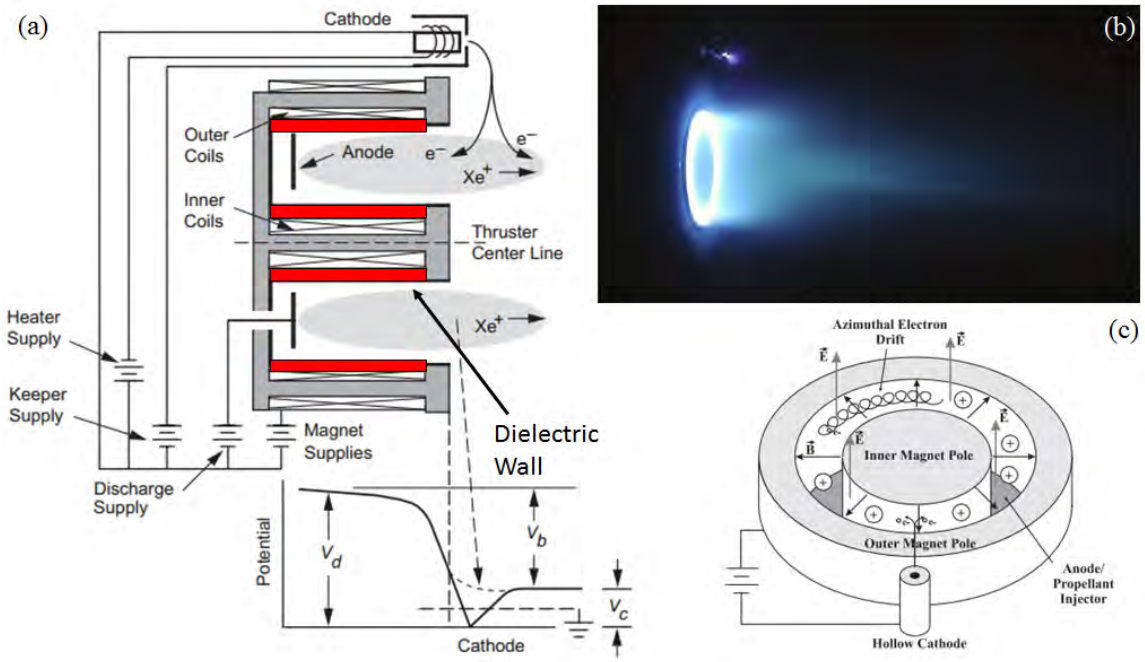

Figure 2.20: Hall thruster operation: (a) Hall thruster electrical schematic and potential distribution [45], (b)Photograph of the NASA 173 Mv1 operating at 300 V-15 A [12], (c) 3D view of Hall thruster geometry [72]

2.4.5 Complex Interactions

In a complex crossed field device such as a HET, several phenomena happen simultaneously. Some of these phenomena include rotating spokes [73], breathing (oscillating modes) [74], wall sputtering [11], secondary electron emission [75, 76], and anomalous transport [77]. All these methods are complex individually and tend to be inter-related to each other. In particular, however, most of these effects have known to vary due to surface variations suggesting SEE plays a role in each and every phenomena. Figure 2.21 shows the same.

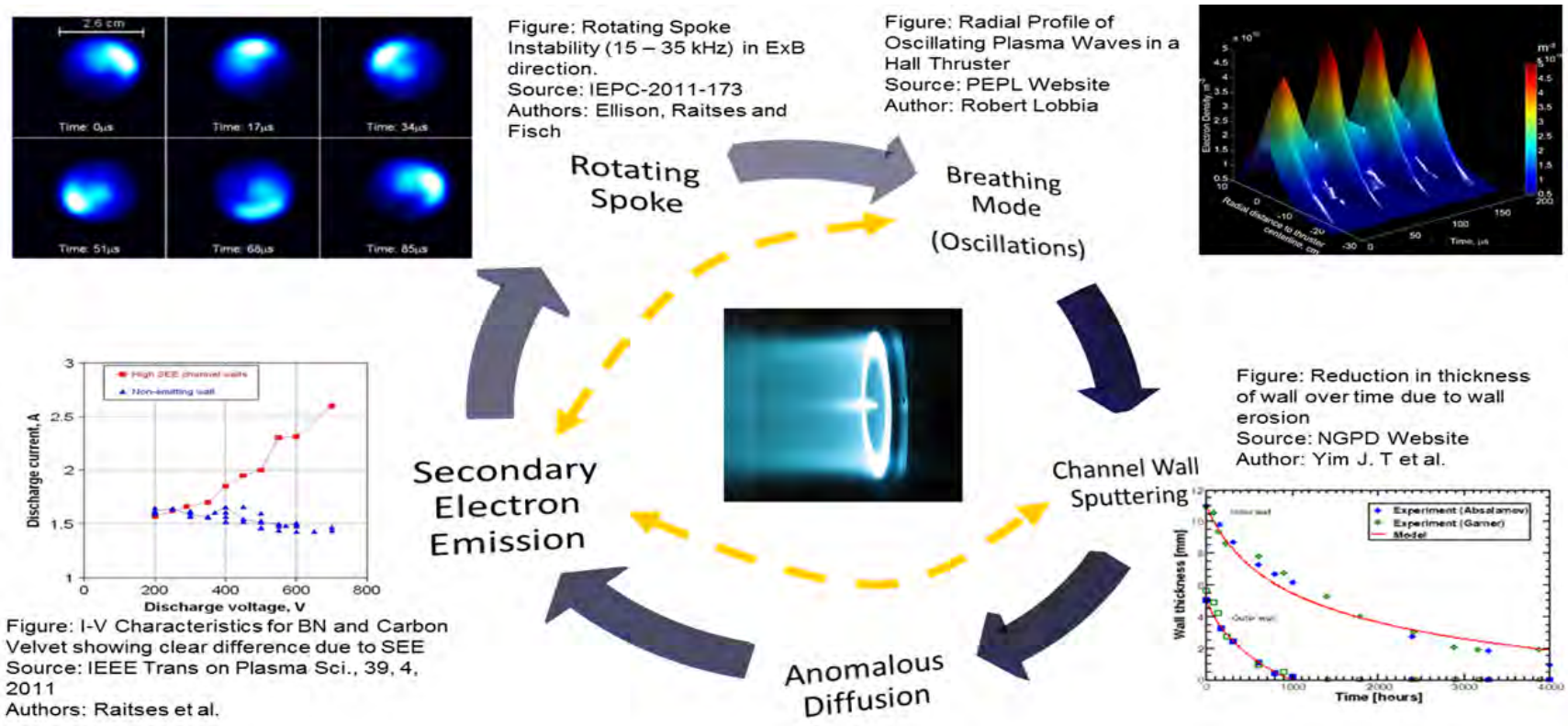

Figure 2.21: Different phenomena that take place in a HET and their relation to each other

2.4.6 Magnetic Shielding

Magnetic shielding of Hall thrusters have been recently proposed to have significant benefits in terms of lifetime of the thruster. This is due to the ability to shield the plasma from interacting with the boron nitride (BN) channels of a conventional HET. The reduced interactions lead to significantly lower sputter yield by energetic ions and thus extend the life of Hall thrusters by order of magnitude [78, 79].

2.5 SEE and Hall Thrusters

Besides the complex interactions that exist in HET, the transport of SEE in HET channel requires special consideration. The SEE generated from one wall of a thruster is partially trapped by the bulk plasma, whereas the remainder drifts into the sheath of the opposite wall along with the modified bulk plasma. The contribution at any given moment is due to both SEE production as well as the continually evolving bulk plasma change due to SEE and other processes. Thus it is important to note that both the SEE coefficient and trapping coefficient significantly impact the distributions of plasma as well as the energy loss to the wall.

Meezan and Cappelli used kinetic models to show that the electron wall collisions resulting in SEE play a critical role in the Hall thruster discharge power balance[80]. In particular, they highlighted that SEE selectively removes high energy electrons from the EEDF and significantly lower the mean electron energy and skew the distribution towards low energies. These results for Hall thrusters are also evident from the discussion of SEE effects in plasma sheath and EED discussed in section 2.3.5 and 2.3.4. Similar to Ahedo [7], Zhongua et al. [81] developed a sheath model for a SPT and showed that the particle (ion and electron) densities as well as ionization rate increases with increasing SEE. It was further shown by both that in case of a SPT, the characteristics of the sheath depend on both the product of the SEE coefficient

and a trapping coefficient.

In general, SEE at channel walls regulates energy transport to the wall by controlling the sheath potential profile. This can impact the ionization efficiency of the thruster as the tail of the distribution depletes due to loss of energetic particles to the channel walls. The energy transport can result in saturation of electron temperatures. Although, not significantly, the change in sheath potential due to SEE can also affect the sputtering rate of the wall material [82, 11, 5].

SEE can also lead to relaxation oscillations under certain conditions which ultimately affects the engine stability as well as crossed field diffusion rates. This can feed instabilities via mechanisms such as two stream interactions [6, 7].

Another contribution of SEE towards HETs is that the control and regulation of the electrically insulating properties of a Hall thruster channel by a phenomena known as near wall conductivity [83, 84, 77].

Secondary electrons can also modify the temperature by 'heating' or 'cooling' the plasma electrons depending on the condition. This effect may be enhanced by SEE trapped between two channel walls [85, 86, 87, 7, 5].

CHAPTER III

Bench-top Experimental Apparatus and Setup

"*An experiment is a question which we ask of Nature, who is always ready to give a correct answer, provided we ask properly, that is, provided we arrange a proper experiment.*"

- Charles Vernon Boys

3.1 Introduction

The experimental setup comprises of a bench-top system designed to simulate the conditions similar to that seen a typical Hall thruster. While the essential physics is sought to be replicated in this work, the current apparatus eliminates the complexity encountered in real devices such as rotating spokes [73, 88], wall sputtering [89, 12, 11] and oscillating (breathing) modes [90, 74]. These complex phenomena along with secondary electron emissions from the wall govern the electron transport in Hall thrusters. Existing literature indicates the difficulty of understanding the effects of all these phenomena which occur under different operation conditions, and relating them towards better understanding transport in Hall thrusters. The isolation of physics using the bench-top facility suggested here would account purely for secondary electron emission effects to the bulk plasma properties as well as variation within the sheath. This isolation is accomplished by operating various subsystems, described in

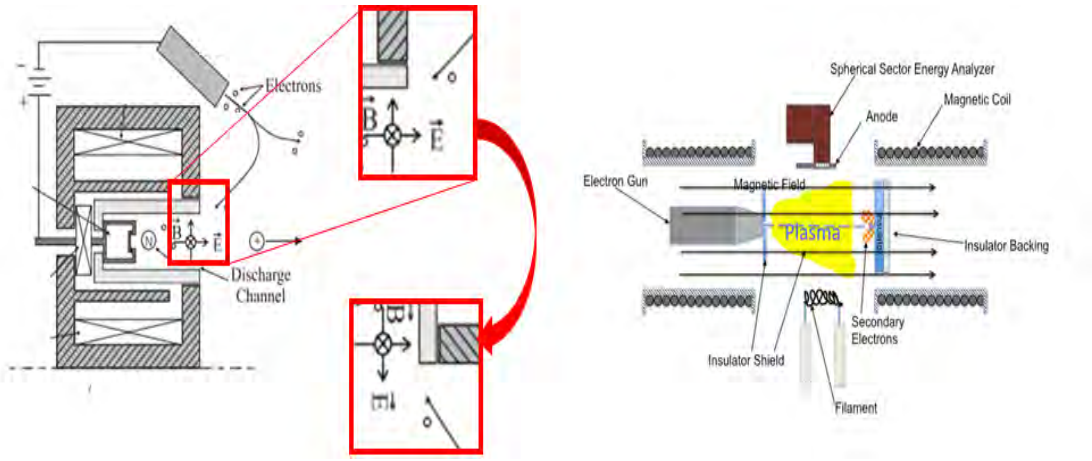

Figure 3.1: Image of the experimental concept showing similarity between a Hall effect thruster and the bench-top apparatus.

this chapter, to simulate the conditions encountered in a region closer to the walls of the acceleration channel. Table 3.1 gives the target goals for the bench-top apparatus which are very similar to a typical Hall thruster parameters given in table 2.2.

Property	Typical Range
System Dimensions	11 - 25.4 [cm]
System Pressure	$\approx 10^{-4}$ [Torr]
Plasma Density	10^{7} - 10^{9} [cm^{-3}]
Electron Temperature	1 - 5 [eV]
Magnetic Fields	0 - 200 [G]
Ion Temperature	$\approx$ 300 [K] = 0.03 [eV]
Electron Beam Energy	20 - 80 [eV]
System Electric Fields	5 - 10 [V/cm]
Electron Beam Current Density	$\geq$ random thermal flux of plasma

Table 3.1: Experimental bench-top apparatus parameters.

The role of the electron gun in the bench-top apparatus is to simulate hot electrons seen in HETs and the magnetic fields are operated under similar ranges to that of a HET. The density on the bench-top apparatus is intentionally kept 3 - 4 orders of magnitude lower to enable production of thick sheath. The think sheath would allow electrostatic probes to resolve the behavior of sheath and pre-sheath during exposure to electron beam and SEE production upon irradiation. In order to compare the two

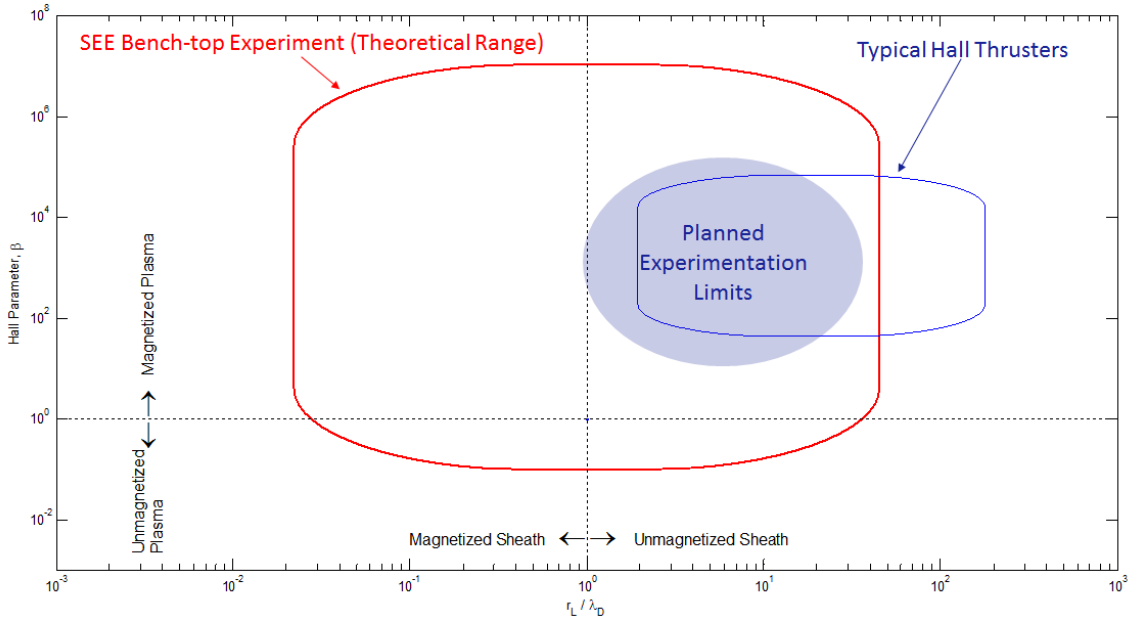

Figure 3.2: Hall Parameter vs Ratio of Larmor radius to Debye length for HETs and Bench-top apparatus.

systems, non-dimensional parameters are employed. The ratio of electron Larmor radius to Debye length, and the Hall parameter, which is a ratio of cyclotron frequency to collision frequency, allow us to compare the capability of the bench-top apparatus to that of a Hall thruster. Figure 3.2 shows the two non-dimensional parameters for both the bench-top apparatus as well as typical HETs as defined in Table 2.2.

3.2 Vacuum Facilities

All experiments were conducted in vacuum facilities at the Plasma Science and Technology Laboratory (PSTL) located in the Cooley Building at the University of Michigan. Vacuum experiments were conducted at base pressures lower than $1\text{x}10^{-5}$ Torr. Plasma experiments operational pressures range was $1\text{x}10^{-4}$ - $5\text{x}10^{-4}$ Torr using high purity experimental grade (99.999%) Xenon gas. The base pressure for all the systems was in the range of $2\text{x}10^{-6}$ - $4\text{x}10^{-6}$ Torr. Details about the facilities are described below.

3.2.1 Tall Cylindrical Chamber

The tall cylindrical chamber, also known as 'Bessie', contains a Pfieffer-Balzers TPU170 turbopump controlled using the Pfieffer Balzer TCP 121 with a capability of pumping 170 L/s. The roughing pump used to back the turbopump was a Pfeiffer Duo 005M rotary vane device. The turbomolecular pump in this system required water cooling and is supported by a NESLAB RTE-111 chiller. The base pressure obtained in this chamber was close to $6\text{x}10^{-6}$ Torr. Xenon was pumped into this chamber, which has a diameter of 45 cm and a height of 62 cm, using a Alicat mass flow controller, which had a maximum flow rate of 20 sccm. The pressure diagnostics used for this system include the thermocouple gauge and an ionization gauge operated using the KJL 4500 ion gauge controller. An additional Pirani gauge (SuperBEE) was placed near the Xenon feed lines to measure the runtime pressure as well as feedline leakage rates.

Figure 3.3 shows the 'Bessie' vacuum chamber and figure 3.4 shows the experimental facility used to support tests conducted in this chamber.

3.2.2 'Rocket' Chamber

The horizontal vacuum chamber referred to as the 'Rocket Chamber' is shown in figure 3.5. The chamber has a diameter of 64 cm and is 190 cm long. The turbomolecular pump used in this chamber is an air-cooled Pfeiffer TMU 521 P backed by an Edwards 28 rotary vane roughing pump. The base pressure reached by this pump is $\approx 2\text{x}10^{-6}$ Torr. An MKS Type 1159 B mass flow controller is used to inject xenon gas at flow rates of 3.81 sccm and 5.53 sccm. This corresponds to a stable operation pressure of $2.7\text{x}10^{-4}$ Torr and $4.4\text{x}10^{-4}$ Torr. The chamber has a SuperBEE Pirani gauge and a KJL 6000 thermocouple gauge (readout: KJL-205BM). At pressures below 10 mTorr, a cold cathode gauge is used for pressure measurement.

Figure 3.6 shows the experimental facility adjacent to the rocket chamber used

Figure 3.3: Image of vacuum facility called 'Bessie' is a tall cylindrical chamber.

for SEE plasma interaction studies.

3.3 Variable Magnetic Field Bench-top Apparatus

In order to generate a variable controlled magnetic field, a pair of electromagnets were designed. The electromagnets are made using the Helmholtz coil arrangement.

3.3.1 Helmholtz Coil

In such an arrangement we require the radius of the magnet spool be equal to the length between the two spools. In this system, R = L = 5.08 cm. The copper wire used for winding the magnet is AWG 12 and a total of 120 5 turns (5 layers of 24

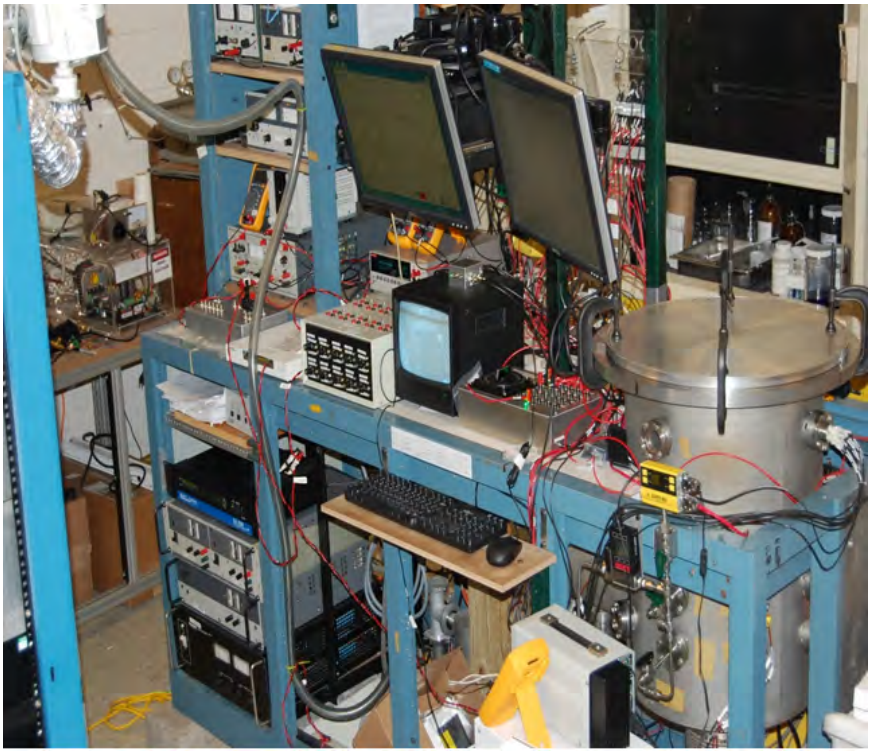

Figure 3.4: Image of the external facility to conduct experiments on 'Bessie' including power supplies, control systems and computer.

turns ± 1 turn) are given to each spool.

3.3.1.1 Design

Figure 3.7 shows the 3D schematic of the electromagnet coils used to simulate the HET magnetic field. As the electromagnet is expected to be run in a vacuum systems without any water cooling, the class of magnet wire chosen was the MW 16-C. This rating indicates a polyimide film used to insulate the conducting wire and is very resistant to high temperatures. The temperature at which the insulation of the electromagnet wire would fail is ≈ 513 K. The magnet wire was wrapped on a spool made using aluminum and the inner diameter of the spool was chosen to be 8.5 cm whereas the outer diameter was ≈ 12 cm. These sizes ensured sufficient space for both the electron gun and the target to be held in their respective spools.

The circuit diagram for the Helmholtz coil arrangement is shown in figure 3.8. In

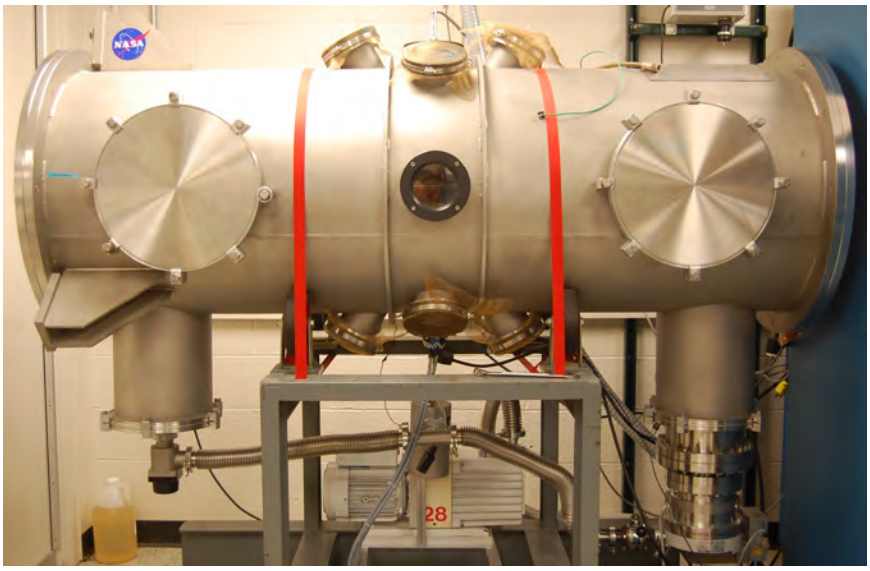

Figure 3.5: Image of vacuum facility called the 'Rocket Chamber'.

order to achieve uniform magnetic fields, the two spools are connected in series such that the direction of current flow is the same across both.

3.3.1.2 Simulation

The design of the electromagnet employed commercial simulation packages namely Maxwell and Comsol. Figure 3.9 shows the analysis of the electromagnet in COMSOL. The black colored vectors indicate the magnetic field vector for a given coil current. The direction of current flow through the coils is indicated by the red colored vectors. To obtain a uniform magnetic field, same current must flow through equal number of coils on each spool. Centerline data is used for comparison with experimental measurement discussed in section 3.3.1.3

3.3.1.3 Experimental Characterization

Figure 3.10 shows the experimental results compared with the simulation data. The data matches closely and shows a rough relationship of 1 ampere $\approx$ 10 Gauss relationship for this setup. Near the poles the field is not as uniform as expected from

Figure 3.6: Image of the external facility to conduct experiments on 'Rocket chamber' including power supplies, control systems and computer.

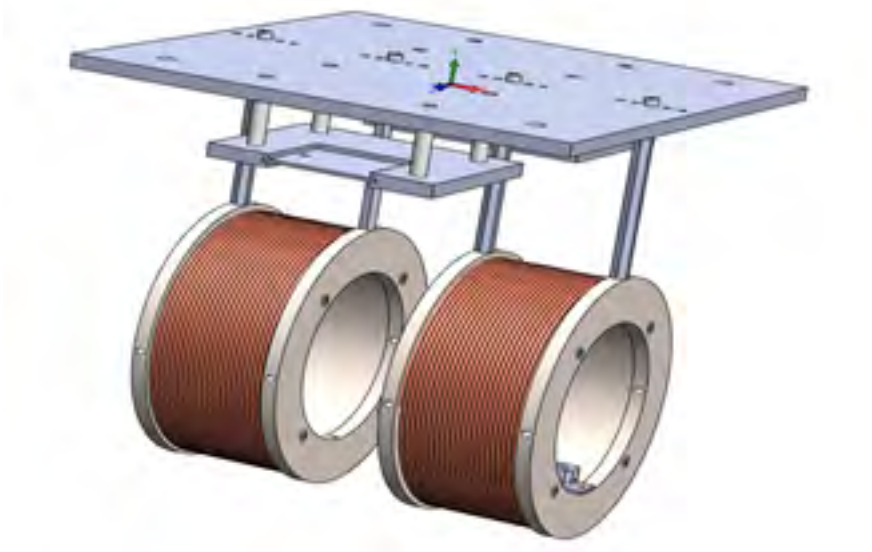

Figure 3.7: 3D drawing of the electromagnet coils oriented in Helmholtz coil arrangement.

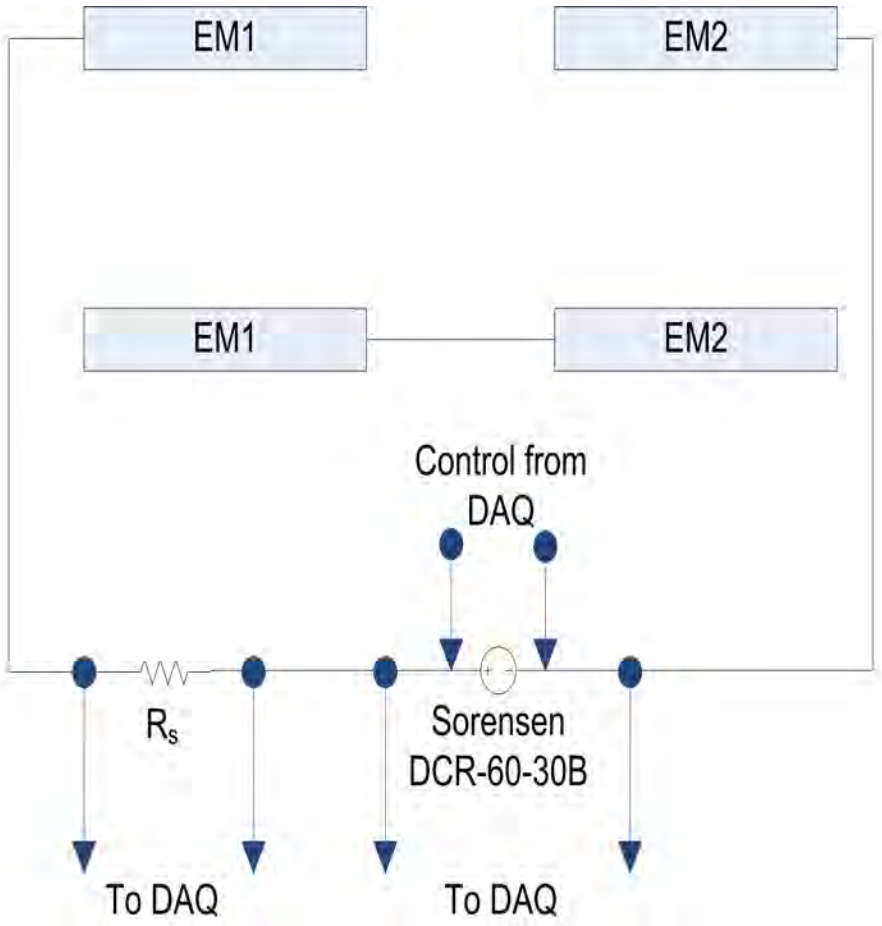

Figure 3.8: Circuit diagram for the Helmholtz coil. EM1 and EM2 are spool 1 and 2 of the electromagnet and the current flows in series to maintain uniform magnetic fields.

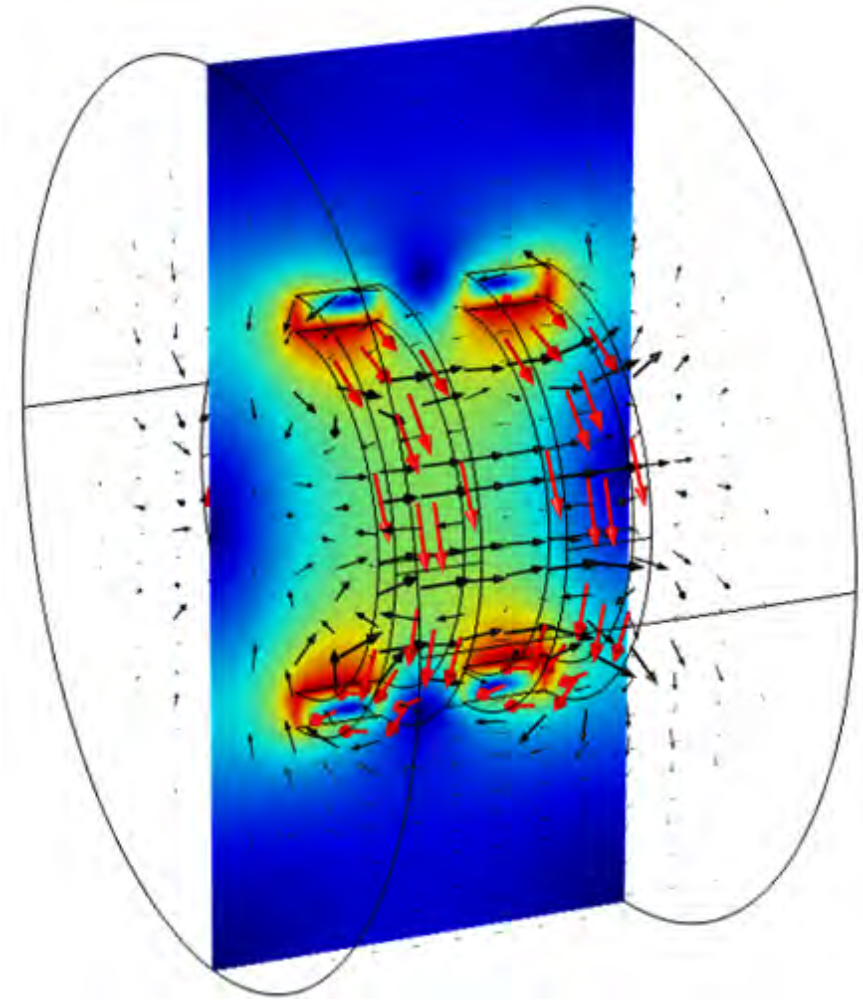

Figure 3.9: Simulation of a Helmholtz coil geometry. The red colored vectors indicate the direction of the current flow and the magnetic field vector is plotted using black arrows.

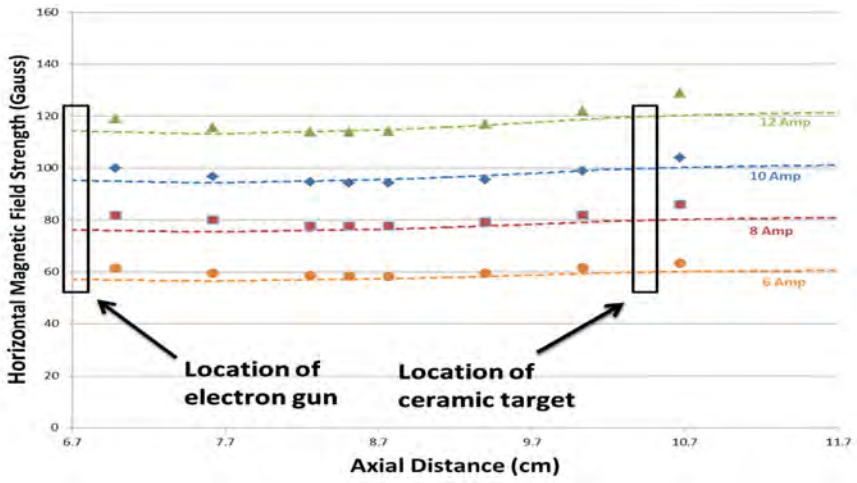

Figure 3.10: Experimental characterization of the Helmholtz coil geometry.

the theory. This is because the ideal Helmholtz coil expects to be a plane whereas real systems have a finite width associated due to thickness of wires and restriction based on spool design.

The purpose of the electromanget spools, besides providing the required magnetic fields, was also to act as structural members to hold the electron gun and the target. Figure 3.11 shows the electromagnet as a structural member to hold the target using a target holder and angle fixture. These components are discussed in section 3.4

3.4 Impact Angle

The angle of incidence of the electron beam is known the change the SEE yield in vacuum. In order to accommodate a study on the angular effects of SEE on plasma, a target holding assembly along with the impact angle fixture was designed and created. The impact angle fixture can control the angle with respect to the beam in 15 degree increments. Figure 3.12 shows the impact angle fixture with target holding assembly and a computer aided design (CAD) output displaying the various angles that are fixed and locked.

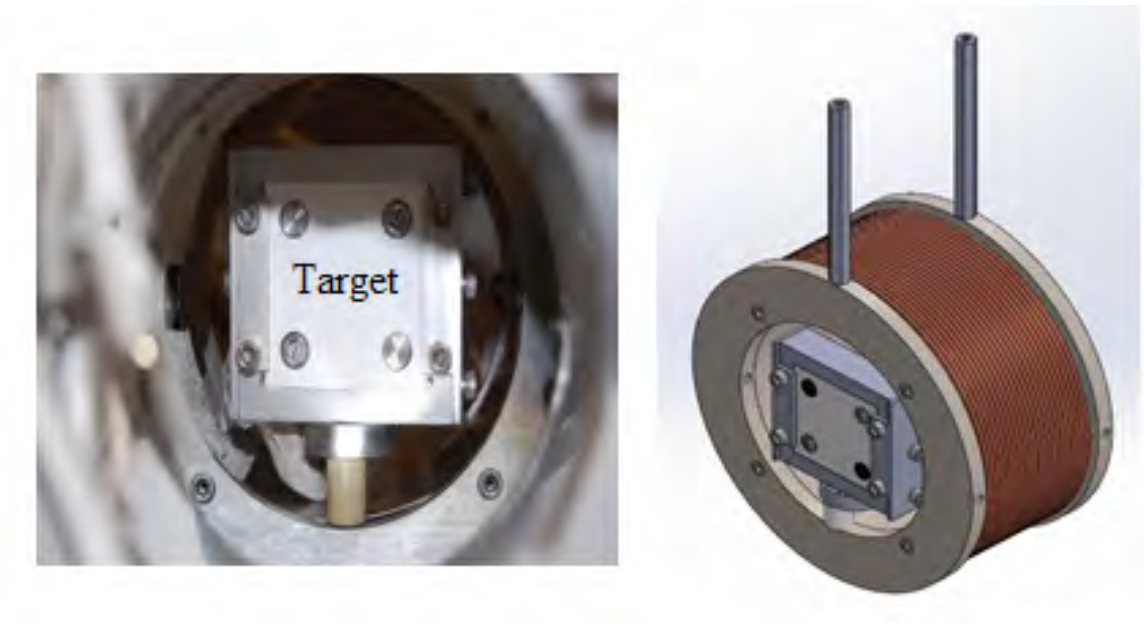

Figure 3.11: Electromagnet as a structural member to hold the target.

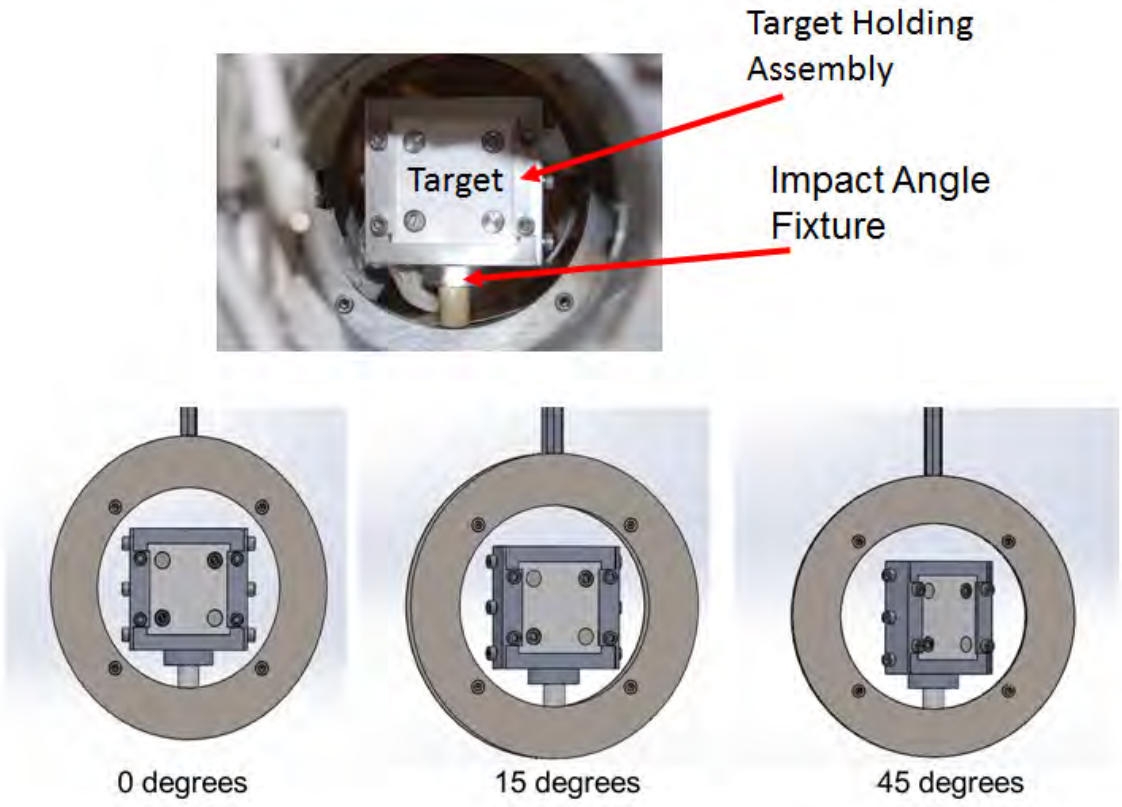

Figure 3.12: Impact angle fixture with target holding assembly. Also shown is a CAD example of different angles with respect to the electron beam.

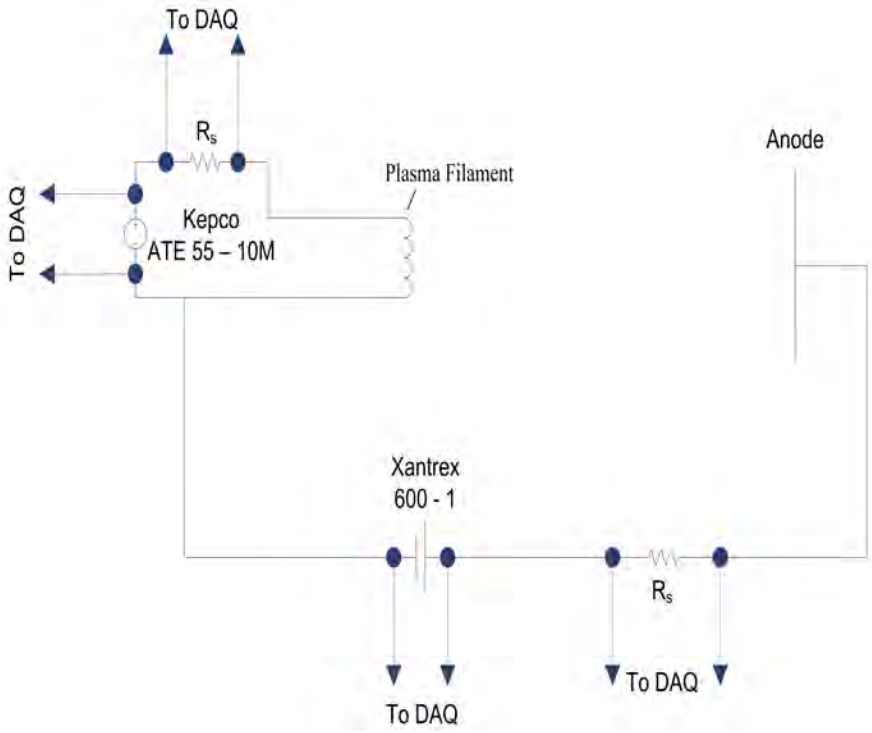

Figure 3.13: Circuit diagram for the thermionic plasma source.

3.5 Plasma Sources

The plasma source used in the experiment was a thermionically driven cathode. A thoriated tungsten filament of length 12 mm was looped with a diameter of 3.5 mm, producing a total of 13 turns. This filament was mounted on a molybdenum bar with set screws. Details on thermionic emission are discussed along with the electron gun in chapter V. Figure 3.13 shows the electrical circuit diagram for the plasma connection.

The systems on which the final tests were conducted is shown in figure 3.14. Figure 3.15 shows the plasma source in operation using Xenon gas.

3.6 Electron Beam Source

The main task to simulate a beam that resembles the Hall thruster electron population is by generating the beam from an electron gun. The design of this electron

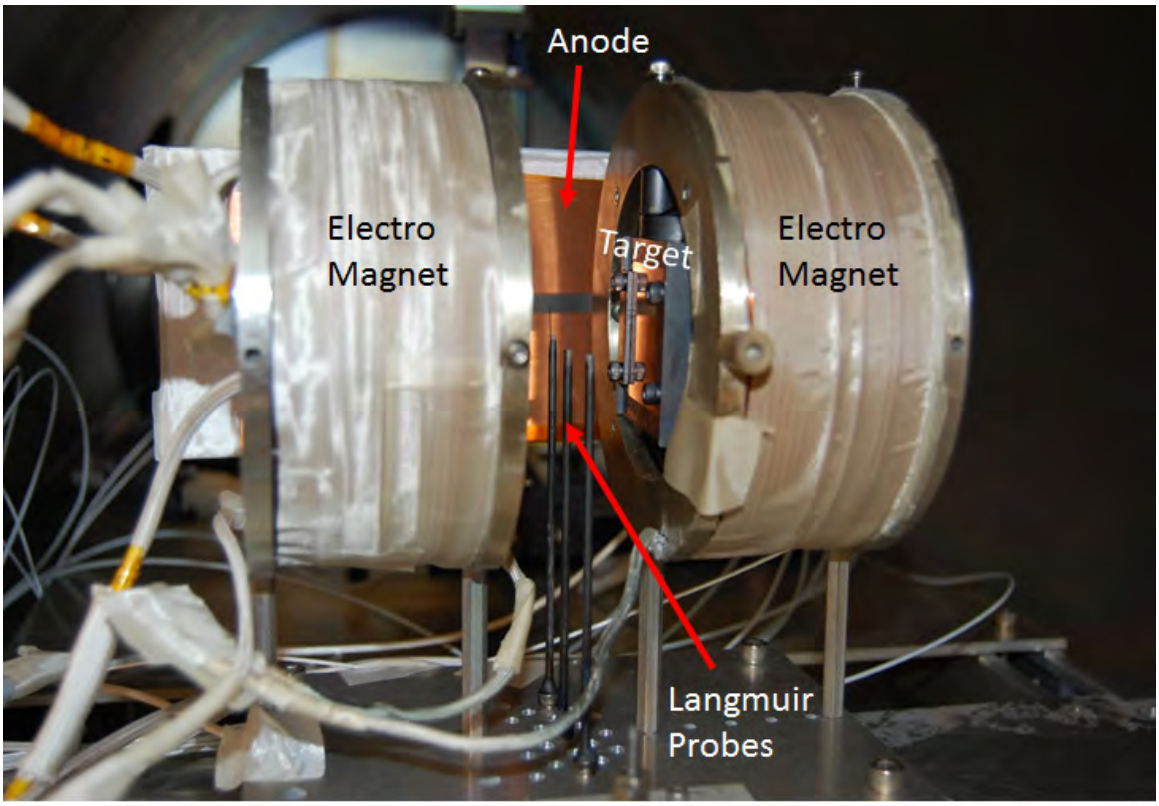

Figure 3.14: The bench-top apparatus in vacuum facility.

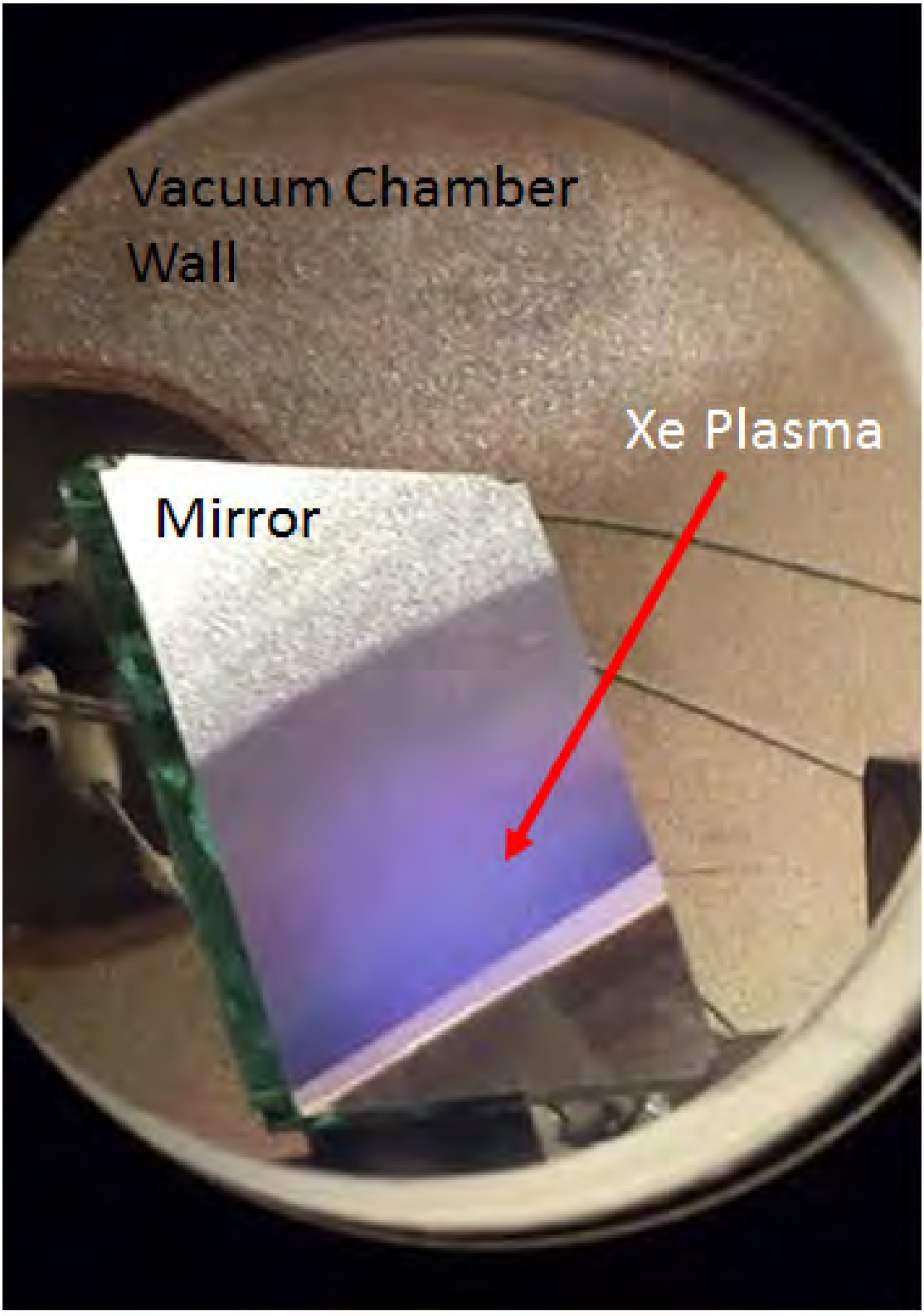

Figure 3.15: Bench-top apparatus in operation using Xenon plasma.

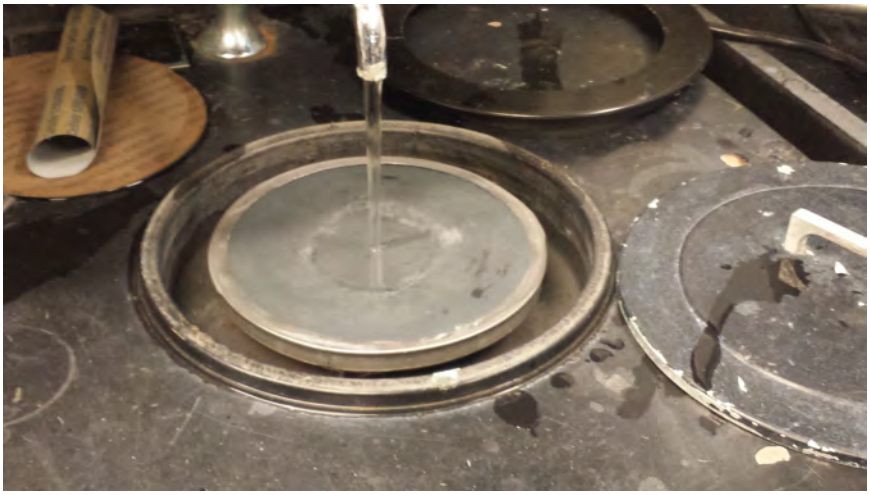

Figure 3.16: Polishing materials before tests on a grinding wheel using continuous supply of water.

beam source and associated results are discussed in chapter V.

3.7 Materials: Preparation and Surface Characterization

The samples used in this study are copper, BN (HP grade) and graphite. These materials were polished on a sanding wheel shown in figure 3.16 using silicon carbide sand papers with grit size P400, P2400, P4000 corresponding to particle sizes of 35 μm, 15.3 μm, and 5 μm .

The measurements of surface roughness was performed using the Dektak surface profilometer by having the tip pass on the surface 10 times on each direction and averaging the average surface roughness per sweep. The Dektak is shown in figure 3.17 and a close-up of the tip on a BN surface is shown in figure 3.18.

3.7.1 Copper

All metals have the tendency to grow a layer of oxide when exposed to oxygen rich environments (including air at STP). The thickness of this oxide layer depends on the conditions under which the material is kept. Temperature and pressure play a key role in determining the oxide film thickness, along with environment of exposure.

Figure 3.17: Image of the stylus profilometer - Dektak System.

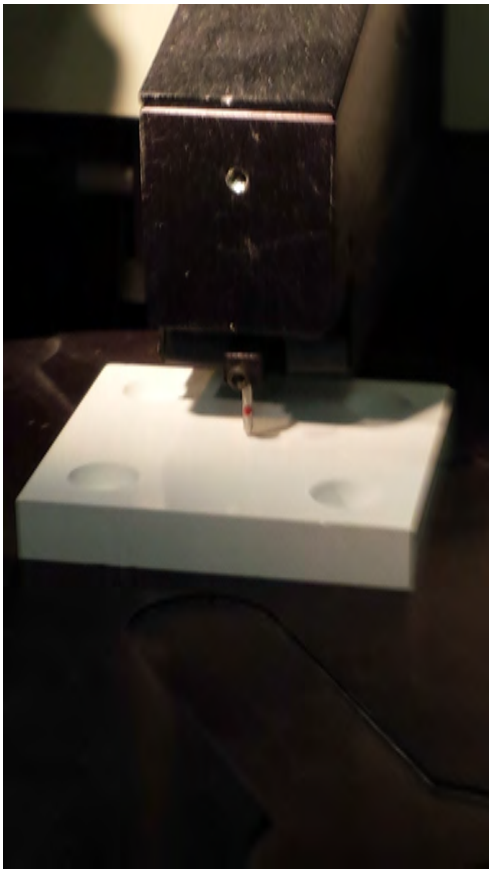

Figure 3.18: Measurement of surface roughness of HP grade BN performed using a stylus profilimeter

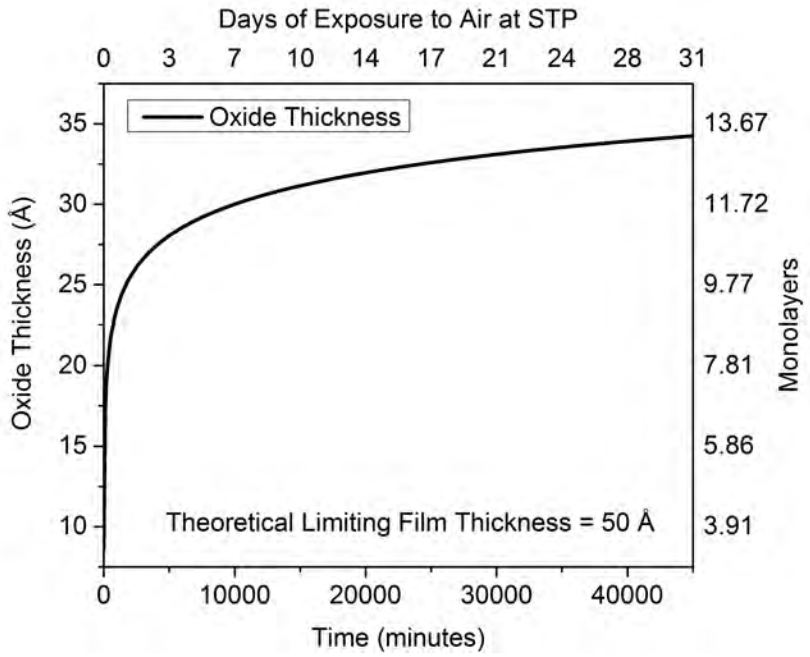

Figure 3.19: Oxide growth on Copper at room temperature

At room temperature (STP) there also exists a slow but finite growth of oxide film. However, there is a theoretical limiting thickness under these conditions for any metal oxide film.

Different theories exist to explain oxide growth on metals. For thick films (typically $\geq$ 6000 Å) Wagner's theory is used to explain the oxide growth, whereas for thin films (typically $\leq$ 40 Å) the Cabrera-Mott [91] theory of oxide growth is used. The growth of copper is shown in figure 3.19

Depending on the temperature at which the oxide growth is carried out, various empirical laws exist to describe the oxidation kinetics [92]. These are summarized below.

1. Linear Law:

   This is typical for metals with porous or cracked oxide films.

2. Parabolic Law:

   Typically seen for oxides grown in low temperature.

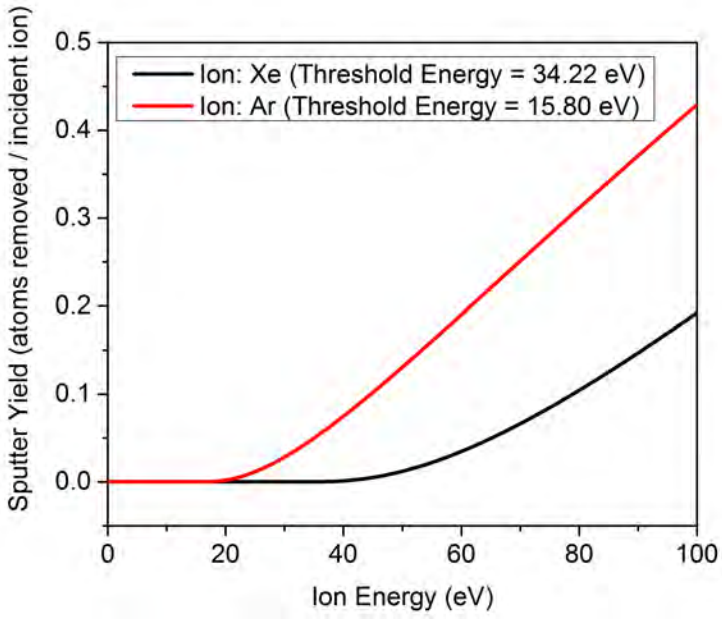

Figure 3.20: Sputter yield of Cu in Xe and Ar

3. Logarithmic Law:

   At elevated temperatures, the growth of oxides initially is much more rapid and rate decreases with time.

To treat copper, it is sputtered in plasma at a discharge current of 250 mA for 90 seconds. No feedback is employed to know how clean the surface is prior to test. The sputter yield of copper in a xenon and argon environment is shown in figure 3.20

3.7.2 Graphite

A high density graphite is machined for this study. The surface is polished to a mirror like finish.

3.7.3 Boron Nitride (HP Grade)

HP grade BN is used for this study.

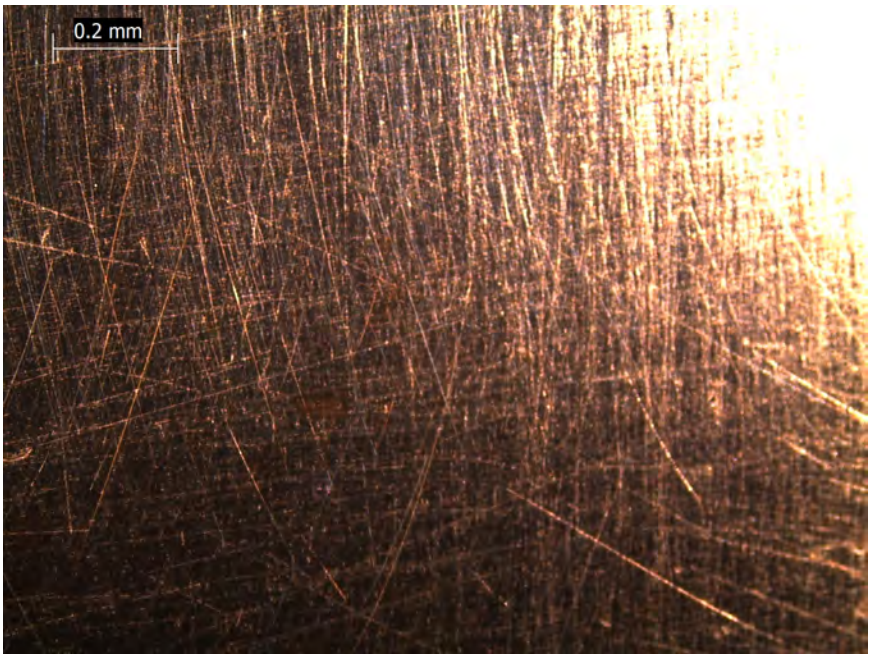

Figure 3.21: Pretest material image of copper (Magnfication: 8x).

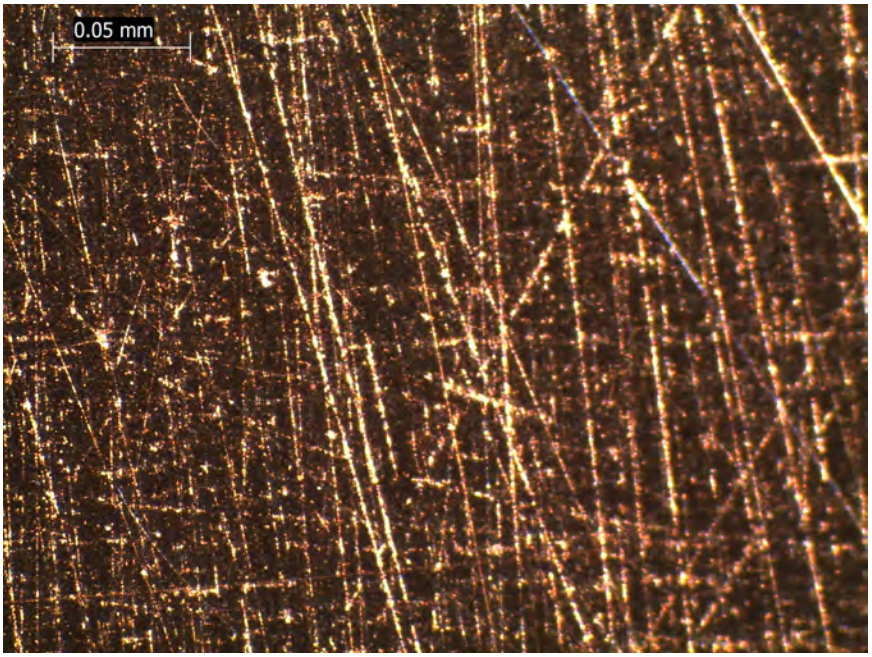

Figure 3.22: Pretest material image of copper (Magnfication: 35x).

Figure 3.23: Pretest material image of graphite (Magnfication: 8x).

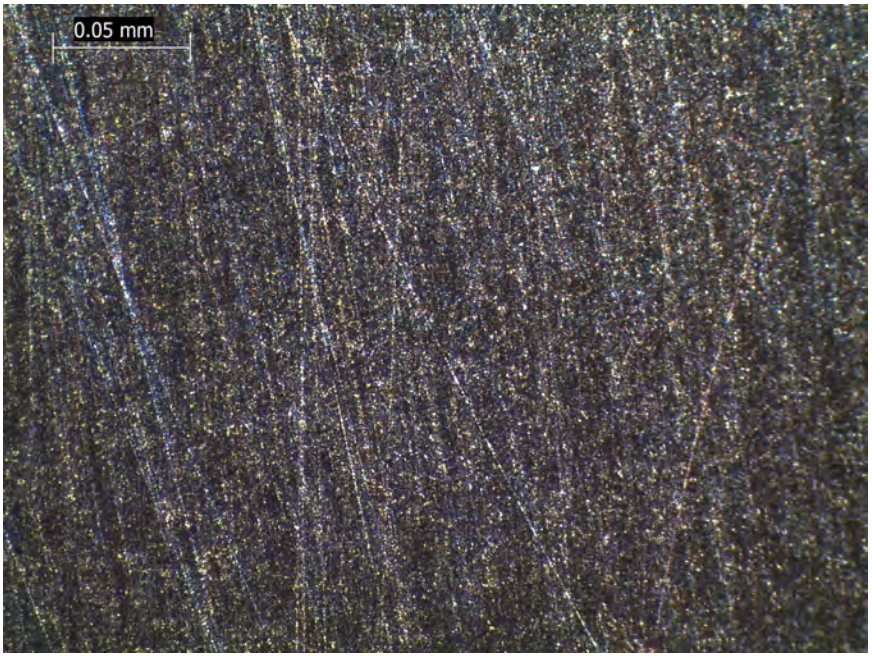

Figure 3.24: Pretest material image of graphite (Magnfication: 35x).

Figure 3.25: Pretest material image of BN (Magnfication: 8x).

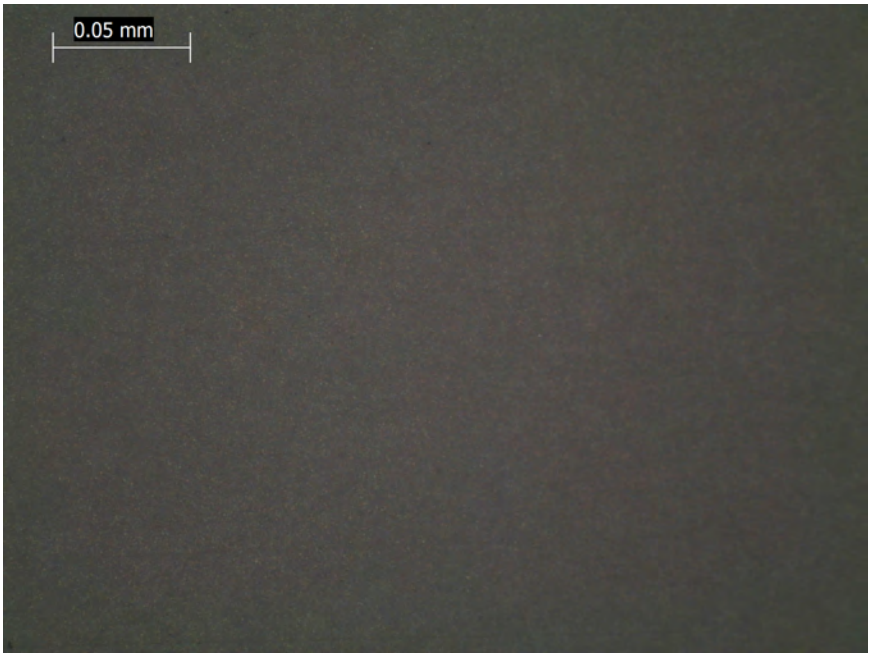

Figure 3.26: Pretest material image of BN (Magnfication: 35x).

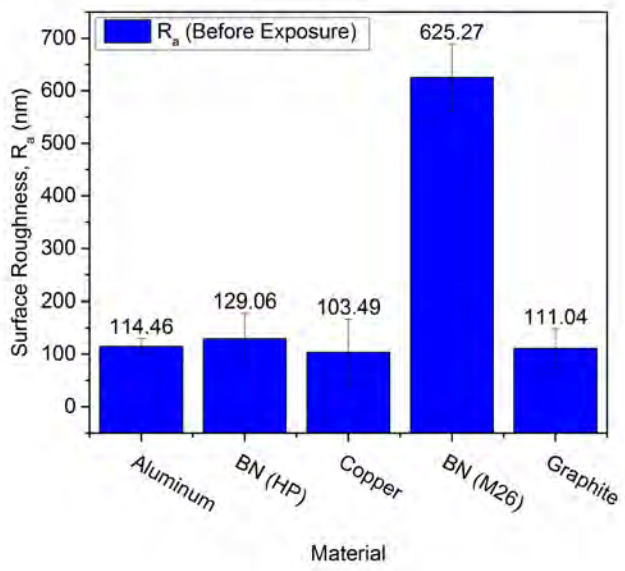

Figure 3.27: Surface roughness measurements before exposure to plasma for Aluminum, BN (HP Grade), Copper, BN (M26), Graphite.

3.8 Manufacturing and Assembly

A range of manufacturing tools were used for machining the different components in order to conduct these experiments. Wherever possible, vacuum manufacturing principles have been applied. These include drilling vent holes on mounting screws for components such as the electron gun and electromagnet spools, as well as the aluminum extruded legs used for support. Also, anodized aluminum is used only for the structural support and care has been taken to sand blast area and ensure electrical continuity to have these structures grounded effectively. Epoxy mixes were used sparingly, with the only exception being ceramic cement used to bond ceramic tubing to metal fasteners for diagnostics. After machining and prior to installing in the vacuum chamber, all components were cleaned in an ultrasonic bath for 120 seconds, following by cleaning with isopropyl alcohol to remove all machining oils. The following list provides a brief description of the tools utilized in manufacturing process.

1. CNC Mill

   All components designed for this system have been milled using vertical CNC milling machines. Two machines were used at different times - the milltronics VKM 3 centurion 7 and the milltronics partner centurion 1. Carbide cutters were used at speeds ranging from 270 rpm to 1200 rpm depending on the material such as stainless steel 304/316, molybdenum and aluminum. Precaution was taken while machining graphite and BN samples using a milling machine due to the brittle nature of these materials as well as due to production of powders during machining. The holes on the grids for the electron gun are also machined on a stainless steel shim stock using the CNC mills.

2. Lathe

   All diagnostics were mounted inside the vacuum chamber on the experimental test bed using hex-head machine screws and nuts. Description of the probes construction is highlighted in chapter IV. In order to drill holes for a ceramic tube to be secured inside the screw, a central hole had to be drilled through the machine screw. This was machined using the Hardinge HLV-H lathe with digital readouts. All machine screws used in diagnostics were stainless steel 304 screws and the holes were drilled in steps at cutting speeds of no greater than 300 rpm. Sufficient oil was used during machining.

3. Water Jet

   The OMAX 2626 jet machining center was used to machine the repeating pattern holes used to mount diagnostics on the base plate of the setup. Also, the original grids for the electron gun were machined using water jet. However due to the limitation on the minimum hole size, a function of the nozzle diameter, the final electron gun grids were machined using CNC milling. Water jet allows rapid prototyping with relative ease for 2D parts.

4. Saws, Drills, Shears, Sand Blaster and Grinding Wheel

   All minor tasks were carried out using additional shop tools. JET floor drill press (JDP-17DX) was used to drill additional holes on structure. All bar stock metals were cut to length using vertical contour saw (DoALL). In order to clean surfaces, as well as get rid of anodized coating, a Trinco sandblasted was employed. Flat plate materials were machined to size using the national hydraulic shear tools. In case of machining ceramic tubing to size, diamond wheels and grinders were employed and sufficient water was provided for cooling.

   Assembly of all components was done based on the 3-D models generated in Solidworks. Due to the design with redundant support structures and mounting holes, additional components could easily be integrated in the assembly process.

3.9 Computer Programs for Data Acquisition and Control

Computer controlled programs were developed as part of the project to allow for real time monitoring of macroscopic electrical parameters such as voltages and currents of various components as well as control of multiple power supplies. The remote operation mode allowed for a single point observation and control of the experiment as well as provided limited capability in analyzing large collection of data files. The file management system included redundancies and event tracking to allow large collection of data. To speed the data collection, newer versions of the software minimized the number of read - write requests and stored a large array of data in memory. Four main programs were developed - the main control code, electron beam energy code, electron beam profile code, and sheath profile code.

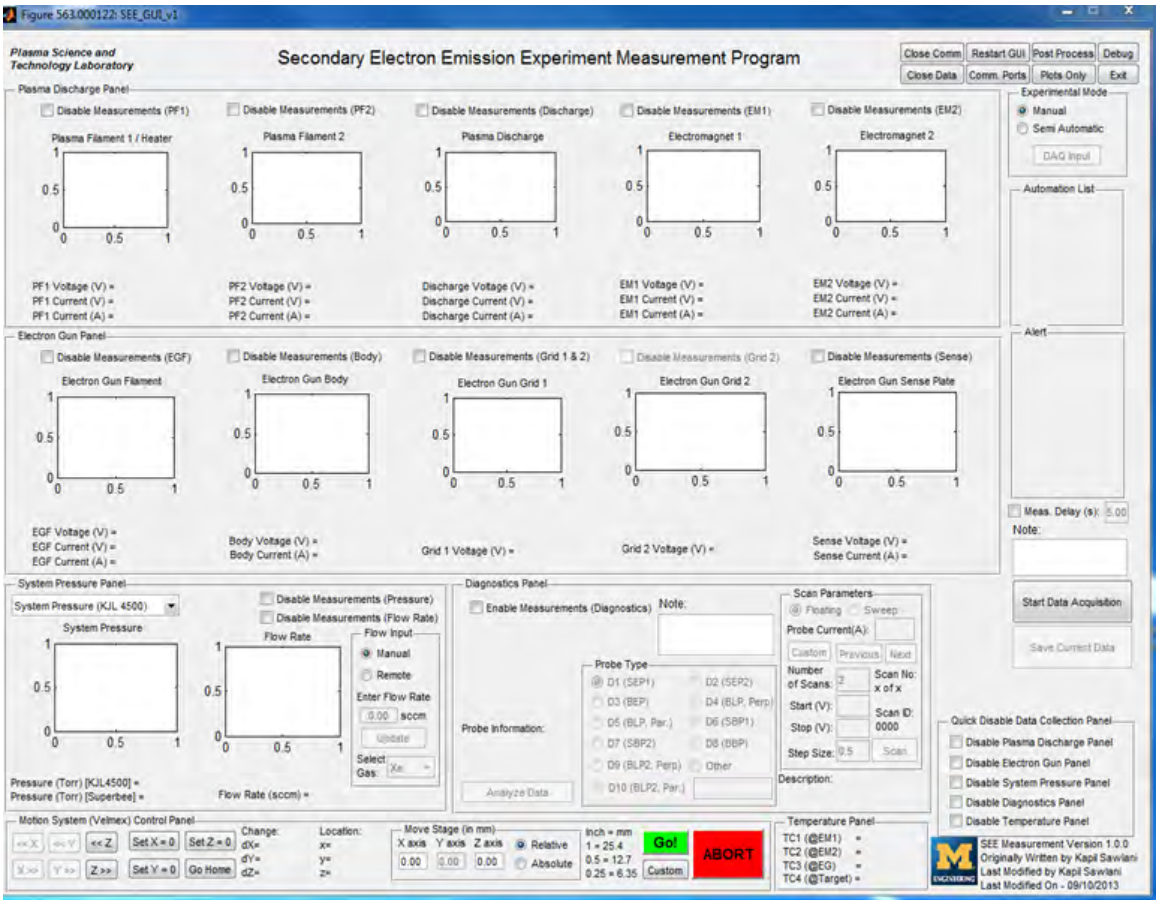

Figure 3.28: Main Control Program for Data Acquisition and System Control. This program allowed real time monitoring of system parameters as well as provided control of multiple power supplies, flow rate meters and perform diagnostics based on user choice.

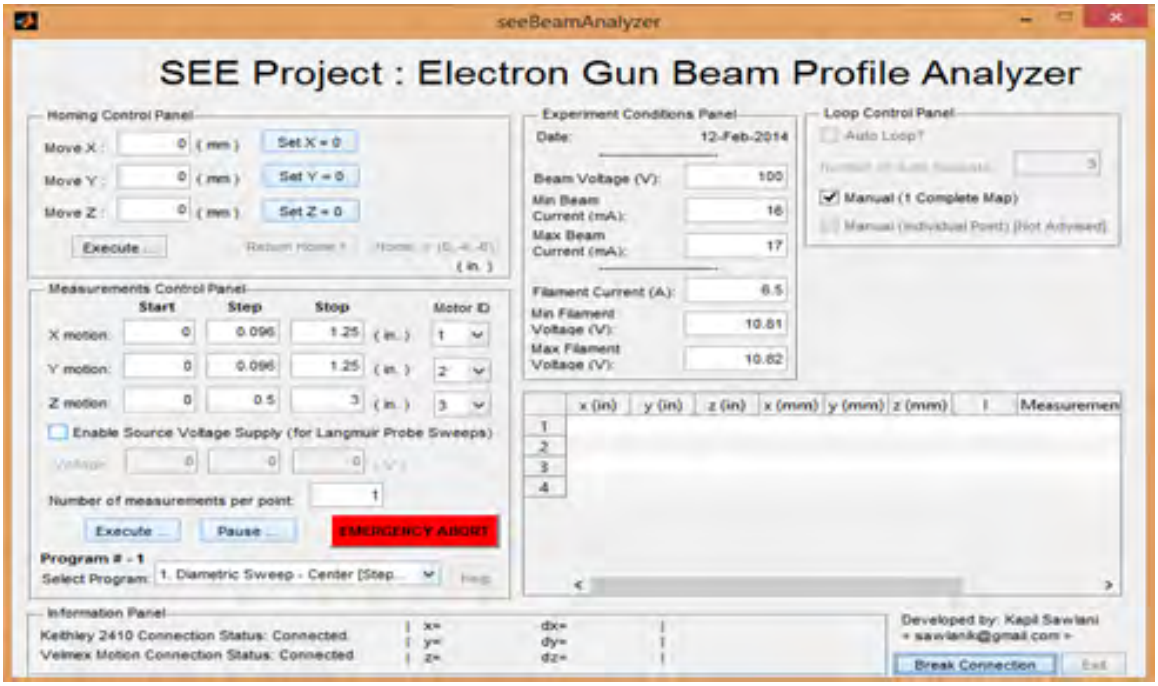

Figure 3.29: Electron beam profile analyzer program. This program controlled the multi-axis motion system as well as diagnostics to perform the profile analysis of the electron gun in vacuum conditions.

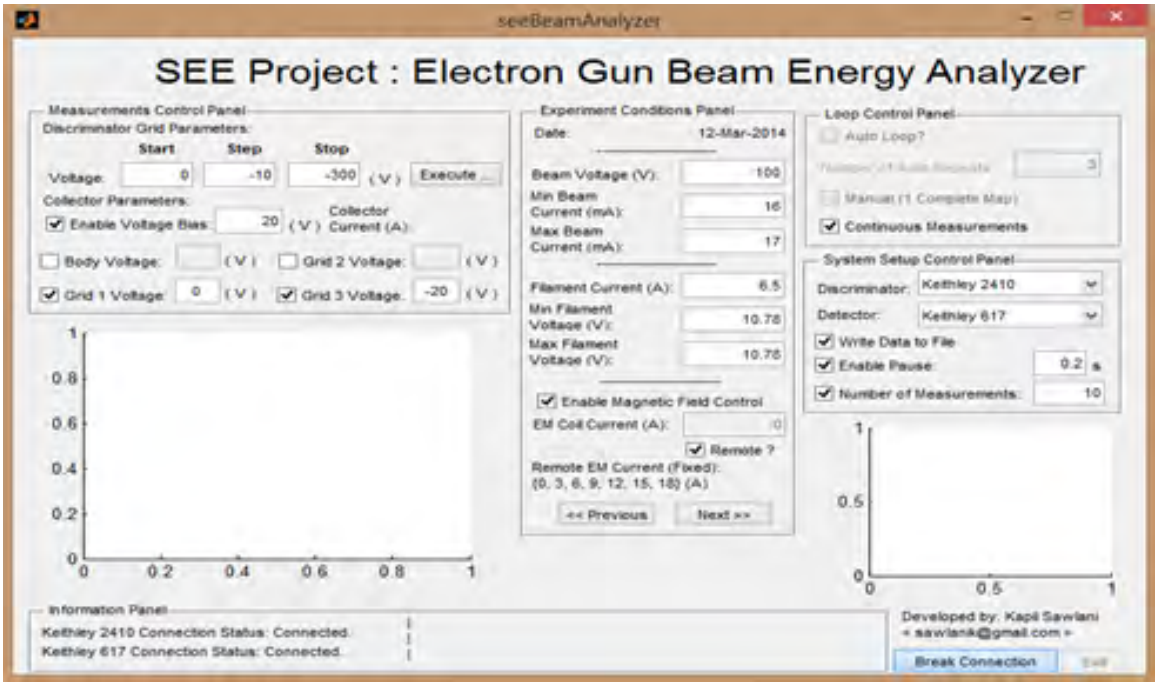

Figure 3.30: Electron beam energy analyzer program. This program controlled the power supplies used in the retarding potential analyzer to provide an energy map of the electron gun in both vacuum and plasma conditions.

CHAPTER IV

Plasma and Electron Beam Diagnostics

"Measurement is the first step that leads to control and eventually to improvement. If you can't measure something, you can't understand it. If you can't understand it, you can't control it. If you can't control it, you can't improve it."

- H. James Harrington

A number of plasma diagnostics were used in this study to characterize the system as well as quantify the changes made in plasma parameters due to SEE. The diagnostic techniques featured electrostatic probes discussed in the following sub sections.

4.1 Langmuir Probes Diagnostics

A Langmuir probe is an intrusive diagnostic used to determine basic plasma parameters such as electron temperature and plasma density. It can also provide information on the local EEDF. These probes are inexpensive and easy to construct. They provide a fast way to measure plasma parameters such as plasma density, electron temperature, plasma potential, floating potential and also give information on the electron energy distribution function (EEDF). These probes have been used for plasma diagnostics in almost every plasma system to date - DC plasmas, RF plasmas[93], ECR discharge [94, 70], hollow cathode discharges [95, 96], magnetron discharges

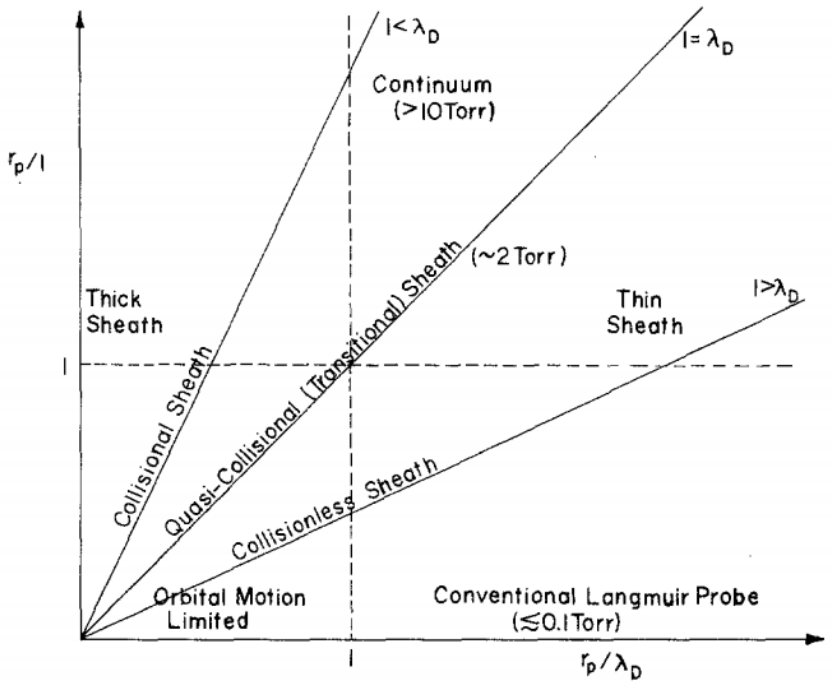

Figure 4.1: Probe operation regimes in terms of probe size, r_p, mean free path, $l(\lambda_{mfp})$, and Debye length, λ_D. Reproduced from Figure 1 of Ref. [105].

[97], microwave plasma [98], low density plasma system [99, 100], flowing plasmas [101], magnetized plasmas [102] and highly density plasmas [103]. Langmuir probes have also been used for checking the applicability of the analytical theories. Sudit and Woods measured the accuracy of various Langmuir probe theories showing good agreement for electron densities but found huge inconsistencies with ion densities for cylindrical probes [104].

The current collection by a Langmuir probe depends on the relative size of the probe and the region of disturbance it produces within the plasma. It also depends on the degree of collisions that take place within the plasma sheath that is formed when the probe is placed within a plasma. Cherrington [105] shows the different region of the probe theories depend on the ratio of probe radius to Debye length (r_p/λ_D) and the ratio of probe radius to the mean free path (r_p/λ_{mfp}). This dependence is shown in Figure 4.1.

Despite its relative ease of construction and measurement methods, Langmuir

probes have a number of limitations. These include:

1. The ability to distinguish between the kinetic energy and potential energy of plasma particles

2. The ability to non-invasively probe plasma, particularly at higher positive potential bias.

3. Secondary electron emission from materials used to construct the probe (ceramic tubing, tungsten wire etc) affects the I-V characteristics leading ot an understimation of the value of the electron temperature.

4. At higher pressures and in presence of mangetic fields, the I-V characteristics are difficult to interpret.

5. The ability to determine energy spread and relate it to beam temperature.

Langmuir probe theory depends on certain characteristics length scales. These are listed in Table 4.1. In the absence of magnetic field and when the plasma is collisionless, the only parameters that determine the appropriate theory for analysis is the ratio r_p/λ_D.

If $r_p/\lambda_D \gg 1$, thin sheath analysis is performed. When $r_p/\lambda_D \geq 1$, the region is considered to be in the transition regime and no analytical results exists for such a system. Finally, if $r_p/\lambda_D < 1$, the resulting sheath is thick and orbital motion limited theory must be applied to analyze the data.

Length Scale	Symbol
Probe radius	r_p
Debye length	λ_D
Mean free path	λ_{mfp}
Electron Larmor radius	r_{Le}
Ion Larmor radius	r_{Li}

Table 4.1: Characteristic length scales of importance in Langmuir probes.

In Hall thrusters, and other devices where magnetic fields are present, the charged particles orbit about a gyro-radius as given by equation 2.29. This can be simplified for any electrons and written as equation 4.1

$$r_{Le}[cm] = \frac{2.4\sqrt{T_e\,[eV]}}{B\,[G]} \tag{4.1}$$

For Hall thrusters, the electron Larmor radius is much smaller than the characteristic length scale of the system which in turn is smaller than the ion Larmor radius. If r_{Le} is much smaller than the radius of the probe (r_p), the electron saturation current decreases at a given bias voltage [70]. The probe current may not saturate and under such conditions the current depends on crossed field transport processes [106].

It is also important to take into consideration the power flux into and from a probe surface. In general the power going into the probe results from the contribution of ions and electron fluxes under appropriate conditions. For ions, this is given by equation 4.2a, while for electrons this is given by the equation 4.2b.

$$P_i = I_i \left[(V_f - V_{pr}) + \frac{k_B T_e}{e} \sqrt{\ln \frac{M_i}{2\,\pi\, m_e}} + \frac{k_B\, T_e}{2e} \right] \tag{4.2a}$$

$$P_e = I_i \exp\left[\frac{e(V_{pr} - V_f)}{k_B\, T_e} \right] \left(\frac{2\, k_B\, T_e}{e} \right) \tag{4.2b}$$

$$P_{in} = P_i + P_e \tag{4.2c}$$

The power going out a probe is a combination of radiation and conduction losses depending on the mode of probe operation. This is given by equation 4.3

$$P_{out} = (\epsilon\, \sigma_{SB}\, T_{tip}^4)\, A_p + \frac{K(T_{tip} - T_{end})\, A_p}{L_p} \tag{4.3}$$

where σ_{SB} is the Stefan-Boltzmann constant (= 5.67x10^{-8} W m^{-2} K^{-4}).

4.1.1 Orbital Motion Limited Theory

When the ratio of the probe radius to the Debye length(λ_D) is much less than one, indicating that the plasma sheath for the probe is much larger than the probe dimension (r_p), the collection of charged particles using an electrostatic probe is determined using the orbital motion limited (OML) theory.

The ion saturation current for a thick sheath ($r_p/\lambda_D < 3$) is given by equation 4.4

$$I_{sat,i}^2 = \left(\frac{2\,e^3\,n_e^2\,A_p}{\pi^2}\right)\left(\frac{1}{M_i}\right)(V_p - V_b) \tag{4.4}$$

Sudit et al [107] also describe a computer controlled workstation to run the Langmuir probe experiment and conduct analysis using the OML theory.

For a given slope S of the I^2 - V_b curve, the number density using the OML theory can be given by the equation 4.5.

$$n_e = \sqrt{\frac{\pi^2\,m_e}{2\,A_{pr}\,q^3}}\,\sqrt{S} \tag{4.5}$$

4.1.2 Electron Energy Distribution Function

Many methods to determine the EEDF experimentally have been employed by researchers around the world. Since plasmas are inherently noisy and all instruments used for its measurement superimpose additional noise, it often becomes difficult to accurately estimate the EEDF as the differentiation process amplifies the noise. A requirement of any such method is that of suppressing the noise from the signal in order to get a reliable assessment. One method involves the use of a differentiation amplifier circuit. Another method is to superimpose a small AC signal to the probe voltage. The second derivative of the current is proportional to the second harmonic of this superimposed input signal as extracted from the current signal. Using a lock-in amplifier, this second harmonic can be obtained. While these methods have been

used successfully for years, they are hardware intensive. In general, such methods are complex and can require expensive equipment. An alternative to experimental methods for post-processing of raw probe I-V characteristic data is using numerical differentiation on a digital computer after smoothing the noisy I-V characteristic.10 Smoothing can obscure important features of the EEDF such as the presence of primary electrons. So in general, great care must be taken in the application of smoothing the I-V characteristic.

Godyak discusses the various ways to measure and control the non-equilibrium EEDF in plasma systems [21]. Godyak and Demidov [24] provide a detailed description of the various situations in which EEDF results can be obtained and their reliability based on years of conducted research.

4.1.3 Sheath Size in Langmuir Probe Operations

As discussed in section 2.2.5, when any body is immersed in plasma, the process of Debye shielding occurs. This shielding phenomena results in formation of a sheath. Knowledge of the sheath dimension is important for Langmuir probe design as it allows selection of the appropriate theory for analyzing the I-V characteristics.

A charged particle that comes in contact with the exposed probe tip directly gets collected by the probe. However, not all charged particles entering the sheath will be collected. The trajectory of the charge particles depends greatly on the potential within the sheath. In absence of magnetic fields, particles may still experience an orbital path within the vicinity of the probe. These trapped orbits depend on the thickness of the probe sheath. If the ratio of the sheath thickness to probe radius is small ($\delta_s/r_p << 1$), we are in the thin sheath regime and all the current collected is a result of collision of charged particles with the probe. Increasing sheath thickness results in increased current collection due to the potential well that surrounds the probe. When sheath thickness is much larger compared to the probe radius ($\delta_s/r_p >>$

1), the particles execute orbits about the probe and the orbital motion limited theory best describes the collection of the current.

The sheath thickness (δ_s) can be expressed as a function of Debye length (λ_D). Hershkowitz [108] states that it is often assumed that sheath thickness are approximated to the Debye length. This, however, can lead to underestimation of the sheath thickness especially for a strongly negative bias. For a large negative bias ($\frac{e(V_p - V_{pr})}{T_e} >> 1$), the primary source of probe current is due to the ion collection. The space charge limit in this region can be given by the Child-Langmuir current

$$j_{CL} = \frac{\frac{4}{9}\sqrt{\frac{2e}{m_i}}\epsilon_0 (V_p - V_{pr})^{3/2}}{d^2 \beta^2} \tag{4.6}$$

In equation 4.6, d is the separation of the probe surface and the plane at which there exists a finite electron density and β^2 is a correction factor as defined in table 4.2.

Probe Type	β^2
Planar Probes	1.00
Cylindrical Probes	$\mathcal{O}(\delta_s/r_p)$
Spherical Probes	$\mathcal{O}(\delta_s/r_p)$ for $\delta_s/r_p < 3$

Table 4.2: Correction factors for different kinds of probes to determine the Child Langmuir current in the space charge limit near the probe at large negative bias (ion currents). Data taken from Hershkowitz [108].

On equating the Child-Langmuir current to the Bohm current, the sheath thickness can be estimated as a function of the probe bias relative to the plasma potential. This is given by equations 4.7a and 4.7b for planar and cylindrical probes respectively

[109, 110].

$$\delta_s = 1.023\lambda_D \left[\frac{e(V_p - V_{pr})}{T_e}\right]^{3/4} \ldots \quad \text{Planar probe} \tag{4.7a}$$

$$\delta_s = 1.015 r_p^{1/3} \lambda_D^{2/3} \left[\frac{e(V_p - V_{pr})}{T_e}\right]^{1/2} \ldots \quad \text{Cylindrical probe} \tag{4.7b}$$

4.1.4 Plasma Parameters

4.1.4.1 Floating Potential

The floating potential for a plasma system is perhaps the easiest measurement to carry out in absence of fluctuations. This is done when the net electron current and the net ion current collected by the probe are equal.

4.1.4.2 Plasma Potential

The measurement of plasma potential is very important in order to experimentally quantify macroscopic properties such as local electric field. In the case of crossed field devices like a Hall thruster, this gives information on the accelerating zone field and is important for design and modeling. Knowledge of the plasma potential allows us to understand fundamentally the general particle transport in a plasma. It also plays role in confinement of the plasma.

The measurement of plasma potential is complicated in comparison to the floating potential. There are several techniques that allow us to determine the plasma potential.

1. Determination of the "Knee" of a Ln (I_{pr}) vs V_p plot

2. Calculation from the Floating Potential

   If we assume that the electron temperature does not fluctuate during a measurement cycle, the floating point can provide an estimate for the plasma potential.

This is true for Maxwellian plasmas and is given by eq. 4.8

$$V_p = V_f + \left(\frac{m_e}{m_i}\right) T_e \tag{4.8}$$

This technique often yields incorrect measurement due to the errors associated with measurement of T_e.

3. Estimation from the Derivatives of the I-V Characteristics

4.1.5 Second Derivative of a Langmuir Probe

The second derivative of the probe I-V characteristic is used to provide accurate determination of plasma potential, the electron energy distribution function, the electron temperature and the electron density of the plasma[111]. This method has been used by several researchers and Lin et al [112] tested the reliability of the second derivative using numerical methods and compared it to a differential circuit from Godyak[113, pp. 95 - 134]. The results were reliable with errors within 7%. Habiger et al. [114] used this technique to determine the EEDF in an MPD arc jet. Dias and Popov discuss the noise and errors associated with Langmuir probe EEDF measurements with the instrument function point of view and provide guidelines how to perform analysis using numerical differentiation techniquesto improve results [115].

The EEDF, f(ε) is determined using the Druyvesteyn method and is given by eq. 4.9

$$f(\varepsilon) = \frac{2\sqrt{2m}}{e^3 A_p} \frac{d^2 I_p}{dV_p^2} \tag{4.9}$$

This formula is valid for low gas pressures, i.e., when the electron mean free path, $\lambda_{mfp,e} \gg r_p + \delta_s$. At higher pressures, the second derivative is distorted due to the depletion of electrons which sink on the probe surface [111, 110]

$$I_p^{''}(V_p) = Cf(eV_p) - C\int_{eV_p}^{\infty} K^{''}(\varepsilon, V_p) f(\varepsilon) d\varepsilon \tag{4.10}$$

where $K^{''}(\varepsilon, V_p) = \dfrac{2\Psi(\varepsilon)\varepsilon^2}{[\varepsilon(1+\Psi) - \Psi eV_p]^3}$, $C = \dfrac{e^3 A_p}{2\gamma\sqrt{2m}}$, and $\Psi(\varepsilon) = \dfrac{r_p \ln(\pi l_p / 4r_p)}{\gamma\lambda(\varepsilon)}$

4.1.6 Numerical Smoothing and Differncing Schemes

With the advent of digital computers, numerical smoothing and differencing schemes have become a popular choice to determine the EEDF from a Langmuir probe I-V characteristic. This method has several advantages compared to the hardware related counterparts listed earlier. The user has control over smoothing and the data can always be compared with the original noisy signal to assess the accuracy of smoothing and loss of essential information in the smoothing process. Smoothing routines are typically available with most plotting software and numerical analysis packages. Among the numerical methods used for noise reduction in plasma applications, the Savitkzy-Golay method has been widely used by many experimentalists[116, 117, 118]. Besides the common least-squares method, convolution methods such as Hayden method using a Gaussian filter has been implemented by Palop et al [34]. Dias and Tatarova[117] showed that using a 7-point numerical differentiator was more effective in noise reduction for EEDF measurements. Azooz[119] developed an empirical four parameter fitting technique for Langmuir probe I-V characteristics based on non-linear fitting that fits most experimental data and showed an analytical solution for obtaining the second derivative. Advanced signal processing concepts such as using a family of wavelet transforms for the analysis of Langmuir probe data has also been performed and Park et al. showed promising results[120]. Dias and Popov[121] studied numerical smoothing using an iterative method under collisional conditions. Magnus and Gudmundsson[122] did the first systematic comparison, to the author's

knowledge, of more than three methods for a test function and concluded that the Blackman window provided a better solution among the methods they compared.

It is important to note that on application of any smoothing technique there is a certain amount of distortion introduced to the EEDF. A few of these numerical methods used to obtain the smoothed I-V characteristic from the noisy signal are discussed below. These methods include the Savitzky-Golay filter, Hyadens method using a Gaussian filter, a free four parameter empirical fitting technique, polynomial fitting, and the general cosine window methods.

4.1.6.1 Savitzky-Golay Method

In this method Savitzky and Golay recommended using a least-squares fitting of a few consecutive data points to a polynomial as opposed to simple averaging for smoothing fluctuating data. Savitzky and Golays seminal paper [123] has been cited over 8700 times and finds application in many fields of science and engineering that require smoothing and differentiation of data.

The essential idea behind this method is to fit a polynomial $\mathrm{p}_i(\mathrm{x})$ of degree M, by the principles of least squares through a total of n ($\mathrm{n} = \mathrm{n}_L + \mathrm{n}_R + 1$) data points[124]. The center point of the fitted polynomial is the smoothed data point. This polynomial can be written as eq. 4.11

$$p_i(x) = \sum_{k=0}^{M} b_k \left(\frac{x - x_i}{\Delta x} \right)^k \tag{4.11}$$

Although it is usual to assume the spacing between data points is uniform for this filter, an algorithm that supports non-uniform spacing can also be written. The coefficients of b_k should be made such that a cost function is defined by eq. 4.12

$$\sum_{j=i-n_L}^{i+n_R} \left[p_i(x_j) - f_j \right]^2 = \text{minimum} \tag{4.12}$$

This can be written in matrix form as explained in reference [124] as eq. 4.13

$$\left\| Ab - f \right\|_2 = \text{minumum} \tag{4.13}$$

where A is a matrix of dimension n x (M+1), b is a vector of dimension (M+1) x 1 and f is the vector of data points under consideration having a dimension of n x 1. The solution of b is found using the QR (orthogonal - upper triangular) decomposition method. Despite its low efficiency the QR method is considered to be the best general purpose method for solving such problems because it is more stable compared to other methods[125].

While there is no restriction in choosing different values of n_L and n_R, the need for weighing one side over the other is not required for smoothing the I-V characteristics of a Langmuir probe, except at the starting and ending points in the transition region of the I-V characteristics. Ignoring the biased weighing on these points does not affect the solution considerably especially when the data set is large. Thus the values of n_L and n_R are constrained to be same for the current discussion. As a consequence, the span will always be made of odd number of points and as a requirement for fitting any polynomial to the data points, the order of the polynomial should be less than the number of points under consideration. These are the parameters (n and M) that need to be varied to obtain the optimal smoothing for a given set of data points. For instance, if there are 182 data points obtained in an experiment, one possible choice could be fitting a 4th order polynomial with a filter span length of 19, i.e., M = 4 and $n_L = n_R = 9$.

As can be seen from the example, there are many possible combinations for fitting these parameters. The choice of these parameters is not apparent as they depend mainly on the noise intensity and number of data points available. Thus one will need to optimize a cost function to determine the ideal parameters. Optimizing is only possible for test functions where the actual solution is known and a comparison is

possible. For real plasmas, one has to rely heavily on experience to judge the right set of parameters to obtain fine smoothing without losing a lot of essential information. A large value of n can result in more smoothing but can significantly distort important features, while a large value of M helps in preserving such high-frequency features of the signal. However, due to limitations of numerical methods on solving large matrix systems the solution may not be accurate[124]. Another problem of the method is smoothing at the boundary points. These end points are usually ignored in the smoothing process or one can form a smoothing function at these points by setting n_L or n_R as zero at the extremes. As a result of the constraint that $n_L = n_R$, the boundary points will not be smoothed. This is not necessarily a problem as the EEDF is determined from the electron retardation region of the probe characteristic. It is important to note that Savitzky-Golay filters are usually less successful for noise reduction as compared to standard moving averages.

Despite the disadvantages listed above, the method has been popular because of the ease to determine the derivatives. The zeroth order derivative (no differentiation) results in smoothing. Higher order derivatives are calculated based on the center point of each polynomial. More information on Savitzky-Golay filters and differentiators can be found in references [126] and [127] (and the references therein).

4.1.6.2 Hayden's method using Gaussian Filter

Haydens method relies on an instrument function which indicates the response of the measuring apparatus. Mathematically, it is defined by the finite Fourier cosine transform of an apodization (window) function. The appropriate instrument function when convolved with the measured signal results in elimination of some errors. However, accurately determining the instrument function is complicated[128].

Hayden[129] argued that the method of least squares fitting and many-point averaging was not suitable for experimental data as most of the methods following those

principles destroy valuable information. In that work, it was suggested that if the noise is uncorrelated with the instrument function, a convolution product of the two produces a smooth signal. The measured signal can be written in the form given by equation 4.14

$$h(x) = h_n(x) + N(x) \tag{4.14}$$

where N is the noise and h_n is the nth approximation to the smoothed function. If g is the instrument function, the convolution of g and N would be zero ($g * N = 0$) as they are statistically uncorrelated and the first approximation of the smooth function can be given by equation 4.15

$$h_1 = h * g \tag{4.15}$$

Following the work of Hayden, the n^{th} approximation to the smoothed function is given by equation 4.16

$$h_n = h_{n-1} + (h - h_{n-1}) * g \tag{4.16}$$

While Hayden proposed an iterative procedure to solve this convolution method and obtain a noise-free signal, Jacobson[130] proposed a non-iterative procedure which would result in faster computation. His suggestion was to perform a single convolution (eq. 4.17

$$h_n = h * g_n \tag{4.17}$$

where g_n is the filter function of the n^{th} approximation. Palop et al.[34] applied this method for smoothing data obtained from a Langmuir probe. Due to the complexity of determining the instrument function for a given experimental system, in their work a Gaussian distribution function was chosen as the instrument function. They

suggested that the approximation of a Gaussian distribution is applicable for most systems and the filter function g_n in this case is given by equation 4.18

$$g_n(x) = \sum_{k=1}^{n} \binom{n}{k} (-1)^{k+1} \frac{1}{\sigma_G \sqrt{2\pi k}} \left(\frac{-x^2}{2\sigma_G^2 k^2} \right) \tag{4.18}$$

The parameters that control the degree of smoothing are the number of iterations, n and the standard deviation of the Gaussian filter, σ_G. Usually the number of iterations is restricted to one[122] or two[34] and the parameter varied for smoothness is $_G$. It should, however, be mentioned here that this method behaves like a Gaussian window function and there is a data shift due to convolution which should be taken into account to avoid any inaccuracy. This data shift is discussed in section III.A of this paper. The filter function acts as a weight applied to the original data and thus needs to be normalized. This is done by dividing each element of g_n with the sum of all elements of g_n. This method has been compared with the Savitzky-Golay filter of polynomial order 2 and 4, and with a B-spline approximation by authors of reference [34] and they concluded that the Hayden method is the best method as surmised from several noted advantages. Firstly, the smoothed data is obtained carrying only one smoothing procedure. Secondly, no limit is imposed on the sensor resistance used for measurements. Thirdly, a significant change in $_G$ does not affect the smoothing greatly. Lastly, as the second derivative is a smooth function, higher derivatives can be obtained. Magnus and Gudmundsson also compared this with several other methods and concluded that the Gaussian filter generally gave good results consistently.[122]

4.1.6.3 Windowing Methods

It is well known that associated with the FFT of a non-periodic signal is the frequency spread function. In general, any non-periodic pulse can be decomposed into its spectral components. The frequency spread function represents the amplitude of

the contributions of the various spectral components that make up the pulse. On the other hand, a signal that is periodic has a single spectral line (delta function) in the frequency spectrum.

Windowing methods essentially divide the signal into finite segments over which a smooth periodic function is applied. The filter coefficients rise (and fall) based on this periodic function thereby minimizing the effects of the jumps due to the noise present in the signal. These segments when applied to the entire signal result in a relatively smooth output signal. Thus we can define windowing as the process in which we multiply the data by a smooth function that approaches zero at both the boundary points within the given interval of consideration. The smooth function is called the window function, denoted by w[n] and the interval is called the window size or window length. Application of windows suppresses the side-lobes usually present in the frequency domain.

Windows are thus weighting functions used to diminish the ill-effects of the sudden transitions caused by the noise in the signal. Numerous windows have been proposed, each having a particular advantage. Since the figure of merit used to characterize and compare the performance of these windows is beyond the scope of this thesis, interested readers are recommended to read references [131, 132, 133, 134] which focus on digital signal processing. Harris did a comprehensive review of many window functions along with their performance parameters [135]. The window function in all cases truncates the length of the signal in the time domain and the finite impulse response of a filter is given by equation 4.19

$$y[n] = x[n]\, w[n] \tag{4.19}$$

where w[n] = 0 outside of $0 \leq n \leq M\text{-}1$.

Although several windowing schemes exist, only the general cosine window is discussed here. The general cosine window can be represented by eq. 4.20 with a_k

representing the cosine coefficients. However, restricting to a maximum of three term cosine window results in equation 4.21

$$w[n] = \sum_{k=0}^{N-1} (-1)^k \, a_k \, \cos\left(\frac{k2\pi n}{M-1}\right) \tag{4.20}$$

$$w[n] = a_0 - a_1 \cos\left(\frac{2\pi n}{M-1}\right) + a_2 \cos\left(\frac{4\pi n}{M-1}\right) \tag{4.21}$$

where n = 0, 1, 2, , M - 1.

Figure 4.2 shows the various cosine windows of length 65, i.e., 65 data points are considered at a time and are weighed based on the window considered. These windows when applied to the noisy I-V probe characteristics will smooth the signal. However, as with a Gaussian filter, they have to be normalized either by dividing each element by the sum of all elements, or alternately using the value of the coherent gain along with the window size. The convolution of the signal with the window length causes a data shift by (M-1)/2 points if the window size is odd, and (M/2 -1) if the window size is even. Table 4.3 gives the values of the a_k coefficients along with values of coherent gain of these windows.

Window Type	a_0	a_1	a_2	Coherent Gain
Rectangular	1.00	0.00	0.00	1.00
Hann (Hanning)	0.50	0.50	0.00	0.50
Hamming	0.50	0.46	0.00	0.54
Blackman	0.42	0.50	0.08	0.42

Table 4.3: Values of coefficients and coherent gain for general cosine windows

The width of the window is the distance between the closest zeros on each side of the main lobe. The side lobes are responsible for the occurrence of the Gibbs phenomenon (formation of wiggles). A rectangular window is essentially a window when no weighting is used and thus is more likely to suffer from the wiggles produced at the boundary points (discontinuities). Other windows are used to reduce the oscillatory behavior. In case of a Hann window named after Julius von Hann (also known as

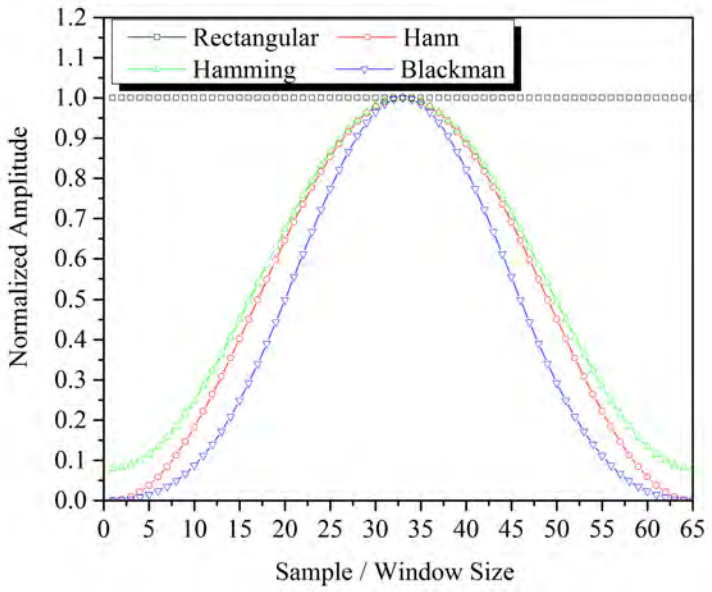

Figure 4.2: General cosine windowing methods - Rectangular, Hann, Hamming, and Blackman window of sample window size 65 normalized.

raised cosine window) both the window and its first derivative are continuous. However, the second derivative is discontinuous. The side lobes are greatly reduced for a Hann window in comparison with the rectangular window. It is used to reduce the problem of aliasing observed in Fourier transform. The frequency response of a Hann window shows that it has a part of its side lobe of opposite sign. This causes a local maximum in the side lobes and can be reduced by using a Hamming window, also known as raised cosine window with a platform. This is clearly seen in figure 4.2. Although these methods produce good results, we ideally want a tall narrow window to capture the original function accurately. The Blackman window has a narrow main lobe as compared to the other general cosine windowing methods and has a steep roll-off on the sidelobes. This method also minimizes the spectral leakage better than the other methods. Magnus and Gudmundsson[122] applied the Blackman window to the noisy Langmuir probe characteristic and were able to smooth the data with some distortion of the second derivative maximum and minimum for the

given window length.

4.1.6.4 Polynomial Fitting Method

Polynomial fitting is one of the most popular fitting methods. It is based on fitting the noisy data to an n^{th} order curve based on the least squares analysis. Mathematically, it is given by eq. 4.11 as mentioned in Savitzky-Golay method. While Savitzky-Golay method considers a few consecutive data points for smoothing, the polynomial fitting method uses the entire data set. The only parameter of consideration is the degree of the polynomial. As the function generated is continuous, it can be easily differentiated. The advantage of this method is its easy implementation, and most mathematical tools have built in commands for least square polynomial fitting.

However, smoothing by polynomial fitting is not ideal for the data obtained from Langmuir probe analysis. Even a non-noisy signal cannot be described accurately by polynomials. As suggested by Steffen [136] one reason for this is that all signals have to be bounded which is not the case for polynomials. Though theoretically, we can fit an nth order curve passing through (n + 1) points, however, due to limitations of matrix operation algorithms the degree of the polynomial is much smaller than the number of data points available. This invariably causes the polynomial to oscillate between the data depending on the noise amplitude and the degree of polynomial. Since it is based on the principle of least squares, the smoothed polynomial function may not overlap with the original signal completely. Figure 4.3 shows a zoomed in view of a noisy characteristic smoothed using polynomial of degree 35. The original data in the figure is a smooth function on which a Gaussian noise is superimposed.

4.1.6.5 Free Four Parameter Fitting

Azooz [119] proposed a method that fits most Langmuir probe characteristics based on four parameters (a_1, a_2, a_3, and a_4). These parameters essentially define the

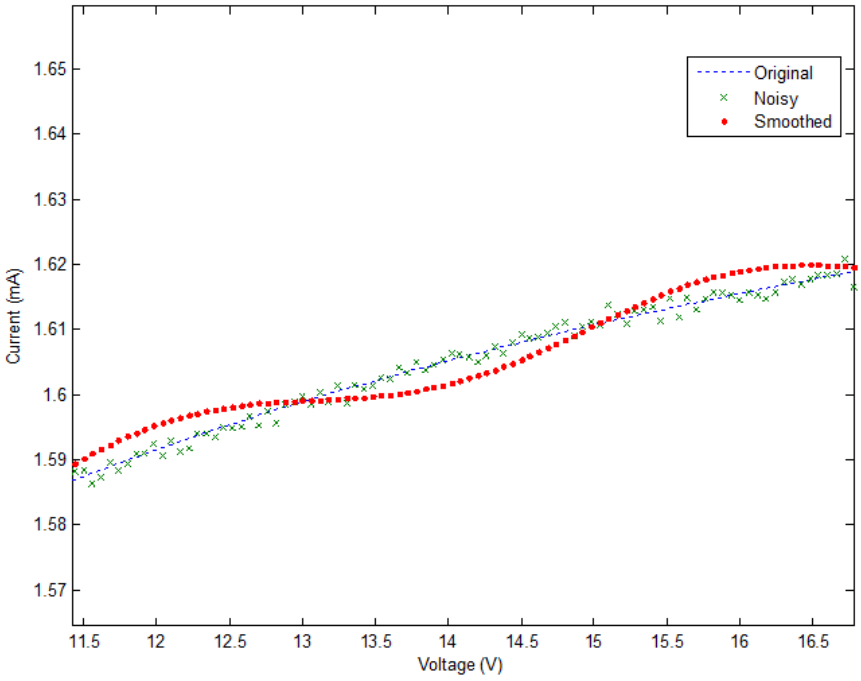

Figure 4.3: Demonstration of polynomial fitting of an I-V characteristic. The original data is a continuous function on which a Gaussian noise is super-imposed. The final smoothed signal is shown in red.

shape of the curve based on the experimental data obtained. The probe trace contains an electron saturation region and an ion saturation region that are best represented mathematically by a hyperbolic tangent function. Azooz suggested that since the hyperbolic tangent function is representative of the double probe characteristic and an electrostatic probe behaves differently compared to the double probe, an exponential transformation to the tangent hyperbolic function would resemble a single probe characteristic. The parametric model is represented by eq. 4.22. The parameters are important and need to be chosen carefully.

$$I_{pr} = \exp\left[a_1 \tanh\left(\frac{V_{pr} + a_2}{a_3}\right)\right] + a_4 \tag{4.22}$$

When the probe bias voltage is made negative (ion saturation region), the equation reaches a limiting value of the ion saturation current (I_{0i}). Similarly, on positive bias the equation reaches a limiting value of the electron saturation current (I_{0e}). These

are represented by eq. 4.23a and eq. 4.23b respectively. The floating potential (V_f) is determined by equating I_{pr} with zero in eq. 4.22 and rearranging the terms to get eq. 4.23c.

$$I_{0i} = \exp(-a_1) + a_4 \ldots \quad \text{Ion Saturation} \tag{4.23a}$$

$$I_{0e} = \exp(a_1) + a_4 \ldots \quad \text{Electron Saturation} \tag{4.23b}$$

$$V_f = a_3 \tanh^{-1}\left[\frac{\ln(-a_4)}{a_1}\right] - a_2 \ldots \quad \text{Floating Potential} \tag{4.23c}$$

It is clear from these equations how to make the initial guess for a few parameters. The parameter a_4 is always a negative number as the natural log of negative number or zero would not be correct. In most cases it is usually possible to make an initial guess of the ion saturation current. This aids in making a good initial guess for a_1, and the appropriate shifting of the axis can be given by a_4. While it has been suggested that the influence of a_2 is minimal on the plasma properties, the choice of a_3 can certainly lead to varying results. This is because of the mathematical model in which the parameter a_3 defines the steepness of increase in probe current. Since the floating potential is always less than the plasma potential, the knowledge of plasma potential can aid in determining the parameters a_2 and a_3.

As the mathematical model given by eq. 4.22 is of the exponential form, it is of the class C^∞, i.e., it is continuously differentiable. We can thus find an analytical expression for the second derivative of the probe current with respect to the probe voltage (eq. 4.24). The inflection point gives the value of the plasma potential and it is represented by eq. 4.25.

$$\frac{d^2 I_{pr}}{dV_{pr}^2} = a_1 \left[\tanh^2\left(\frac{V_{pr}+a_2}{a_3}\right)\right]$$
$$\left[2\tanh\left(\frac{V_{pr}+a_2}{a_3}\right) - a_1 + \frac{a_1}{a_3^2}\tanh^2\left(\frac{V_{pr}+a_2}{a_3}\right)\right]\exp\left[a_1\tanh\left(\frac{V_{pr}+a_2}{a_3}\right)\right] \quad (4.24)$$

$$V_p = a_3\tanh^{-1}\left[\frac{\sqrt{1+a_1^2}-1}{a_1}\right] - a_2 \quad (4.25)$$

The advantage of this method is its easy implementation. Since the second derivative is exactly known we avoid any rounding errors caused by the truncation of the Taylor expansion in the finite difference discretization. Another advantage is that this method allows for extrapolation of data points that are not obtained experimentally under certain circumstances.

Although the method is simple in its application, determining the parameters a_2 and a_3 accurately is tricky. The fitted characteristic is affected by the choice of all the parameters, and a_3 in particular, has the strongest influence on accuracy of the EEDF (and thus the electron temperature). A trial-and-error method may at best determine the parameters that fit a simulated dataset accurately. Fitting real probe characteristics with this method may include certain errors based on the assumptions of the fitting function and the initial choice of the parameters. One way to overcome this difficulty is to update the initial guess by principles of least square analysis, but there exists a possibility that the solution would never converge and the results would be erroneous. The method cannot accurately reproduce EEDFs with plasmas involving two groups of electrons having distinct temperature. In such cases, the method yields averaged EEDFs at best. Table 4.4 summarizes the constraints on possible numerical values of the parameters. Azooz provided the link to a computer program in his paper which works on the above empirical formula and is fit using a

non-linear least square regression.

Parameter	Possible Value	Description
a_1	Always positive	Value depends mainly on ion saturation current.
a_2	No restrictions imposed	Value less than or equal to a_3 is prefered
a_3	Always positive	Strongly influences the slope and the EEDF
a_4	Always negative	Value depends on the amount of shift necessary

Table 4.4: Parameters and their possible value for the four free parameter fitting method

4.1.7 Multi-Component Plasma Environment

Hoegy and Brace [137] discuss the implications of non-Maxwellian plasmas having multiple temperature electrons as well as energetic beams for planar, cylindrical, and spherical probes. Shown in figure 4.4 are their results for planar and cylindrical probes only.

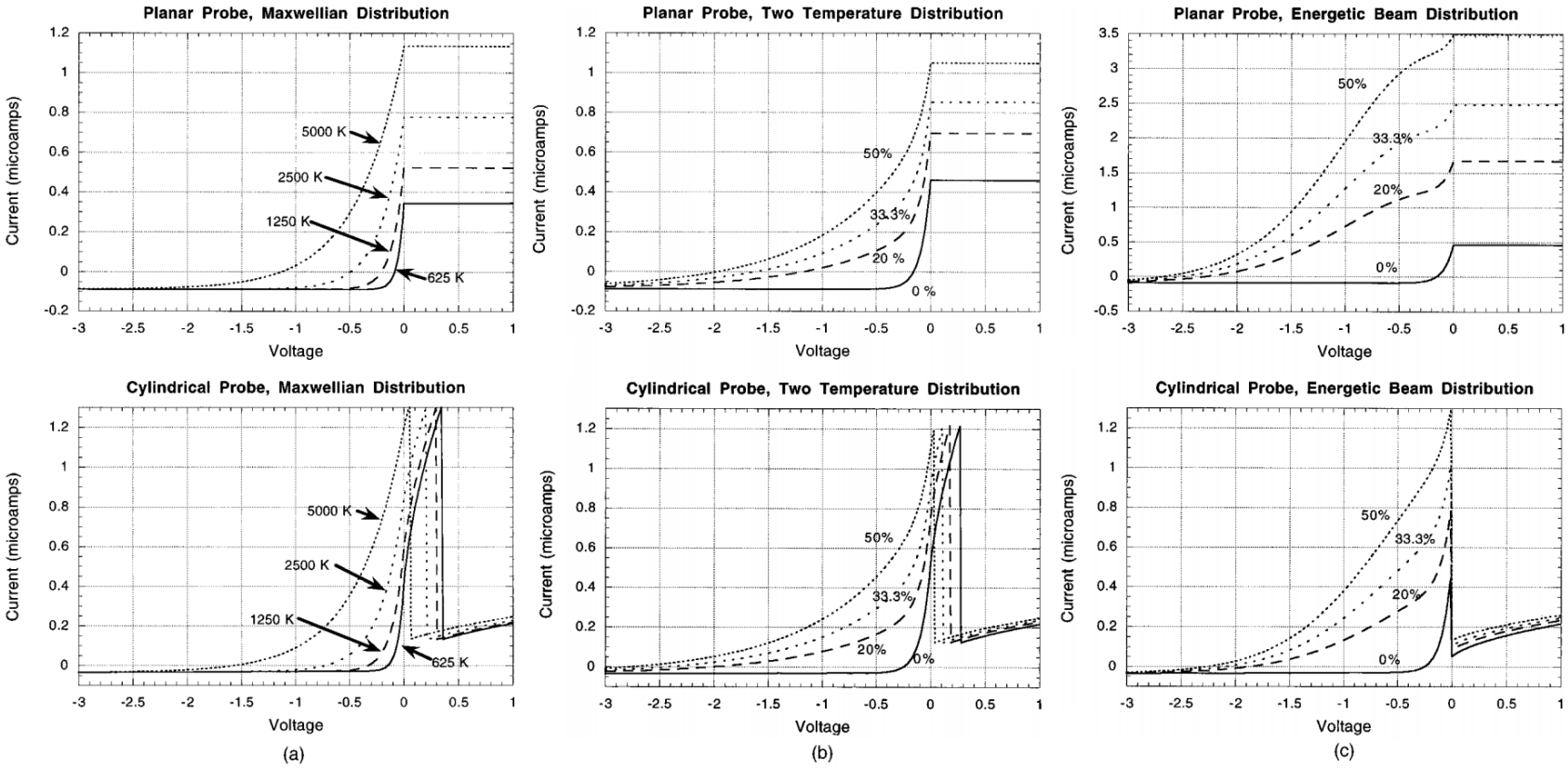

Figure 4.4: Planar and cylindrical Langmuir probe I-V characteristics in different scenarios. (a) Maxweillian distribution of electrons with varying electron temperatures (represented in K), (b) Presence of multiple electron species at 1000K and 10,000K (The different percentage represents the difference in total density represented by the higher temperature), and (c) Presence of a 1eV energetic beam with a 2000 K spread along with a 1000 K thermal plasma (the percentage represents the total density of the beam relative to the plasma). See reference [137] for more details.

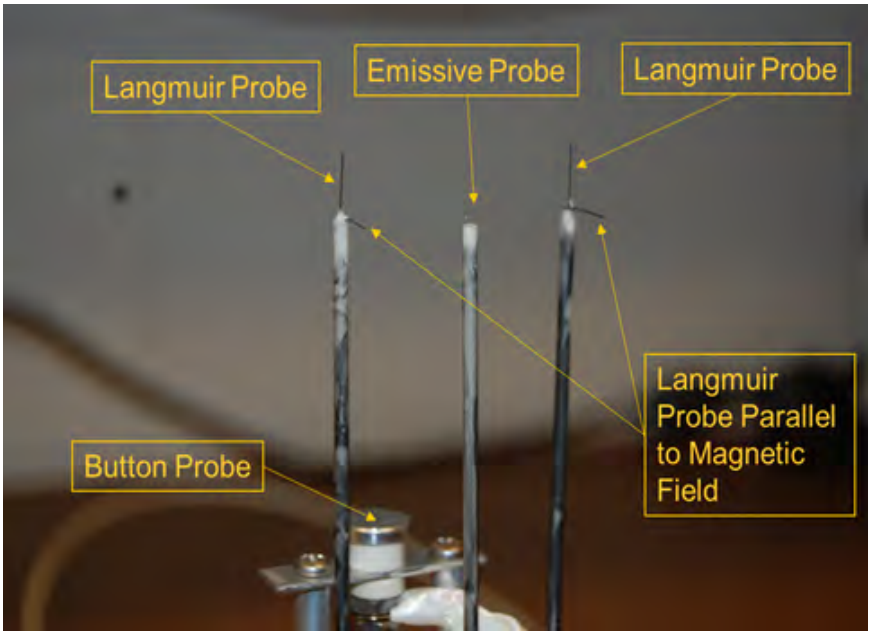

Figure 4.5: Suite of diagnostic probes built for the experiment. The probes consist of parallel and perpendicular Langmuir probes, planar probes (button probes), and emissive probes.

4.1.8 Experimental Approach

The experiment consists of using multiple Langmuir probe wires at locations separated by 2.54 cm. These probes are located at $\approx$ 2.54 cm in front of the electron gun. Figure 4.5 shows the probes containing both parallel and perpendicular Langmuir probes. The parallel probes measure the current contribution parallel to the magnetic field lines whereas the perpendicular probes measure the current contribution perpendicular to the field lines.

4.1.8.1 Presence of Magnetic Fields

The presence of magnetic fields leads to enhance the anisotropy of the plasma. Depending on the strength of the magnetic field, the particles may gyrate in circular Larmor orbits. In Hall thrusters, the electrons are magnetized but the ions remain unmagnetized. This causes the electron motion to be highly restricted and the effective mean free path is the order of Larmor radius. For magnetized plasmas, the ratio

of Larmor radius to the probe dimension gives the amount of influence the magnetic field has on the diagnostic. In the collisionless regions where $\mathrm{r}_L \gg \mathrm{r}_{\ p} > \mathrm{l}_p$, where l_p is the mean free path, the regular probe theory will yield acceptable results. However, electrons are usually magnetized and have a very small Larmor radius. This causes a decrease in saturation current as seen in figure 4.6.

At zero probe potential the current collected by a perpendicular probe [138] can be given by 4.26

$$I_{pr} = \frac{2\, l_p\, e\pi\, T_e}{B_0\, \ln l_p\pi\, /\, 4r_p} \tag{4.26}$$

The use of parallel and perpendicular probes allow determination of electron temperature components parallel and perpendicular to the magnetic field. The use of such probes has been used successfully by Sugawara [106] and [102] successfully. From the works of Sugawara, the ratio of current densities between various probes are given by equations 4.27a through 4.27c.

$$\frac{J_{e,||}}{J_{e0}} = \left[\left(1 + \frac{32}{3}\frac{\lambda_e}{\pi\, r_p}\right)\sqrt{\alpha}\right]\left[1 + \frac{32}{3}\frac{\lambda_e}{\pi\, r_p}\sqrt{\alpha}\right]^{-1} \tag{4.27a}$$

$$\frac{J_{e,\perp}}{J_{e0}} = \frac{\pi\,\sqrt{\alpha}}{2\,K(k)}\frac{\left(1 + \frac{32}{3}\frac{\lambda_e}{\pi\, r_p}\right)}{\left(1 + \frac{16}{3}\frac{\lambda_e\sqrt{\alpha}}{K(k)\, r_p}\right)} \tag{4.27b}$$

$$\frac{J_{e,\perp}}{J_{e,||}} = \frac{\pi\,\sqrt{\alpha}}{2\,K(k)}\left(1 + \frac{32}{3}\frac{\lambda_e\,\sqrt{\alpha}}{\pi\, r_p}\right)\left(1 + \frac{16}{3}\frac{\lambda_e\,\sqrt{\alpha}}{K(k)\, r_p}\right)^{-1} \tag{4.27c}$$

Figure 4.6 shows a schematic of the contribution of current collected by a parallel and perpendicular probe by Sugawara [106]. Clearly seen from the graph is how the magnetic field reduces the electron saturation and results in different electron temperatures.

The parallel and perpendicular EEDF can be obtained from the first derivative

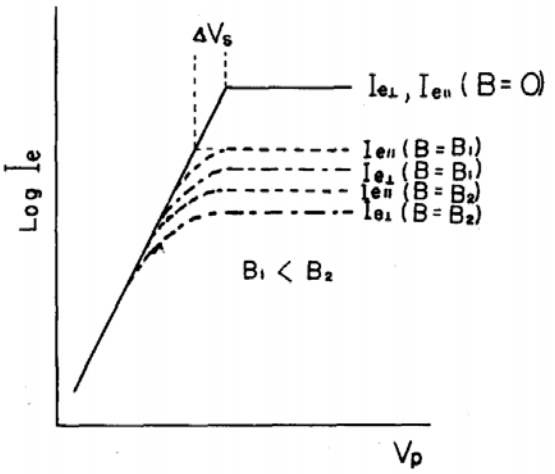

Figure 4.6: Schematic effect of a magnetic field on the probe characteristics [106].

[24] given by equations 4.28a and 4.28b

$$f_{\parallel}(\varepsilon) = -\frac{3\,\omega_c\, m_e^{5/2}}{64\sqrt{2}\,\pi\, e^2\, r_p\, (eV)^{3/2}} \frac{d\, I_e}{dV} \ldots \quad \text{Probe parallel B} \tag{4.28a}$$

$$f_{\perp}(\varepsilon) = -\frac{3\, m_e^2\, \ln\left(\frac{\pi\, L_p}{4\, r_p}\right)}{16\,\pi^2\, e^3\, V\, r_{Le}} \frac{d\, I_e}{dV} \ldots \quad \text{Probe perpendicular B} \tag{4.28b}$$

Figure 4.7 and figure 4.8 clearly show the usefulness of this method for magnetized plasmas by plotting the first derivative and EEDF in magnetized plasmas with probes oriented in two directions.

4.1.9 Langmuir Probe Construction and Circuit

The Langmuir probe is operated using either the Keithley 2410 or the smart probe system. The smart probe system is an automated Langmuir probe diagnostic system from scientific systems used for measuring I-V characterstics and determining plasma parameters. Figure 4.9 shows the circuit configuration for the operation of the electrostatic probe.

Using the smart probe system, measurements are carried out by averaging 400

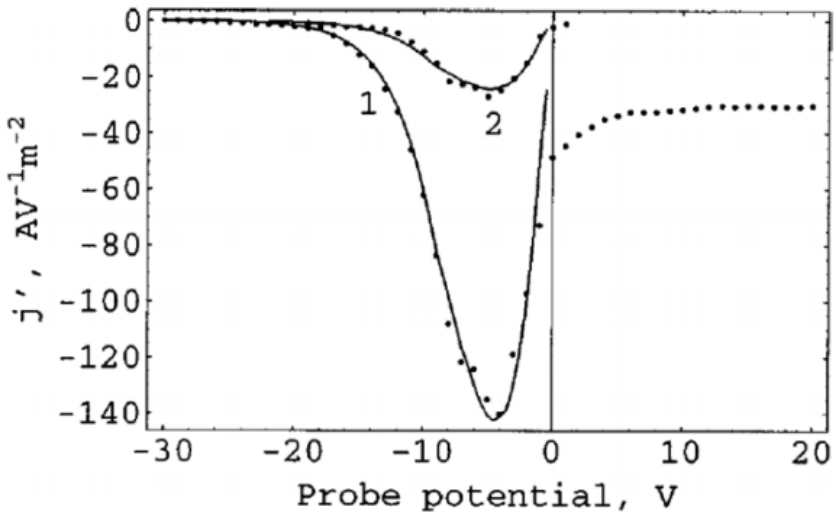

Figure 4.7: Measured (dots) and calculated (line) dI_e/dV in a magnetized plasma for perpendicular (1) and parallel (2) probes [24].

measurements per bias voltage and then averaging 25 individual traces to produce a single I-V characteristic. This ensures good statistics as well as ability to use lower quality smoothing filters prior to numerical differentiation.

4.1.10 Sample Langmuir Probe Data Analysis

Analysis of the Langmuir probe is done by first subtracting the ion contribution from the plasma. In beam generated plasmas the choice of the exact ion saturation slope is not well defined and has to be adjusted until all beam components are visible. Figure 4.10 shows an example of the I-V characteristics obtained from the experiment. Figure 4.11 corrects for the ion contribution from the data and the beam component is clearly seen.

Using the corrected characteristic, basic plasma parameters are obtained as shown in figure 4.12. This information is further used to obtain EEDF using the second derivative method. The ion density information is obtained using the OML theory and the slope is obtained as shown in figure 4.13.

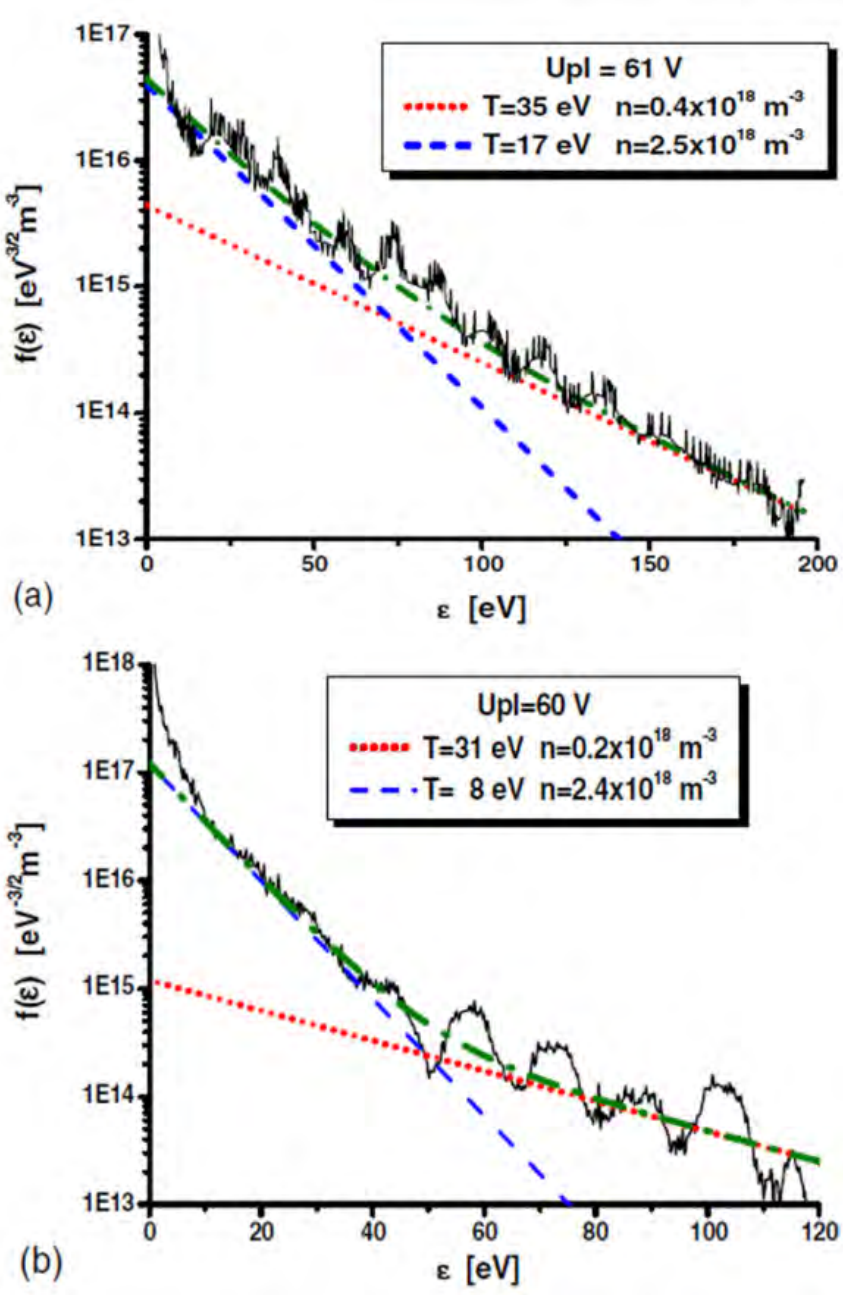

Figure 4.8: The EEPF obtained from a perpendicular (a) and parallel (b) Langmuir probe in a mangetized plasma with B = 1.3 T. The tashed-dotted lines are a bi-Maxwellian approximation and the dashed line represents the distribution of low energy electron population [24].

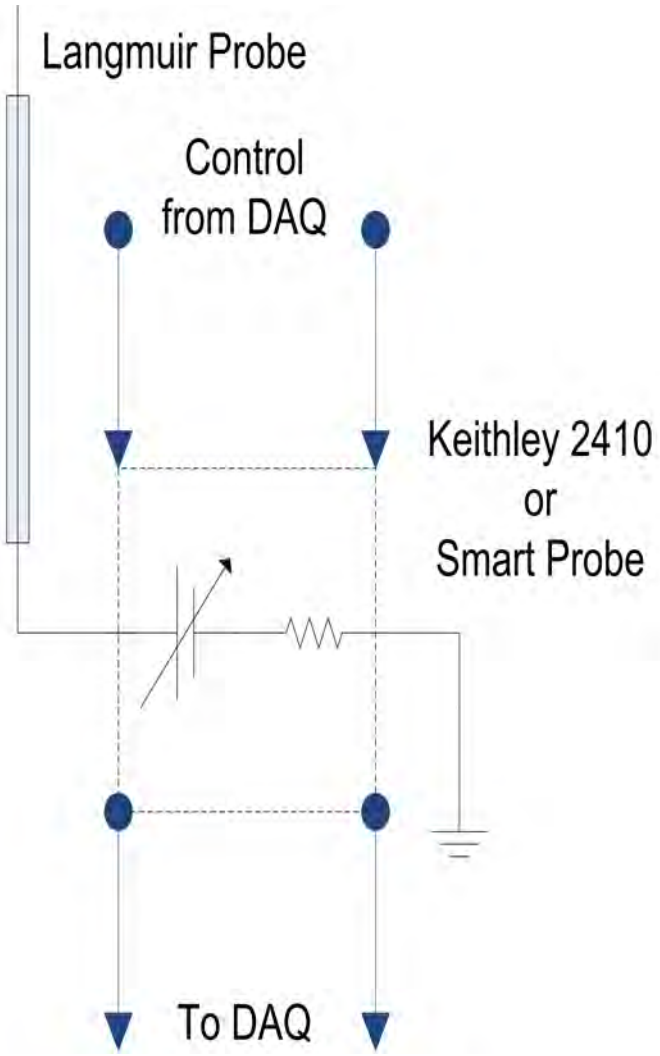

Figure 4.9: Langmuir probe circuit

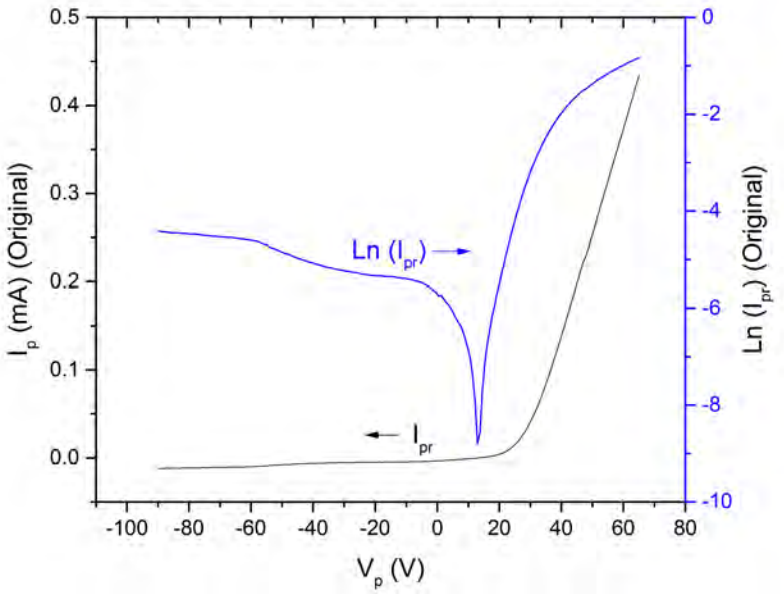

Figure 4.10: Raw I-V characteristics from a Langmuir probe.

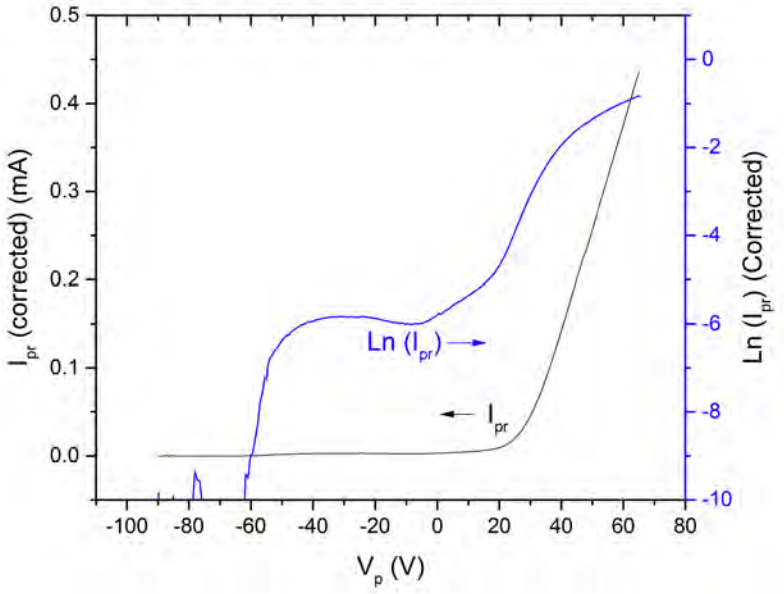

Figure 4.11: Ion saturation correction applied to a raw I-V characteristics obtained from a Langmuir probe.

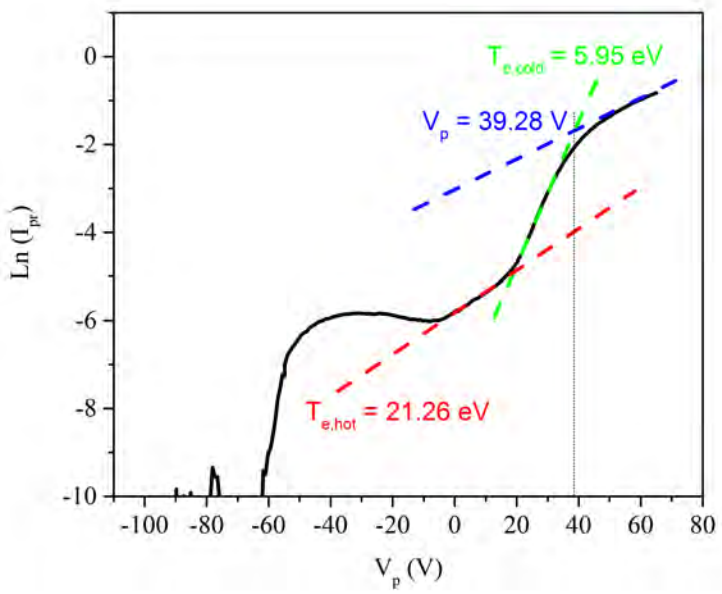

Figure 4.12: Analysis of I-V characteristics to obtain plasma properties.

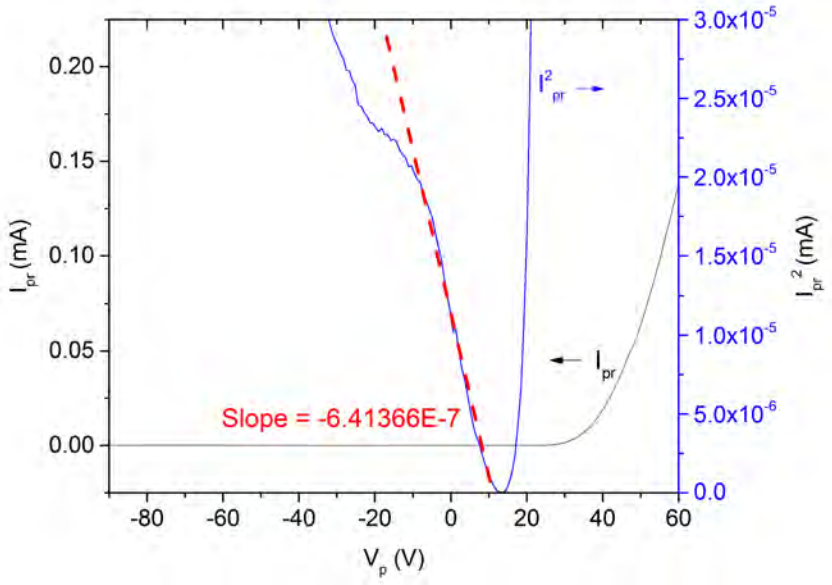

Figure 4.13: I-squared analysis for obtaining ion density.

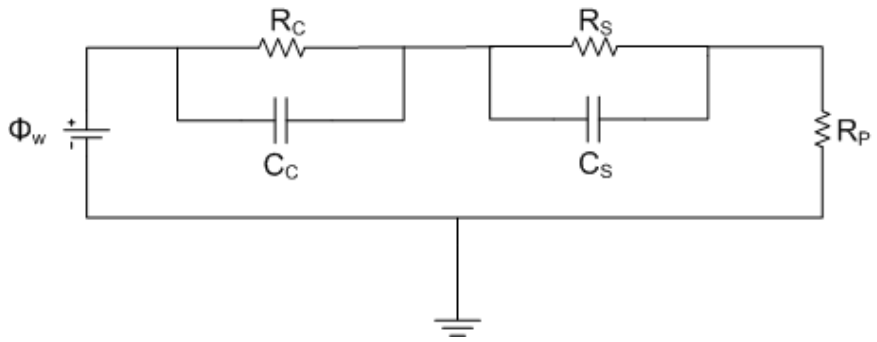

Figure 4.14: Equivalent electrical circuit with contamination layer on Langmuir probes.

4.1.11 Problems with Langmuir Probes

One of the most common problems with Lanmguir probes is the development of a contamination layer on the probe surface. Surface layer contamination may be due to sputtered components within the plasma system or from adsorption of gases used in the plasma source. The build up of contamination layer leads to erroneous temperature (typically higher T_e) measurements at best and lack of any detectable current signal at worst. The contamination layer can be highly resistive or even insulating. These contaminants are a serious problem in space plasma diagnsotics as well as laboratory diagnostics [139, 140, 141, 142] .

Figure 4.14 shows the equivalent electrical circuit when a contaminant layer is present. This leads to additional impedance due to capacitance charging ($\chi_c = 1/\omega_C$) and the voltage drop across the contaminant layer is given by equation 4.29. The additional impedance results in hysteresis when a up-down voltage ramp sweep is performed.

$$\Delta V_C = \frac{V_{pr}}{R_s + R_c} R_c \tag{4.29}$$

From the above equation it is clear that if the sheath resistance is much greater than the resistance of the contaminating layer, the voltage drop is small. However, when the contaminating layer resistance is much greater than the sheath resistance,

the voltage drop is the same order of magnitude as the probe bias and that can lead to incorrect results. In extreme situations, the contamination layer will not allow the passage of any current to flow through. This is seen in images 4.15(a) through 4.15(c).

Figure 4.15(a) shows a well behaved I-V characteristic both in forward and reverse bias operations. The lack of hysteresis is because of a pristine tungsten wire is used. Here all plasma current is readily collected based on the bias voltage. When a small contamination layer is added, the characteristics look like regular I-V characteristics but are not truly representative of the plasma due to additional displacement current across the the contamination layer. This can be determined in the hysteresis test of the probe and is shown in figure 4.15(b). Finally, when the contamination layer is thick, the current to the probe is approximately zero as seen in figure 4.15(c). Heavy ions at larger negative bias can penetrate the contamination layer, but the lighter electrons are lost. This good, bad, and ugly behavior of the I-V characteristics depending on the probe contaimination is a serious issue and needs to be taken into consideration.

In order to assess the status of the probe, these hysteresis tests for each probe are conducted prior to every experiment. Figure 4.16 shows the voltage ramp up and down as a function of time and the response of the plasma current collected by the probe.

When the probe hysteresis check suggests that the probe is contaminated, it is a good idea to improve the quality of the probe wire. Some ways to do this are listed below:

1. Operating the probe in saturation modes (ion bombardment or electron bombardment) for a finite period of time. This technique requires a good understanding of the contaminant adsorption rates and is often difficult to determine in practice.

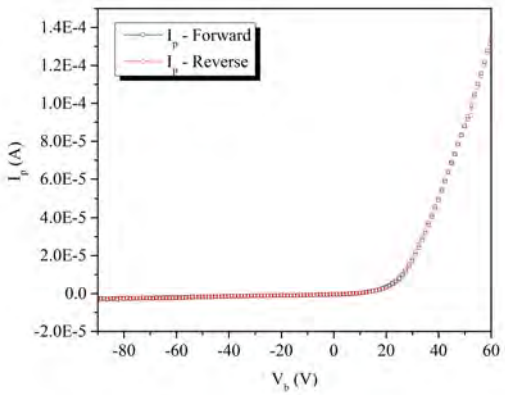

(a) The Good Characterstics

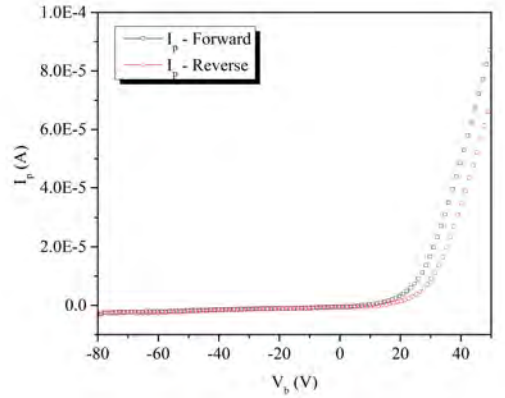

(b) The Bad Characteristics

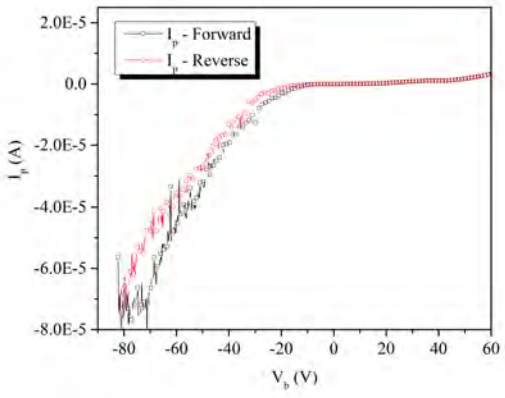

(c) The Ugly Characteristics

Figure 4.15: Various I-V characteristics depending on the level of probe contamination. As the contamination increases, the collected current decreases leading from inconsistent results at best to no signatl at worst.

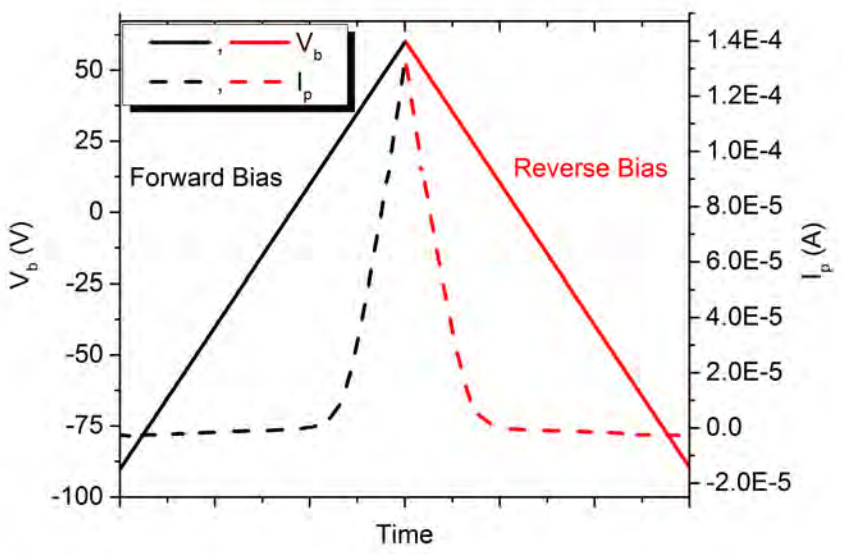

Figure 4.16: Hysteresis check for Langmuir probes. The black line shows the voltage ramp up and its associated plasma response. The red line shows the voltage ramp down and the current collected by the plasma.

2. Heating the probe tip to thermally desorb any contaminant layer. This requires special equipment and probe design.

3. Using a pulsed plasma probe with carefully selected on and off times to minimize hysteresis by minimizing the charging effects ($\tau \ll RC$) [143].

4. By using a new electrode for each test.

Figure 4.17 shows build up of an insulating layer and is compared to a pristine probe wire. Closeup of the image clearly shows a significant build up and this leads to incorrect results.

In this experiment, biasing at high potentials was tested but no significant benefits was found. Hence, prior to data collection a hysteresis check was performed. If there was no hysteresis, the probe was used to collect plasma data. In case of any inconsistency of data during hysteresis check was observed, the probes were replaced.

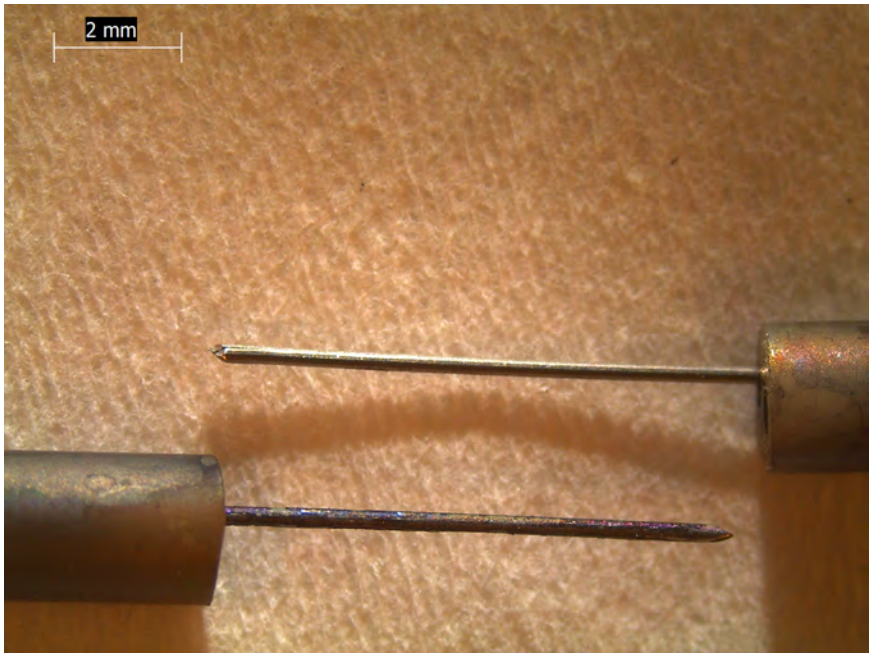

(a) 8x zoom

(b) 35x zoom

Figure 4.17: Pristine Langmuir probe and coated probe are shown. Clearly seen in a 35x zoom is a thick non-conductive coating. A small portion of the coating is peeled to reveal the original tungsten wire.

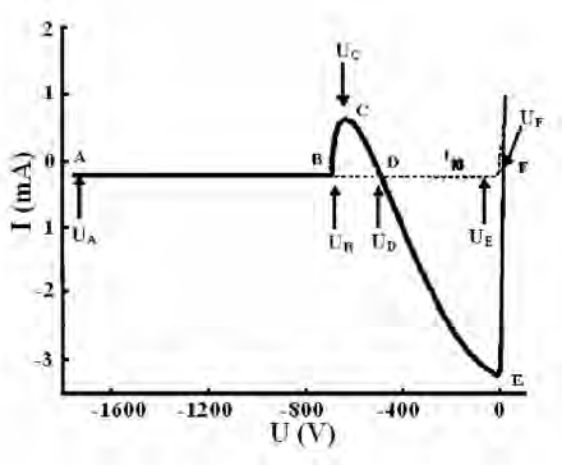

Figure 4.18: Hysteresis check for Langmuir probes. The black line shows the voltage ramp up and its associated plasma response. The red line shows the voltage ramp down and the current collected by the plasma.

Another problem associated with Langmuir probes in presence of high energy electrons is the ability of the probe structure to produce secondary electrons when subject to electron bombardment. For example, the insulating probe body (typically Al_2O_3) has a SEE yield of 1.00 at approximately 20 V [45]. Tungsten wire typically has a SEE yield of 1.00 at energies around 250 V. In either circumstances, there is a possibility to generate SEE from the Langmuir probe which in-turn affects the probe results. Solomon et al. [144] demonstrated these effects for stainless steel probe at high electron energies. Figure 4.18 shows the behavior of ion saturation current of the probe in presence of SEE.

Figure 4.19 shows the effects of SEE due to high energy bombardment on the probe insulating surface.

In order to avoid this, graphite coating is used. The graphite coating (Bonderite L-GP G Aerosolized graphite commonly known as Aerodag G) was either sprayed or painted on the ceramic tubing. This is due to the very low SEE coefficient of graphite at the operating voltages compared to alumina.

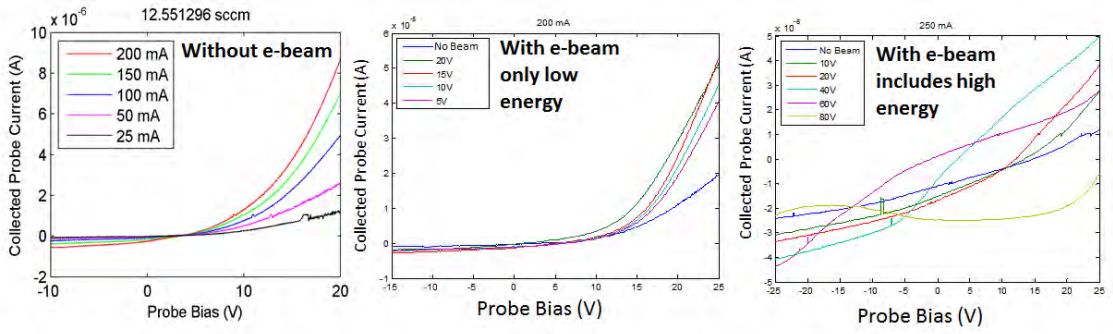

Figure 4.19: Effects of low and high energy beam on plasma..

4.2 Emissive Probe Diagnostics

Determination of plasma potential in general is problematic because often the plasma is not Maxwellian, so the floating potential can't be corrected to yield the plasma potential. Additionally, the location of the "knee" in the electron retarding region is often difficult as its position is usually rounded and ambiguous. One method to accurately determine plasma potential measurements is by using laser induced fluorescence (LIF). This technique is expensive requiring expensive optics and complex. A cheaper and relatively accurate method to determine the plasma potential is by using emissive probes. The emissive probes float very close to the plasma potential and are thus used to measure the plasma potential directly. These probes, in comparison to Langmuir probes, also allow for rapid measurements of plasma potential with a sufficient spatial resolution. They are also free from the errors associated with the first derivative analysis of Langmuir probe which assumes a Maxwellian plasma, and as discussed in section 2.2.6.1, low temperature plasmas in presence of multi-electron populations is far from Maxwellian. The potential variation across two points in a plasma can be dependent on both the plasma as well as the boundary conditions [145] and gives information about the plasma system. However, there is an error incurred in the floating point method for strongly emitting probes. This is because the space charge prevents the probe from floating to the true plasma potential.

4.2.1 Theory of Emissive Probes

In Langmuir probes, primarily due to the large mass imbalance of the species ($M_i/m_e \gg 1$), the electrons have a higher mobility and can charge the floating electrode negative relative to the plasma. It is for this reason, the plasma potential is different from floating potential. The floating potential of an emissive probe can be made to be close to the plasma potential by increasing the emission current from the emissive probe. This is the principle of emissive probes.

For an ideal Maxwellian plasma, it was shown in equation 4.8, that the plasma potential is dependent on the electron temperature. In most systems, there exists temperature gradients as well as the temperature can fluctuate during measurements due to localised instabilities and plasma operation modes. The equation also relies on strong isotropic velocity distribution and can lead to erroneous results in presence of electron beams as those in thermionic sources and in presence of secondary electron beams. Equation 4.8 can be re-written in terms of saturation currents given by equation 4.30

$$V_p = V_f + \left(\frac{I_{sat,e}}{I_{sat,i}}\right) T_e \tag{4.30}$$

When emission current from an emissive probe is included, the equation transforms

$$V_p = V_f + \left(\frac{I_{sat,e}}{I_{sat,i} + I_{em}}\right) T_e$$

When sufficient heat is provided to the wire to emit electrons, the emission current reaches a point comparable to the electron saturation such that $I_{em} = (I_{sat,e} - I_{sat,i})$, the resulting potential is given by equation 4.31, and is the plasma potential.

$$V_p = V_f \tag{4.31}$$

4.2.2 Probe Construction Techniques

There are several designs suggested in literature to heat the probe causing it to emit electrons. These include Joule heating [146] in which current is passed through a wire in order to reach a temperature to thermionically emit electrons, self emissive probes that rely on ion bombardment at a highly negative voltage [147, 148], secondary electron emissive probes [149], and laser heated [150, 151, 152]. Each technique has its own merits in terms of ease of construction or lifetime of the emitting wire.

Additional details on techniques used to emit electrons from a metal as well as analyzing the data can be found on the review article by Sheehan and Heershkowitz [153] and the references therein.

4.2.3 Emissive Probe Methods for Plasma Potential Determination

1. Separation Point Technique In this technique, the I-V characteristic of a cold probe and a sufficiently hot emitting probe are compared. The point at which the two curves start to separate is called the separation point and the value corresponds to plasma potential. Figure 4.20 shows an example of separation point technique analysis using emissive probes [153].

2. Floating Point Method

   The floating point technique is one of the most common techniques employed for determination of plasma potential using an emissive probe. In this technique, the filament is heated to a sufficient temperature at which the plasma potential is given by the floating potential of the probe. Figure 4.21 shows the floating potential as a function of the emission current of the filament [153].

3. Inflection Point Method

   This method relies on ability to determine the inflection point from the first

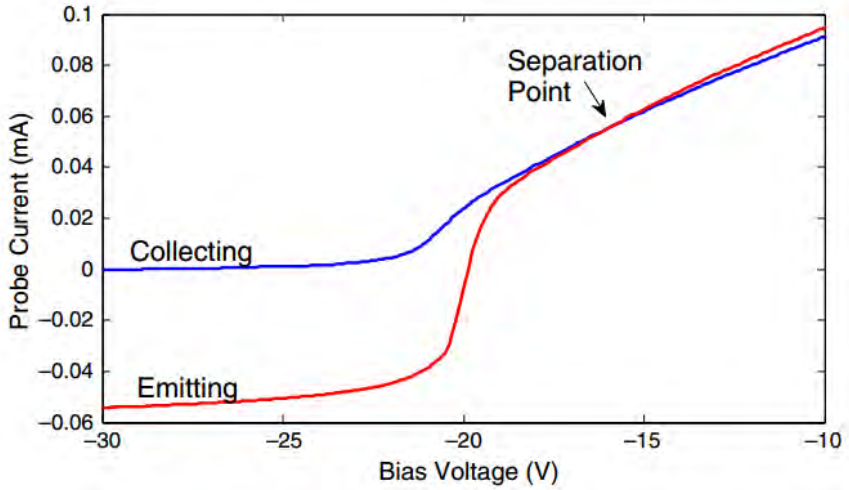

Figure 4.20: An I-V trace illustrating the curves used to determine the separation point [153].

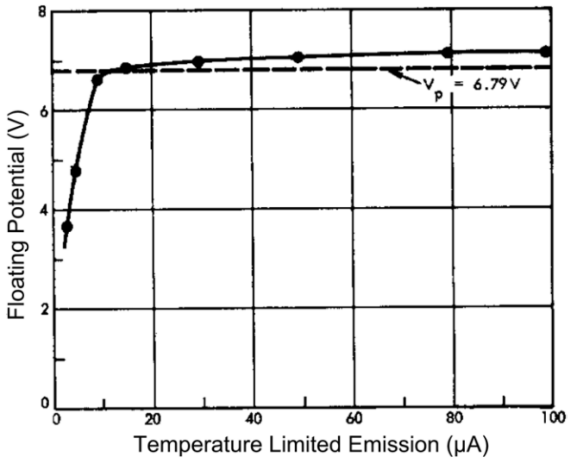

Figure 4.21: Floating potential of an emissive probe vs emission current of the filament. Source: Sheehan and Hershkowitz [153].

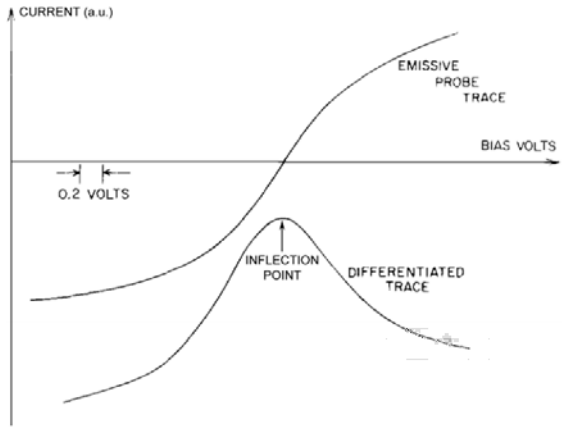

Figure 4.22: An experimental emissive probe I-V characteristic and the first derivative used to determine the inflection point [153].

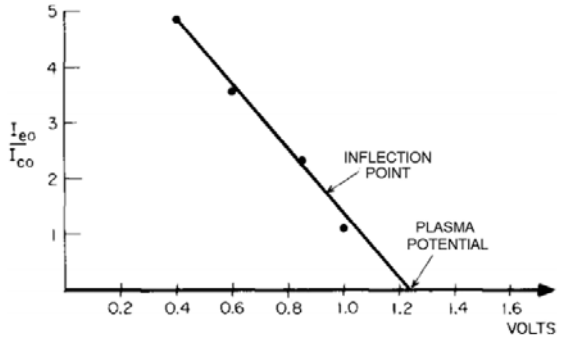

Figure 4.23: Technique to determine the floating potential using inflection point method from an emissive probe. The vertical axis in this graph is temperature limited emission normalized to the electron saturation current. The line fit to inflection point yields the plasma potential [153].

derivative of the I-V characteristic obtained at different emission currents. Due to the noisy nature of measurement, some level of smoothing maybe necessary to determine the inflection point. Plotting the different voltages at various emission currents, the true plasma potential can be obtained when a line-fit is made to the inflection points at various emission currents. Figures 4.22 and 4.23 show an example of the obtaining the plasma potential using inflection point method [153].

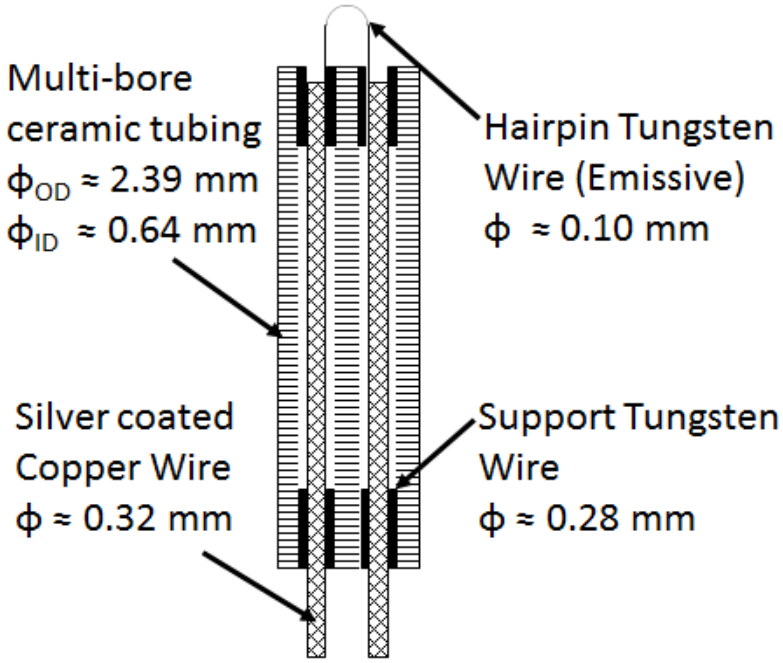

Figure 4.24: Schematic of an emissive probe used in this work.

4.2.4 Emissive Probe Construction

Figure 4.24 shows the construction of a simple hair-pin emissive probe. It consists of a $\approx$ 23 mm long two-bore ceramic (high temperature non-porous alumina) tubing and is coated with the graphite coating as explained in section 4.1.9 to reduce secondary emission from the ceramic tubing. A thin tungsten wire ($\phi \approx 0.1$ mm) is inserted between the two bores forming a loop. To ensure electrical continuity a 28 AWG ($\phi \approx 0.32$ mm) silver coated copper wire is placed in the remaining length of the probe. The thin hair pin wire is inserted roughly about 25 mm into both bores overlapping with the silver coated copper wire. The wires make physical contact and to ensure no gaps exist, additional tungsten wires ($\phi \approx 0.28$ mm) is pressed in gaps from both directions. A D-sub pin connector is used to connect the probe wires to the vacuum feedthrough. On Joule heating under vacuum conditions, the thin wire would heat the copper and fuse thus no spot weld is necessary for this design due to the tight tolerances.

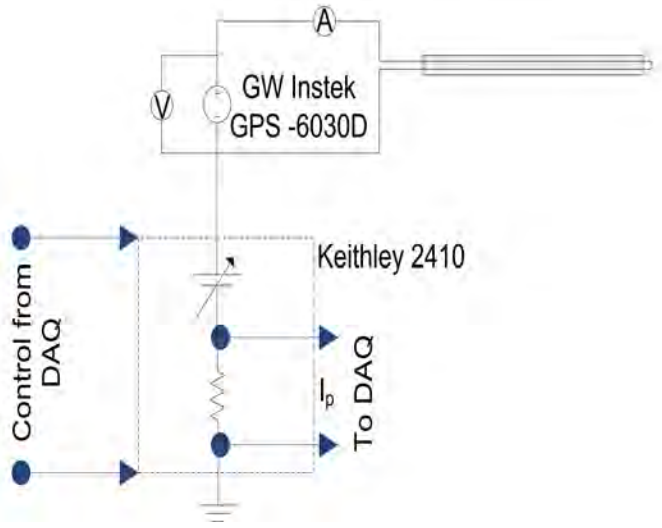

Figure 4.25: Emissive probe circuit employed in inflection point tests.

4.2.5 Experimental Procedure and Electrical Circuit

Two different techniques are used to measure the plasma potential using the emissive probe. The floating point method in the limit of large emission and the inflection point method in the limit of zero emission.

1. Inflection point in the limit of zero emission:

   Due to the large amount of time required to carry out inflection point analysis, only 2 axial locations with 5 different current conditions are tested. The circuit used for this method is shown in figure 4.25

2. Floating point method in the limit of large emission:

   In this method, a probe was kept at a fixed current, large enough to be emitting strongly and moved at multiple locations from 0 mm (close to the wall) to 14 mm. Multiple passes were made to enable statistical data collection. The circuit used for this method is shown in figure 4.26

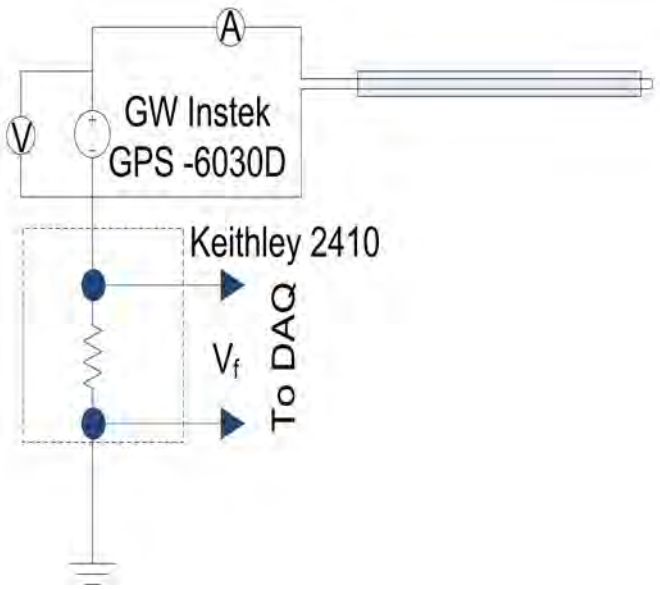

Figure 4.26: Emissive probe circuit employed in floating point tests.

4.2.6 Sample Analysis of Emissive Probe Data

Figure 4.27 shows the floating point method in action. As can be seen from the figure that increasing current through the filament increases the power and thus the emission current. Under sufficiently large conditions the probe provides the plasma potential.

Figure 4.28 shows the data obtained using the separation point technique. As can be seen the two techniques agree fairly well with each other.

The inflection point test proved to be rather difficult due to low emission values chosen. The data agrees with the work of Sheehan and Raitses [153] and the plasma potential is off by 1.8 - 2 T_e . The data obtained is shown in figure 4.29

4.2.7 Influence of Magnetic Field on Emissive Probes

Magnetic fields in presence of a current carrying wire produces a force. This force can cause the wire to bend at very large magnetic fields and large currents. The force on a wire of length l (section dl) with magnetic field at an angle θ is given by equation 4.32 in the vector form and the magnitude is given by 4.33

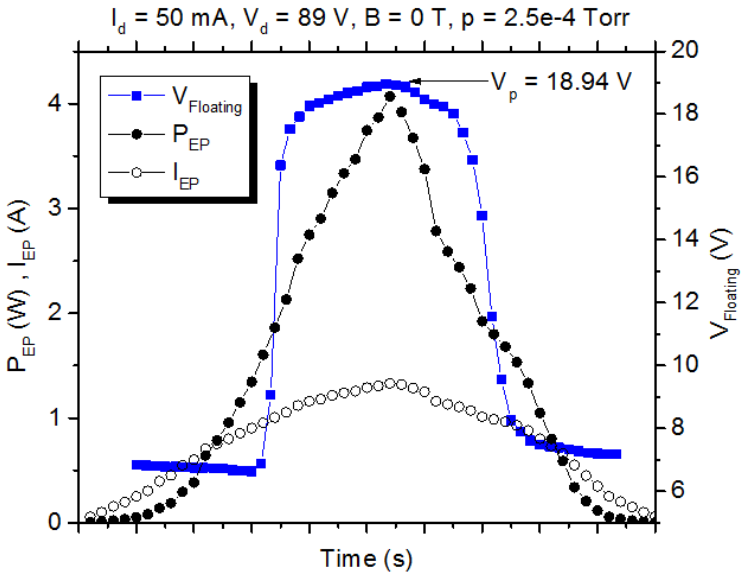

Figure 4.27: Sample analysis using floating point technique.

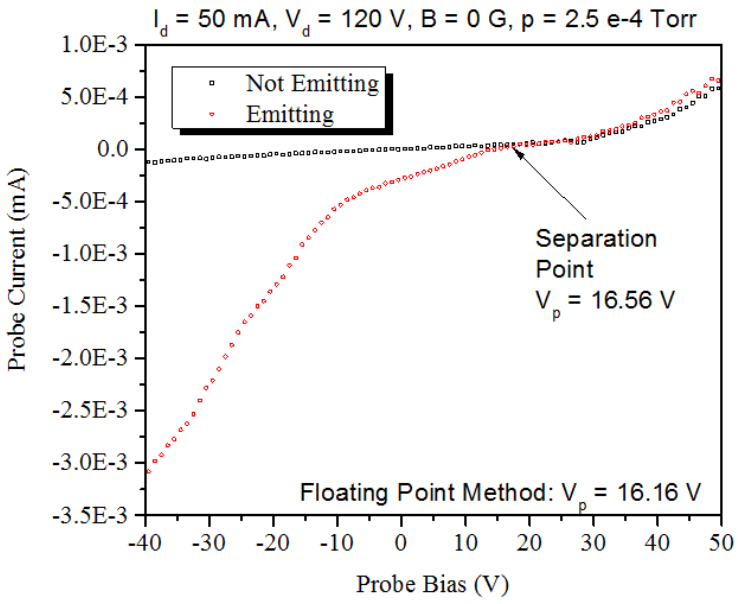

Figure 4.28: Sample analysis using separation point technique.

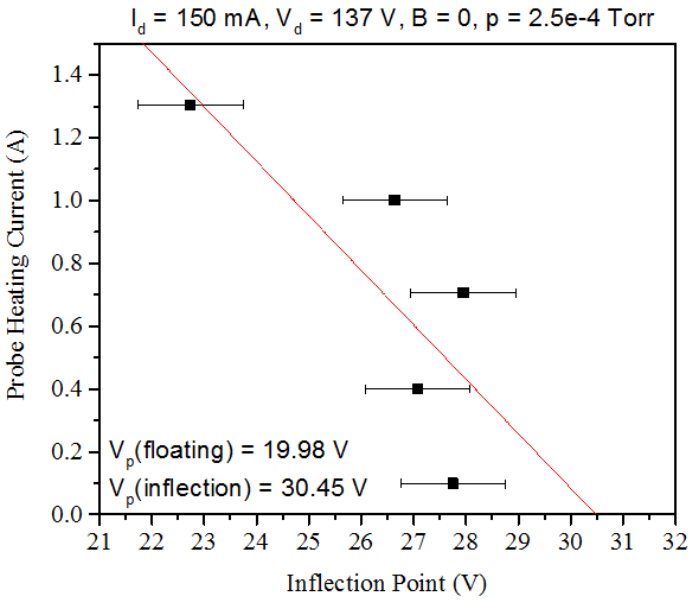

Figure 4.29: Sample analysis using inflection point technique.

$$\overrightarrow{\mathrm{F_B}} = \int I_{EP} d\overrightarrow{\mathrm{l}} \times B(r) \tag{4.32}$$

$$|F_B| = I_{EP} l B sin\theta \tag{4.33}$$

In emissive probe applications for Hall thrusters, this force is not too large as the current is typically 1.3 amperes and the magnetic fields is 50 - 200 Gauss results in 100 to 300 μN, which is far too low to bend the wire.

4.3 Retarding Potential Analyzer

An electrostatic retarding potential analyzer (RPA), sometimes referred to as retarding field energy analyzer (RFEA), is used to determine the energy distribution of the charge particle population under observation. In principle, these analyzers are easy to construct and straightforward in operation. These analyzers have been used to analyze hollow cathode discharges [154, 155], hall thruster plumes [156], flowing

plasmas [157] and vacuum tubes [158].

The operating principle relies on electrically biased grids that establish equipotential planes. The current collecting plate, also called a Faraday cup, is shielded from the plasma by several grids. These grids included the first grid labeled here as G_1 which is grounded and serves to shield the RPA from the plasma and reduces plasma perturbation. When used to measure ion distribution, the second grid is negatively biased to repel electrons and is called the electron repelling grid. In this experiment, the second grid G_2 is grounded as the goal is to measure the electron distribution from an electron gun. The third grid (G_3 or D) is the discriminator and is biased at a voltage (V_D) to repel electrons. Only electrons with energy higher than the discriminating voltage ($V_b = eV_D$) are allowed to pass through to the collector. The innermost grid, G_4 or S, is the secondary electron repeling grid used to repel electrons produced when energetic electrons hit the collector surface. In order to collect electrons, this grid is positively biased.

For the RPA to operate as a particle filter in the single particle limit, it is required that the grid spacing should be no more than a few λ_D and the transparency of the grid (hole size) should be less than λ_D. These requirements ensure that the plasma is shielded from the RPA as well as to minimize localized space charge effects. Another requirement for an effective RPA measurement is that the average beam energy should be greater than the random velocity of the particles, i.e., $< \varepsilon_{beam} > > \sqrt{\frac{8\,k_B\,T_e}{\pi\,m_e}}$.

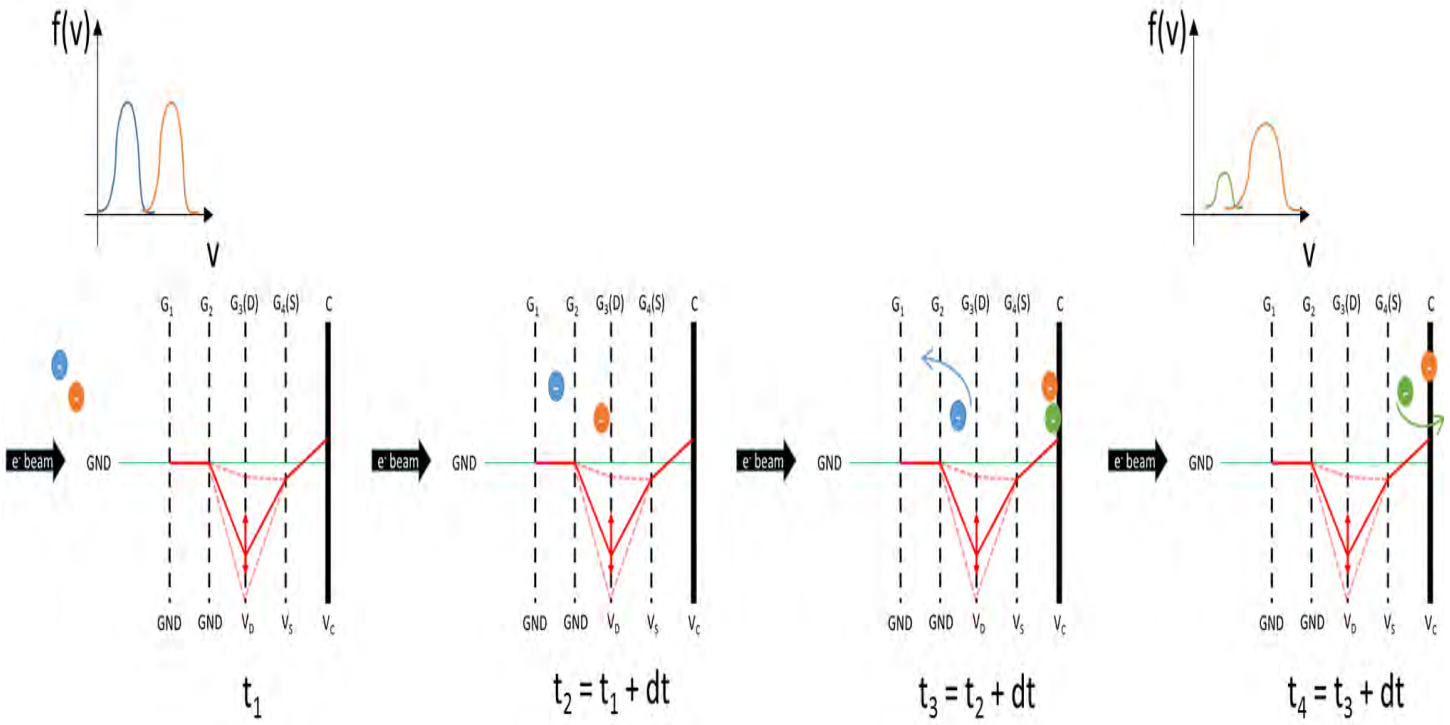

Figure 4.30: Schematic of RPA grid bias and electron response, illustrating the effects of discrimination. The distribution clearly indicates that the electrons represented by orange color have higher average energy compared to the blue colored electrons. The energy of the orange colored electrons are greater than the discriminator bias and are allowed to pass through the grid whereas the blue colored electrons are repelled. On striking the collector, secondary electrons may be produced which are repelled by grid S and collected by the collector.

Despite the simplicity of RPA, there are some issues with the planar RPA [159]. Collisional events can lead to widening of the width of energy distribution as well as decrease in peak flux directed towards the probe. Also, depending on local pressure, there could be a rapid plasma development within the grids at sufficiently large discriminating voltages leading to destruction of the RPA. The magnitude of error [158] associated with a planar RPA measurements is given by equation 4.34

$$\left(\frac{\Delta E}{E}\right)_{width} = 1 - \frac{2\pi(\delta/a) - \ln(4)}{2\pi(\delta/a) - 2\ln[2\sin(\pi r/a)]} \tag{4.34}$$

where δ is the distance between the grids, r is the radius of the wire used for the grids, and a is the effective distance between the wires which gives information on the transparency of the grids. Another source of error in RPA measurements is due to the measurement carried out at normal incidence from a beam. In reality there are particles that enter the RPA at an angle. Due to this, a small shift occurs in the mean energy of the particles in a given plasma / beam environment. The magnitude of this shift [160] is given by equation 4.35.

$$\left(\frac{\Delta E}{E}\right)_{shift} = \sin^2\theta \tag{4.35}$$

where θ is the angle of incidence of the particles into the RPA.

4.3.1 Probe Design

The probe is made of stainless steel housing and contains four tantalum grids and a Faraday cup that acts as a collector. The RPA was fabricated at Electrodynamics Application Inc.

Figure 4.31 shows the image of the RPA and when it is connected to an experiment [154]. The grids are designed in such a way that they remain aligned to allow an unobstructed flow of charged particles based on the potential bias. These grids are

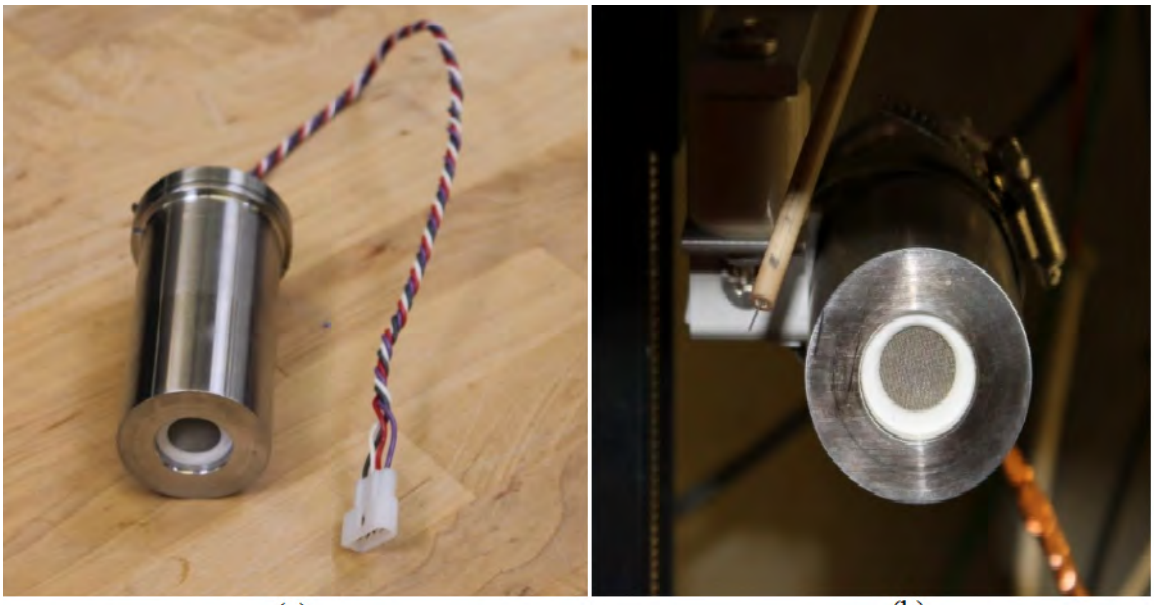

Figure 4.31: Images of the RPA used in this experiment to determine the distribution of electrons based on their energy. Source: Electrodynamic Applications Inc.

shown in figure 4.32.

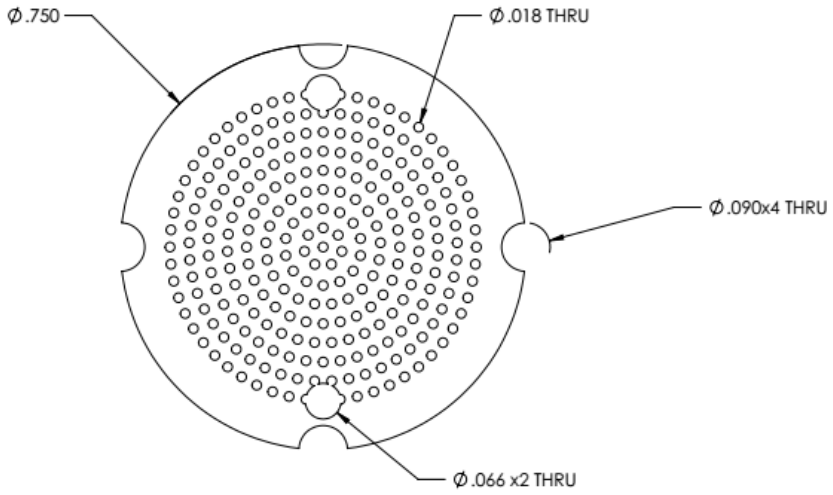

Figure 4.32: Images of the RPA grids used in this experiment. The grids are made using tantulum. Source: Electrodynamic Applications Inc.

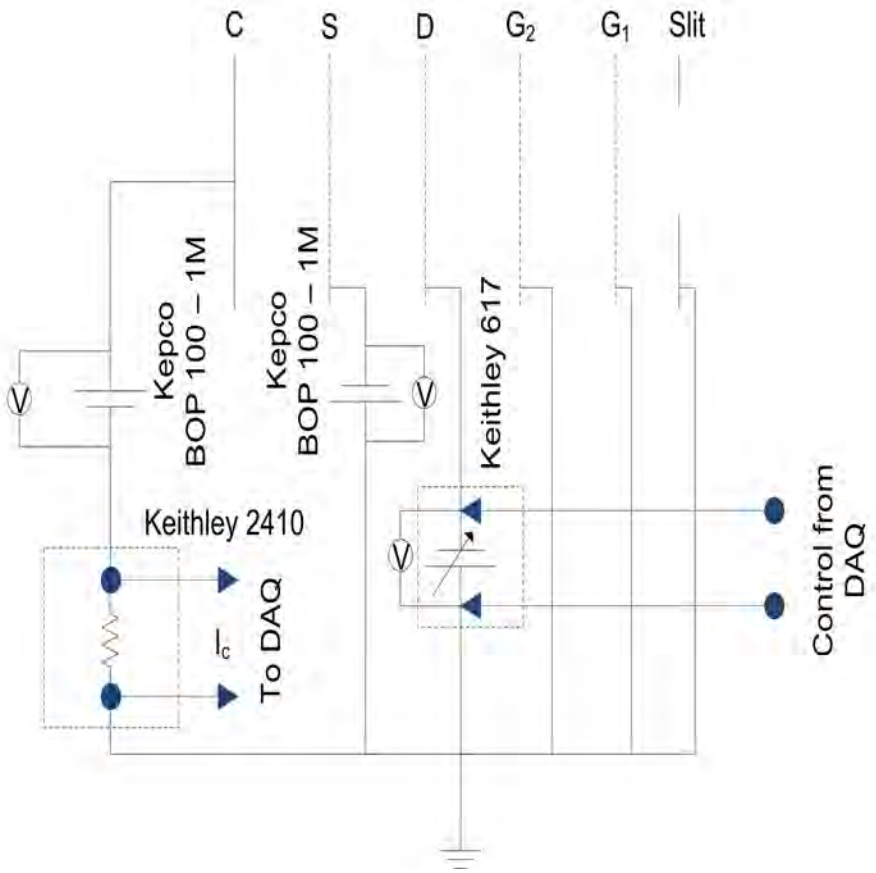

Figure 4.33: RPA circuit.

CHAPTER V

Low-Cost, Low-Energy, High-Current Electron Gun

"*Those who know no history are doomed to repeat it.*"

- George Santayana

5.1 Introduction

Low energy electron beams find application in several areas. Examples of these include electron sources for material characterization (microscopy using SEM / LEED) [161, 162, 163], material processing, lithography, electron impact cross-section measurements [164], and many more.

An electron beam is a collection of electrons moving in a direction with some average momentum. The accelerating method for these electron beams can be electrostatic (quasi-static electric fields) or electrodynamic (time-varying electromagnetic). Several electron gun designs exist in literature to produce sub-nanosecond electron pulse widths [165], glow discharge created electron beams [166], and microwave electron guns [167]. There exists a number of numerical tools that allow modeling of electron gun beams, such as SIMION and MICHELLE[168].

The total charge of a beam can be given by equation 5.1

$$Q = \sum_i q_i \tag{5.1}$$

Each particle obeys the equation of motion given by eq. 5.2

$$F = m\,a = m\frac{d\,v}{dt} = q(E\,+\,v \times B) \tag{5.2}$$

In general, the boundary where a beam can be defined as relativistic or Newtonian is poorly defined. The beam considered here does not account for relativistic effects as they are operated at or below 60 eV. The relativistic factor γ_R (Eq. 5.3) is 1 for all practical purposes at these low energies.

$$\gamma_R = \frac{1}{\sqrt{1 - \frac{v^2}{c^2}}} \tag{5.3}$$

The linear motion of a non-relativistic beam in a static homogeneous electric field (B = 0) is derived below and the distance traversed by a non-relativistic electron beam is given by equation 5.4

$$F = m\,a = m\frac{d\,v}{dt} = qE_0$$

On integration of the above equation, and setting the initial limits of v(0) = 0 m/s, we see

$$v = \frac{d\,z}{dt} = \frac{q}{m}E_0\,t$$

The distance travelled by the beam in a given time can be obtained by integrating the above equation and setting the initial limits of z(0) = 0 m.

$$z = \frac{q\,E_0}{2\,m}\,t^2$$

For an electron beam, the charge q = -e, resulting in the non-relativistic beam traverse distance during a given time.

$$z = \frac{-e\,E_0}{2\,m}\,t^2 \tag{5.4}$$

In general, electron beams have a natural tendency to spread with respect to its axis of propagation due to associated space charge in the vicinity of the beam. This transverse spread is a function of the input beam energy. Higher energy beams tend to be cylindrical (i.e., collimated) for a longer axial distance before the space charge deteriorates the beam. This par-axial approximation for particle beam suggests that in most applications the beam makes a small angle with respect to the axis such that $\cos\phi \approx 1$ and $\sin\phi \approx \phi$.

5.2 Thermionic Emission

The work function of a material is the potential barrier at a surface of a metal that prevents free electrons from leaving the surface at low temperatures. When a metal is heated to a high temperature, some of these surface electrons gain enough energy to overcome the barrier.

On application of an electric field, the electrons that are released from the surface can be taken away from the metal surface and measured using an ammeter. Electrons emitted from the filament go towards the anode in the circuit and the anode current is a function of the filament temperature.

The Richardson - Dushman law provides an estimate of the theoretical current density (j_{RD}) of electrons that escape the heated metal in a direction perpendicular to the heated surface. The total current density for the electrons at different energies is given by equation 5.5

$$j = \int q n_e(\varepsilon) v_x(\varepsilon) d\varepsilon \tag{5.5}$$

The electrons density n(ε) is given by 5.6

$$n(\varepsilon) = g(\varepsilon) f(\varepsilon) \tag{5.6}$$

Since electrons are fermions and obey the Fermi-Dirac statistics, we can give the degeneracy of states and distribution of the particles by equation 5.7 and 5.8.

$$g(\varepsilon) = \frac{8\sqrt{2}\pi}{h^3} m^{3/2} \sqrt{\varepsilon} \tag{5.7}$$

$$f(\varepsilon) = \left[1 + \exp\left(\frac{\varepsilon - E_F}{k_B T} \right) \right]^{-1} \tag{5.8}$$

Only electrons with energy $\varepsilon \gg \mathrm{E}_F$ can escape the metal, so f(ε) tends to a Boltzmann distribution (Eq. 5.9)

$$f(\varepsilon) = \exp\left(-\frac{\varepsilon - E_F}{k_B T} \right) \tag{5.9}$$

For $\varepsilon = \frac{1}{2} m_e v^2$, it can be shown that

$$n(\varepsilon) d\varepsilon = \frac{8\pi}{h^3} m^3 \exp\left(-\frac{\varepsilon - E_F}{k_B T} \right) v^2 dv$$

The work function of a material is determined by its chemical composition and the surface plane that is exposed to the surroundings. Table 5.1 lists the work function for various materials along with the constant used in the Richardson-Dushman equations.

Material	W (eV)	A_0 b(A cm^{-2} K^{-2})
Molybdenum	4.15	55
Nickel	4.61	30
Tantalum	4.12	60
Tungsten	4.54	60
Barium	2.11	60
Cesium	1.81	160
Iridium	5.40	170
Platinum	5.32	32
Rhenium	4.85	100
Thorium	3.38	70
Barium (on Tungsten)	1.56	1.5
Cesium (on Tungsten)	1.36	3.2
Thorium (on Tungsten)	2.63	3.0
(Barium Oxide + Strontium Oxide)	0.95	10^{-2}
Tantalum Carbide	3.14	0.3
Lanthanum Hexaboride (LaB_6)	2.70	29

Table 5.1: Work function for various metals along with correction factors used in Richardson-Dushman equation (A_0 is the constant in the equation and b is the correction factor for the given material [169, 170, 171].)

5.2.1 Richardson-Dushman Equation

$$j_{RD} = \frac{I_{RD}}{A} = A_0 T^2 \exp\left(\frac{-\Phi_{WF}}{k_B T}\right) \tag{5.10}$$

$$A_0 = A_R \; b$$

$$A_R = \frac{4\pi q m k_B^2}{h^3} = 120.4\text{A/cm}^2\text{K}^2$$

For tungsten the temperature of operation is typically between 2300 to 2640 K and the thermally radiated power (ξ = 0.3 - 0.4) is given by equation 5.11

$$P = A\xi\sigma T^4 \tag{5.11}$$

The total heating power experienced by the filament is given by equation 5.12

$$P_{total} = A\xi\sigma T^4 + \frac{j_{RD}A}{e(\Phi_{WF} + k_B T)} \tag{5.12}$$

The lifetime of a filament can be estimated by the evaporation rate (q) of the material given by equation 5.13

$$t_{lifetime} \approx C_1 \exp\left(\frac{-q}{k_B T}\right) \tag{5.13}$$

Filament efficiency is given by the ratio of the current density to the specific power of heating applied to maintain the filament stable operation. This is given by equation 5.14

$$\eta = \frac{j_{RD}}{P_{total}/A} \tag{5.14}$$

With increasing temperature of the filament, the current emission increases as well as the efficiency. However, the lifetime of the filament decreases significantly.

5.2.1.1 Determining Thermionic Properties

Estimation of an approximate electron current can be obtained using the Richardson - Dushman equation for a known filament length (and thus its surface area).

The heat energy released by the filament is given by the Joule equation (eq. 5.15),

$$Q \propto RI^2t \tag{5.15}$$

The resistance changes with temperature and is expressed by ($R = R_0 + \alpha T$) where R_0 is filament resistance at room temperature.

In the presence of an electric field to accelerate the electrons out of the heated metal, the Richardson-Dushman equation (eq. 5.10) becomes the Fowler-Nadhein-Bethe-Sommerfield formula given by equation 5.16

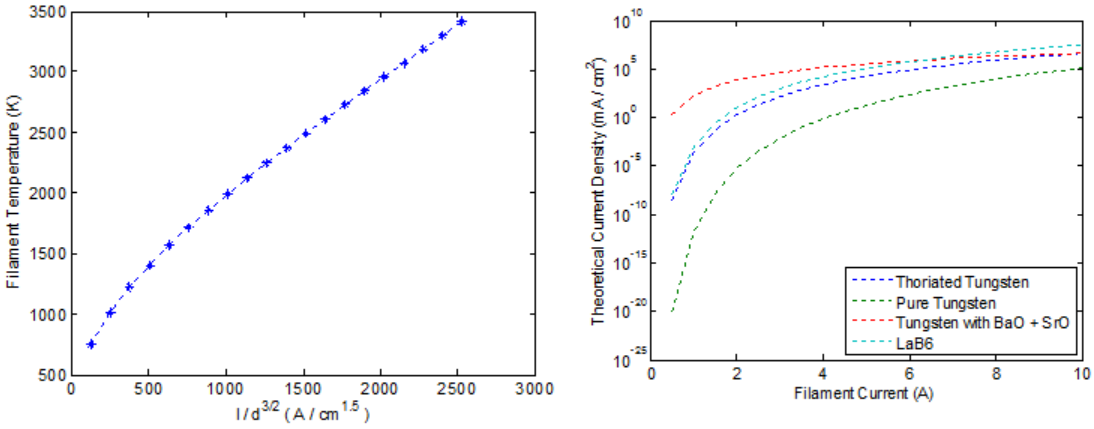

Figure 5.1: Determination of temperature of a filament and comparison of emission current from different materials.

$$j_{RD} = \frac{I_{RD}}{A} = A_0 T^2 \exp\left(\frac{-\left[\Phi_{WF} - \left(\frac{q^2 E_0}{\varepsilon_0}\right)\right]}{k_B T}\right) \tag{5.16}$$

From the data of Jones and Langmuir, determining the temperature for tungsten wire at a given current is possible using equation 5.17. This equation is valid for 400 $<$ T $<$ 3000 K.

$$T_I = 117 + 56\sqrt{a} + 0.00036\, a^{1.8} \tag{5.17}$$

where a = I / $d^{3/2}$. Figure 5.1 shows the filament temperature for an applied current. It also shows the advantage of using thoriated tungsten over pure tungsten wire as to acheive a higher current density for the same power, thus allowing longer lifetime at a given emission level.

5.2.2 Cathode Coatings

From Richardson Dushman equation (5.10) it is clear that the current emission from a cathode surface is directly related to the work function of the emitting surface. The higher the work function, the lower the emission and vice versa. Thus it is

beneficial add surface coatings to the base metals in order to reduce its work function.

Oxide coatings reduce the work function of the base metal and enhance thermionic emission. Details of oxide coating for thermionic applications can be found in Ref. [172]. Addition of compound layers of barium, strontium and oxygen on tungsten has been shown to reduce the work function significantly than that of the pure refractory metal. Thus the same emission can be obtained at lower temperatures with oxide coatings. This improves both the life time and stability of the cathode. Table 5.1 lists the various work functions of different coatings on its base metal.

When a tungsten filament is immersed in a barium carbonate solution, the following reaction occurs

$$3\,BaCO_3 + W \longrightarrow Ba_3WO_6 + 3\,CO$$

The person credited with the discovery of the oxide coating on cathode is Wehnelt [173]. It is shown from x-ray studies that the alkali metal oxides used to coat a base metal form single crystals with a lattice spacing that satisfies the Vegard's approximation[§].

In general, for an oxide coated cathode, the electron emission current of the cathode is proportional to the conductivity of the oxide layer. From semiconductor theory (with X as the electron affinity of the semiconductor), this relationship can be expressed by equation 5.18

$$\frac{j_0}{\sigma} = \frac{3(1-r)k_BT}{4e\lambda_{mfp}} \exp\left(\frac{-X}{k_BT}\right) \tag{5.18}$$

Tungsten like most materials does have lattice defects and these can be divided into four types - point defects, line defects, plane defects and volume defects. The

[§]Vegard's approximation states that unit cell parameters should vary linearly with composition for a continuous substitutional solid solution in which atoms or ions that substitute for each other are randomly distributed. The empirical law lacks a sound theoretical foundation and with known experimental deviations, suggests that it is only an approximation. For details on a thermodynamic analysis of the Vegard's law refer [174]

concentration of these defects depend on the state of the material (deformation) as well as the temperature it is exposed to and presence of impurities. The defects can result in alteration of electrical and mechanical properties of the cathode material. This causes pre-mature failure of filaments.

5.3 Experimental Setup

A low energy, high current electron gun is used as a source of primary electrons. The electron gun body and flanges were designed and constructed using stainless steel (SS-316). The 2.54 cm diameter electron beam source has been tested with several grids of transparencies ranging from approximately 18% open area fraction (OAF) to approximately 79% OAF. The emitting filament is made from a thoriated tungsten (1-Th-99-W) and tested in both a bare (uncoated) configuration as well as a coated configuration using a barium-strontium-calcium carbonate [(Ba-Sr-Ca)CO3 56-31-13%] solution. The coated filaments provided inconsistent results. This could be due to an inconsistent coating of the filament as the solution used was not electrolytically transferred but the filament was just dipped a few times. Another reason for the inconsistent performance could be due to cathode poisoning at the operational conditions. The bare filament performed consistently and was used in all tests to study SEE-plasma interactions. Figure 5.2 shows the electron gun with a high transparency grid along with its 3D model.

The electron gun was built to allow additional grid to shape the beam as an expansion for future projects. An exploded view of the electron gun is shown in figure 5.3 containing multiple grids. In this work, however, only a single accelerating grid is used.

Figure 5.2: Figure shows an electron gun with high transparency grid used for SEE tests along with a 3D model.

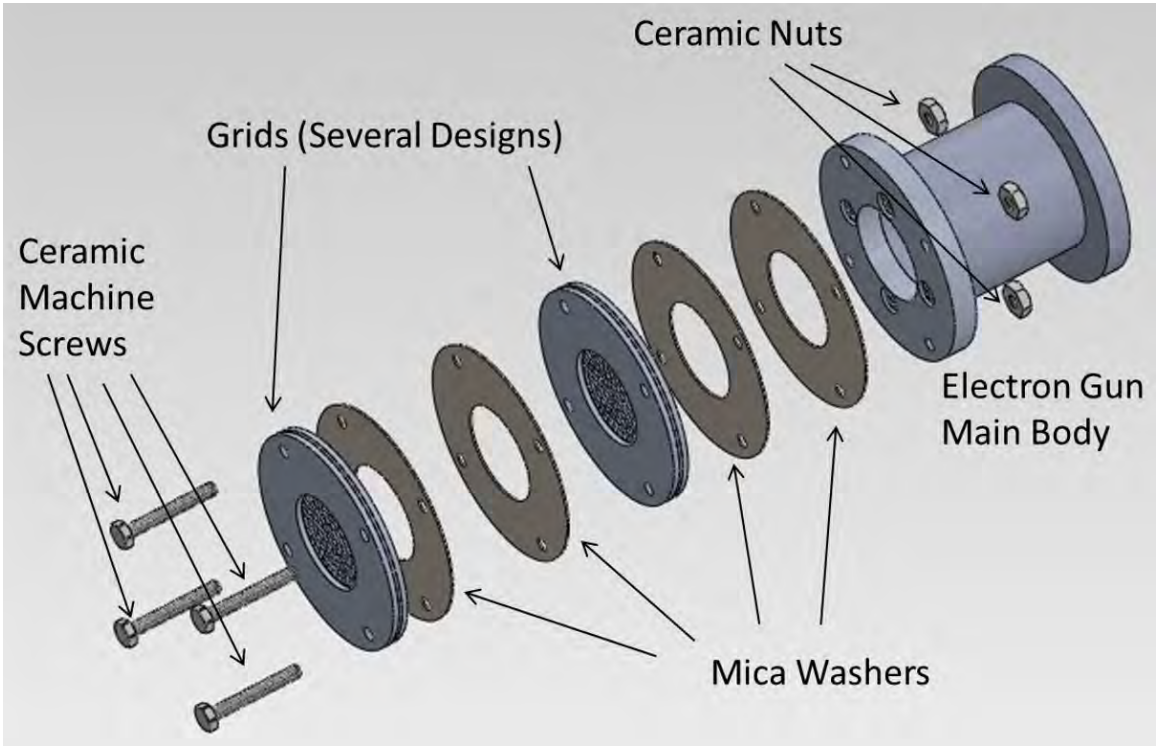

Figure 5.3: Exploded view of the electron gun.

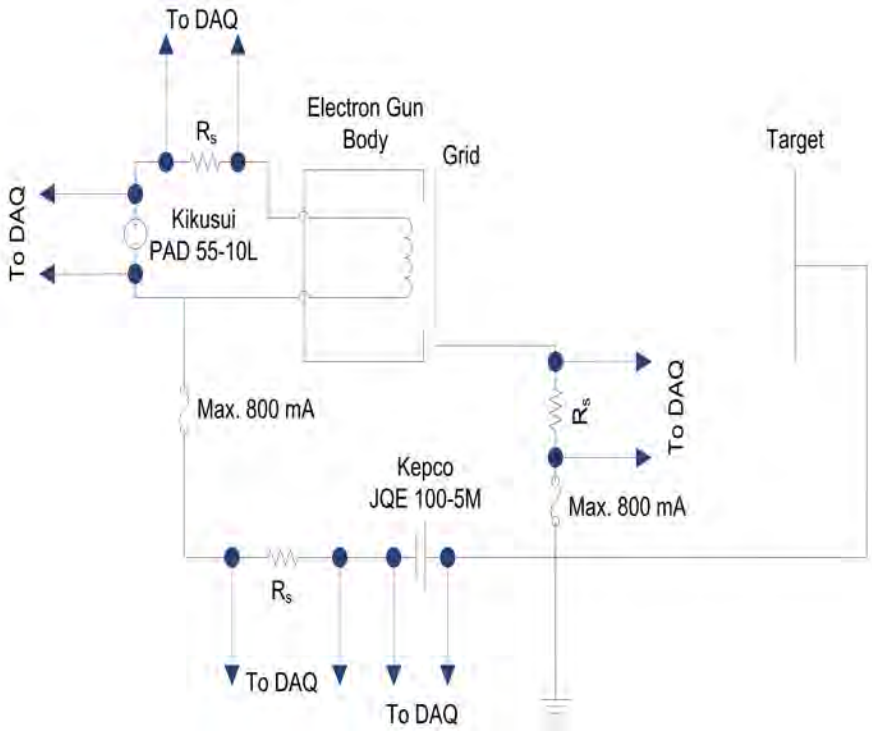

Figure 5.4: Circuit diagram showing the operation of the low energy high current electron gun.

5.3.1 Electrical Circuit for the Electron Gun

The electron gun was operated using a constant current source and the beam accelerated using a voltage source towards the target. Based on several tests it was deemed that for a 2.3 mm diameter thoriated tungsten wire (1/99 - Th/W), a current between 6.5 A to 7 A provided the longest life. For the purpose of this experiment, currents $\approx$ 1 mA to 10 mA were desirable in the range of 10 eV - 80 eV beam voltage which was consistently obtained at 6.5 A filament current. The total power supplied was between 65 and 72 W. Figure 5.4 shows the electrical circuit for the electron gun.

It is important to note that the electron beam source is grounded as it forces the target holder to attain the same potential as other structural members around the target holder. Also, it allows the conducting materials tested in this thesis to be grounded, as opposed to floating bodies. A floating body as discussed acts as an insulator whereas grounded targets provide a pathway for the excess electrons being

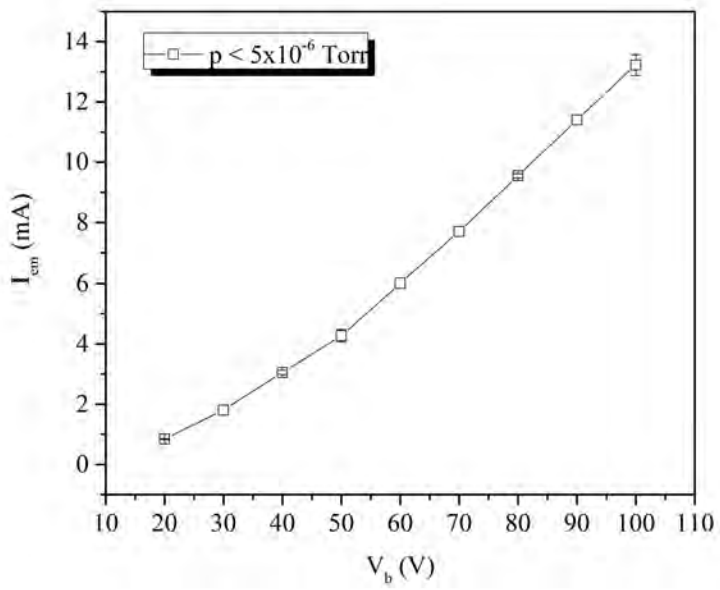

Figure 5.5: Emission current of electron gun in vacuum.

pumped into the target.

5.4 Electron Beam Characterization in Vacuum

The electron gun was characterized initially under vacuum (p $<$ 5x10^{-6} Torr). Figure 5.5 shows the emission current from the gun at a given operational voltage. Some portion of the beam is lost to the grid as the OAF is $\approx 50\%$. The ratio of the emission current to the current lost at the grid is shown in figure 5.6.

5.4.1 Beam Perveance

The perveance of the beam is a measure of the influence of space-charge on the quality of the beam and is defined by equation 5.19

$$P = \frac{J}{V^{3/2}} = \frac{4}{9}\varepsilon_0\sqrt{\frac{2\,e}{m_e}}\frac{1}{d^2} \tag{5.19}$$

The perveance of the electron gun is very high ($\gg 1\ \mu$ perv) and as a result can

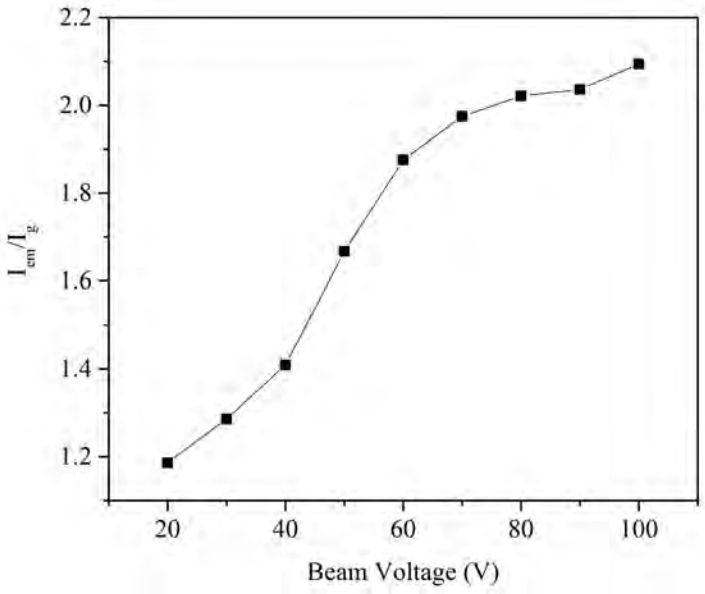

Figure 5.6: Ratio of emission current to grid current in vacuum operation.

cause strong field perturbations. Compensating electrodes were not employed in this study, but the design of the electron gun provides ability to add compensation grids easily. Figure 5.7 shows the perveance of the beam at different voltages and compares it to the theoretical values at gap distances of 3.175 mm, 6.35 mm, and 9.525 mm. The actual gap distance is $\approx$ 7 mm.

5.4.2 Spatial Profile of Beam

The beam profile is mapped out using an electrostatic probe mounted on the Velmex motion control system. The probe consists of a SS 316 cylinder of diameter $\approx$ 2.5 mm and length $\approx$ 1.5 mm. The probe maps out a 3D profile of the electron beam at different beam voltages. The axis of the electron gun was defined as the starting point and measurements are made end to end in both x and y directions from the center to 25 mm on each side. This is done at axial separations of 12.7 mm till the probe reacheed 63.5 mm from the surface of the electron gun grid. Figure 5.8 shows the profile at the plane of the target ($\approx$ 50.8 mm from the electron gun grid)

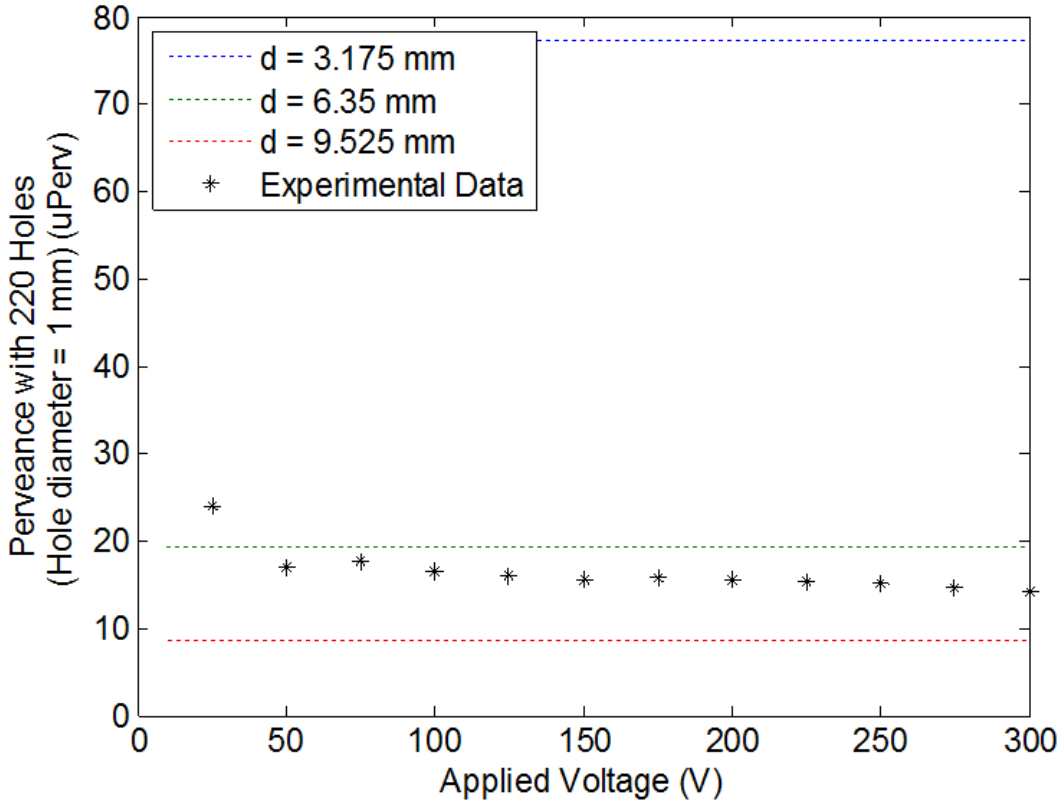

Figure 5.7: Theoretical and experimental beam perveance for the electron gun.

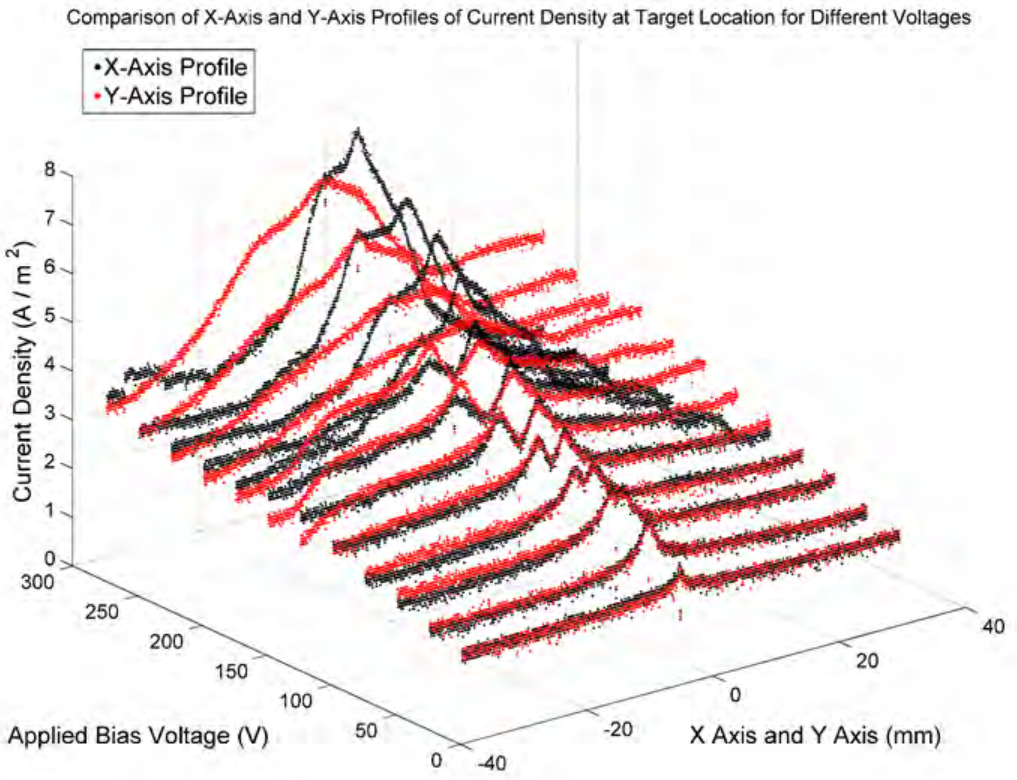

Figure 5.8: Current density of the electron beam at the target plane for different beam voltages.

at different beam voltages.

For the range of interest in this experiment, i.e., between 20 eV and 80 eV, the beam shape is a reproducible Gaussian profile. However, with increasing beam energy further, it is seen to deviate from the Gaussian profile to intially having a wing like pattern. At very large voltages, the beam is completely chaotic and doesn't possess any structure. The reason for these shifts from a nice profile may be due to one of the following reasons - At higher beam voltages the electric field locally distorts to produce different beam patterns [175], the filament tends to warp due to thermal expansion [176], or it could be due to 2-D Child - Langmuir effects [177].

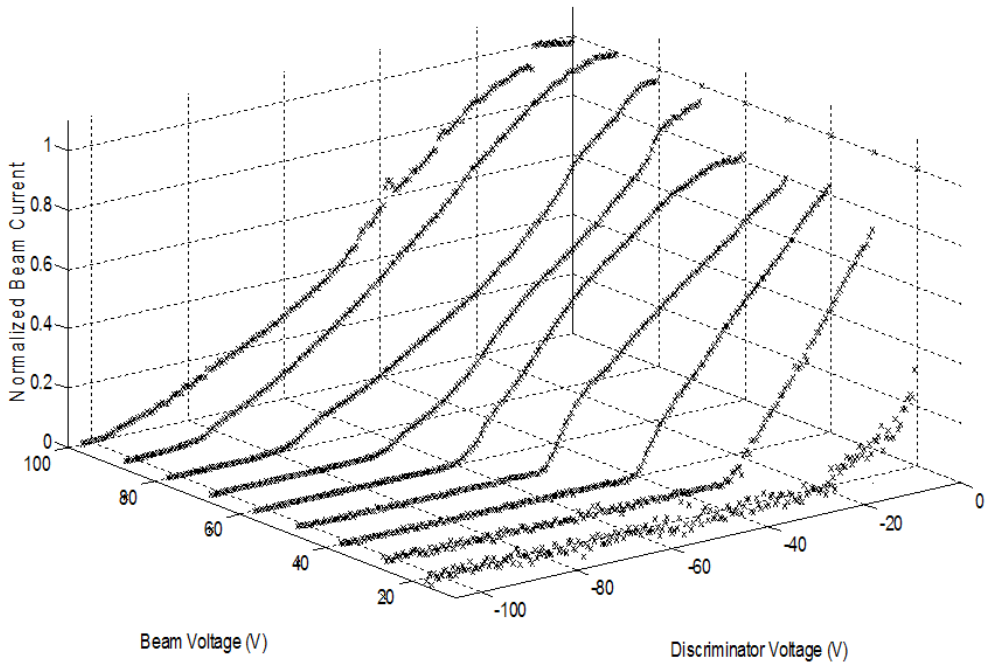

Figure 5.9: Electron gun energy map obtained using a RPA in vacuum.

5.4.3 Beam Energy Characteristics using RPA

The RPA described in section 4.3 was used to map the energy of electron beam. Figure 5.9 shows the normalized current distribution collected by the Faraday cup of the RPA.

It is seen from figure 5.9 that the discriminator successfully blocks beams with a certain energy depending on the beam energy. Differentiating these data provides information on the energy distribution. In order to get smooth profiles after the derivative of the current is taken with respect to voltage, a Savitsky-Golay filtering technique was employed with polynomial of order 2 and number of points considered varying between 10 - 30. The results are shown in figure 5.10. The beam has a wide spread of energy and is expected as there are no compensating electrodes to help shape the beam profile or enhance energy confinement. The profiles between 20 V and 60 V is of interest to this experiment and the profiles show similarity with a much better peak when compared to higher voltage cases which has a spread.

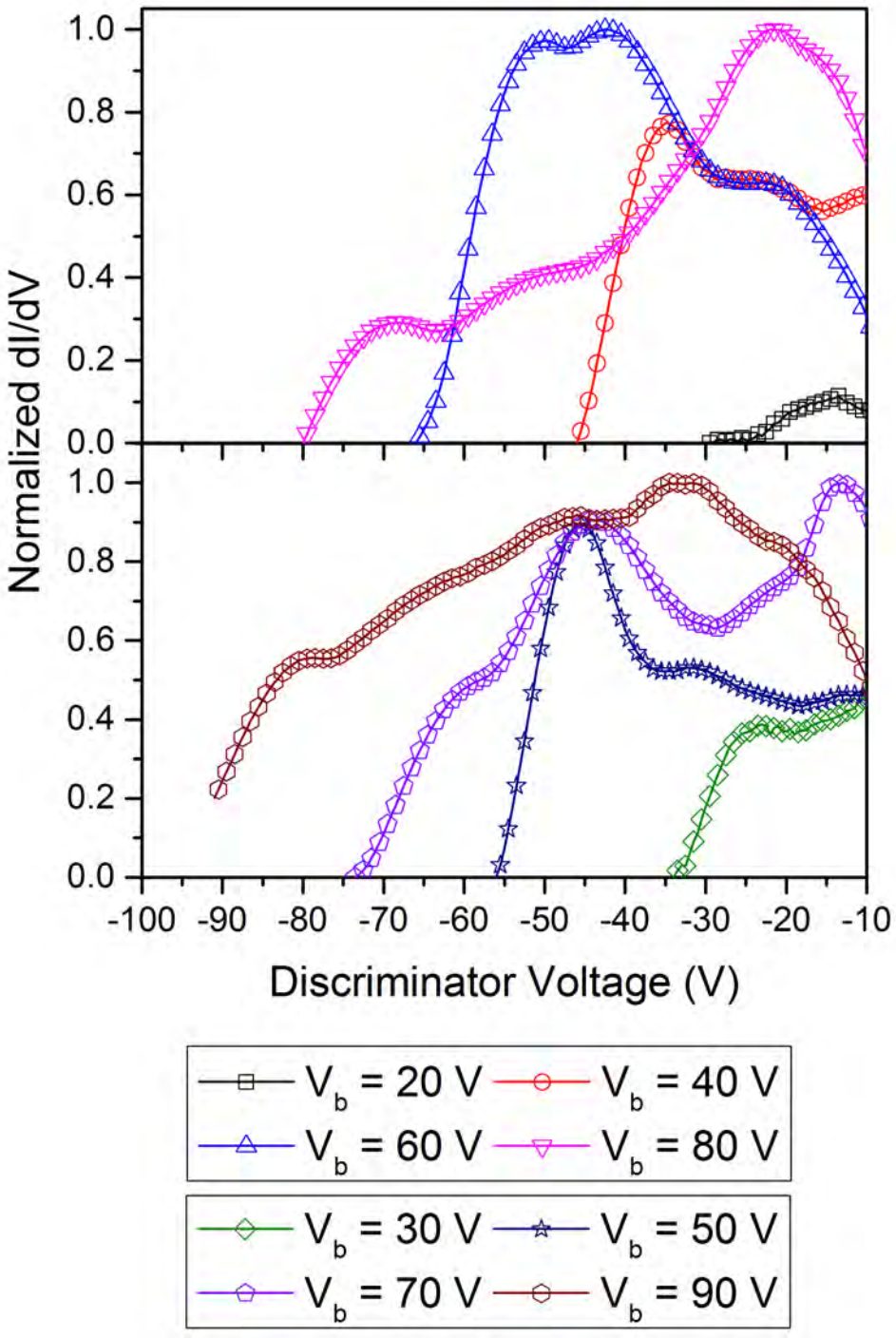

Figure 5.10: Normalized first derivative of RPA data in vacuum.

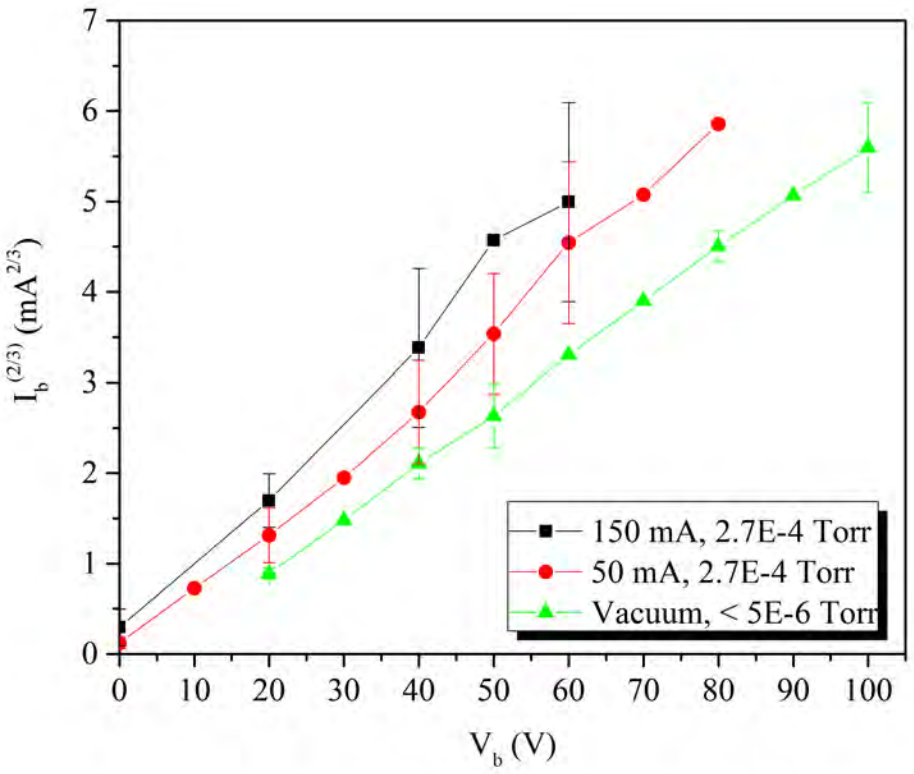

Figure 5.11: Emission current of electron gun in plasma.

5.5 Electron Beam Operation in Plasma

The operation of electron beam in plasma increases the emission current. Figure 5.11 shows the emission current from the electron gun in plasma. As expected the plot of $I^{2/3}$ and V is a straight line for the electron beam in plasma indicating the operation in space charge limit.

5.5.1 Beam Energy Characterization using RPA

Figure 5.12 shows the energy distribution of the electrons in plasma. The pressure is 2.7x10^{-4} Torr and the discharge current is 50 mA. Similar curves are obtained for higher discharge currents and pressure.

Figure 5.13 compares the energy distribution of electrons for different discharge

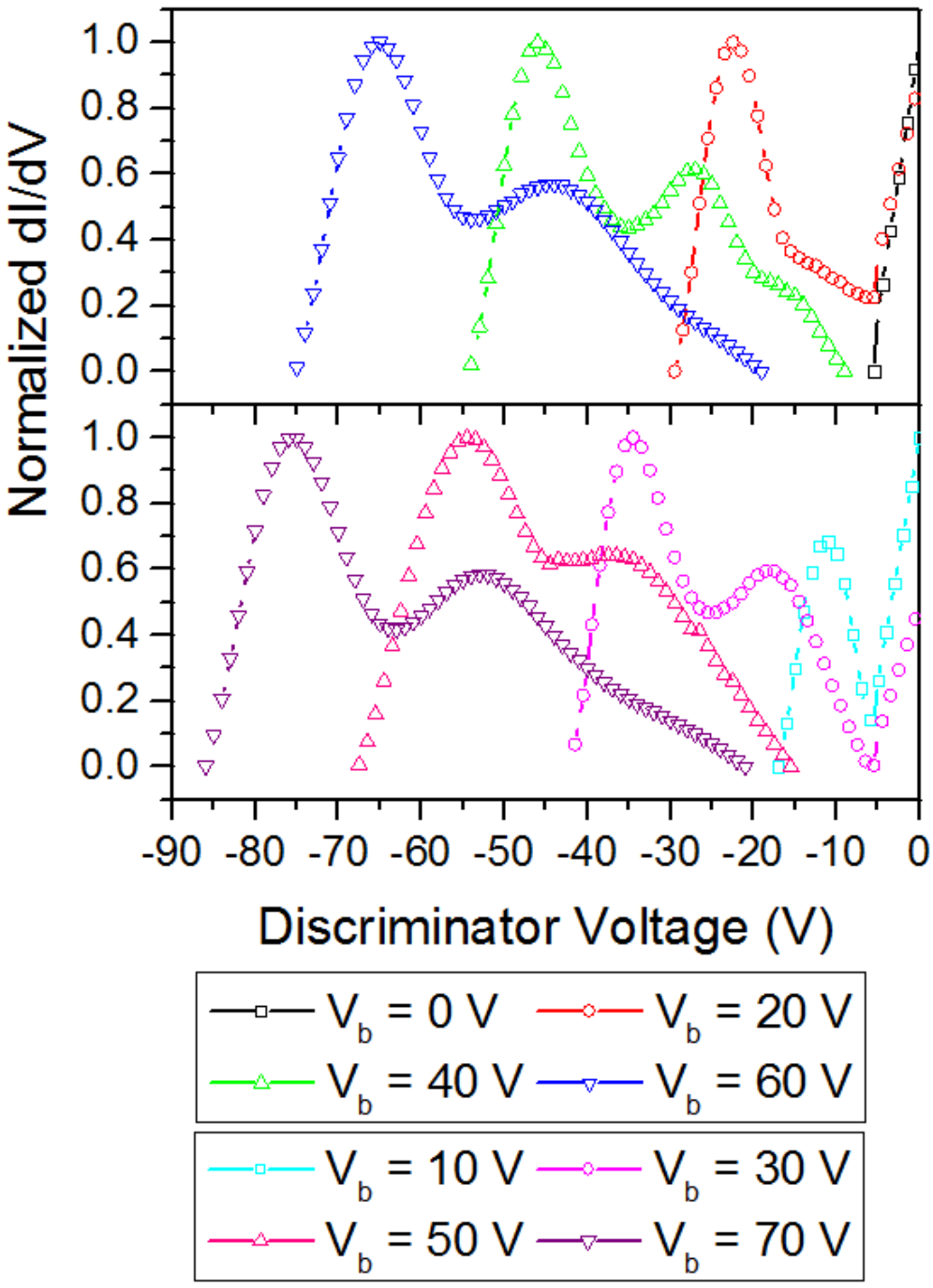

Figure 5.12: Normalized first derivative of RPA data in plasma at pressure of 2.7e-4 Torr and discharge current of 50 mA.

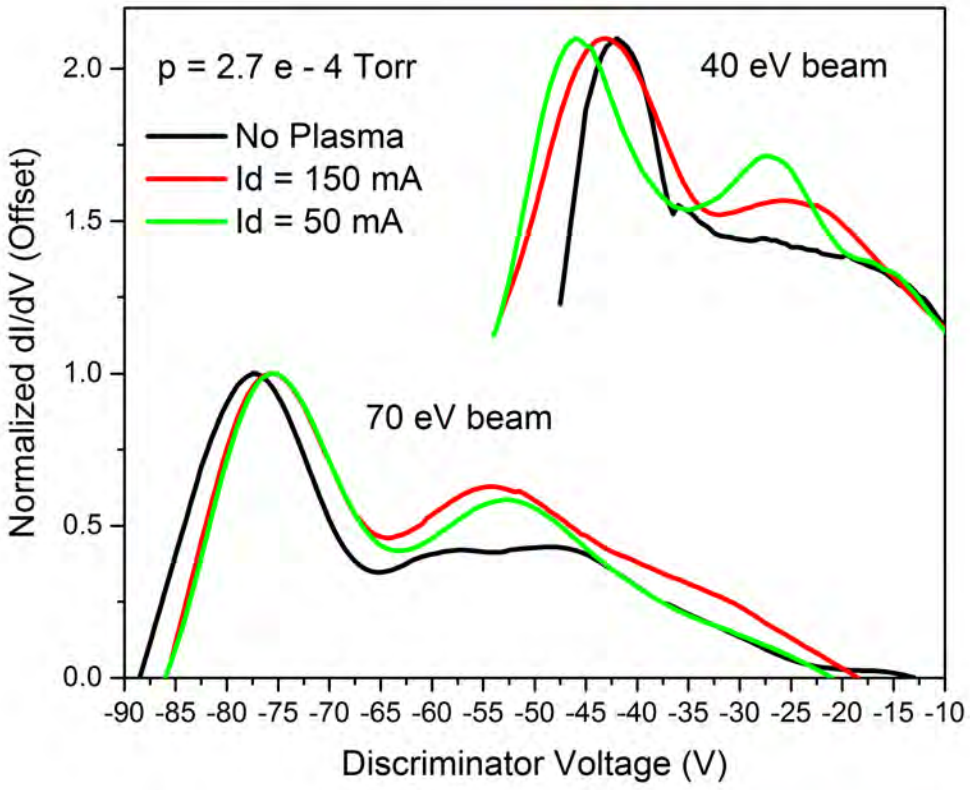

Figure 5.13: Comparison of the energy distribution of electron beam in plasma at different discharge currents. Representative examples of 40 eV and 70 eV beams used to demonstrate the effect of plasma on plasma operation. The two cases are offset to be placed on the same graph but are normalized from 0 to 1.

currents as well as in the absence of plasma but at a higher gas pressure. The normalized distribution is not corrected as in the previous cases.

The presence of multiple humps (in this case, a double peaked distribution) can result in instabilities. Instabilities in plasma beam interactions are not uncommon and have been studied extensively [178]. Getty and Smullin [179] showed that a beam-plasma discharge system can result in an rf discharge in which the interaction generates an rf field. In general, for a double humped distribution, it is possible to easily determine the stability of the beam-plasma system using the Penrose criterion. The Penrose criterion states that a double peaked distribution is unstable if and only

if equation 5.20 is satisfied.

$$\int_{-\infty}^{\infty} \frac{F(u_0) - F(u)}{(u - u_0)^2} < 0 \tag{5.20}$$

The implications of the Penrose criteria are the following:

- Any void space in a distribution with multiple bumps would imply the distribution is unstable.
- Unstable distributions cannot be stabilized easily by adding particles with the velocity u_0.
- A distribution having multiple bumps may still be a stable system.

On application of the Penrose criterion to all the distributions, it was found that the beam-plasma system was marginally unstable for all bias voltages.

5.6 Electron Beam Characterization in a Uniform Magnetic Field in Vacuum

The application of magnetic field tends to trap the charged particle in a gyro-orbit. In principle, increasing magnetic fields should increase the current at the target. Figure 5.14 shows the result of magnetic field on the beam current leaving the electron gun. The two-thirds law still holds as expected, however, the current is seen to decrease with increasing magnetic field. This is due to the fact that the OAF for these test is ≈ 50 %. This suggests that magnetic field collimates the beam enough that a greater percentage of the beam hits the webbing of the grid and is lost to the grid before making it out to the target.

Figure 5.15 shows the ratio of emission current to grid current in the presence of magnetic field.

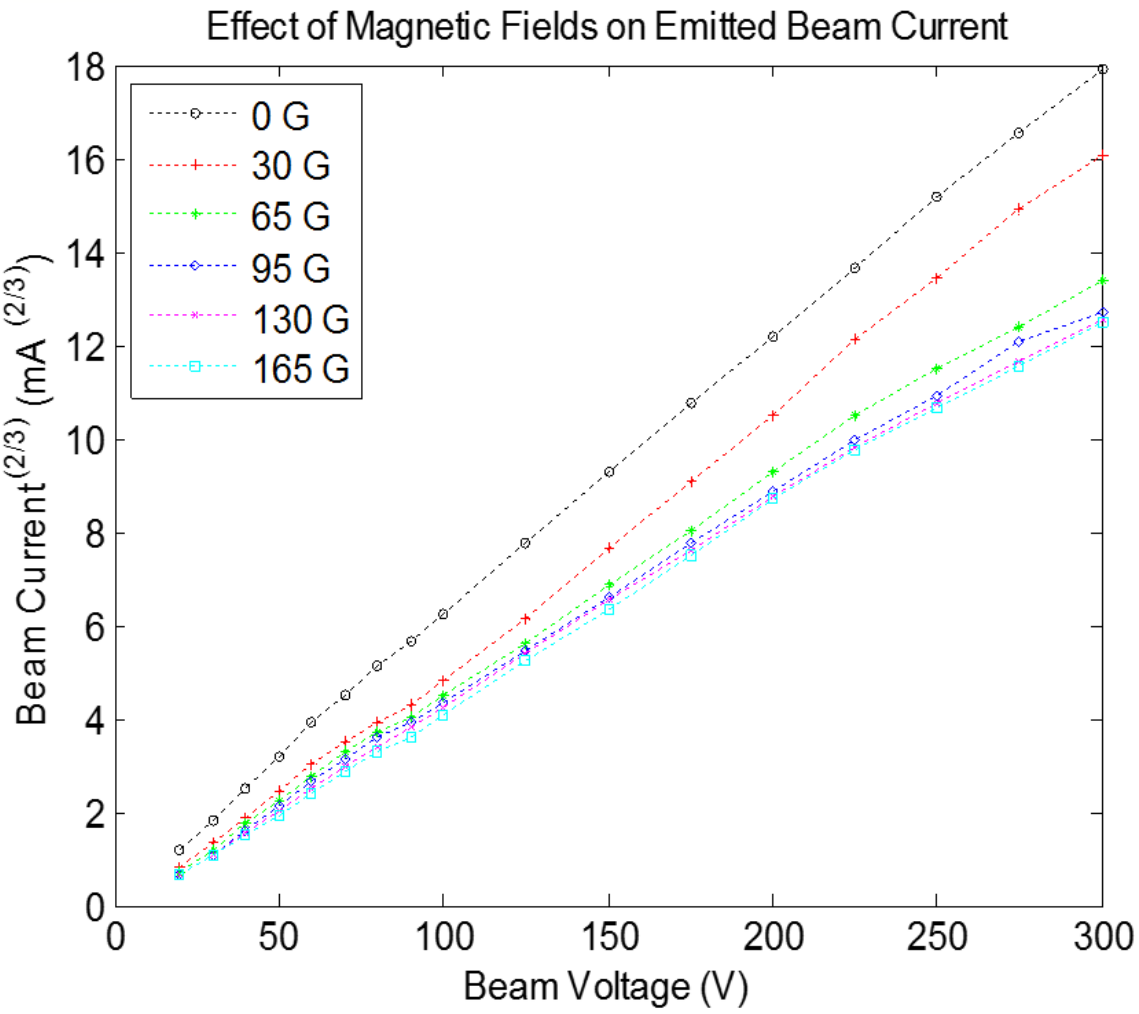

Figure 5.14: Effect of magnetic field on electron beam.

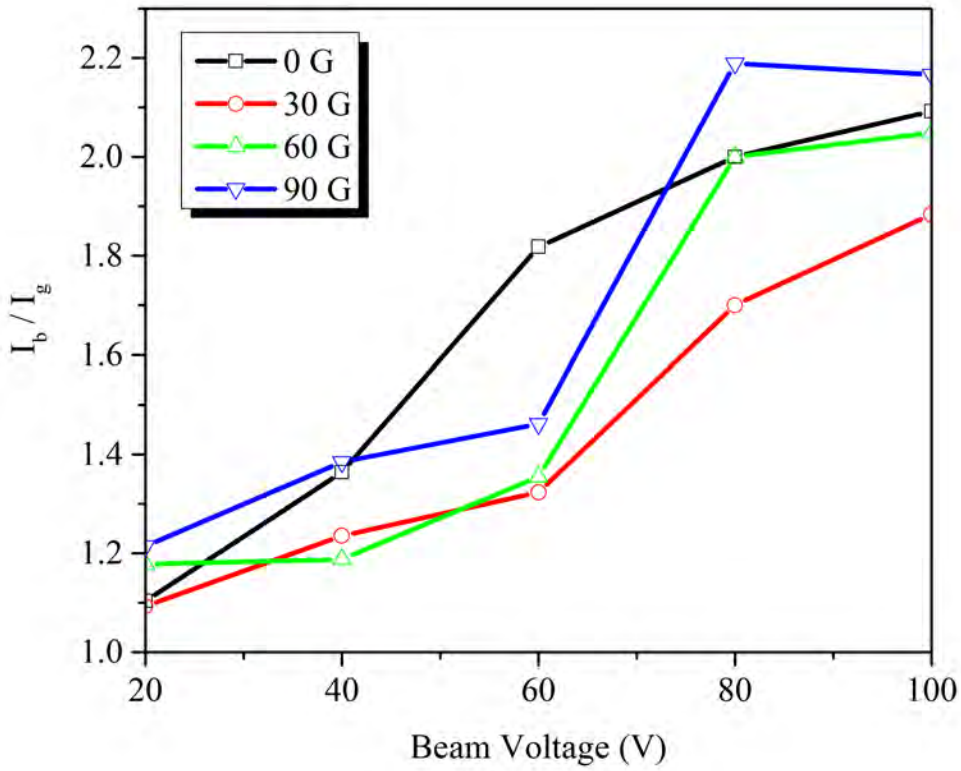

Figure 5.15: Ratio of emission current to grid current in presence of magnetic fields.

In order to reduce the influence of magnetic field within the electron gun, a layer of μ-metal is placed on top of the electron gun body as well as on the magnetic field spools.

CHAPTER VI

Results and Discussion

"If a scientist is not befuddled by what they're looking at, then they're not a research scientist."

- Neil deGrasse Tyson

The goal of this experiment was to understand how SEE effects plasma properties and sheath behavior. The theoretical basis for the work was discussed in chapter II. This chapter discusses the discharge properties of the plasma in presence of an electron beam on 3 targets - graphite, copper and HP grade BN. In chapter III the experimental layout was discussed. There are many parameters that impact the SEE yield in vacuum and may have an impact on the plasma as well. While the experiment is designed to be capable of studying the influence of several parameters, in this chapter the parameter of focus is the electron beam energy. The construction, operation and characterization of the electron gun is discussed in chapter V. A simplified configuration of the experimental study discussed in this chapter is shown in figure 6.1.

6.1 Discharge Characterization

One of the goals of the study is to have the ability to probe the plasma sheath using emissive probes to assess the sheath response. In order interrogate the sheath,

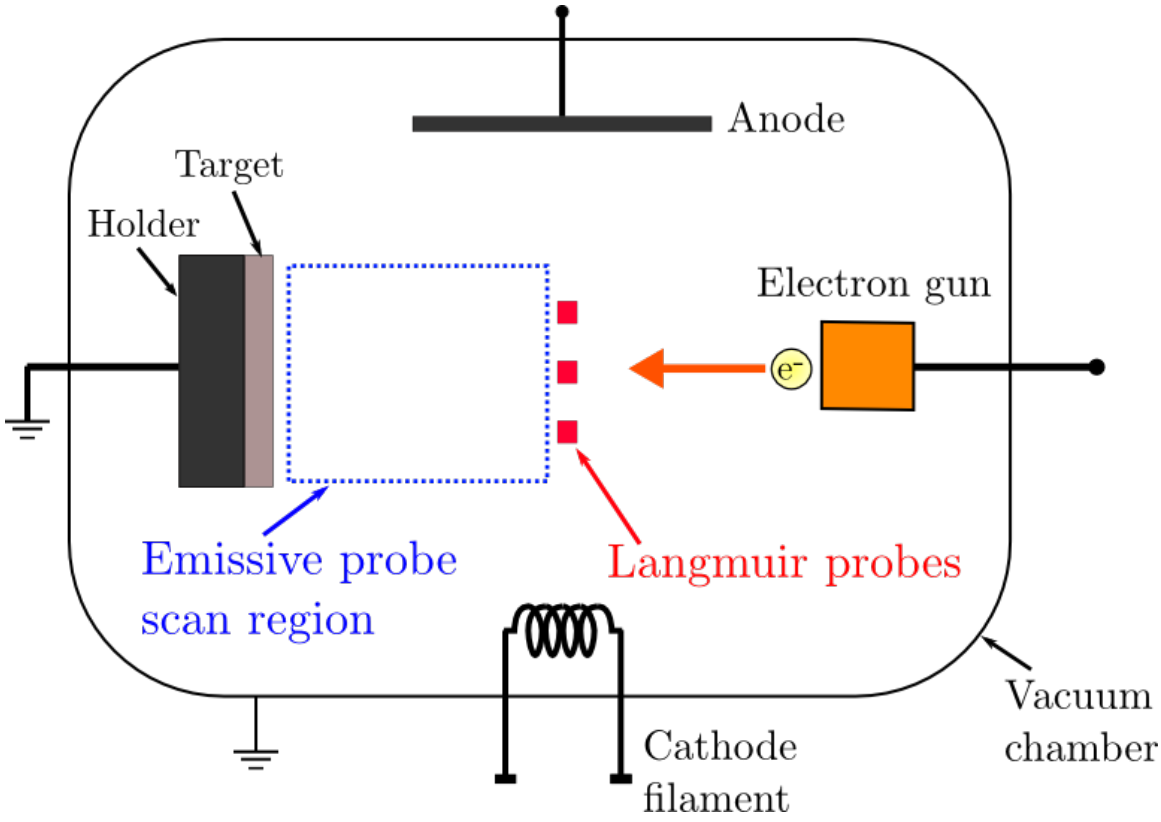

Figure 6.1: A simplified schematic of the experimental test-bed and diagnostics for measuring sheath profile and EEDF. The target is either copper, BN (HP grade), or graphite. The anode is copper and the filaments used in both plasma generation and electron beam generation are made using thoriated tungsten.

a reasonably low density plasma is desirable such that the Debye length is large. To obtain such low density plasmas, a low pressure environments and low discharge currents are desirable. To enable that, all experiments carried out in this study operated at either a filament discharge current of 50 mA or 150 mA and at pressures $2.7\text{x}10^{-4}$ Torr or $4.4\text{x}10^{-4}$ Torr.

The material targets under investigation had a noticeable effect on the discharge voltage. Figure 6.2 shows the discharge characteristics of different materials at pressure of $2.7\text{x}10^{-4}$ Torr operated at different discharge currents. The presence of an insulator (BN) in the system requires a larger voltage to sustain plasma as opposed to the conductors. Among the conductors graphite had lower operational voltage compared to copper. All these could be attributed to the SEE effects of the materials due to the plasma discharge.

The discharge behavior was fairly consistent during each experiment with a small drift over time. The maximum drift observed was $\approx$ 10 V at the higher discharge current mode. In order to ensure repeatability, tests were repeated by cycling different materials. Figure 6.3 shows the behavior of copper operated at the same pressure at a discharge current of 150 mA. Similar characteristics were obtained for BN operated at different discharge currents as shown in figure 6.4.

As seen from the figures, the discharge voltage is fairly consistent for the given electron beam voltage irrespective of the material being investigated. While the operation voltage was reproducible, there exist a small hysteresis effect as expected in plasma systems. This small change in discharge voltage maybe attributed to changing environments between successive runs. Noticeable is the evolution of both the materials being investigated and the anode surface. The pristine materials first tested tend to have different layers of particulate deposition. The quality of the surface post test is discussed in section 6.5.

The evolution of the anode surface, however, did impact the breakdown voltage.

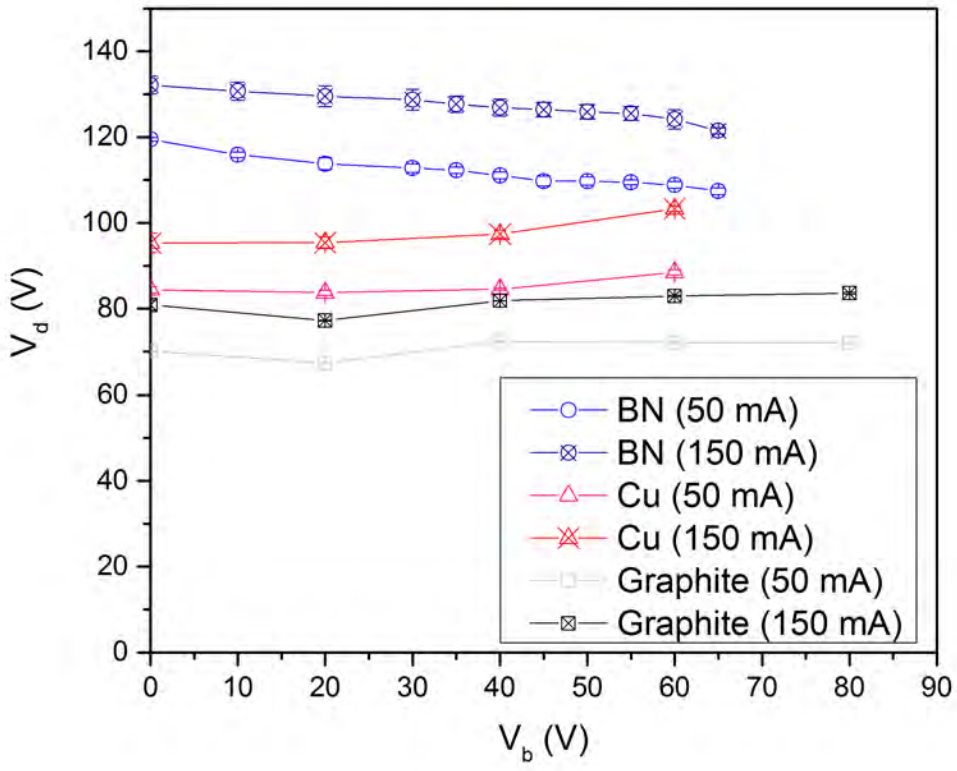

Figure 6.2: Plasma discharge characterization of different materials

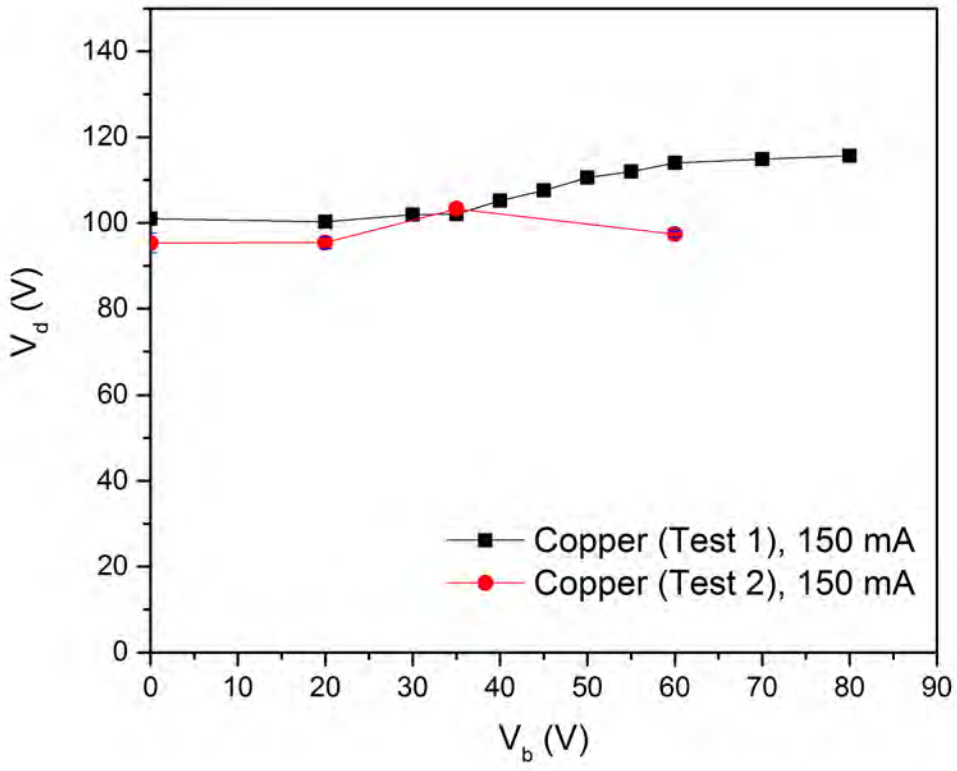

Figure 6.3: Plasma discharge characterization of copper at 150 mA

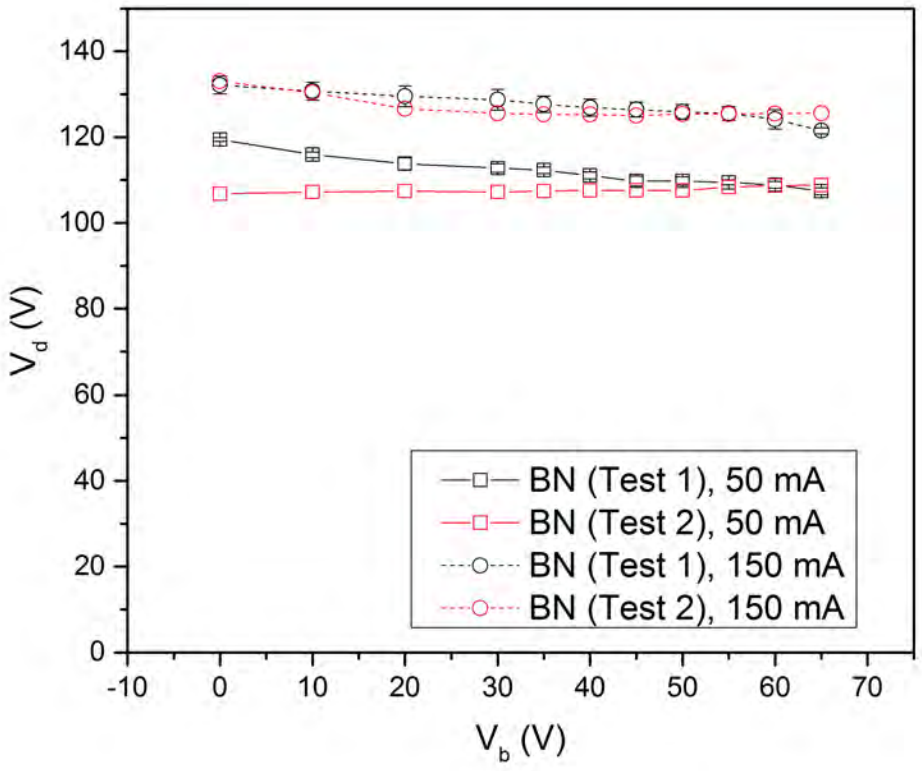

Figure 6.4: Plasma discharge characterization of BN at different discharge currents

It was observed that the voltage required to first ignite the plasma tended to increase between successive tests and was not consistent. The exact breakdown values were not recorded due to difficulty in ensuring repeatable filament power (and primary emission current from plasma filament). The filaments were made using the same procedure but due to material variations they had a small power variation under different tests.

When operated at higher pressures, the discharge voltage for all materials was reduced. This is expected as with increasing pressure the mean free path are smaller, thus the ionization frequency increases and under these conditions the discharge power for fixed discharge currents also decreases.

The discharge supply circuit shown in figure 3.13 was intentionally not grounded. This was done to enable the low discharge current operation as every structural component including the chamber was grounded. Such floating systems are possible at the voltages for this system and power supplies were chosen which can allow the system to float at such voltages. In order to assess whether the plasma was drifting significantly, the anode voltage was measured with respect to ground. It was observed that the anode-to-ground potential was only 0.5 V higher than the discharge voltage for all operating conditions.

6.2 Presence of SEE

Every experiment left a characteristic signature indicating the presence of secondary electrons from the beam - target interaction. The most direct indication of this was by measuring the collected current at the target using an ammeter.

In presence of a plasma, the target potential is negative with respect to the plasma potential and any secondary electron produced at the surface gets accelerated out of the sheath into the plasma. This would be seen on the ammeter as difference between the current entering the target and the current leaving the target. However, under

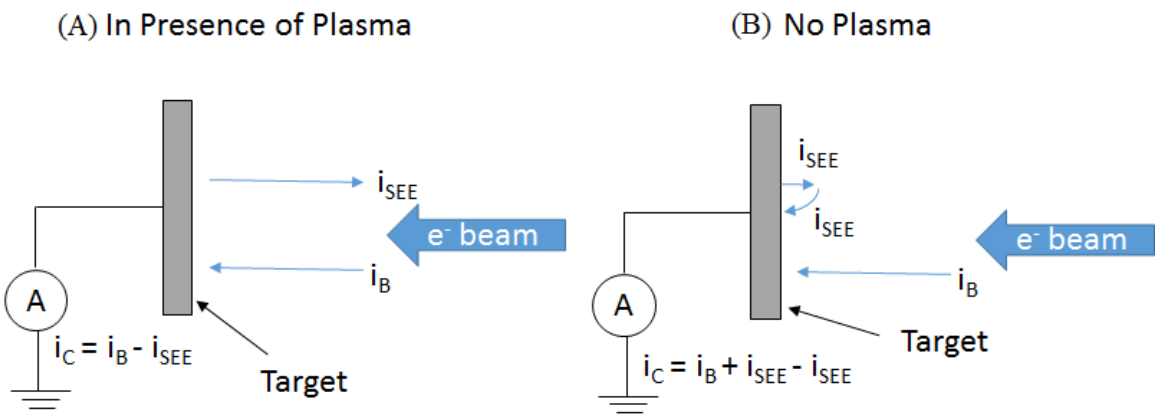

Figure 6.5: Detection of the presence of SEE in the system. (A) Current collected by an ammeter in presence of a plasma, and (B) Current collected by an ammeter in absence of plasma.

vacuum conditions, when sufficiently large beam voltage is applied, the secondary electrons produced at the target surface would experience a negative potential and would be forced to return back into the target. This would result in only the beam current being recorded by the ammeter. Beam current is directly related to beam voltage as seen in Chapter V. Since, in vacuum the only contributing factor is the beam current, the results expected would be very different from those in plasma. Figure 6.5 explains the collection of current graphically.

From the experiments conducted, it was observed consistently that in presence of the plasma, the collected current would rise with increasing beam voltage to a certain maximum before dropping below. This maximum roughly corresponds to the point where SEE yield is ≈ 1.00. Figure 6.6 shows the collected current by a copper target in presence and absence of plasma. At 50 mA and 150 mA discharge current at $2.4\text{x}10^{-4}$ torr, it is observed that the collected current increases with increasing beam voltage and reaches a maximum before dropping down again. This is because when the SEE yield coefficient crosses the first cross-over point, the number of secondaries produced per incident primary is greater than 1.00 and as a result the collected current decreases. The tests were carried out to ≈ 90 V, but further increase would

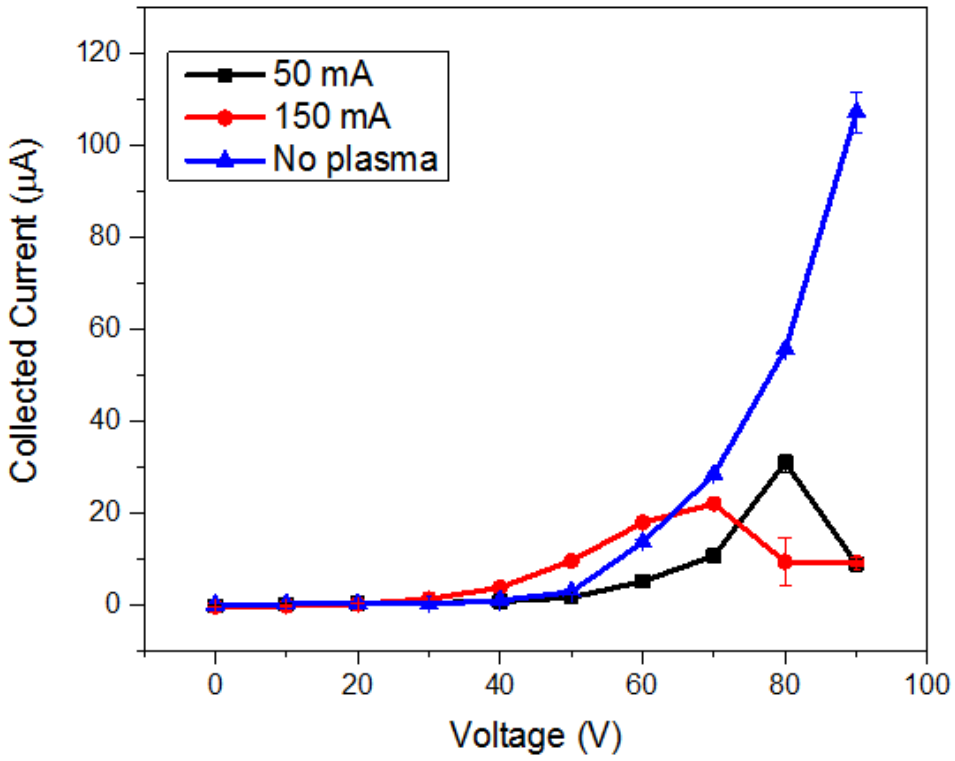

Figure 6.6: Current collected at the target in presence and absence of plasma and an electron beam.

have resulted in increasing collected currents as the SEE yield would start dropping. In contract, in the absence of plasma, the secondary electrons produced at the surface are pushed back due to a large negative current. The behavior of this curve is very similar to space-charge limit current curves seen in Chapter V. The minor deviation maybe due to ionization events due to the energetic electron beams at higher beam voltages.

6.3 Sheath Behavior in Presence of SEE

The sheath measurements were conducted using the floating point method with an emissive probe as discussed in section 4.2. The spatial resolution of these probes

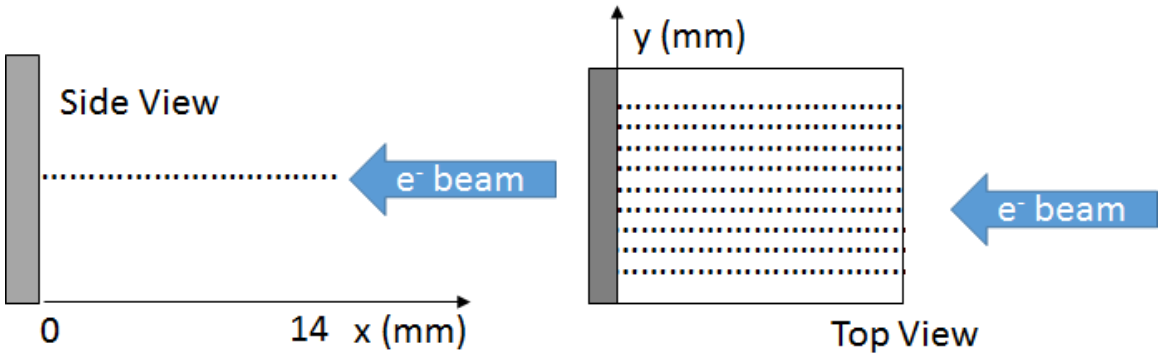

Figure 6.7: Top view and side view of the emissive probe path. The axial motion comprised of 250 μm steps from the wall surface to 14 mm in the direction towards the electron gun. 9 measurements were made at intervals of 3 mm each along the target surface.

is approximately the size of the probe loop. This leads to an uncertainty of ≈ 0.5 mm in its spatial measurements. Also, the ceramic tubing in which the probe is held has a finite thickness which did not permit to touch the target surface. The wall thickness of the probe's ceramic insulator was ≈ 1.25 mm. The probe location closest to the wall surface was set as the zero position. The emissive probes was swept to a distance of 14 mm in the axial direction towards the electron gun with step resolution ≈ 250 μm. Across the target surface, 9 spatial locations were mapped at intervals of 3 mm. These measurements were repeated 3 times to provide a detailed potential map. Figure 6.7 shows the top view and side view of the measurements carried out using the emissive probe.

Detailed maps at different electron beam energies for all materials was produced. Figure 6.8 shows a detailed potential profile map of copper at different locations for various electron beam energies.

From this map it is seen that the behavior of beam on plasma sheath is similar in all cases where increasing beam causes the sheath potential to become more negative until a point comes after which the potential starts increasing. Also observed from this is that the sheath response to the beam at different location varies. As will be

shown later that the surface evolves under operation. This may be one of the reason for changing behavior. The main reason for different profiles at different spatial locations is likely due to the beam profile and energy spread. The electron beam has a spatial and energy spread as discussed earlier. This spread causes the secondary electron yield to vary at different locations causing different profiles.

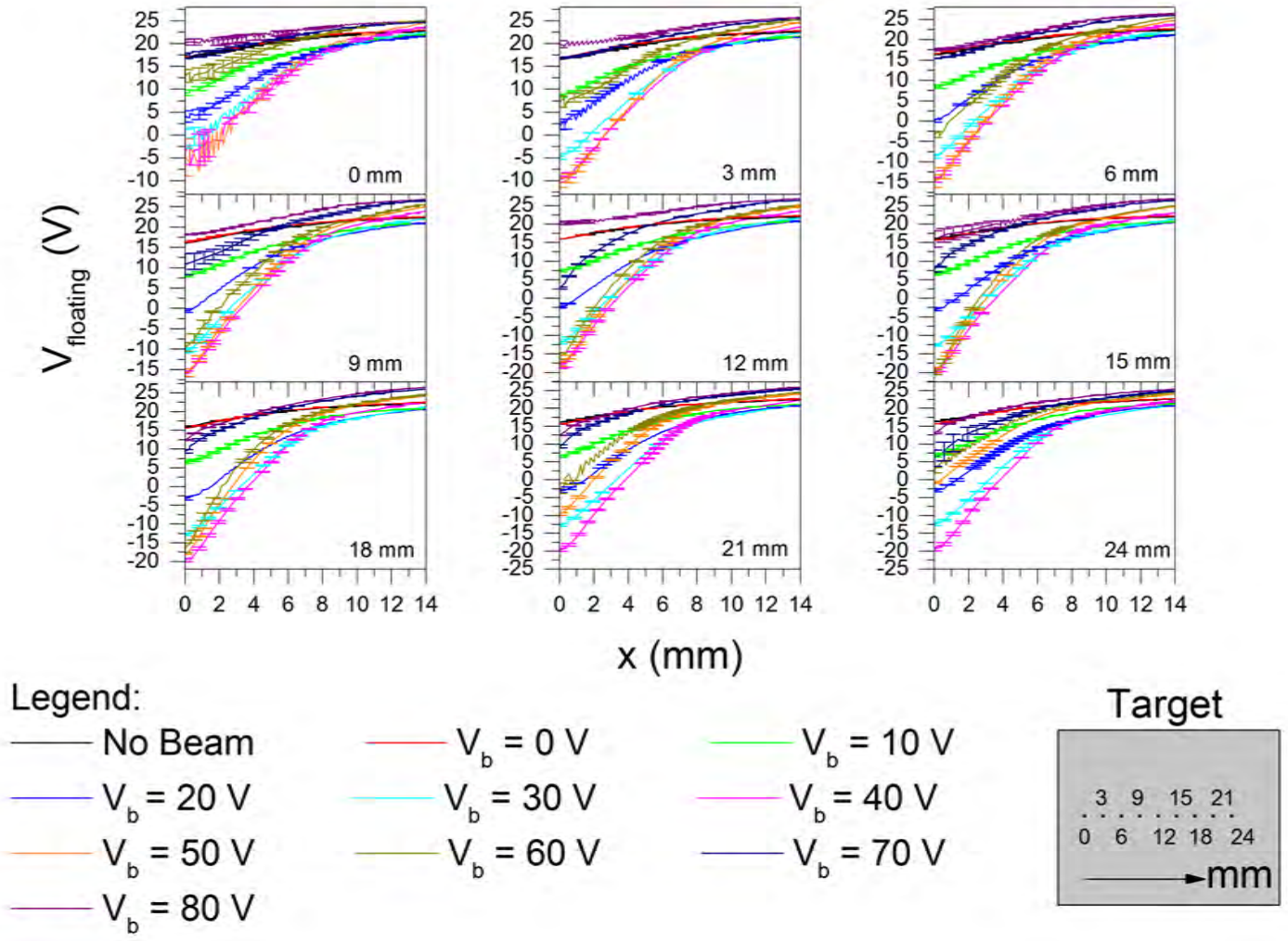

Figure 6.8: Sheath potential measured for copper at various axial locations

Figure 6.9 compares the behavior of the sheath potential for the different materials at a fixed location. The location chosen for this example is the closest to the beam center. Clearly seen from the graph is the different response from different materials as a function of beam energy. Noticeably the three materials under investigation have varying response to a similar beam energy and current. This is also suggestive of SEE playing different roles in different materials.

The detailed map allows to obtain equipotential maps as well as provides information on the charge distribution. Figures 6.10 through figure 6.13 show the potential map obtained for a copper target operated at 150 mA. Clearly seen from the graph is the changing potential as a function of energy with changing sheath potentials. At high beam voltage the equipotential behavior becomes more positive suggesting contribution of secondary emissions.

The charge distribution can be calculated using the Poisson's relationship and the results obtained are shown from figure 6.14 through 6.17. In order to obtain the instantaneous charge distribution, a second derivative was taken of the potential map and resulting data was smoothed using the Savitzky Golay smoothing filter using a second order polynomial and 20 point distirbution.

The charge distribution profile clearly indicates the rise of ion population with increasing beam voltage in response to compensate for electrons being lost to the target and with further increase in beam voltage shows a higher electron population suggestive of secondary emission. The information obtained from the contour maps as well as spatial profiles indicates the influence of secondary electrons on the plasma. However, the increasing beam energy also increases the effective plasma temperature due to energetic electrons being forced in the system via the electron gun.

The competition between rising electron temperature as a consequence of beam injection and the cooling of plasma due to low energy secondaries is best understood by observing the sheath potential drop. Since the exact sheath edge is not easy to

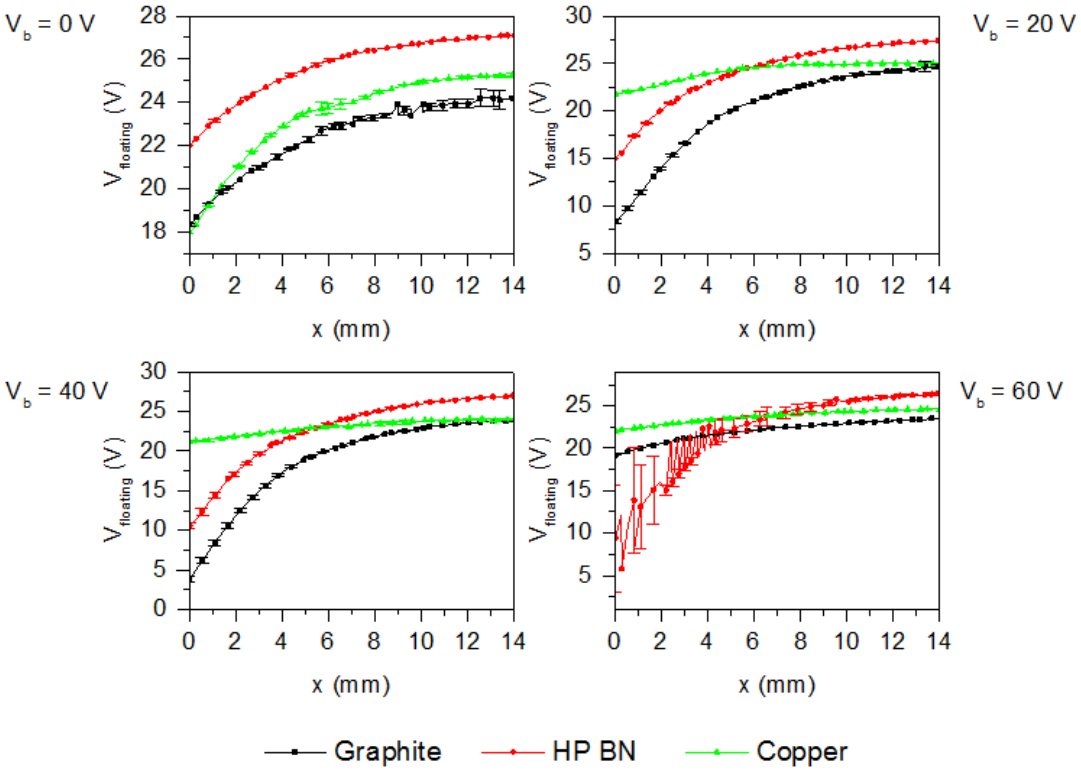

Figure 6.9: Comparison of sheath potential for different materials.

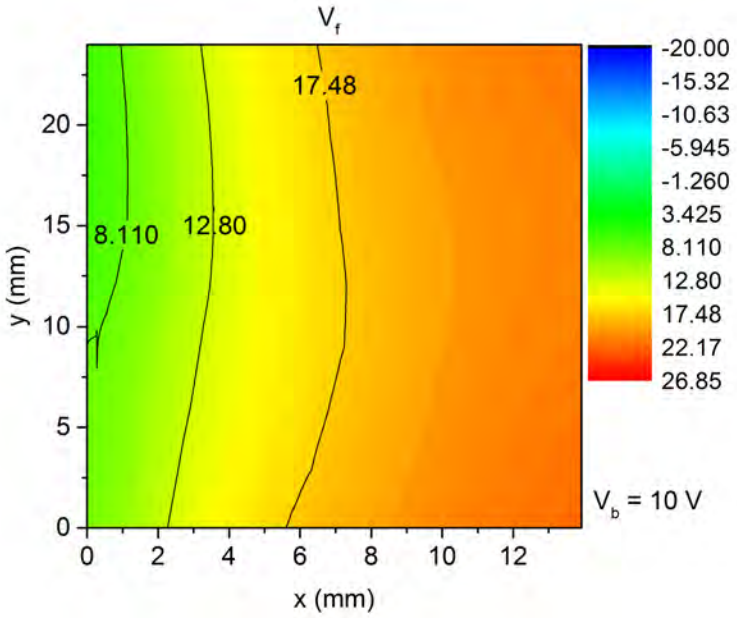

Figure 6.10: Equipotential profile for copper operated under 150 mA discharge current with 10 V beam voltage (Units: V).

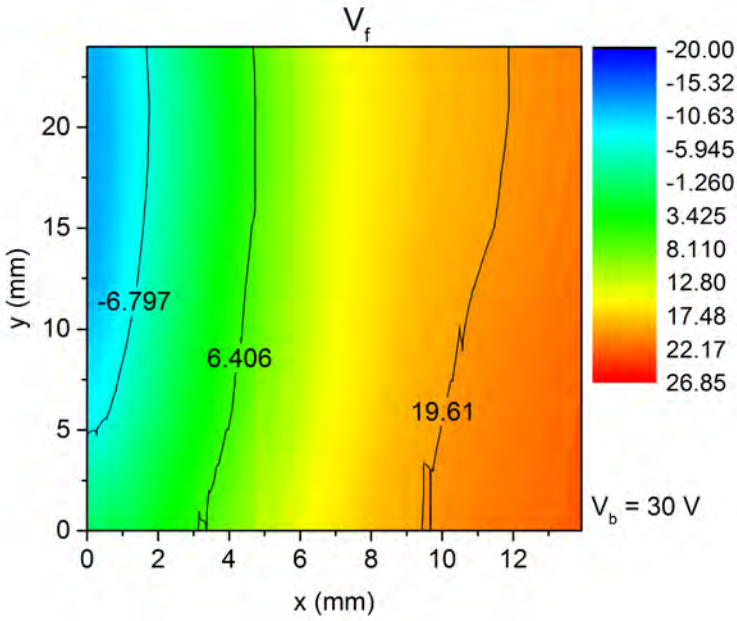

Figure 6.11: Equipotential profile for copper operated under 150 mA discharge current with 30 V beam voltage (Units: V).

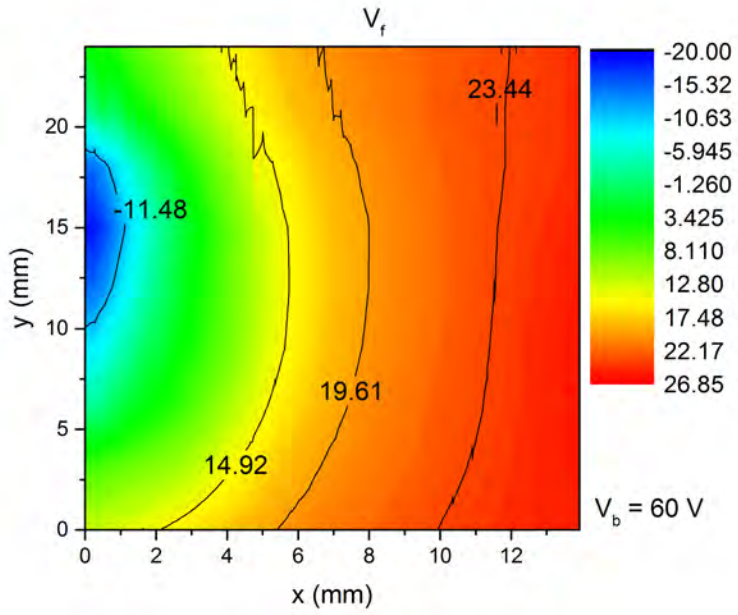

Figure 6.12: Equipotential profile for copper operated under 150 mA discharge current with 60 V beam voltage (Units: V).

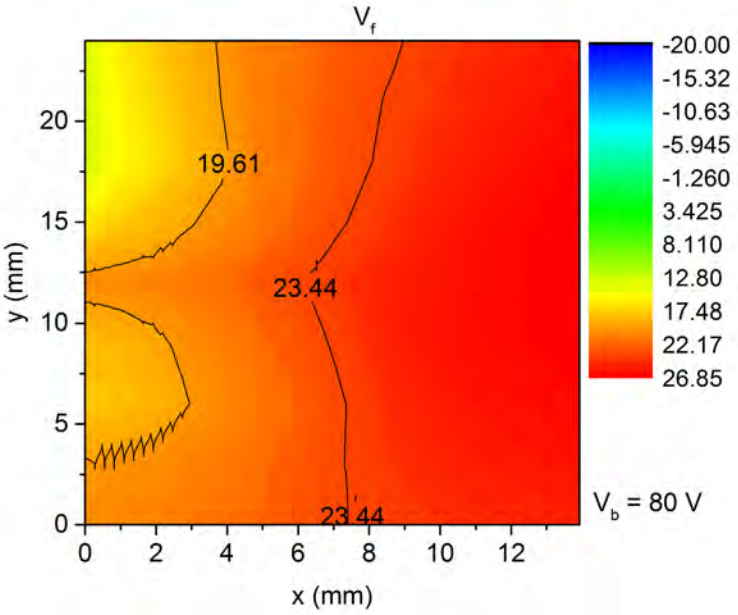

Figure 6.13: Equipotential profile for copper operated under 150 mA discharge current with 80 V beam voltage (Units: V).

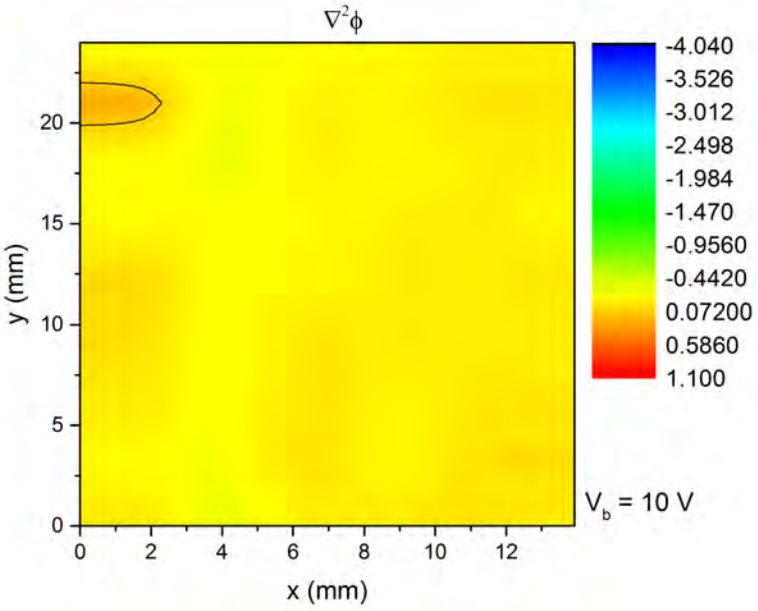

Figure 6.14: Uncorrected charge distribution profile for copper operated under 150 mA discharge current with 10 V beam voltage (Units: V/mm^2).

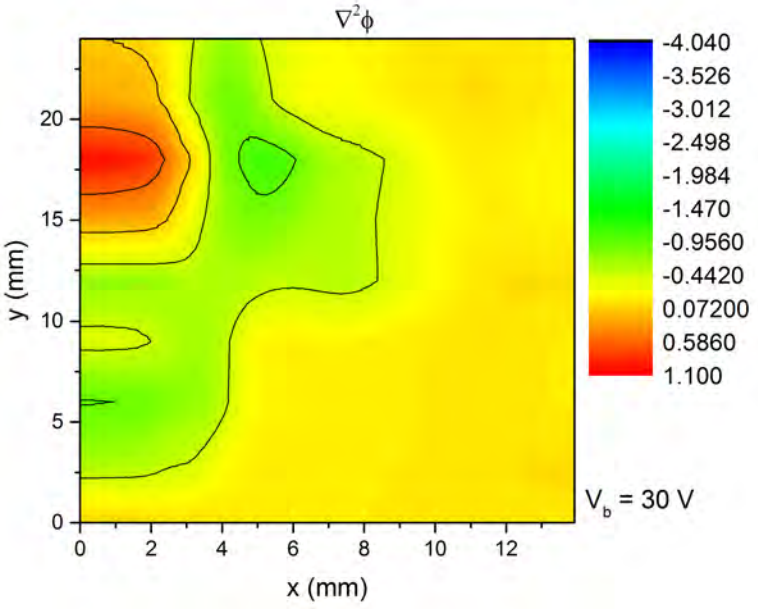

Figure 6.15: Uncorrected charge distribution profile for copper operated under 150 mA discharge current with 30 V beam voltage (Units: V/mm^2).

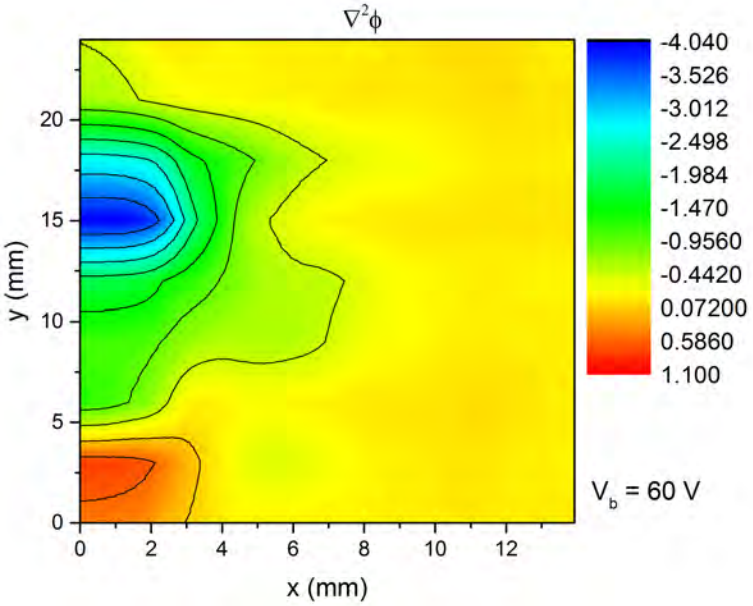

Figure 6.16: Uncorrected charge distribution profile for copper operated under 150 mA discharge current with 60 V beam voltage (Units: V/mm^2).

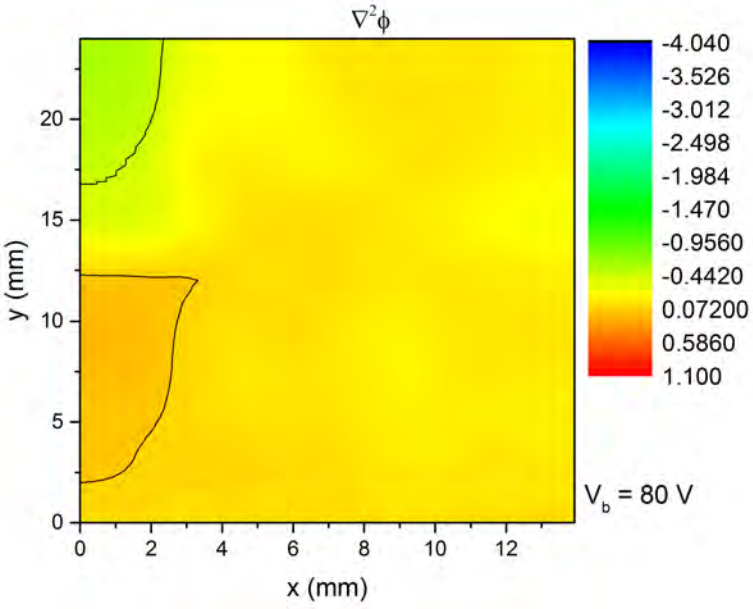

Figure 6.17: Uncorrected charge distribution profile for copper operated under 150 mA discharge current with 80 V beam voltage (Units: V/mm^2).

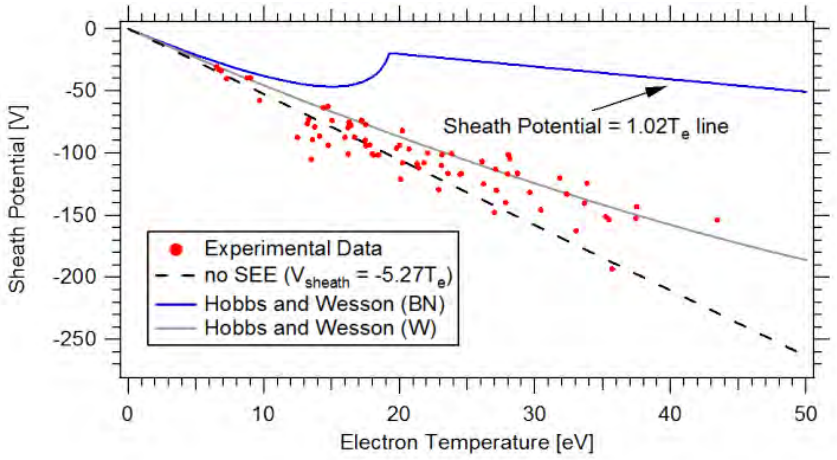

Figure 6.18: Measured sheath potentials as a function of measured electron temperature using internal wall-mounted probes within the 6-kW Hall thruster. [11]

estimate, in this study, the wall potential is obtained by subtracting the most closest point to the wall with the most positive value obtained at a distance of 14 mm. This potential at 14mm is a potential in the pre-sheath. Due to the small size of the experimental domain ($\approx$ 50 mm) the assumption of the entire experimental domain being in the pre-sheath is reasonable.

The expected wall potential behavior with increasing electron energy was studied by Shastry [11] for a 6kW Hall thruster. Figure 6.18 shows the experimental data obtained from an internal wall mounted probe in a Hall thruster and shows the expected behavior of a BN sheath including the saturated behavior predicted by Hobbs and Wesson [49]. In that study, the sheath behavior observed correlated with tungsten data and the energy required to reach the first crossover point on the SEE yield curve for tungsten is much higher than BN.

Figure 6.19 and 6.20 show the wall potential as a function of beam energy for various materials tested at two different locations. It is important to note that the beam voltage corresponds to an effective energy as the beam is not mono-energetic and has a distribution of particles at different energies.

From the images it is evident that different materials respond to the beam differ-

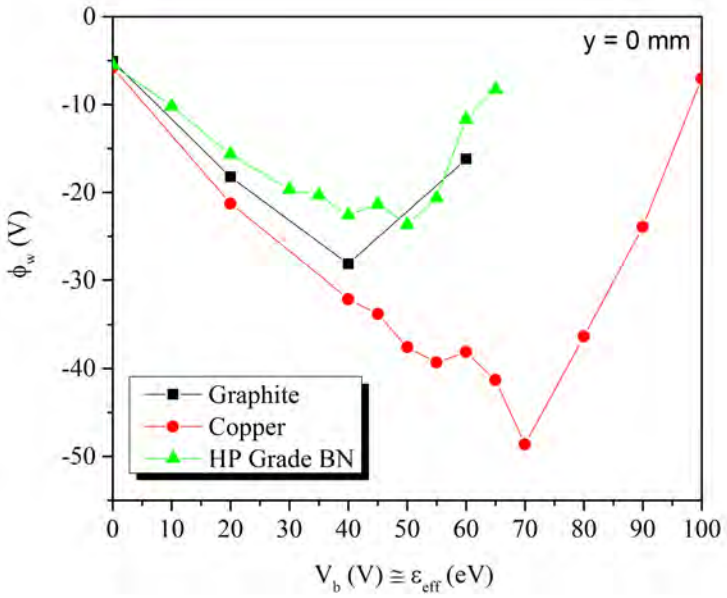

Figure 6.19: Wall sheath potential for different materials at y = 0 mm.

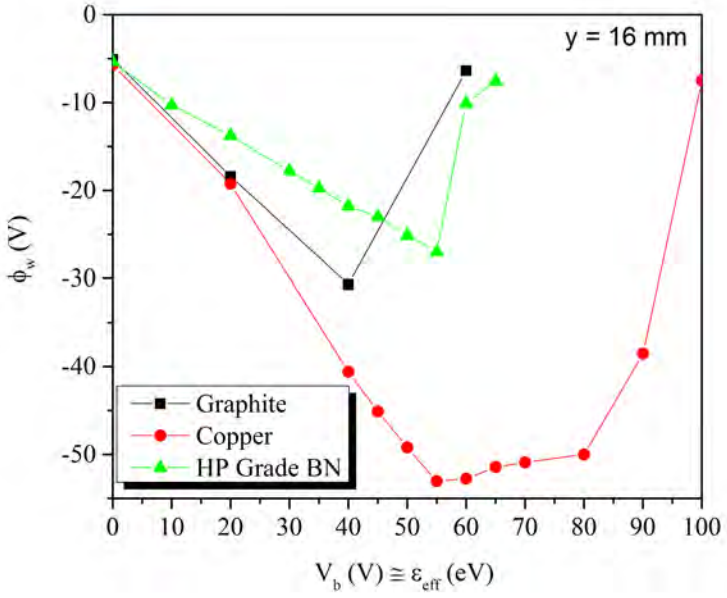

Figure 6.20: Wall sheath potential for different materials at y = 16 mm

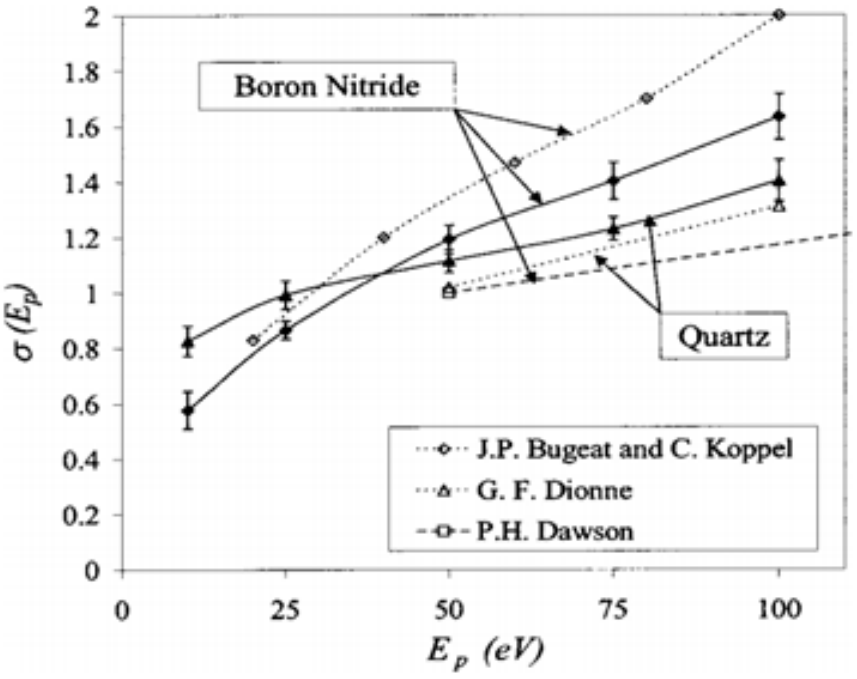

Figure 6.21: Various SEE coefficient for BN in literature, with first crossover point at 28 eV, 40 eV and 57 eV [181].

ently and correspond to the SEE yield. BN reaches a maximum SEE yield of 1 at low energy in the range of 30 - 60 eV based on literature. This variation is due to the variations of BN composition and surface conditions such as roughness, material surface structure, and temperature. Zidar and Rovey [180] present their findings on structure and composition of various grades of BN sold commercially that are used in Hall thruster and discuss their properties both in pristine and after hundreds of hours of testing in a Hall thruster. Figure 6.21 shows the SEE yield obtained from various sources of BN.

The crossover point for pure copper without any contamination or oxide film is $\approx$ 100 V. However, exposure to air even for a short duration results in growth of oxide films as discussed earlier. The oxide coating on copper reduces the energy required to obtain a given yield value in comparison to a oxide free copper surface. As can be seen from fig. 6.22, exposure to air leads to oxide formation, and this reduces the energy required to have a higher SEE yield at a lower energy.

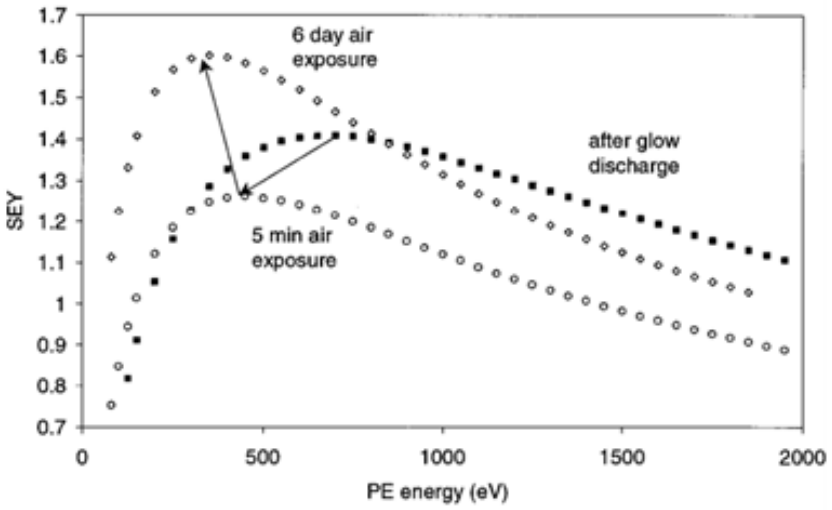

Figure 6.22: SEE coefficient for copper at normal incidence under different conditions, sputter cleaned plasma, 5 minute air exposure, and 6 days air exposure [182].

For pure graphite, the SEE yield crosses 1 at very high voltages. However, the literature widely varies on the SEE yield of graphite that is contaminated with different coatings. Figure 6.23 shows the SEE yield curve for graphite by Patino et al. [183]. It is thus desirable to conduct this experiment by baking out the material to reduce surface impurities. Controlled sputtering may be desirable, however the sputtered material may contaminate the probe and other surfaces.

Figure 6.24 compares the behavior of sheath response on BN across multiple tests. While the exact values are hard to repeat due to changing plasma condition as well as minor power differences in the electron gun filament resuilting in small changes in the beam flux to the target, the general trend is very similar and repeatable. The change may also be due to particulate deposition on the BN surface as discussed later.

It is also shown that the general behavior is consistent across the target surface, but varies slightly due to difference in beam exposure as well as energy variation across the target surface. This is shown in figure 6.25.

The response as a function of pressure produces similar trends. This may be due to change in the interactions of the beam and plasma at given pressures or may in

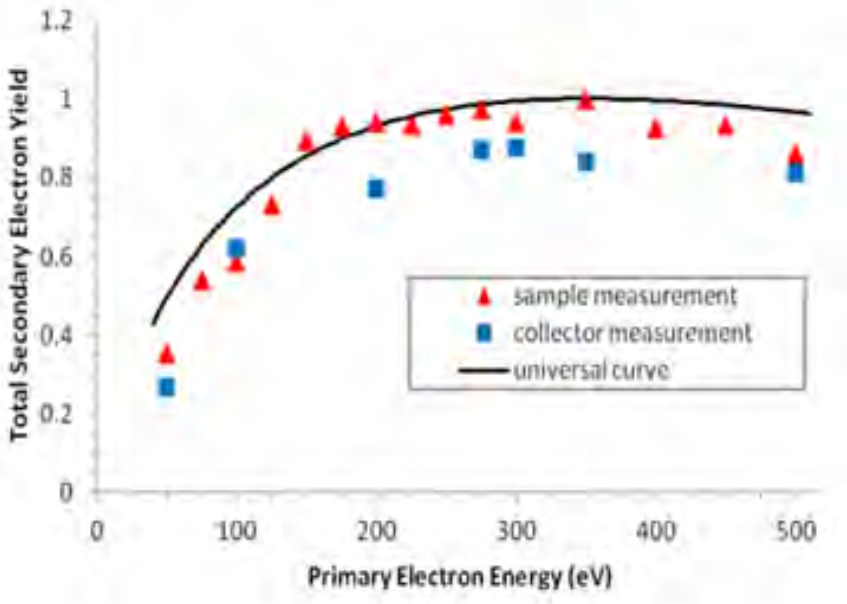

Figure 6.23: SEE coefficient for graphite at normal incidence.

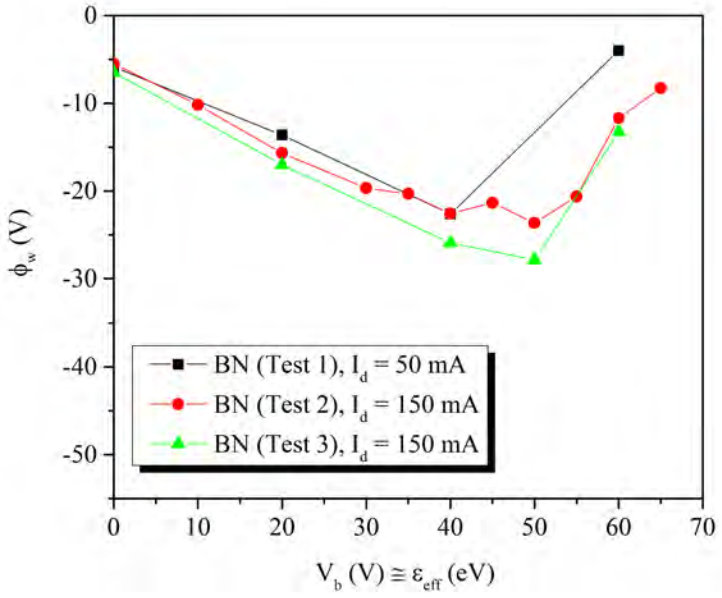

Figure 6.24: Wall sheath potential for BN at y = 16 mm under different tests

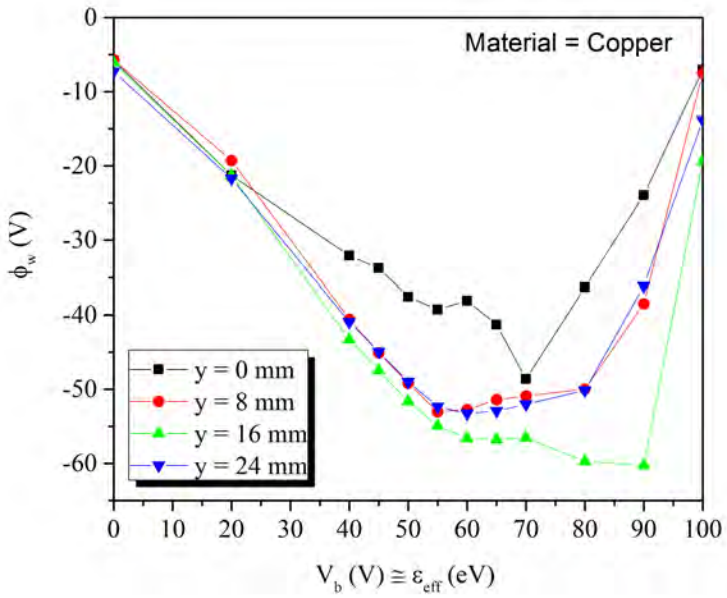

Figure 6.25: Wall sheath potential for copper at different locations in a 150 mA plasma environment.

general be due to surface contamination effects. The behavior is shown in figure 6.26.

Based on all the data the general phenomenological behavior of the a wall sheath profile as a function of beam energy (or beam voltage) can illustrated as shown in figure 6.27. In order to gain greater insight into the microscopic dynamics of the plasma, the EEDF and plasma properties need to be measured. The plasma temperature rise is expected with increasing beam energy. Increasing beam energy also gives rise to the SEE yield. As a consequence the energetic electrons are lost to the walls causing a drop in effective temperature. A rise in density may also indicate the dominance of SEE. On the right hand side of the graph, the SEE dominates and causes the wall potential to decrease. The decrease in potential would cause loss of high energy electrons from the tail of the distribution.

The sheath profile can be empirically modeled using equation 2.68. In equation 2.68 the electron temperature is assumed to be Maxwellian and the associated secondary yield is calculated for a Maxwellian temperature electron beam impacting a

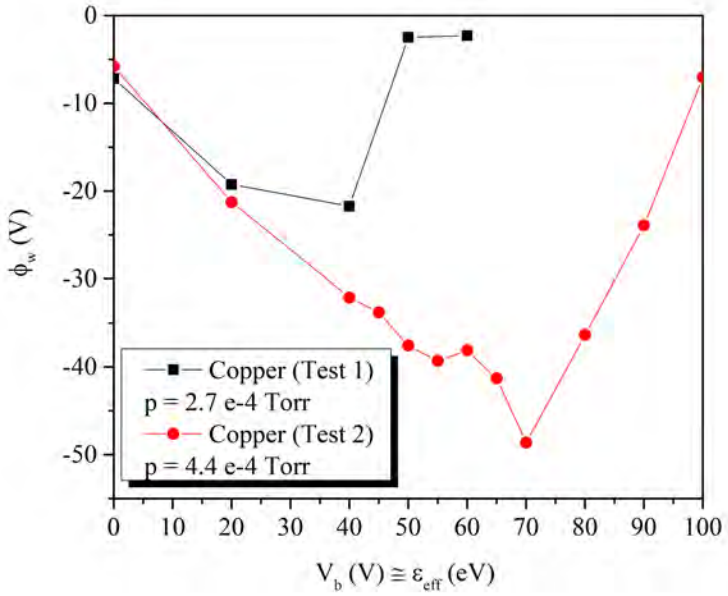

Figure 6.26: Wall sheath potential for copper at different pressures.

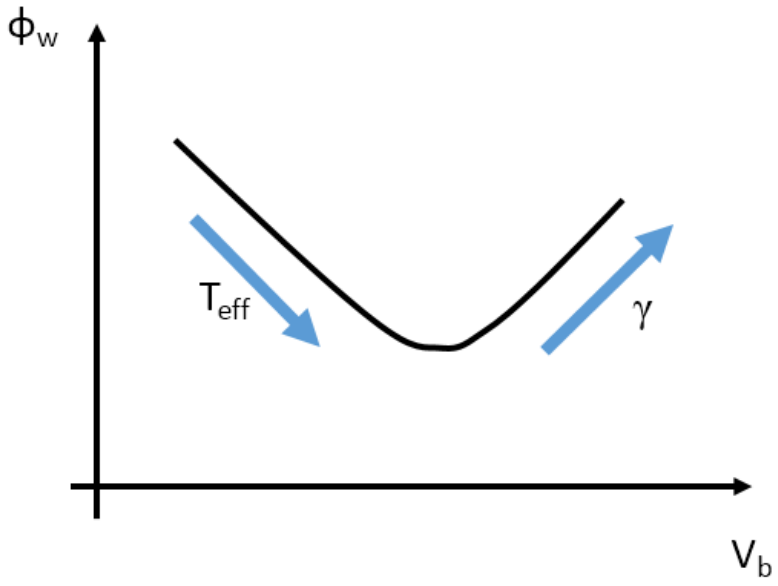

Figure 6.27: General behavior of sheath potential in presence of SEE. Competition between the effective electron temperature rise and the increase in SEE yield results in a behavior where increase in electron temperature dominates at low energy of the beam whereas SEE causes the sheath potential to become more positive with increasing beam energy.

surface. This system has multi temperature electrons and a distribution of beam energies from the electron gun. As a result, we could define a system in terms of an effective temperature $T_{e,eff}$ and a effective SEE rate given by γ_{eff}. Equation 2.68 can be thus converted to equation 6.1

$$\phi_w \approx -T_{e,eff} \ln \left[(1 - \gamma_{eff}) \sqrt{\frac{M_i}{2\pi m_e}} \right] \tag{6.1}$$

It can be shown that $\gamma_{eff} = \gamma(\phi_w, T_e, V_b)$. The effective SEE rate can be defined by equation 6.2

$$\gamma_{eff} = \int_0^\infty \sigma(\varepsilon) f_{target}(\varepsilon) d\varepsilon \tag{6.2}$$

where σ is the SEE coefficient for a given electron energy ε and f_{target} is the normalized energy distribution of the electrons bombarding the target. This distribution is a superposition of the primary electrons from the plasma (which can be assumed Maxwellian) and the electron beam distribution from the electron gun. This is expressed by equation 6.3

$$f_{target} = (1 - \alpha) f_{pe,target} + \alpha f_{eb,target} \tag{6.3}$$

where $f_{pe,target}$ is the primary electrons from the plasma at the target and $f_{eb,target}$ is the electrons due to the electron beam at the target.

The quantity $\alpha = n_{eb,target}/(n_{pe,target} + n_{eb,target})$. It can be shown that equation 6.3 is valid only when $V_b > \phi_w$. Thus, the effective SEE rate can be given by equation 6.4

$$\gamma_{eff} = (1 - \alpha)\gamma_{pe}(T_e) + \alpha \gamma_{eb}(V_b) \tag{6.4}$$

where γ_{pe} and γ_{eb} are the SEE yield induced by the primary electrons and electrons

from the electron gun. The distribution for the Maxwellian primary electrons when ($u \leq 0$) can be given by

$$f_{pe,target} = \exp\left(\frac{-e\phi_w}{k_B\, T_e}\right)\left(\frac{m_e}{2\pi k_B T_e}\right)^{1/2} \exp\left(\frac{m_e u^2}{2}\right)$$

The distribution of the electron beam at the target can be found from the RPA data obtained in Chapter V.

For a Maxwellian primary beam, it is shown that the SEE yield can be averaged over a Maxwellian and is given by equation 6.5 [45].

$$\gamma(T_e) = \Gamma(2+b)\, a\, T_e^b \tag{6.5}$$

where Γ is a gamma function and a and b are parameters of an exponential fit. For BN, the values of a = 0.141 and b = 0.567 [45].

In the limiting case when α is zero, we have the conventional Hobbs and Wessons solution. As seen from figure 6.28, there is a huge difference between Hobbs and Wessons solution compared to what was experimentally observed. This is due to the non-Maxwellian nature of the system as well as additional complexity with multi-temperature components. However, the shape resembles greatly.

In order to understand if charging - discharging timescales play a role in the sheath dynamics a simple R-C time constant model was developed. It was seen from this model that the time constant was typically in the range of 10 - 100 μ second timescale. The sheath measurements were conducted using Keithley 2410 with a time resolution of milliseconds. It is thus concluded that that the charging - discharging timescales are too fast to influence the potential measurements.

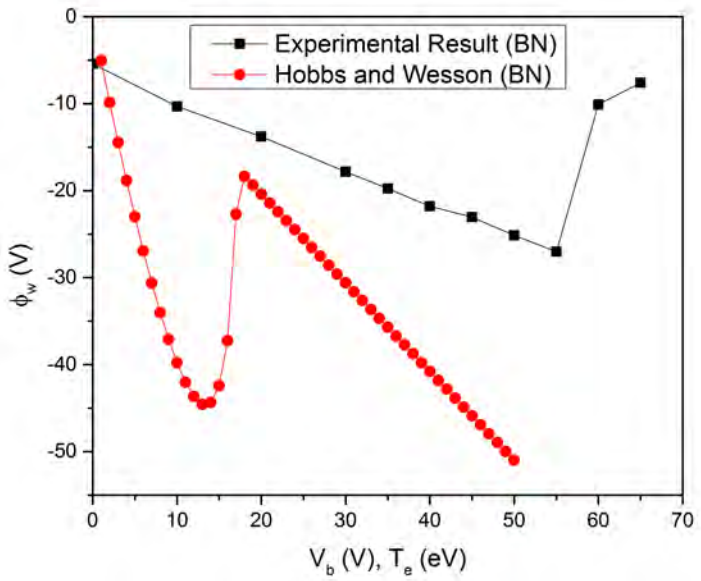

Figure 6.28: Comparison of experimental solution to that of Hobbs and Wesson [49].

6.4 EEDF Behavior in Presence of SEE

In order to obtain the EEDF, multiple Langmuir probes were used. These probes were located at a distance of 2.54 cm away from the target. The collected current by a Langmuir probe would represent the sum of plasma electrons, primary beam electrons from plasma filament, electrons from the electron gun directed towards the target and also a relatively smaller contribution from the low energy secondary that would stream out from the target. The electrons are accelerated via the sheath and may either thermalize in the bulk or be directed towards another location within the system based on the potential profile.

The plasma in presence of electron beam contains two electron temperature distributions. It can be defined by an effective temperature in terms of a non-dimensional parameter that defines the relative contribution of each electron species. This is given by equation 6.6

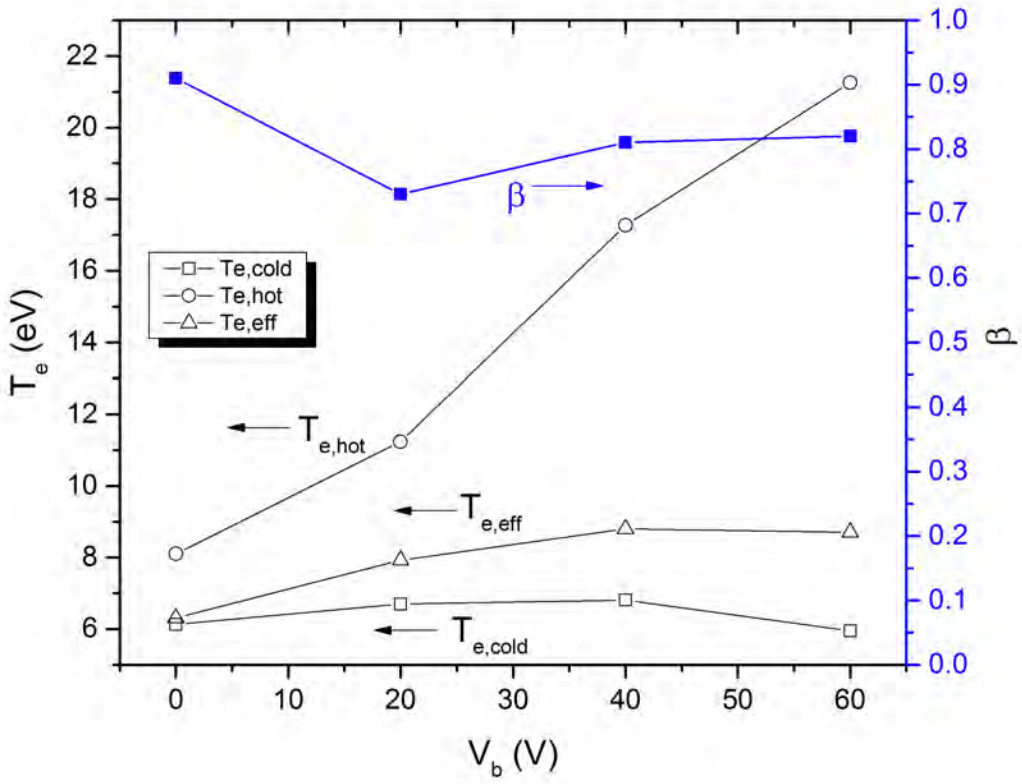

Figure 6.29: Temperature distribution for a copper target based on beam energy.

$$T_{e,eff} = \beta\, T_{e,cold} + (1-\beta)\, T_{e,hot} \tag{6.6}$$

where β is defined by the ratio $(i_{cold}/i_{hot})\sqrt{T_{e,hot}/T_{e,cold}}$ and the hot temperature corresponds to the average temperature obtained from the beam component. The effective temperature varies from 0.95 at low beam energies to 0.8 at higher beam energies. Figure 6.29 shows the behavior of the temperature for a copper target operated at 150 mA (at a pressure of 2.7x10^{-4} Torr).

In this example, it is clear that although the hot component obtained from the I-V characteristics increases, the effective temperature however saturates and slowly decreases at higher energy. The dominance of SEE related effects are found at higher beam voltages but at lower beam voltages, the effective temperature plays a stronger

role in defining the wall behavior. It must be noted here that in Hall thrusters thermalization of the secondary plays a role due to presence of magnetic fields. These magnetic fields increase the residence time of the electrons, however, in this experiment, the mean free paths are long and the collisionless nature of the plasma reduces the thermalization events. Most energy transfer in this system is due to losses at the target.

The electron temperature variation can also be understood on application of the energy balance. Under the assumption of steady state operation, the energy balance can be expressed by equation 6.7,

$$0 = \frac{Power}{Volume} - \sum_j \Delta\varepsilon_j R_j - \frac{3}{2} k_B (T_e - T_g) R_m - Losses \tag{6.7}$$

where $\Delta\varepsilon_j$ is the threshold energy and R_j is the reaction rate of inealastic collisions j. T_g is the temperature of the gas and R_m is the momentum transfer collision rate. Thus we get equation 6.8

$$T_e = T_g + \frac{2}{3\,k_B\,R_m} \left(\frac{Power}{Volume} - \sum_j \Delta\varepsilon_j R_j - Losses \right) \tag{6.8}$$

As the electron beam voltage is increased, based on the space charge limit the current also increases for a given filament current. This increase in power is directly related to the electron temperature causing the electron temperature to rise. The gas temperature is fairly constant and the contribution of inelastic collisions rate (R_j) and momentum transfer collision rate (R_m) are not significant. With increasing power flux, as has been discussed earlier, the particle losses due to reducing sheath also increases. When more particles are lost from the system than the input power, the electron temperature starts to fall. This would happen at higher SEE yield, which is consistent with other observation. Thus we see that the electron temperature increases initially, reaching a maximum and then steeply falls as the rate of losses far

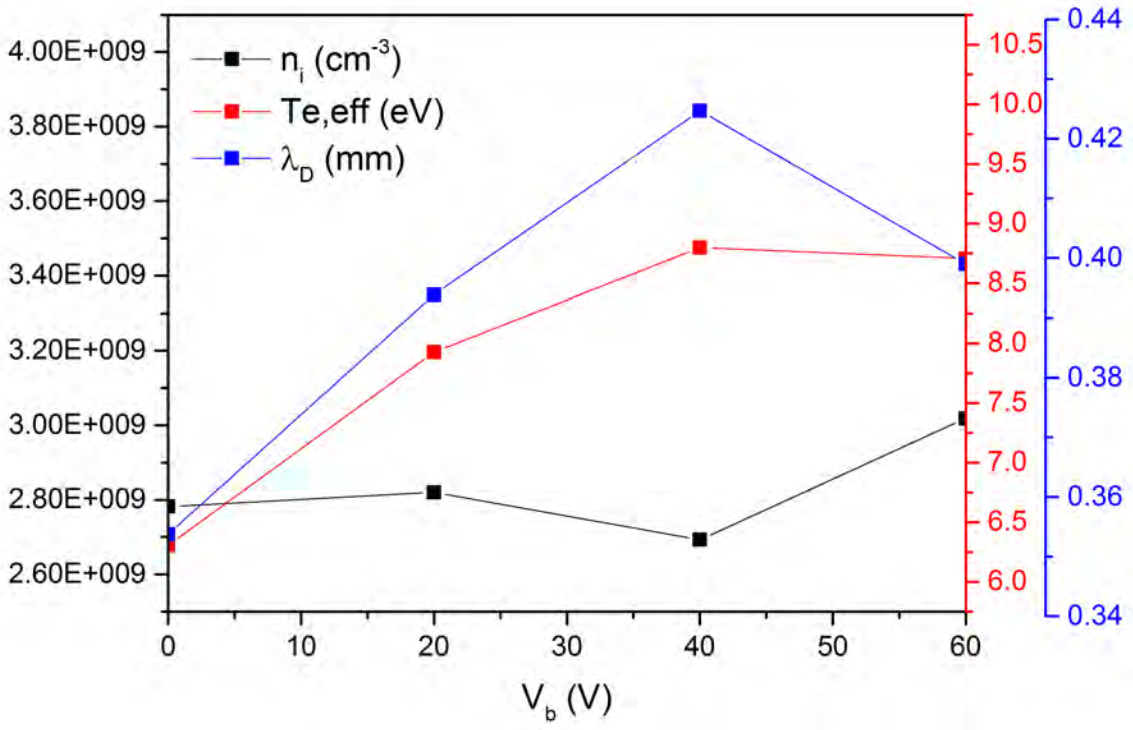

Figure 6.30: Plasma properties for copper in a plasma of current 150 mA as a function of beam voltage.

exceeds the power input.

Further analysis on copper operated at 150 mA discharge reveals the plasma properties and EEDF. This is shown in figures 6.30 and 6.31. The EEDF is normalized because as the beam energy increases, the emission current (and beam number density) increases. This increases the magnitude of the EEDF with increasing beam voltage. In order to avoid incorrect interpretation based on amplitude, a normalized distribution is used to compare similar behavior.

For the case of copper at 150 mA it is seen that the effective temperature does not rise as rapidly at higher voltages and the production of ion density obtained using OML theory suggests higher density. The Debye length obtained is between 0.3 to 0.4 mm suggesting a sheath thickness of 3 mm or greater. This is consistent with

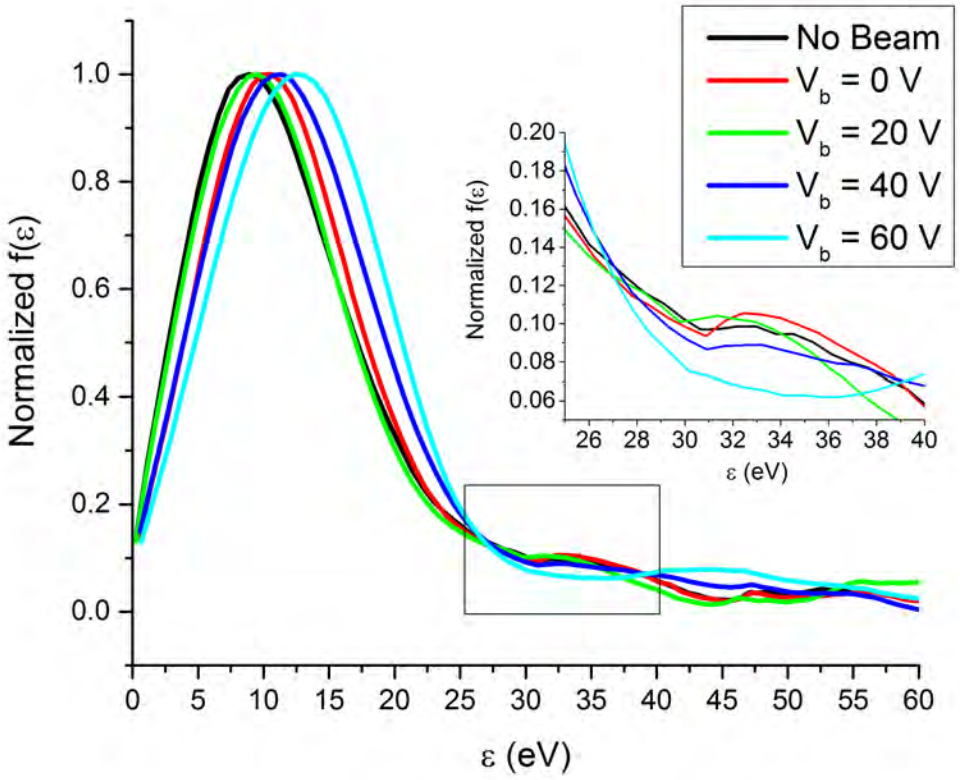

Figure 6.31: Normalized EEDF of copper operated at a plasma discharge of 150 mA as a function of beam voltage.

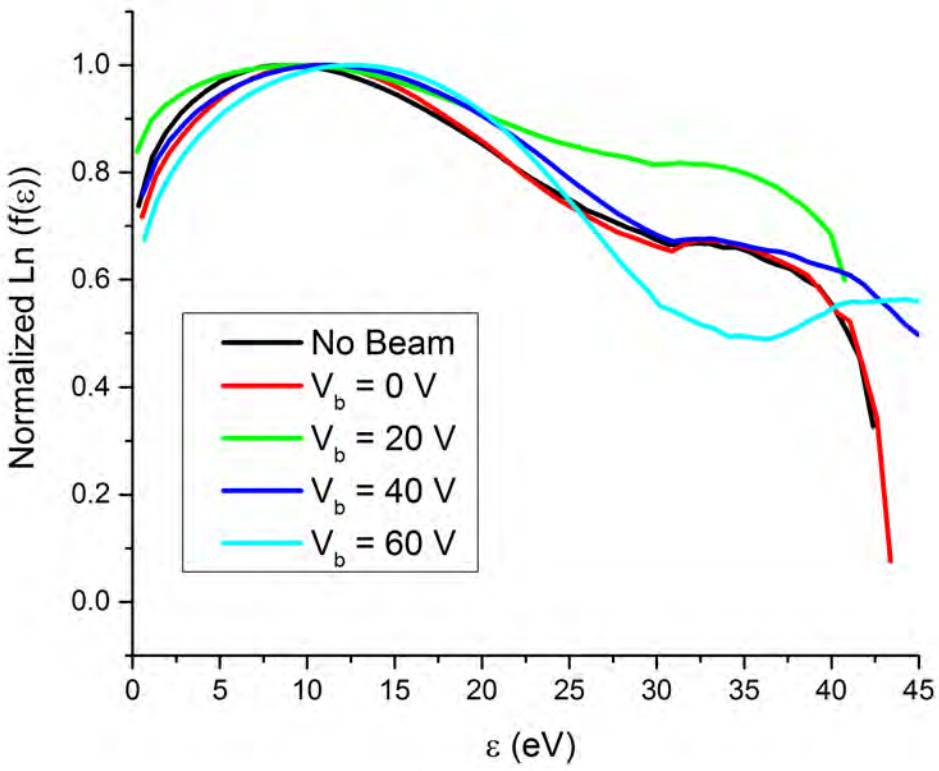

Figure 6.32: Normalized Log (EEDF) of copper operated at a plasma discharge of 150 mA as a function of beam voltage.

the data obtained using emissive probes where the probe was capable of resolving near sheath profiles. From the inset on the EEDF, it is seen that the the tail of the distribution does change and decreases with increasing beam energy. Interestingly, the tail also shows growth at higher energies. This is likely due to electron beam heating.

Plotting the normalized log data for the EEDF suggests that some component of the distribution is Maxwellian due to straight slopes in the log plot, however, there are clearly non-Maxwellian components too. This is shown in figure 6.32 for the same case of copper operated in 150 mA discharge current.

Similar trends are seen when the copper target is operated at a lower discharge current of 50 mA. The plasma parameters are shown in figure 6.33 and the eedf is

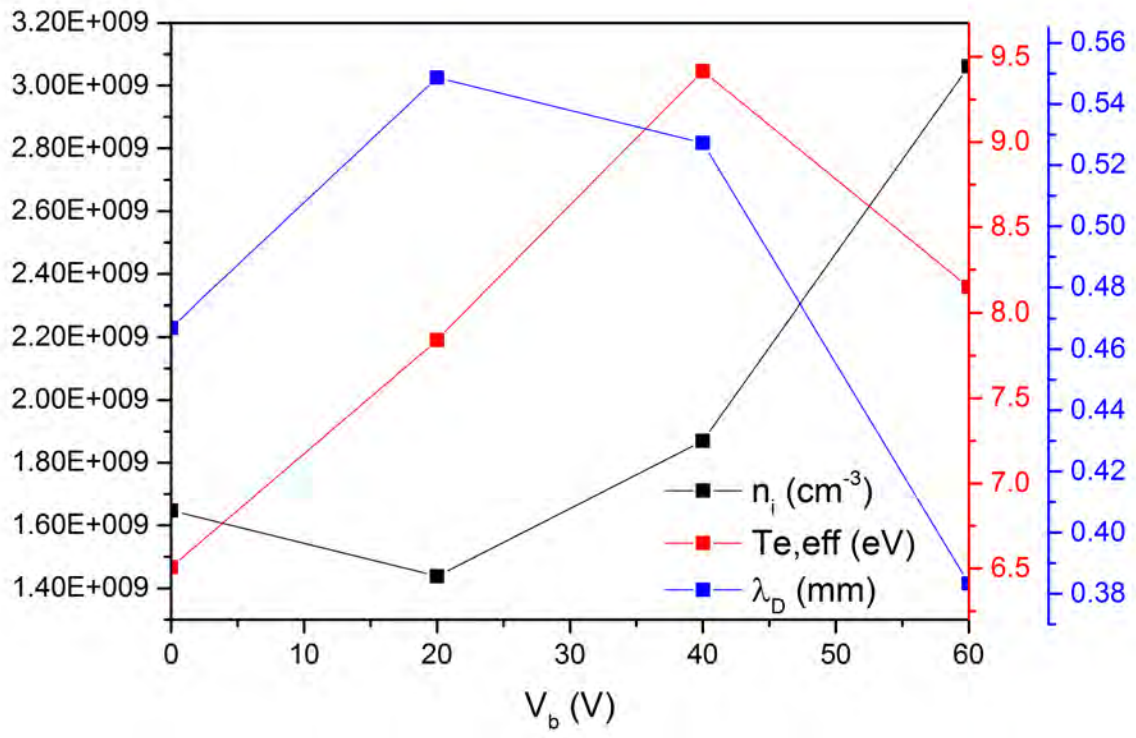

Figure 6.33: Plasma properties for copper in a plasma of current 50mA as a function of beam voltage.

shown in figure 6.34. Figure 6.35 shows the plasma properties of a probe closer to the cathode.

While the behavior of the EEDF in the inset suggests similar behavior as in the previous case, there is no conclusive evidence of a trend. This may be due to the fact that there are multiple beams present within the system and the EEDF signal is saturated with information from the electron beams from both the electron gun and the discharge filament. Also the signal to noise ratio is poor despite numerical smoothing using the Savitzky-Golay filtering technique.

Figure 6.36 and 6.37 show the plasma properties and eedf information for graphite at 50 mA discharge current.

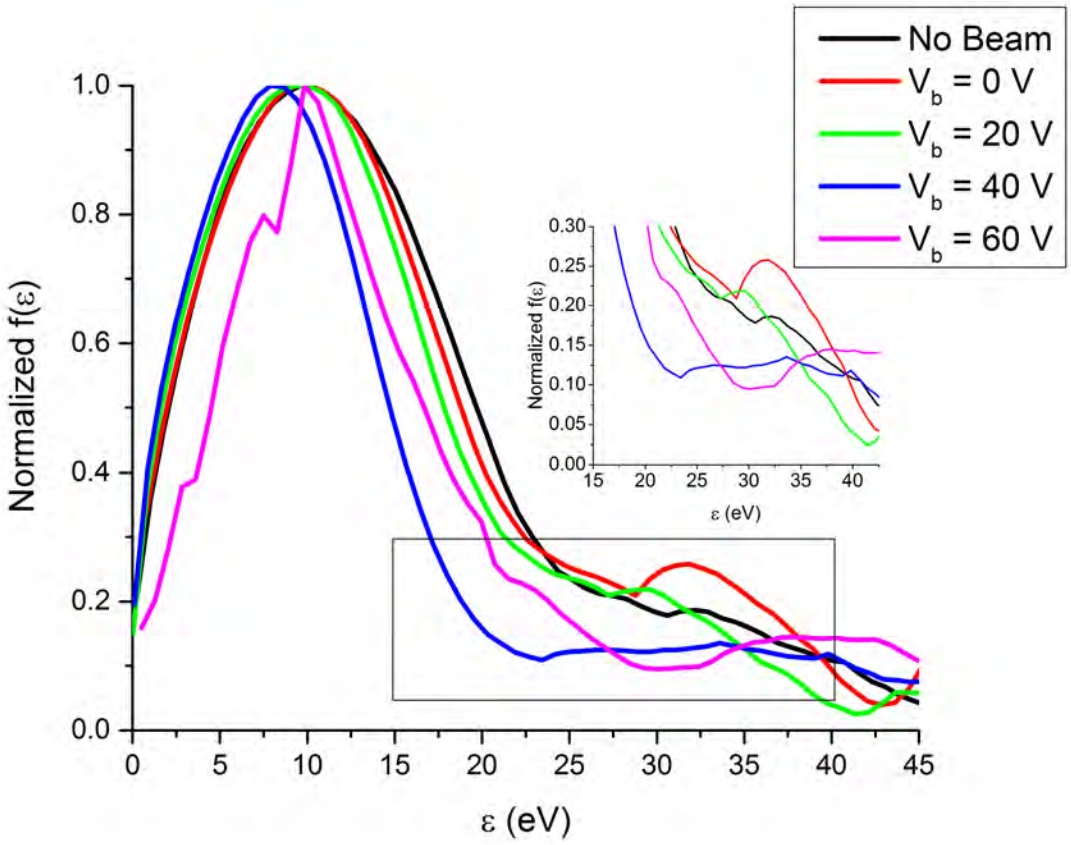

Figure 6.34: Normalized EEDF of copper operated at a plasma discharge of 50 mA as a function of beam voltage.

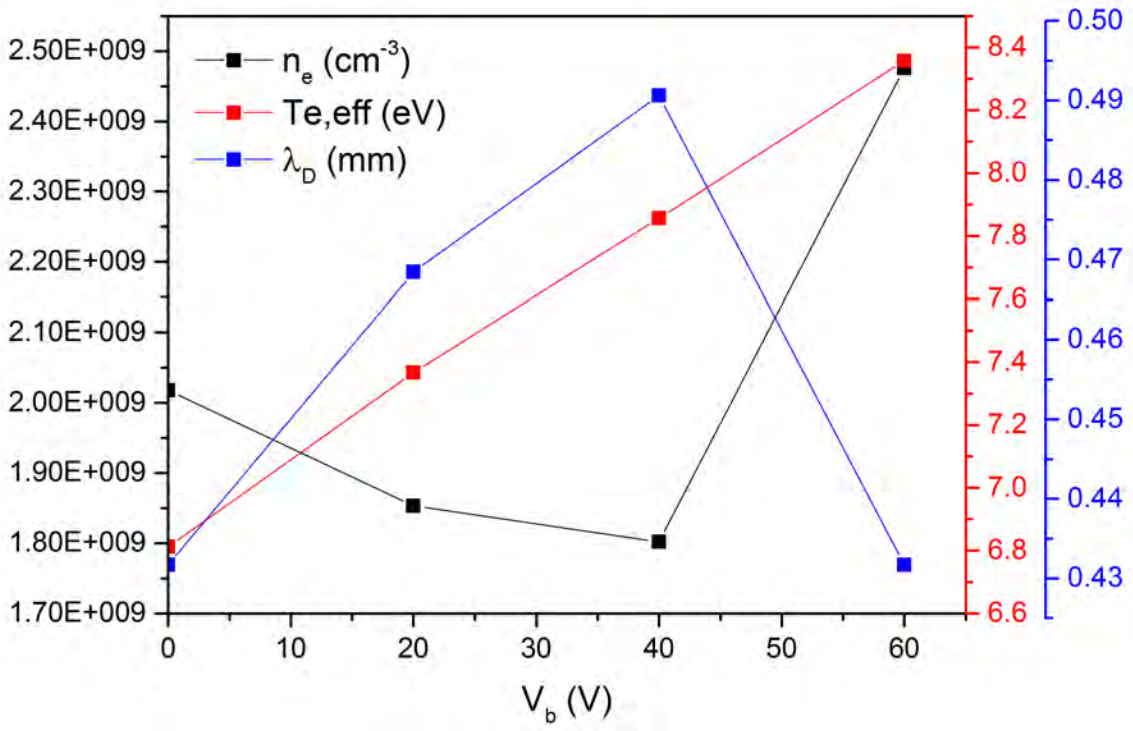

Figure 6.35: Plasma properties for copper in a plasma of current 50mA as a function of beam voltage. Langmuir probe is closer to the cathode of the discharge supply.

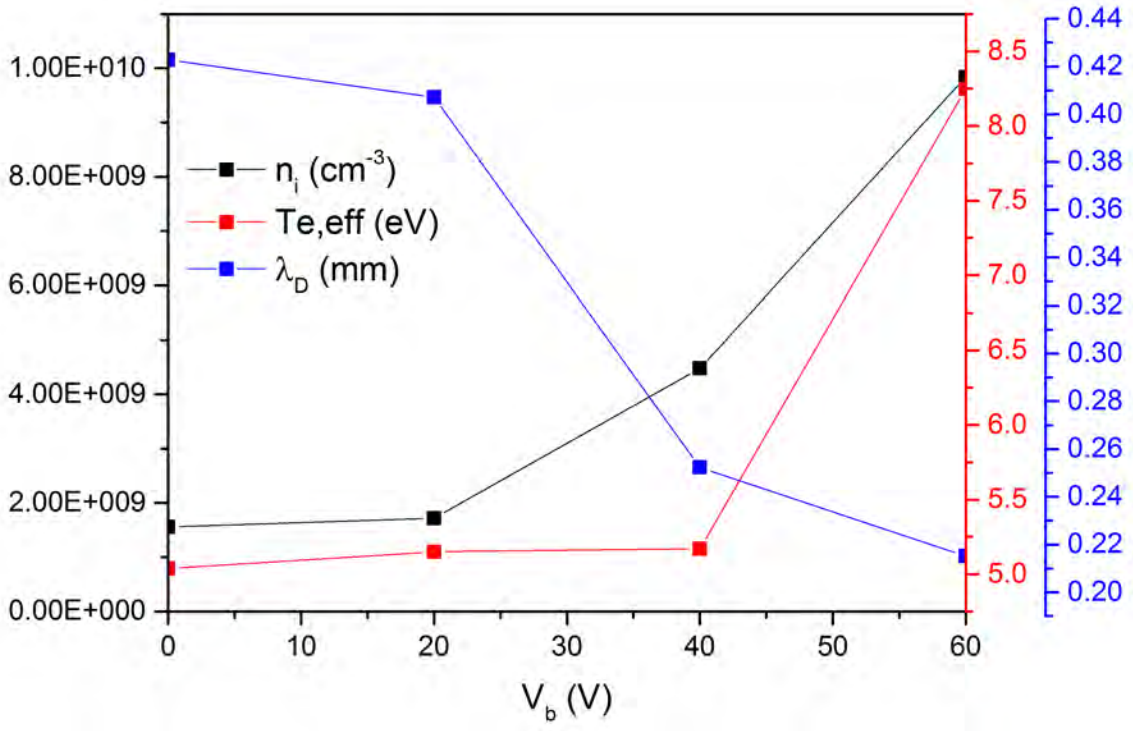

Figure 6.36: Plasma properties for graphite in a plasma of current 50mA as a function of beam voltage.

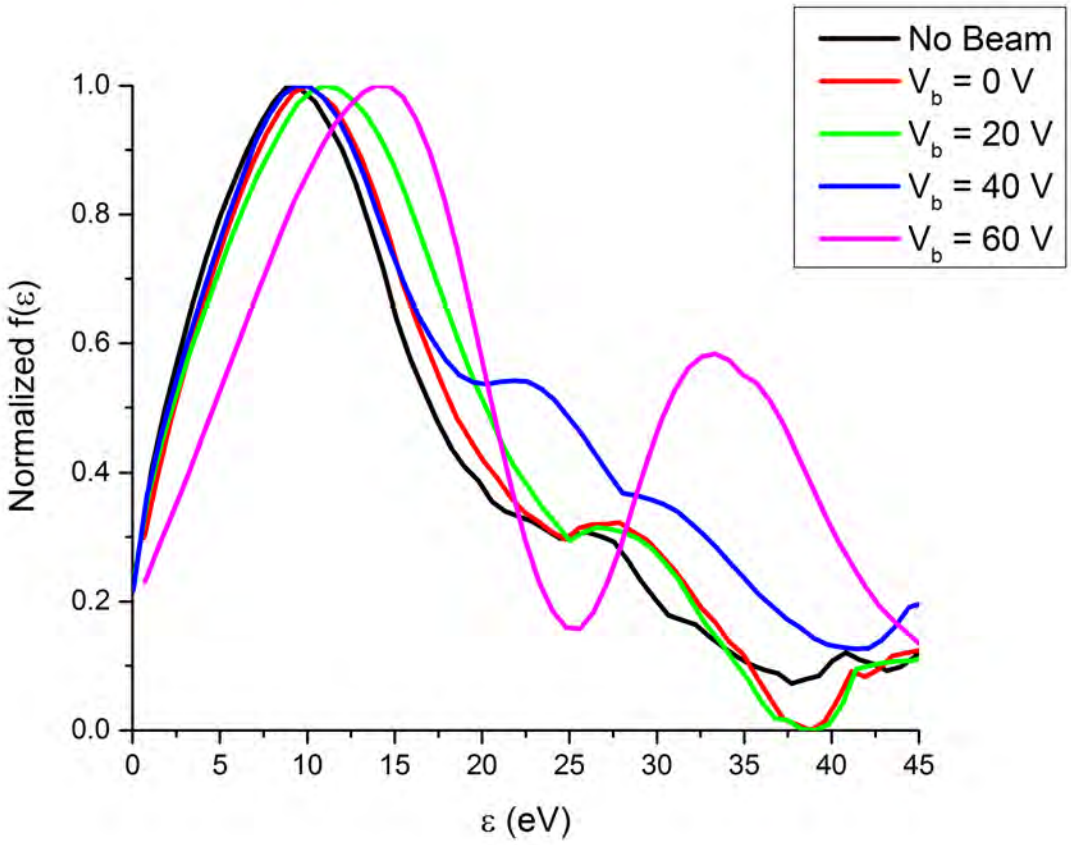

Figure 6.37: Normalized EEDF of graphite operated at a plasma discharge of 50 mA as a function of beam voltage.

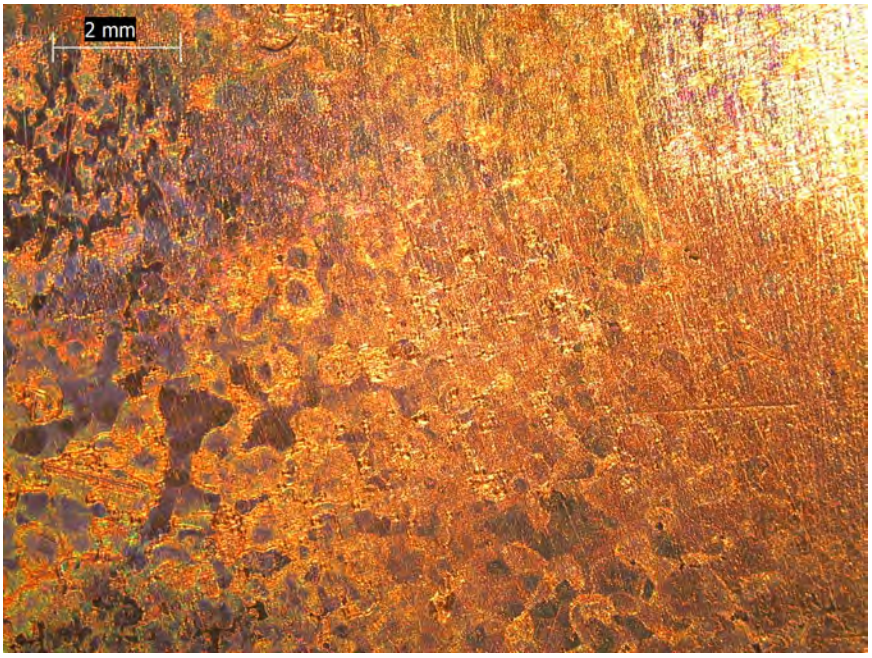

Figure 6.38: Post test copper image (8x zoom).

6.5 Post Operation Material Analysis

The materials used in this experiment were polished and cleaned prior to operation. In post plasma tests it was seen that the surface was significantly modified. Figures 6.38 and 6.39 show the surface of copper. Clear signs of deposition is evident on the surface.

Figure 6.40 and 6.41 shows the impact of plasma operation on graphite. As with copper, there is some noticable deposition on the surface.

The images for BN (Figure 6.42 and 6.43) do not show major surface change but based on the Langmuir probe studies it was speculated that e-beam evaporation of BN surface does take place. The Lieca microscope used to image in this study does not provide the resolution to see surface details. However, figure 6.44 obtained when observing an area that was exposed to plasma with an area covered by the material holding assembly shows clearly a deposition layer on the area that was exposed to plasma.

The observed evolution of surfaces may impact the magnitude of the SEE flux into

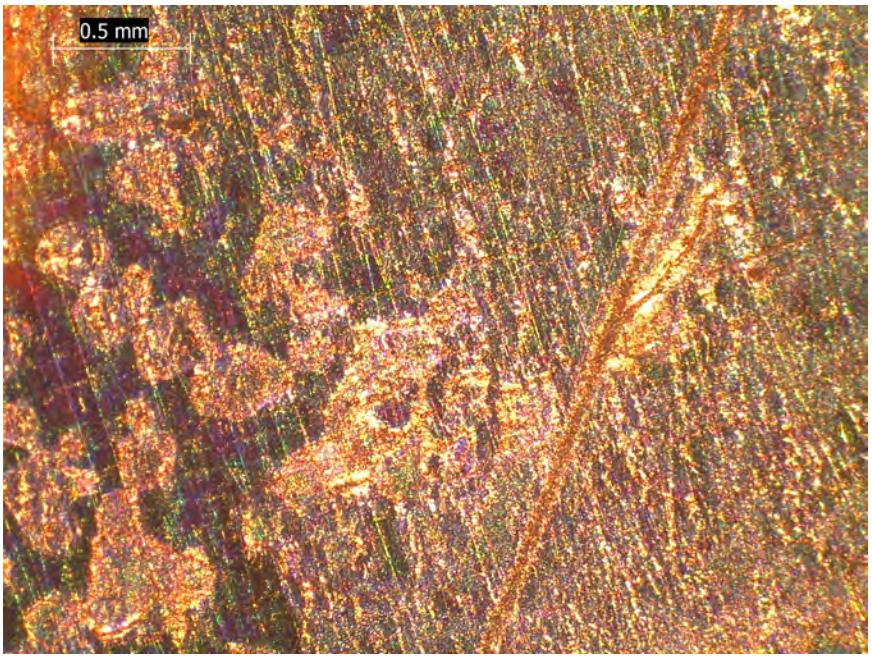

Figure 6.39: Post test copper image (35x zoom).

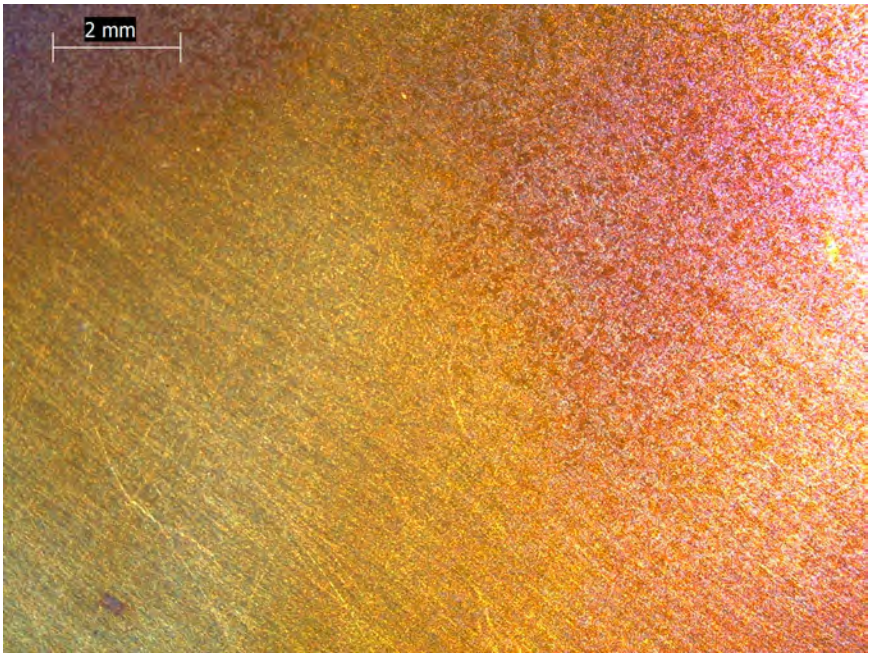

Figure 6.40: Post test graphite image (8x zoom).

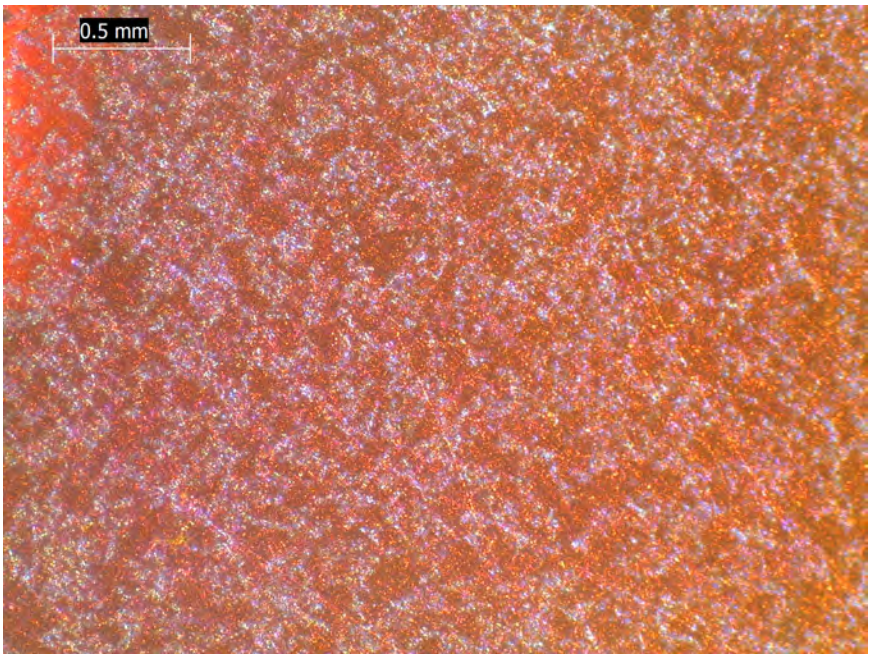

Figure 6.41: Post test graphite image (35x zoom).

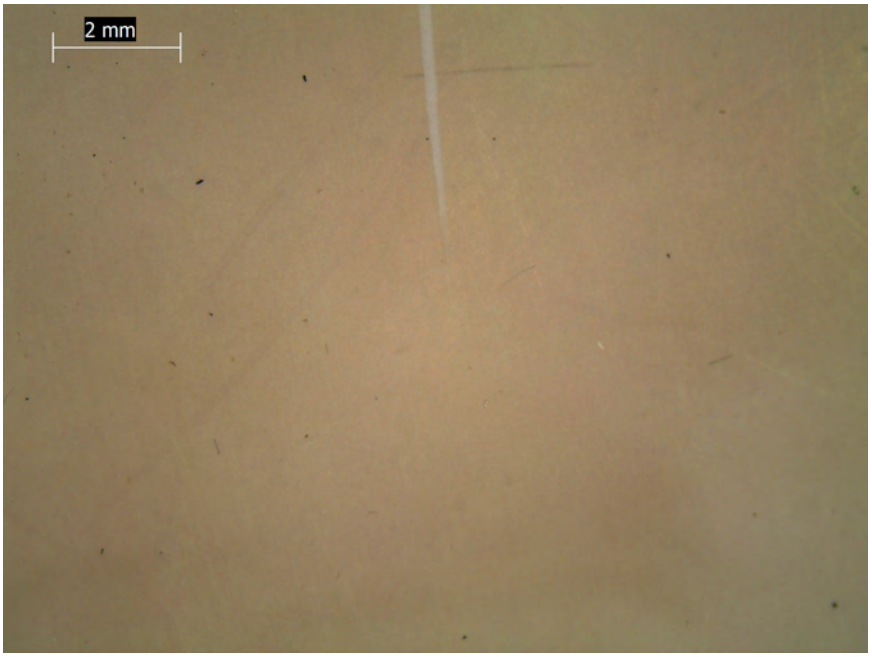

Figure 6.42: Post test BN image (8x zoom).

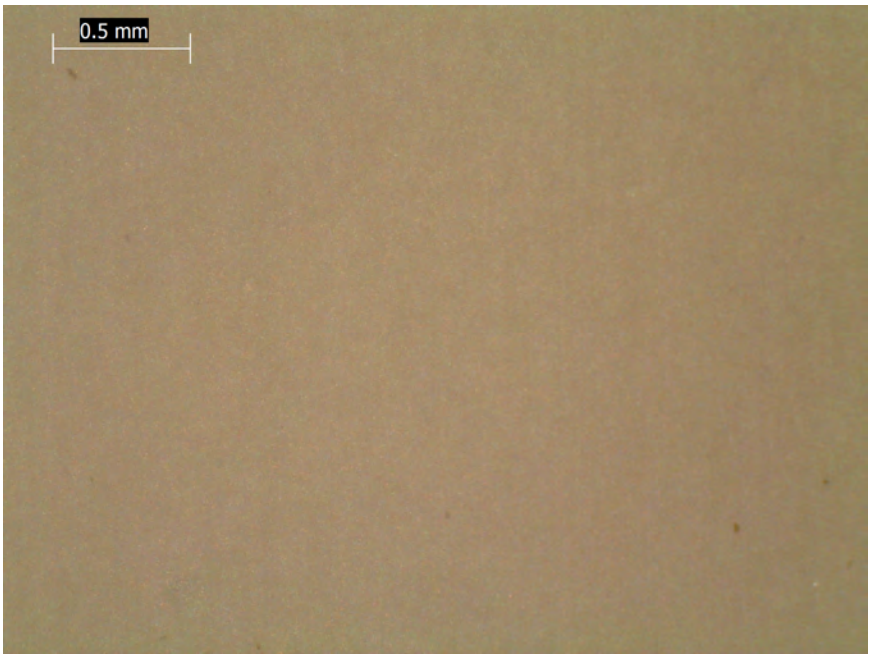

Figure 6.43: Post test BN image (35x zoom).

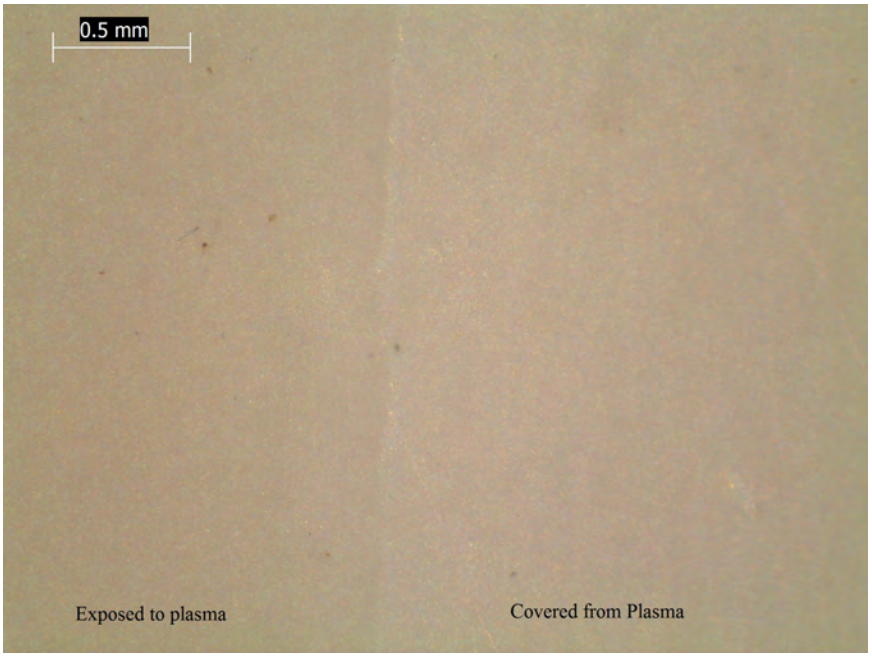

Figure 6.44: Comparison of plasma treated area vs untreated area of BN (35x zoom).

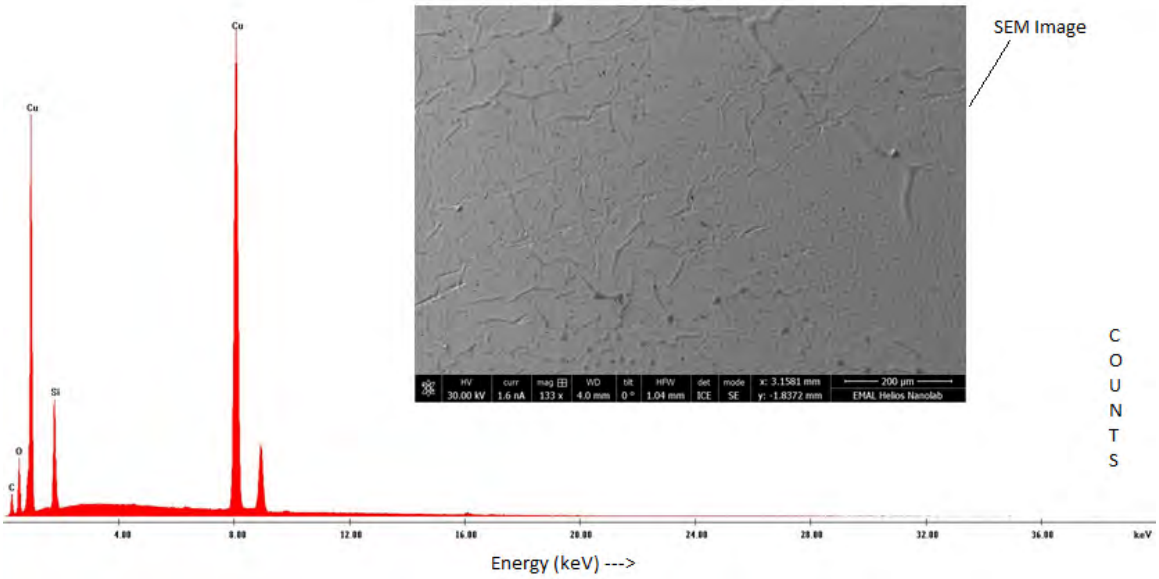

Figure 6.45: Energy dispersive spectroscopy of Copper.

the plasma. A more detailed surface characterization may yield additional information on the nature of the coatings. While oxide layers (for copper) strongly suggest change in SEE yield, the non-uniform deposition yields different results at different sections of investigation.

In order to understand the surface properties post test, all samples were analyzed using scanning electron microscope (SEM) imaging and energy dispersive spectroscopy (EDS). On all surfaces (copper, graphite, and HP BN) a spread of carbon, oxygen and silicon was found. Figure 6.45 shows the EDS information and allows determination of elements as seen on the surface. Figure 6.46 shows the relative intensity of each contributing element. Similar graphs were obtained for BN and graphite showing contribution from their respective compositions but also surface contaminants of silicon, oxygen, and carbon.

The presence of oxygen for copper is indicative of oxide layers, and carbon is likely due to facility and experimental effects. Silicon may have been deposited during the polishing process which used silicon carbide paper to polish the surface. SEM images of both BN (HP grade) and copper are shown in figure 6.47. Further analysis of the

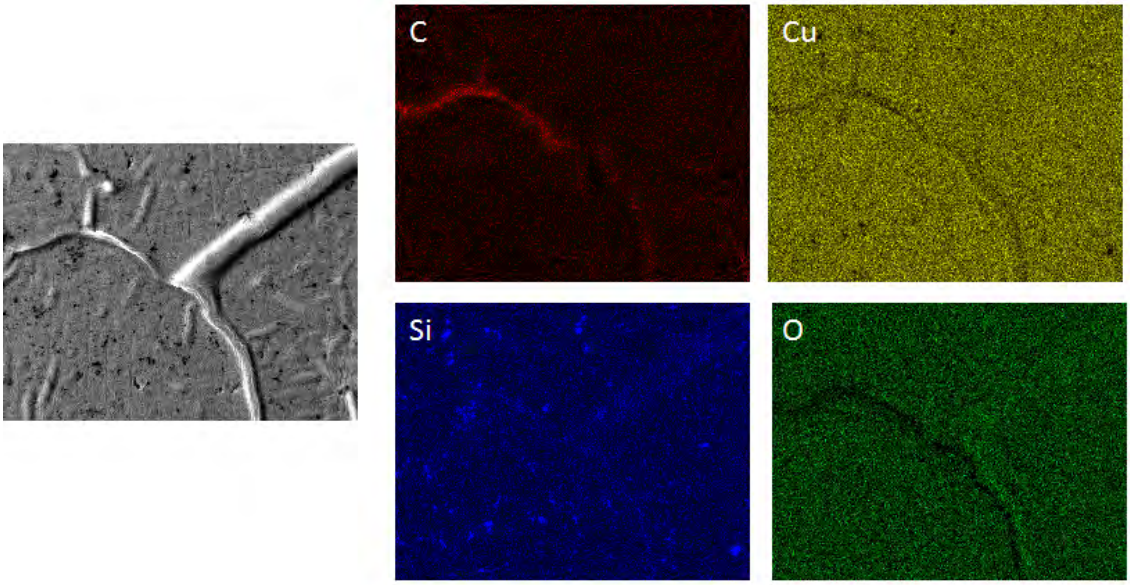

Figure 6.46: Elemental contribution on surface of copper.

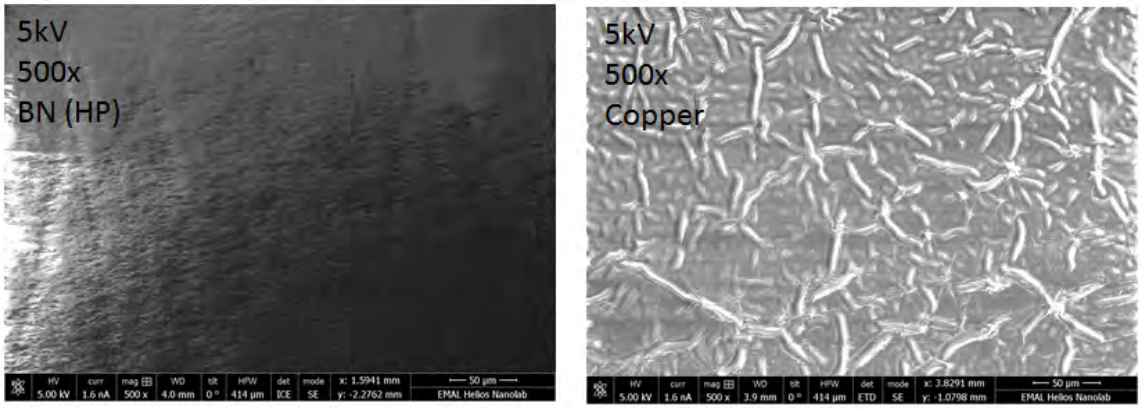

Figure 6.47: SEM images of BN (HP grade) and copper.

materials and material processing protocols need to be followed to understand the material impact of SEE.

CHAPTER VII

Conclusion and Future Work

"*It is better to know some of the questions than all of the answers.*"

- James Thurber

"*Questions may be more important than answers. In the sciences, most answers found are temporary, and the questions remain.*"

- Benjamin F. Plybon

7.1 Summary of Research Intent

A better understanding of the effects of secondary electrons in plasma devices can not only aid our current understanding of such systems but also provide an additional way to optimize plasma systems. For Hall thrusters, the SEE generated due to plasma interaction with the channel walls have been suggested to impact several macroscopic phenomena such as rotating spokes and wall sputtering rate and to modify microscopic elements such as plasma electron temperature and local energy distributions of electrons. The goal of this work is to design a system capable of studying the effects of SEE on a known plasma environment using a controllable electron beam source and study the interactions on the plasma sheath near the wall as well as the bulk plasma parameters. Information obtained would be used to better model SEE interactions with plasma to aid in future designs and improve system

performance.

7.2 Conclusions

In order to study the effects of SEE on plasma, a bench-top apparatus was proposed, designed and tested. The design sought to include a wide range of parameters that could impact SEE yield and thus the response of plasma in SEE. The experimental apparatus contains of a pair of Helmholtz coils capable of generating up to 200 Gauss of magnetic field continuously (or up to 300 Gauss pulsed) without external cooling. The choice of magnetic field strength was to provide similarity to those used in Hall thrusters. This can be seen in Figure 3.2. Under these conditions, for the system dimensions, the electrons are magnetized while leaving the ions unmagnetized.

The plasma source employed for this experiment was generated using a coiled thoriated-tungsten filament. The cathode source had a long life ($>$ 25 hours per test). It was changed after each experiment to ensure repeatability of measurements. Although the coiled filaments were made by hand, care was taken to ensure repeated number of coils without any kinks. The power consumption for all filaments used to create a plasma discharge had a variation of less than 10 W and was made from the same batch of wire. The discharge was set between a copper plate (anode) and the filament (cathode). While the discharge fluctuated around 10 V during the source operations, the general trend was consistent with all materials tested. The hysteresis in voltages (and discharge power) is consistent with other plasma source hysteresis and could be attributed to the evolving nature of the anode plate and other grounded surfaces. Visible deposition layer was observed on the anode surface causing the breakdown voltage to increase.

A low energy, high current electron gun was designed, built and characterized. The small size of the electron gun chosen to fit in the electromagnet spool was operated using a coiled thoriated tungsten filament. Like the filament used to generate plasma,

these filaments had a very long lifetime and were made using the same spool of wire of diameter 2.28 mm. The electron gun was tested both in vacuum as well as in plasma environments prior to being used for the test with different materials. The beam behaved as expected at low energies having a Gaussian profile. However, at higher energies the beam was highly anisotropic across both axes and showed wing like structures. From beam theory, these structures are expected at higher voltage operation and can be attributed to one of many factors - warping of filaments due to thermal expansion, 2-D Child-Langmuir evolution as well as optics effects due to large grid openings. From RPA data, it is was evident that the beam quality improved in plasma in comparison to vacuum operation. This is possibly due to large degree of ionization closer to the electron gun grid. Also, the ratio of current produced by the filament to that lost to the grids increased in a plasma environment.

Different materials were used in this study to understand the effect of SEE on plasma properties. These materials included HP grade BN, high density graphite, and Copper. The materials have varying SEE coefficient as well as different electronic behavior. The conducting materials such as copper and graphite were grounded, whereas the insulator (BN) acted as a floating target in the study. The material size was chosen to enclose it in a framed holder with an angle fixture allowing the target material to be held at different angles in 15 degree increments with respect to the electron beam. This increases the capability of the system to study the angular dependence of SEE. Also, a Peltier thermoelectric device was chosen to fit in the center of the target to allow temperature based studies. All materials used in this study were polished and had the surface roughness characterized.

Computer controlled programs were developed as part of the project to allow for real time monitoring of macroscopic electrical parameters such as voltages and currents of various components as well as control of multiple power supplies. The remote operation mode allowed for a single point observation and control of the

experiment as well as provided limited capability in analyzing large collection of data files. The file management system included redundancies and event tracking to allow large collection of data. To speed the data collection, newer versions of the software minimized the number of read - write requests and stored a large array of data in memory. Four main programs were developed - the main control code that performed data acquisition and control of several key systems from a single point using serial communication interfaces, electron beam energy code controlled diagnostic tools to change discriminator bias as well as capture current signals, electron beam profile code allowed control of 3-axis motion system as well as diagnostic power supplies to map the beam profile at different bias voltages, and sheath profile code used to control a 2-axis motion system and diagnostics at various axial and transverse locations to map the sheath potential profile.

The design goal of the thesis was to develop a bench-top apparatus capable of studying all parameters that could change SEE yield and thus its impact on plasma properties. However, the characterization goal for this thesis was to study the influence that primary electrons have on the plasma for the materials of interest. The analysis of the characterization led to observations that are summarized in the following list:

- The presence of electron beam in plasma contributes to not only a rise in temperature but also instability. Two bumps were observed in RPA analysis of electron beam in plasma and on application of Penrose criterion, it was found that the beam-plasma system was marginally unstable. This unstable system could enhance ionization and should be investigated in future.

- The sheath of the irradiated samples changes and is a clear function of the beam energy. In particular, a trend was observed when electrons at higher beam energy were injected in to the target surface compared to the SEE yield threshold. The competition between the increasing effective temperature of the

plasma and the rise of SEE yield as a function of beam energy was consistently observed for all materials.

- The EEDF shows the depletion of tail which suggests loss of energetic electrons due to SEE. However, the presence of other beam components make the analysis non-trivial.

- It is seen that the material evolves constantly, with layers of deposited materials that have the potential to change the SEE yield. It is therefore suggested that future work should include some form of surface monitoring / characterization between tests.

7.3 Implication for Hall Thrusters

From the sheath potential profiles mapped in this study, it is clearly seen that as the beam energy into the target increases, the absolute sheath potential increased with increasing plasma temperature. This is accompanied by increasing secondary electron yield which is a function of the material for a given energy. Further increase would result in lowering of electron temperature as most energetic particles are lost to the wall. Based on these observations, the following can be concluded for HETs:

- The high energy electrons in the tail of the EEDF get depleted and lost to the wall with increasing SEE yield. This loss of energetic particles can lower the ionization efficiency of the thruster.

- Energy lost by the plasma leads to cooling of the plasma which is not desirable in terms of ionization efficiency. Although this cooling maybe beneficial in terms of allowing low temperature materials to be used for construction.

- The power lost to the wall is manifested by heating the wall surface. This is usually seen as an orange glow of the discharge channel.

Also, it was seen that presence of beams in plasma under certain conditions can lead to instabilities of the discharge. This can be seen by observing the curvature of the multi-bump distribution by measuring the local plasma distribution. These instabilities could be responsible for some of the known characteristics of HETs such as rotating spoke. Further study is required to quantify the influence of SEE induced instability.

7.4 Future Work

Based on the study, a number of questions have arisen. A few of these questions are summarized below and some potential avenues of future research discussed further.

- How does the marginally unstable beam-plasma system impact fundamental processes and SEE processes?
- How does the evolving material surface due to facility effects and other deposition sources impact the plasma? At different time scales?
- What is the role of ions to the walls in presence of plasma at different operation conditions, such as pressure, discharge current, and magnetic fields?
- What would be the sheath profile under varying magnetic fields?
- Is it possible to accurately determine the SEE yield by conducting in-situ measurements with and without plasma?

The experiment was designed to be as comprehensive as possible which could see continuation of work by other researchers in the plasma science and technology laboratory (PSTL) over the years to come. Figure 7.1 shows a sample set of experiments that can be conducted on this test bed both for academic and research interests. This dissertation only covered a small subset of the potential applications that can be explored with the testbed.

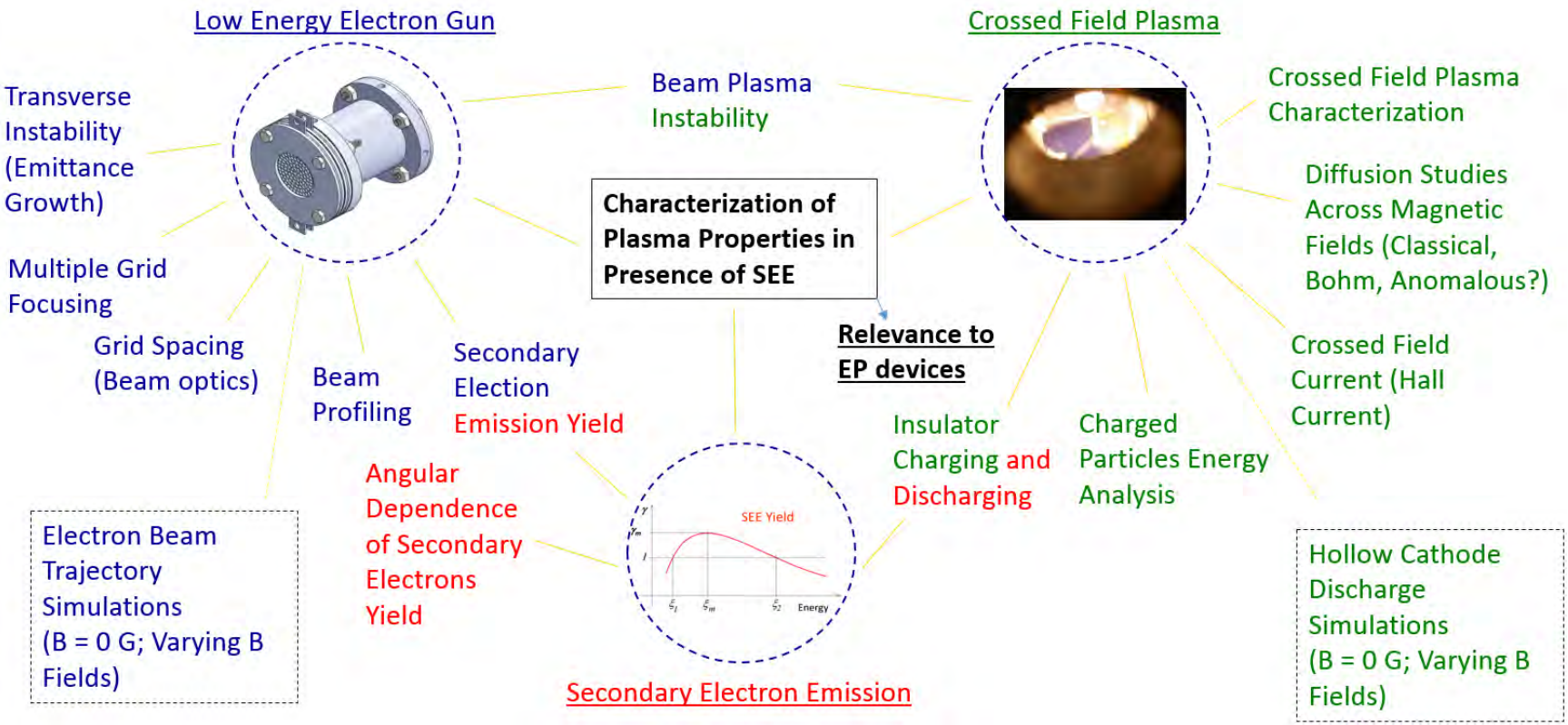

Figure 7.1: Range of experiments that can be conducted on this test-bed.

The following provides some possible suggestions on development of future experiments with respect to SEE interactions in a crossed field plasma device.

7.4.1 Electron Gun Experiments

A low energy, high current electron gun was built and characterized for this experiment. The design allows implementation for multiple grids as seen in chapter V. Multiple grids provide the ability to shape the beam profile with greater control[175]. An improvement in electron gun profile and reduction in the energy spread of the beam will be useful in plasma SEE interaction studies.

Another aspect for improvement for this experiment would be the ability to operate the electron gun in pulse modes. The pulsing could be accomplished using electrical methods by rapidly reducing the power supply voltage or by mechanical methods such as a beam chopper. The pulse operation mode should be helpful in determination of EEDF using Langmuir probes by measuring only during the times when the electron beam from the electron gun is absent. Such measurements would require a better control of both the electron gun operation as well as having the ability to synchronize time resolved measurements leading challenges in not only electron gun design but fast diagnostic measurements too.

Finally, it would be ideal to develop a "constant-power" power supply. In this experiment, the electron current generated from the electron gun is directly related to the applied voltage. The maximum emission current is thus given by the Fowler-Nadhein-Bethe-Sommerfield equation 5.16. In all experiments conducted in this thesis, the filament current was kept constant to provide thermionic electrons. As a consequence of the constant current operation of the filament, the beam current changed as a function of applied beam voltage. The energy of the electrons and the actual current density were coupled. In order to keep a constant beam current but have the ability to modify the energy of the beam, a feedback loop must be developed

which can change the filament current to match the required beam current for a given voltage at the desired target. The choice of feedback signal (emission current or target beam current) is not trivial and would require calibration as it would be coupled to the plasma current. Most commercial systems employ the emission current as a choice of feedback signal and would be an ideal choice for this system as well. There are no commercially available electron guns that work in plasma without significant modification of the electron gun design.

7.4.2 Vacuum SEE Experiments

With the recent addition of a working ultra high vacuum (UHV) facility at PSTL, it would be recommended that the SEE test should be conducted in that chamber which allows the ability to detect SEE due to its operational capability towards 10^{-12} Torr. A hemispherical dome may be used to determine the SEE yield and addition of grids will help obtain the energy distribution of the secondaries for a material.

7.4.2.1 Surface Charge Measurements

It is recommended that the charge of the surface be measured in order to check for charge neutrality on the surface, especially in the case of insulators. This can be achieved using Kelvin probes for measurements of surface potentials. These probes provide a non-intrusive and non-destructive method to study the variation of surface potential and thus can allow determination of surface charges. It also provides a potential for in-situ measurements before and after plasma-beam interactions with the target material. In its simplest form, it uses a vibrating capacitor to measure surface potential differences between the target sample and a vibrating electrode. Details of this technique can be found in the following literature references [184, 185].

7.4.3 Plasma SEE Experiments

In this study, the impact of electron energy on the wall material is studied. As discussed in section 2.3, there are several other parameters that effect the SEE yield and can potentially impact plasma properties. The following lists the suggested parameters that should be investigated for SEE impact on plasma properties. These studies should be conducted in the ultra high vacuum facility as it allows for in-situ measurements of SEE before and after plasma exposure.

1. Influence of Impact Angle
2. Influence of Magnetic Field Strength and Magnetic Field Topology
3. Influence of Surface Roughness
4. Influence of Surface Composition and Morphology
5. Influence of Material Temperature

7.4.4 Suggestion to Improve Plasma Source

The filament driven plasma source is easy, cheap, and a fast way to generate plasma. It also makes obtaining a low density plasma convenient which aids in obtaining a thick sheath. Despite its advantages, which proved useful for this experiment allowing exploration of sheath using electrostatic emitting probes, there is a considerable challenge to extract information from Langmuir probes accurately with multiple beam components - electron gun, primary electrons from plasma filaments, secondary emission from target and other surfaces. Any other source may yield considerably higher plasma density making the sheath considerably smaller, but would provide better I-V characteristics to extract EEDF information as well as temperature and density information accurately. The choice of the source is hard as most RF techniques would give a higher density and a hollow cathode would introduce flowing

conditions which complicates analysis. Allowing a diffusion plasma source may lead to gradients in the plasma. Any technique to generate a plasma may pose challenges for an experiment of this nature. Ability to quickly sweep plasma properties using a fast sweeping Langmuir probe [10] may aid in the operation of the plasma source. In the end, there seem to be limited choices available to improve the source design and a trade-off must be made between thick sheath for electrostatic measurements or a higher density plasma with fewer beam components.

7.4.5 Suggestion to Improve Plasma Diagnostics

From this study, it is clear that the analysis of such systems is complicated due to many parameters such as signal to noise, multiple beam presence, and several parameters that can be potentially investigated. A fast sweeping Langmuir probe which can rapidly collect spatial information of the plasma properties would be ideal as the electron beam operated between 20 - 60 eV is higher than the ionization potential of the plasma. Gathering data on the evolution of plasma both spatially and temporally would aid in better understanding of the system. Other suggestions on improving diagnostics are listed below.

7.4.5.1 Double and Triple Probes

The use of double probes (symmetric and asymmetric) may be useful for this application. Although the fluctuations in the plasma are small, double probes would help in reduction of noise due to reference electrode closer to the system in the presence of an electron beam. Another advantage of double probes is they work better in moderate magnetic fields [142, 186]. The analysis of the I-V characteristics assumes Maxwellian electrons, which may lead to errors in results. Asymmetrical double probes provide better results than symmetrical double probes.

Triple probes are beneficial for use in pulsed environments and can provide infor-

mation on n_e and T_e directly without the need of I-V characteristics. As suggested earlier, development of a pulsed beam source to obtain the impact of SEE on plasma may be a better approach to gain greater insight of the system. These probes can be used in the system. Eckman et al. [187] describe the use of triple probe and its analysis for a pulsed plasma thruster plume.

7.4.5.2 Gridded Langmuir Probes

The I-V characteristics obtained from a Langmuir probe provides information on several plasma parameters and gives the EEDF information. However, the technique does not provide the ability to differentiate between the kinetic energy and potential energy of charged particles. Typically it is seen from the probe characteristics that the ion current is not a strong function of the probe bias, and the energetic electrons in the tail of the distribution are super-imposed and often subtracted out while analyzing the characteristics. Greater control on the populations can be obtained, resulting in better EEDF measurements, using the gridded Langmuir probe. Ingram et al. [188] describe a way to design and use a gridded Langmuir probe for a low - pressure rf argon discharge.

7.4.5.3 Ball-Pen Probes

It was shown in section 4.2 that in order to make the floating potential approach the plasma potential, one technique is to heat the probe to emit electrons strongly such that the potentials match. Since the goal of this work is to study the effects of secondary electrons on plasma, avoiding production of thermionically emitted electrons from the emissive probes would be ideal. Another major disadvantage of emissive probes is the limited lifetime due to potential oxidation of surfaces as well as evaporation and sputtering of the wire when immersed in plasma. The maximum emitted current is also limited by the size of the wire keeping optimized for a finite

experimental lifetime.

In order to avoid the disadvantages of emissive probes, another method to find the plasma potential is to reduce the plasma electron saturation by using a ball pen probe to make the magnitude of the electron saturation with the ion saturation current similar. This is done by retracting the collector pin of the probe until the electron saturation current reaches the ion saturation current of a classical Langmuir probe inside an insulating tube. When the electron current decreases to the ion saturation current, the I-V characteristic becomes symmetric and the plasma potential is equal to the floating potential. References [189, 190, 191] provide information on design and use of such probes, also known as Katsumata probe. These probes have also been applied to low temperature magnetized plasma for potential measurements [192], eliminating the issues of high magnetic field forces on current carrying conductor as discussed in section 4.2.7.

7.4.5.4 Plasma Resonance Probes

It is known that the plasma parameters obtained using Langmuir probes are subject to huge uncertainties. This is mainly due to the presence of noise due to experimental conditions and measurement instruments as well as due to surface contamination. Despite these effects, the electron temperature is reliably measured, but electron density is hard to determine. For low density plasmas, as was seen in this thesis I-V characteristic analysis, the sharp knee distinguishing the electron saturation region was not clear.

In order to improve the accuracy of the probes a number of rf techniques have been suggested [193]. Among these rf methods, the resonance probe method is particularly promising [194] and should be explored in the future. It is capable of making electron density measurements in time scales comparable to a few periods of the plasma frequency (ω_{pe}) and can also be used to obtain the electron-neutral collision frequency.

Using multiple resonance probes allows determination of the electron density independent of the plasma temperature. Details of this technique along with how they operate can be found in the following references [194, 195, 196, 197] and the references therein.

7.4.6 Experimental and Numerical Validation

Design of a complete plasma system with the ability to modify several parameters is a complex and expensive task. With ever increasing computational power, it is often advisable to simulate the system and tweak its performance before an experimental hardware is built and characterized. Required for such an approach is an acceptable code which has been validated with test case data. Many codes exist that are intended for general purpose plasma simulations as well as ones to specifically simulate Hall thruster physics, such as HPHall. Collaboration is underway with Ken Hara to understand the effects seen in this study with his kinetic code.

7.4.7 EEDF Measurement

It was observed from this study that determination of EEDF using numerical smoothing and numerical differentiation methods may not be ideal for this application. Underlying reasons for this is due to the difficulty in accurately determining SEE contribution in presence of other high energy electron species. Fast hardware methods such as second harmonic using lock-in amplifier may work better for determining EEDF.

7.4.8 Sheath Saturation

The tests conducted in this study only captured the effects of increasing effective temperature and SEE yield. In theory, if more energy is provided, a saturation regime can be observed based on Hobbs and Wesson [49]. It would be beneficial to

demonstrate that in future studies.

BIBLIOGRAPHY

BIBLIOGRAPHY

[1] John R Brophy and Brian Muirhead. Near-earth asteroid retrieval mission (arm) study. In *33rd International Electric Propulsion Conference, Washington, DC, October 6–10, 2013*. Pasadena, CA: Jet Propulsion Laboratory, National Aeronautics and Space Administration, 2013, 2013.

[2] Jerome Pearson. Asteroid retrieval by rotary rocket. *AIAA Paper*, pages 80–0116, 1980.

[3] Steven Oleson. Electric propulsion technology development for the jupiter icy moon orbiter project. *AIAA Paper*, 3449, 2004.

[4] Michael Keidar and Isak I Beilis. Electron transport phenomena in plasma devices with e/spl times/b drift. *Plasma Science, IEEE Transactions on*, 34(3):804–814, 2006.

[5] Yevgeny Raitses, Igor D Kaganovich, Alex V Khrabrov, Michael D Campanell, Erinc Tokluoglu, Dmytro Sydorenko, and Andrei Smolyakov. Effect of secondary electron emission on electron cross-field current in exb discharges. In *APS Meeting Abstracts*, volume 1, page 2010, 2012.

[6] D Sydorenko, A Smolyakov, I Kaganovich, and Y Raitses. Plasma-sheath instability in hall thrusters due to periodic modulation of the energy of secondary electrons in cyclotron motion. *Physics of Plasmas (1994-present)*, 15(5):053506, 2008.

[7] E Ahedo. Presheath/sheath model with secondary electron emission from two parallel walls. *Physics of Plasmas (1994-present)*, 9(10):4340–4347, 2002.

[8] L Jolivet and JF Roussel. Effects of the secondary electronic emission on the sheath phenomenon in a hall thruster. In *Spacecraft Propulsion*, volume 465, page 367, 2000.

[9] N Gascon, M Dudeck, and S Barral. Wall material effects in stationary plasma thrusters. i. parametric studies of an spt-100. *Physics of Plasmas (1994-present)*, 10(10):4123–4136, 2003.

[10] Michael J Sekerak. *Plasma oscillations and operational modes in hall Effect Thrusters*. PhD thesis, University of Michigan, 2014.

[11] Rohit Shastry. *Experimental characterization of the near-wall region in Hall thrusters and its implications on performance and lifetime*. PhD thesis, Jet Propulsion Laboratory, 2011.

[12] Richard Robert Hofer. *Development and characterization of high-efficiency, high-specific impulse xenon Hall thrusters*. 2004.

[13] Kurt A Polzin and Steven Peeples. Iodine hall thruster propellant feed system for a cubesat. In *50th Joint Propulsion Conference, Cleveland, OH*, 2014.

[14] FF Chen. Intro. to plasma physics and controlled fusion, vol. 1, 1984.

[15] Alexander Fridman. *Plasma chemistry*. Cambridge University Press, 2008.

[16] Alexander Fridman and Lawrence A Kennedy. *Plasma physics and engineering*. CRC press, 2004.

[17] Michael A Lieberman and Allan J Lichtenberg. Principles of plasma discharges and materials processing. *MRS Bulletin*, 30:899–901, 1994.

[18] Paul M Bellan. *Fundamentals of plasma physics*. Cambridge University Press, 2006.

[19] ESA's Space Environment Information System Sheath and Pre-Sheath. *https://www.spenvis.oma.be/ecss/e_st_20_06c/ecss_14_03_05.htm*. Spenvis, 2014.

[20] Hong Li. *Measurements of electron energy distribution function and neutral gas temperature in an inductively coupled plasma*. PhD thesis, University of Saskatchewan, 2006.

[21] Valery A Godyak. Nonequilibrium eedf in gas discharge plasmas. *IEEE transactions on plasma science*, 34(3):755, 2006.

[22] DR Boris, GM Petrov, EH Lock, Tz B Petrova, RF Fernsler, and SG Walton. Controlling the electron energy distribution function of electron beam generated plasmas with molecular gas concentration: I. experimental results. *Plasma Sources Science and Technology*, 22(6):065004, 2013.

[23] VA Godyak, RB Piejak, and BM Alexandrovich. Probe diagnostics of non-maxwellian plasmas. *Journal of applied physics*, 73(8):3657–3663, 1993.

[24] VA Godyak and VI Demidov. Probe measurements of electron-energy distributions in plasmas: what can we measure and how can we achieve reliable results? *Journal of Physics D: Applied Physics*, 44(23):233001, 2011.

[25] Sang-Heon Song. *Control of plasma kinetics for microelectronics fabrication*. PhD thesis, The University of Michigan, 2014.

[26] Stéphane Mazouffre. Laser-induced fluorescence diagnostics of the cross-field discharge of hall thrusters. *Plasma Sources Science and Technology*, 22(1):013001, 2013.

[27] Christopher J Durot, Alec D Gallimore, and TB Smith. Development of a novel time-resolved laser-induced fluorescence technique. *Rev. Sci. Instrum., in review.*, 2013.

[28] EAD Carbone, S Hübner, M Jimenez-Diaz, JM Palomares, E Iordanova, WAAD Graef, A Gamero, and JJAM van der Mullen. Experimental investigation of the electron energy distribution function (eedf) by thomson scattering and optical emission spectroscopy. *Journal of Physics D: Applied Physics*, 45(47):475202, 2012.

[29] John B Boffard, RO Jung, Chun C Lin, and AE Wendt. Optical emission measurements of electron energy distributions in low-pressure argon inductively coupled plasmas. *Plasma Sources Science and Technology*, 19(6):065001, 2010.

[30] FM Dias. Fast eedf probe measurement in surface wave discharges using a dc coupled stepped signal. *Plasma Sources Science and Technology*, 4(1):86, 1995.

[31] Aasim Azooz. Analog data acquisition for obtaining iv characteristics using sound cards. *Computing in science & engineering*, 8(4):10–15, 2006.

[32] Erhan Kudeki and David C Munson. *Analog signals and systems*. Pearson Prentice Hall, 2009.

[33] PK Chakravarti and SN Sen Gupta. Determination of electron energy distribution in a plasma. *Review of Scientific Instruments*, 48(10):1344–1349, 1977.

[34] JI Fernández Palop, J Ballesteros, V Colomer, and MA Hernandez. A new smoothing method for obtaining the electron energy distribution function in plasmas by the numerical differentiation of the i-v probe characteristic. *Review of Scientific Instruments*, 66(9):4625–4636, 1995.

[35] RH Sloane and EIR MacGregor. Xv. an alternating current method for collector analysis of discharge-tubes. *The London, Edinburgh, and Dublin Philosophical Magazine and Journal of Science*, 18(117):193–207, 1934.

[36] B Crowley and S Dietrich. A langmuir probe system incorporating the boyd–twiddy method for eedf measurement applied to an inductively coupled plasma source. *Plasma Sources Science and Technology*, 18(1):014010, 2009.

[37] JE Heidenreich III, JR Paraszczak, M Moisan, and G Sauve. Electron energy distributions in oxygen microwave plasmas. *Journal of Vacuum Science & Technology B*, 6(1):288–292, 1988.

[38] John Foster. *An Investigation of the Influence of a Transverse Magnetic Field on the Formation of Large Anode Fall Voltages in Low Pressure Arcs*. PhD thesis, University of Michigan, Ann Arbor, 1996.

[39] Robert G Lye and AJ Dekker. Theory of secondary emission. *Physical Review*, 107(4):977, 1957.

[40] H Salow. Sekundarelektronen-emission. *Phys. Z*, 41:434–436, 1940.

[41] Hajo Bruining. Physics and applications of secondary electron emission. 1954.

[42] EM Baroody. A theory of secondary electron emission from metals. *Physical Review*, 78(6):780, 1950.

[43] JR Young. Dissipation of energy by 2.5–10 kev electrons in al2o3. *Journal of Applied Physics*, 28(5):524–525, 1957.

[44] David B Williams and C Barry Carter. *The Transmission Electron Microscope*. Springer, 1996.

[45] Dan M Goebel and Ira Katz. *Fundamentals of electric propulsion: ion and Hall thrusters*, volume 1. John Wiley & Sons, 2008.

[46] XZ Yao and DY Jiang. Effect of secondary electron emission on sheath potential in an electron cyclotron resonance plasma. *Journal of applied physics*, 81(5):2119–2123, 1997.

[47] Michael D Campanell. *Plasma interaction with electron-emitting surfaces*. PhD thesis, PRINCETON UNIVERSITY, 2014.

[48] Pandey B. P and Subrata Roy. Sheath in the presence of secondary electron emission and sputtering yield. In *36th AIAA Thermophysics Conference, Orlando FL*, 2003.

[49] GD Hobbs and JA Wesson. Heat flow through a langmuir sheath in the presence of electron emission. *Plasma Physics*, 9(1):85, 1967.

[50] Kentaro Hara and Iain Boyd. Direct kinetic simulation of collisionless sheath in the presence of secondary electron emission. *DOE Center for Predictive Control of Plasma Kinetics: Multi-Phase and Bounded Systems*, page 54, 2013.

[51] Kentaro Hara, Iain Boyd, and Vladimir Kolobov. One dimensional hybrid-vlasov simulation of a hall thruster. In *48th AIAA/ASME/SAE/ASEE Joint Propulsion Conference & Exhibit*, 2012.

[52] BH Foing, GD Racca, A Marini, E Evrard, L Stagnaro, M Almeida, D Koschny, D Frew, J Zender, J Heather, et al. Smart-1 mission to the moon: status, first results and goals. *Advances in Space Research*, 37(1):6–13, 2006.

[53] Daniel D Mazanek, Raymond G Merrill, Scott P Belbin, David M Reeves, Kevin D Earle, Bo J Naasz, and Paul A Abell. Asteroid redirect robotic mission: Robotic boulder capture option overview. *Paper AIAA-XXX*, 2014.

[54] Edgar Y Choueiri. A critical history of electric propulsion: The first 50 years (1906-1956). *Journal of Propulsion and Power*, 20(2):193–203, 2004.

[55] Frank M Curran. Electric propulsion activities in us industry. In *26th International Electric Propulsion Conference, Kitakyushu, Japan*, 1999.

[56] Vlad Hruby. Review of electric propulsion activites in the us industry. *World*, 80:90, 2003.

[57] Danel A Lichtin. An overview of electric propulsion activities in us industry–2005. *AIAA Paper*, 3532, 2005.

[58] Ronald A Spores, Gregory G Spanjers, Mitat Birkan, and Timothy J Lawrence. *Overview of the USAF Electric Propulsion Program*. Defense Technical Information Center, 2001.

[59] Ronald A Spores and Mitat Birkan. The usaf electronic propulsion research program. Technical report, DTIC Document, 2002.

[60] Alec D Gallimore, Rodney L Burton, Mark A Cappelli, Edgar Y Choueiri, James C Dickens, Nathaniel J Fisch, NikoS A GatSOnis, Andrew D Ketsdever, Manuel M Martinez-Sanchez, and Paul J Wilbur. 37th aiaa/asme/sae/asee joint propulsion conference & exhibit. 2001.

[61] Paul J Wilbur. 38th aiaa/asme/sae/asee. *Ann Arbor*, 1001:48109–2140, 2002.

[62] L Brad King. Review of the ep activities of us academia. 2004.

[63] Franck Darnon, Denis Arrat, Enrico Chesta, Stéphane dEscrivan, and Nicolas Pillet. An overview of electric propulsion activities in france. In *29th International Electric Propulsion Conference*, 2005.

[64] Vladimir Kim, Garri Popov, Boris Arkhipov, Vyacheslav Murashko, Oleg Gorshkov, Anatoly Koroteyev, Valery Garkusha, Alexander Semenkin, and Sergei Tverdokhlebov. Electric propulsion activity in russia. *IEPC Paper*, 5:2001, 2001.

[65] G Saccoccia. Overview of european electric propulsion activities. In *37th AIAA Joint Propulsion Conference, Salt Lake City*, 2001.

[66] Robert G Jahn. *Physics of electric propulsion*. Courier Dover Publications, 2012.

[67] Lyon B King. A (re-) examination of electron motion in hall thruster fields. In *29th International Electric Propulsion Conference*, 2005.

[68] Vadim Khayms and M Martinez-Sanchez. Design of a miniaturized hall thruster for microsatellites. *AIAA*, 3291:1–3, 1996.

[69] Yevgeny Raitses, Artem Smirnov, and Nathaniel J Fisch. Cylindrical hall thrusters. *AIAA*, 3245:2006, 2006.

[70] Brandon Robert Weatherford. *Development and Study of an Electron Cyclotron Resonance Waveguide Plasma Cathode for Electric Propulsion Applications*. PhD thesis, University of Michigan, Ann Arbor, 2011.

[71] Michael Sean McDonald. *Electron transport in Hall thrusters*. PhD thesis, University of Michigan, Ann Arbor, 2012.

[72] Jesse Allen Linnell. An evaluation of krypton propellant in hall thrusters. 2007.

[73] CL Ellison, Y Raitses, and NJ Fisch. Cross-field electron transport induced by a rotating spoke in a cylindrical hall thruster. *Physics of Plasmas (1994-present)*, 19(1):013503, 2012.

[74] EY Choueiri. Plasma oscillations in hall thrusters. *Physics of Plasmas (1994-present)*, 8(4):1411–1426, 2001.

[75] D Sydorenko, A Smolyakov, I Kaganovich, and Y Raitses. Kinetic simulation of secondary electron emission effects in hall thrusters. *Physics of Plasmas (1994-present)*, 13(1):014501, 2006.

[76] Y Raitses, A Smirnov, D Staack, and NJ Fisch. Measurements of secondary electron emission effects in the hall thruster discharge. *Physics of Plasmas (1994-present)*, 13(1):014502, 2006.

[77] L Garrigues, GJM Hagelaar, C Boniface, and JP Boeuf. Anomalous conductivity and secondary electron emission in hall effect thrusters. *Journal of applied physics*, 100(12):123301, 2006.

[78] RR Hofer, BA Jorns, JE Polk, IG Mikellides, and JS Snyder. Wear test of a magnetically shielded hall thruster at 3000 seconds specific impulse. *Proc. 33rd IEPC*, 2013.

[79] Dan M Goebel, Richard R Hofer, Ioannis G Mikellides, Ira Katz, James E Polk, and Brandon N Dotson. Conducting wall hall thrusters. 2013.

[80] Nathan B Meezan and Mark A Cappelli. Kinetic study of wall collisions in a coaxial hall discharge. *Physical Review E*, 66(3):036401, 2002.

[81] , , , , , and . Effect of secondary electron emission on the sheath in spt chamber. *Plasma Science and Technology*, 1:013, 2009.

[82] Y Raitses, D Staack, A Smirnov, and NJ Fisch. Space charge saturated sheath regime and electron temperature saturation in hall thrusters. *Physics of Plasmas (1994-present)*, 12(7):073507, 2005.

[83] S Barral, K Makowski, Zbigniew Peradzyński, N Gascon, and M Dudeck. Wall material effects in stationary plasma thrusters. ii. near-wall and in-wall conductivity. *Physics of Plasmas (1994-present)*, 10(10):4137–4152, 2003.

[84] AI Morozov and VV Savel'Ev. Theory of the near-wall conductivity. *Plasma Physics Reports*, 27(7):570–575, 2001.

[85] E Ahedo and FI Parra. Partial trapping of secondary-electron emission in a hall thruster plasma. *Physics of Plasmas (1994-present)*, 12(7):073503, 2005.

[86] Yevgeny Raitses, D Staack, M Keidar, and NJ Fisch. Electron-wall interaction in hall thrustersa). *Physics of Plasmas (1994-present)*, 12(5):057104, 2005.

[87] Peter G Coakley and Noah Hershkowitz. Secondary electrons in a plasma-wall sheath. *Physics Letters A*, 78(2):145–148, 1980.

[88] Michael S McDonald and Alec D Gallimore. Rotating spoke instabilities in hall thrusters. *Plasma Science, IEEE Transactions on*, 39(11):2952–2953, 2011.

[89] Horatiu C Dragnea, Iain D Boyd, Brian C Lee, and Azer P Yalin. Characterization of eroded boron atoms in the plume of a hall thruster. 2013.

[90] Robert Bryant Lobbia. *A time-resolved investigation of the Hall thruster breathing mode*. PhD thesis, UNIVERSITY OF MICHIGAN, 2010.

[91] N Cabrera and NF Mott. Theory of the oxidation of metals. *Reports on progress in physics*, 12(1):163, 1949.

[92] AU Seybolt. Oxidation of metals. *Advances in Physics*, 12(45):1–43, 1963.

[93] AA Azooz. Parametrization of electron energy distribution function in glow discharge plasma under rf electromagnetic fields. *FIZIKA A*, 13(4):151–160, 2004.

[94] U Wolters, Th Daube, KU Riemann, and K Wiesemann. An experimental study of ion currents to a flush mounted langmuir probe in an ecr discharge. *Plasma physics and controlled fusion*, 41(6):721, 1999.

[95] V Yu Bazhenov, AV Ryabtsev, IA Soloshenko, AG Terent'eva, VA Khomich, VV Tsiolko, and AI Shchedrin. Investigation of the electron energy distribution function in hollow-cathode glow discharges in nitrogen and oxygen. *Plasma Physics Reports*, 27(9):813–818, 2001.

[96] P Kudrna and E Passoth. Langmuir probe diagnostics of a low temperature non-isothermal plasma in a weak magnetic field. *Contributions to Plasma Physics*, 37(5):417–429, 1997.

[97] Sang-Hun Seo, Jung-Hwan In, and Hong-Young Chang. Measurements of electron energy distribution functions and electron transport in the downstream region of an unbalanced dc magnetron discharge. *Plasma Sources Science and Technology*, 13(3):409, 2004.

[98] Jean-Louis Jauberteau and Isabelle Jauberteau. Determination of the electron energy distribution function in the plasma by means of numerical simulations of multiple harmonic components on a langmuir probe characteristicmeasurements in expanding microwave plasma. *Measurement Science and Technology*, 18(5):1235, 2007.

[99] OK Mawardi. Use of langmuir probes for low-density plasma diagnostics. *American Journal of Physics*, 34(2):112–120, 1966.

[100] Ira B Bernstein and Irving N Rabinowitz. Theory of electrostatic probes in a low-density plasma. *Physics of Fluids (1958-1988)*, 2(2):112–121, 1959.

[101] R Johnsen, EV Shunko, T Gougousi, and MF Golde. Langmuir-probe measurements in flowing-afterglow plasmas. *Physical Review E*, 50(5):3994, 1994.

[102] Tsv K Popov, P Ivanova, M Dimitrova, J Kovačič, T Gyergyek, and M Čerček. Langmuir probe measurements of the electron energy distribution function in magnetized gas discharge plasmas. *Plasma Sources Science and Technology*, 21(2):025004, 2012.

[103] Francis F Chen. Langmuir probe analysis for high density plasmas. *Physics of Plasmas (1994-present)*, 8(6):3029–3041, 2001.

[104] Isaac D Sudit and R Claude Woods. A study of the accuracy of various langmuir probe theories. *Journal of applied physics*, 76(8):4488–4498, 1994.

[105] BE Cherrington. The use of electrostatic probes for plasma diagnosticsa review. *Plasma chemistry and plasma processing*, 2(2):113–140, 1982.

[106] Minoru Sugawara. Electron probe current in a magnetized plasma. *Physics of Fluids (1958-1988)*, 9(4):797–800, 1966.

[107] Isaac D Sudit and R Claude Woods. A workstation based langmuir probe system for low-pressure dc plasmas. *Review of scientific instruments*, 64(9):2440–2448, 1993.

[108] Noah Hershkowitz. How langmuir probes work. *Plasma Diagnostics*, 1:113–183, 1989.

[109] Ian H Hutchinson. *Principles of plasma diagnostics*. Cambridge university press, 2005.

[110] M. J. R. Schwar and J. D. Swift. *Electrical Probes for Plasma Diagnostics*. American Elsevier, 1970.

[111] Tsv K Popov, M Dimitrova, FM Dias, VN Tsaneva, NA Stelmashenko, MG Blamire, and ZH Barber. Second derivative langmuir probe diagnostics of gas discharge plasma at intermediate pressures (review article). In *Journal of Physics: Conference Series*, volume 44, page 60. IOP Publishing, 2006.

[112] Lin Kui-Xun, Lin Xuan-Ying, Chi Ling-Fei, Yu Chu-Ying, Yao Ruo-He, and Yu Yun-Peng. The reliability of measurements on electron energy distribution function in silane rf glow discharges. *Chinese Physics*, 12(2):198, 2003.

[113] Orlando Auciello, Alberto Gras-Martí, Jose Antonio Valles-Abarca, and Daniel L Flamm. *Plasma-surface interactions and processing of materials*. Number 176. Springer, 1990.

[114] Harald A Habiger, Monika Auweter-Kurtz, and H Kurtz. Investigation of electron energy distributions in an mpg arc jet flow with electrostatic probes. IEPC-9515, 24th Int. Electric Prop. Conference, Moskau, 1995.

[115] FM Dias and Tsv Popov. Eedf probe measurements: differentiation methods, noise, and error. In *Journal of Physics: Conference Series*, volume 63, page 012005. IOP Publishing, 2007.

[116] H Andrei, V Covlea, VV Covlea, and E Barna. The smoothing and the digital processing of langmuir probe characteristic. *Romanian Reports in Physics*, 55(2):245–252, 2003.

[117] FM Dias and E Tatarova. Noise reduction in eedf numerical differentiation technique. *Le Journal de Physique IV*, 8(PR7):Pr7–257, 1998.

[118] Fumiyuki Fujita and Hatsuo Yamazaki. Determination of electron energy distribution function of plasmas by digital processing from langmuir probe characteristic. *Japanese journal of applied physics*, 29(10R):2139, 1990.

[119] AA Azooz. Four free parameter empirical parametrization of glow discharge langmuir probe data. *Review of Scientific Instruments*, 79(10):103501, 2008.

[120] Bong-Kyoung Park, Dai-Gyoung Kim, and Gon-Ho Kim. Analysis of langmuir probe data using wavelet transform. *Plasma Science, IEEE Transactions on*, 32(2):355–361, 2004.

[121] FM Dias and Tsv K Popov. Iterative method of evaluating the electron energy distribution function from probe measurements under collisional conditions. *Vacuum*, 69(1):159–163, 2002.

[122] Fririk Magnus and JT Gudmundsson. Digital smoothing of the langmuir probe iv characteristic. *Review of Scientific Instruments*, 79(7):073503, 2008.

[123] Abraham Savitzky and Marcel JE Golay. Smoothing and differentiation of data by simplified least squares procedures. *Analytical chemistry*, 36(8):1627–1639, 1964.

[124] Walter Gander and Jiri Hrebicek. *Solving problems in scientific computing using Maple and Matlab®*. Springer, 2004.

[125] Steven C Chapra and Raymond P Canale. Numerical methods for engineers: with programming and software applications. wcb, 1998.

[126] Manfred UA Bromba and Horst Ziegler. Application hints for savitzky-golay digital smoothing filters. *Analytical Chemistry*, 53(11):1583–1586, 1981.

[127] Jianwen Luo, Kui Ying, Ping He, and Jing Bai. Properties of savitzky–golay digital differentiators. *Digital Signal Processing*, 15(2):122–136, 2005.

[128] D Goorvitch. Calculation of instrument functions. *Journal of Quantitative Spectroscopy and Radiative Transfer*, 67(3):253–257, 2000.

[129] Howard C Hayden. Data smoothing routine. *Computers in Physics*, 1(1):74–75, 1987.

[130] LA Jacobson. A fast data smoothing algorithm. *Computers in Physics*, 4(4):400–402, 1990.

[131] Alan V Oppenheim, Ronald W Schafer, John R Buck, et al. *Discrete-time signal processing*, volume 2. Prentice-hall Englewood Cliffs, 1989.

[132] George J Miao and Mark A Clements. *Digital signal processing and statistical classification*. Artech House, 2002.

[133] Richard Wesley Hamming. *Digital filters*. Courier Dover Publications, 1989.

[134] John G Proakis. *Digital signal processing: principles algorithms and applications*. Pearson Education India, 2001.

[135] Fredric J Harris. On the use of windows for harmonic analysis with the discrete fourier transform. *Proceedings of the IEEE*, 66(1):51–83, 1978.

[136] Peter Steffen. On digital smoothing filters: A brief review of closed form solutions and two new filter approaches. *Circuits, Systems and Signal Processing*, 5(2):187–210, 1986.

[137] Walter R Hoegy and Larry H Brace. Use of langmuir probes in non-maxwellian space plasmas. *Review of scientific instruments*, 70(7):3015–3024, 1999.

[138] Svetlana V Ratynskaia, VI Demidov, and K Rypdal. Probe measurements of electron temperature and density in strongly magnetized plasma. *Review of Scientific Instruments*, 71(9):3382–3384, 2000.

[139] K-I Oyama, CH Lee, HK Fang, and CZ Cheng. Means to remove electrode contamination effect of langmuir probe measurement in space. *Review of Scientific Instruments*, 83(5):055113, 2012.

[140] WE Amatucci, PW Schuck, DN Walker, PM Kintner, S Powell, B Holback, and D Leonhardt. Contamination-free sounding rocket langmuir probe. *Review of Scientific Instruments*, 72(4):2052–2057, 2001.

[141] M Shimoyama, KI Oyama, T Abe, and AW Yau. Effect of finite electrode area ratio on high-frequency langmuir probe measurements. *Journal of Physics D: Applied Physics*, 45(7):075205, 2012.

[142] RM Clements. Plasma diagnostics with electric probes. *Journal of Vacuum Science and Technology*, 15(2):193–198, 1978.

[143] Edward P Szuszczewicz and Julian C Holmes. Surface contamination of active electrodes in plasmas: Distortion of conventional langmuir probe measurements. *Journal of Applied Physics*, 46(12):5134–5139, 1975.

[144] ML Solomon, S Teodoru, and G Popa. Secondary electron emission at langmuir probe surface. *Journal of optoelectronics and advanced materials*, 10(8):2011–2014, 2008.

[145] Noah Hershkowitz. How does the potential get from a to b in a plasma? *Plasma Science, IEEE Transactions on*, 22(1):11–21, 1994.

[146] Robert F Kemp and JMs Sellen Jr. Plasma potential measurements by electron emissive probes. *Review of Scientific Instruments*, 37(4):455–461, 1966.

[147] Noah Hershkowitz, Brian Nelson, James Pew, and David Gates. Self-emissive probes. *Review of Scientific Instruments*, 54(1):29–34, 1983.

[148] Francis F Chen. Modern uses of langmuir probes. Technical report, Nagoya Univ.(Japan). Inst. of Plasma Physics, 1985.

[149] En Yao Wang, Noah Hershkowitz, and Tom Intrator. Direct indication plasma potential diagnostic based on secondary electron emission. *Review of scientific instruments*, 57(6):1085–1089, 1986.

[150] M Mizumura, S Uotsu, S Matsumura, and S Teii. Probe system with bias compensation using a laser heated emissive probe for rf discharge plasma diagnostics. *Journal of Physics D: Applied Physics*, 25(12):1744, 1992.

[151] Roman Schrittwieser, Codrina Ionita, Petru Balan, Ramona Gstrein, Olaf Grulke, Thomas Windisch, Christian Brandt, Thomas Klinger, Ramin Madani, George Amarandei, et al. Laser-heated emissive plasma probe. *Review of Scientific Instruments*, 79(8):083508, 2008.

[152] R Schrittwieser, A Sarma, G Amarandei, C Ionita, T Klinger, O Grulke, A Vogelsang, and T Windisch. Results of direct measurements of the plasma potential using a laser-heated emissive probe. *Physica Scripta*, 2006(T123):94, 2006.

[153] JP Sheehan and N Hershkowitz. Emissive probes. *Plasma Sources Science and Technology*, 20(6):063001, 2011.

[154] Foster J. E. Davis C. N. Sommers, B. S and E. Viges. Preliminary characterization of ion energy spectra acquired from high current hollow cathodes. *International Electric Propulsion Conference*, 2013.

[155] Dan M Goebel, Kristina K Jameson, Ira Katz, and Ioannis G Mikellides. Potential fluctuations and energetic ion production in hollow cathode discharges. *Physics of Plasmas (1994-present)*, 14(10):103508, 2007.

[156] Lyon B King, Alec D Gallimore, and Colleen M Marrese. Transport-property measurements in the plume of an spt-100 hall thruster. *Journal of Propulsion and Power*, 14(3):327–335, 1998.

[157] HM Küdyan. Interpretation of electrostatic energy analyzer data of a flowing plamsa. *Review of Scientific Instruments*, 49(1):8–10, 1978.

[158] Karl R Spangenberg. *Vacuum tubes*, volume 1. McGraw-Hill New York, 1948.

[159] CL Enloe. High-resolution retarding potential analyzer. *Review of scientific instruments*, 65(2):507–508, 1994.

[160] J Arol Simpson. Design of retarding field energy analyzers. *Review of Scientific Instruments*, 32(12):1283–1293, 1961.

[161] E Bauer. Low energy electron microscopy. *Reports on Progress in Physics*, 57(9):895, 1994.

[162] David C Joy and Carolyn S Joy. Low voltage scanning electron microscopy. *Micron*, 27(3):247–263, 1996.

[163] GA Somorjai and HH Farrell. Low-energy electron diffraction. *Adv. Chem. Phys*, 20:215, 1971.

[164] EC Zipf. The ionization of atomic oxygen by electron impact. *Planetary and space science*, 33(11):1303–1307, 1985.

[165] MA Khakoo and SK Srivastava. A compact high current pulsed electron gun with subnanosecond electron pulse widths. *Journal of Physics E: Scientific Instruments*, 17(11):1008, 1984.

[166] JJ Rocca, JD Meyer, MR Farrell, and GJ Collins. Glow-discharge-created electron beams: Cathode materials, electron gun designs, and technological applications. *Journal of applied physics*, 56(3):790–797, 1984.

[167] J Gao. Theoretical investigation of the microwave electron gun. *Nuclear Instruments and Methods in Physics Research Section A: Accelerators, Spectrometers, Detectors and Associated Equipment*, 297(3):335–342, 1990.

[168] John Petillo, Kenneth Eppley, Dimitrios Panagos, Paul Blanchard, Eric Nelson, Norman Dionne, John DeFord, Ben Held, Liya Chernyakova, Warren Krueger, et al. The michelle three-dimensional electron gun and collector modeling tool: Theory and design. *Plasma Science, IEEE Transactions on*, 30(3):1238–1264, 2002.

[169] E Leon Chaffee. Theory of thermionic vacuum tubes. *Fundamentals. Amplifiers. Detectors. New York & London, mcGraw Hill*, 8, 1933.

[170] Colin James Smithells. *Metals reference book*, volume 2. Butterworths, 1962.

[171] Erik Lassner and Wolf-Dieter Schubert. *Tungsten: properties, chemistry, technology of the elements, alloys, and chemical compounds*. Springer, 1999.

[172] Günther Herrmann and Siegfried Wagener. The oxide-coated cathode. 1951.

[173] LS Nergaard. Electron and ion motion in oxide cathodes. In *Halbleiterprobleme*, pages 154–202. Springer, 1956.

[174] KT Jacob, Shubhra Raj, and L Rannesh. Vegard's law: a fundamental relation or an approximation? *International Journal of Materials Research*, 98(9):776–779, 2007.

[175] Stanley Humphries. *Charged particle beams*. Courier Dover Publications, 2013.

[176] Marc E Herniter and Ward D Getty. Thermionic cathode electron gun for high current densities. *Plasma Science, IEEE Transactions on*, 15(4):351–360, 1987.

[177] JW Luginsland, YY Lau, RJ Umstattd, and JJ Watrous. Beyond the child–langmuir law: A review of recent results on multidimensional space-charge-limited flow. *Physics of Plasmas (1994-present)*, 9(5):2371–2376, 2002.

[178] RJ Strangeway. Dependence of electron beam instability growth rates on the beam-plasma system parameters. *Journal of Geophysical Research: Space Physics (1978–2012)*, 87(A2):833–841, 1982.

[179] WD Getty and LD Smullin. Beam-plasma discharge: Buildup of oscillations. *Journal of applied Physics*, 34(12):3421–3429, 1963.

[180] David G Zidar and Joshua L Rovey. Hall-effect thruster channel surface properties investigation. *Journal of Propulsion and Power*, 28(2), 2012.

[181] A Dunaevsky, Y Raitses, and NJ Fisch. Secondary electron emission from dielectric materials of a hall thruster with segmented electrodes. *Physics of Plasmas (1994-present)*, 10(6):2574–2577, 2003.

[182] Iouri Bojko, Noël Hilleret, and Christian Scheuerlein. Influence of air exposures and thermal treatments on the secondary electron yield of copper. *Journal of Vacuum Science & Technology A*, 18(3):972–979, 2000.

[183] Marlene I Patino, Yevgeny Raitses, Bruce E Koel, and Richard E Wirz. Application of auger spectroscopy for measurement of secondary electron emission from conducting material for electric propulsion devices. In *33rd International Electric Propulsion Conference, Washington DC*, 2013.

[184] JR Anderson and AE Alexander. Theory of the vibrating condenser converter and application to contact potential measurements. *Australian Journal of Applied Science*, 3:201, 1952.

[185] NA Surplice and RJ D'arcy. A critique of the kelvin method of measuring work functions. *Journal of Physics E: Scientific Instruments*, 3(7):477, 1970.

[186] EO Johnson and L Malter. A floating double probe method for measurements in gas discharges. *Physical Review*, 80(1):58, 1950.

[187] Robert Eckman, Lawrence Byrne, Nikolaos A Gatsonis, and Eric J Pencil. Triple langmuir probe measurements in the plume of a pulsed plasma thruster. *Journal of Propulsion and Power*, 17(4):762–771, 2001.

[188] SG Ingram, BM Annaratone, and M Ohuchi. Design and use of a gridded probe in a low-pressure rf argon discharge. *Review of scientific instruments*, 61(7):1883–1891, 1990.

[189] G Bousselin, J Cavalier, JF Pautex, S Heuraux, N Lemoine, and G Bonhomme. Design and validation of the ball-pen probe for measurements in a low-temperature magnetized plasma. *Review of Scientific Instruments*, 84(1):013505, 2013.

[190] R Schrittwieser, C Ionita, J Adamek, J Stöckel, J Brotankova, E Martines, G Popa, C Costin, L Van De Peppel, and Guido Van Oost. Direct measurements of the plasma potential by katsumata-type probes. *Czechoslovak Journal of Physics*, 56(2):B145–B150, 2006.

[191] J Adamek, M Peterka, T Gyergyek, P Kudrna, M Ramisch, U Stroth, J Cavalier, and M Tichỳ. Application of the ball-pen probe in two low-temperature mag-netised plasma devices and in torsatron tj-k. *Contributions to Plasma Physics*, 53(1):39–44, 2013.

[192] Jiri Adamek, Matej Peterka, Tomaz Gyergyek, Pavel Kudrna, and Milan Tichỳ. Diagnostics of magnetized low temperature plasma by ball-pen probe. *Nukleonika*, 57:297–300, 2012.

[193] FW Crawford and RF Mlodnosky. Langmuir probe response to periodic waveforms. *Journal of Geophysical Research*, 69(13):2765–2773, 1964.

[194] RS Harp and FW Crawford. Characteristics of the plasma resonance probe. *Journal of Applied Physics*, 35(12):3436–3446, 1964.

[195] K Takayama, H Ikegami, and S Miyazaki. Plasma resonance in a radio-frequency probe. *Physical Review Letters*, 5(6):238, 1960.

[196] S Miyazaki, K Hirao, Y Aono, K Takayama, H Ikegami, and T Ichimiya. Resonance probea new probe method for measuring electron density and electron temperature in the ionosphere. *Rept. Ionosphere Space Res. Japan*, 14(2):148–159, 1960.

[197] Yoshi H Ichikawa and Hideo Ikegami. Theory of resonance probe. *Progress of Theoretical Physics*, 28(2):315–322, 1962.